

Doctoral Dissertation

Performance of Muon Trigger Chamber for ATLAS Detector and Development of the Cosmic Ray Test System

「ATLAS 実験用ミュオントリガーチェンバーの性能評価と、宇宙線検査設備の構築」

Graduate School of Science and Technology,
Kobe University

Takuya SUGIMOTO

February 24th, 2006

Contents

1	Introduction	5
2	Physics Motivation	8
2.1	Standard Model	8
2.2	Standard Model Higgs	10
2.2.1	Experimental Constraint of Higgs Mass	12
2.2.2	Higgs Production	12
2.2.3	Higgs Decay	15
2.3	Higgs Search in ATLAS Detector	16
2.3.1	Major Search Mode	16
2.3.2	Higgs Discovery Potential	17
3	Experimental Setup	19
3.1	LHC Accelerator	19
3.1.1	Luminosity	20
3.1.2	Particle Production Rates	21
3.2	ATLAS Detector	21
3.2.1	Inner Detector	23
3.2.2	Calorimetry	24
3.2.2.1	Electromagnetic Calorimeter	25
3.2.2.2	Hadron Calorimeter	25
3.2.3	Muon Spectrometer	27
3.2.3.1	Momentum Measurement	28
3.2.3.2	Muon Detector	29
3.2.3.3	Magnet System	30
3.2.3.4	MDT(Monitored Drift Tube)	31
3.2.3.5	CSC(Cathode Strip Chamber)	33
3.2.3.6	RPC(Resistive Plate Chamber)	34
3.2.3.7	TGC(Thin Gap Chamber)	35
3.2.4	Experimental Environment	35
3.2.5	ATLAS Trigger/DAQ System	37
3.2.6	LVL1 Endcap Muon Trigger	39
4	Thin Gap Chamber (TGC)	41
4.1	Operation Principle	41
4.1.1	Gas ionization by charged particles	41
4.1.2	Drift of electrons and ions in gases	42
4.1.3	Gas Amplification	42
4.1.4	Operation Mode	43

4.1.5	Multiwire Proportional Chamber (MWPC)	45
4.2	Requirements for the Performance	46
4.3	Structure of TGC	46
4.4	TGC Module	50
4.5	ASD(Amp Shaper Discriminator)	52
4.6	Production and Inspection	54
4.6.1	TGC Production	54
4.6.2	Inspection Schedules	54
5	Test Facility	57
5.1	Leak Test	57
5.1.1	Chamber Leakage	57
5.1.2	CO ₂ Channel	58
5.1.3	System Setup	58
5.1.4	Repair	59
5.1.5	Inner Leak	61
5.2	Results	62
5.3	High Voltage Test	65
5.3.1	Test Procedure	66
5.3.2	Short-circuit of the anode wire	67
5.3.3	Gas System	68
5.3.4	Current Monitoring System	68
5.3.4.1	Hardware	68
5.3.4.2	Software	72
5.3.5	Current Stability	74
5.3.6	Results	74
5.4	Cosmic Ray Test	76
5.4.1	Scintillation counter	77
5.4.1.1	Trigger Scheme	77
5.4.1.2	Efficiency of Scintillation counter	79
5.4.1.3	Timing Fluctuation	79
5.4.2	Drift Tube	80
5.4.3	Operation Principle	80
5.4.3.1	Structure of drift tube	81
5.4.3.2	Gas System	81
5.4.3.3	Readout	82
5.4.3.4	x-t relation	83
5.4.3.5	Spatial Resolution	86
5.4.4	DAQ System	86
5.4.4.1	TMC (Time Memory Cell)	88
5.4.4.2	SWINE (Super WireNet Encoder)	89
5.4.4.3	DAQ Process	90
5.4.4.4	Raw Data Format	91
5.4.4.5	Data Conversion	91
5.4.4.6	Data Confirmation	94

5.5	Gas System	98
5.5.1	Chemical Tolerance Test of the Tube	98
5.5.2	Mixing System	99
5.5.3	Distribution System	99
5.6	Measurement of Mixture Rate	101
5.6.1	Cosmic Ray Test	103
5.6.2	HV Test	103
5.7	Operation Condition	103
5.8	System Modification	105
5.8.1	T7T → T7D	105
5.8.2	T7D → T4	105
5.8.3	T4 → T5	105
6	Data Analysis	106
6.1	Analysis Process	106
6.2	Tracking Process	106
6.2.1	Hit Pattern Selection	106
6.2.2	track reconstruction	109
6.2.3	Rejection of Fake Track	109
6.3	Efficiency Measurement	111
6.4	Synthesize the Maps	113
6.5	Time response	118
7	Performance of the Test Station	120
7.1	Geant4 Simulation	120
7.1.1	Cosmic Ray Generator	121
7.1.2	Trigger Rate	121
7.2	Track Reconstruction Efficiency	123
7.3	Tracking Resolution	124
7.3.1	Knife-edge method	124
7.3.2	Estimation of the resolution	124
7.3.3	Multiple Coulomb Scattering	125
7.3.4	Dependence on MCS	127
7.3.5	Dependence on the energy of the cosmic ray muon	127
7.3.6	Dependence on the alignment of the TGC	127
7.3.7	Miss Track Rejection	129
7.3.7.1	χ^2 constraint	129
7.3.7.2	angle constraint	133
7.3.7.3	χ^2 and angle constraint	134
7.3.8	Conclusion for Tracking Resolution	134
7.4	Inspection Progress	137
8	Quality of the TGCs	140
8.1	Efficiency	140
9	Summary	145

1 Introduction

Elementary particle physics is the study of the fundamental particles of matter and their interactions. By “ elementary ” physicists mean that these particles have no measurable internal structure or components. They can thus be treated as ideal or point-like particles to the smallest scale of size available to physicists in the modern era, 10^{-19} meters. By “ fundamental ” we mean that the physical properties such as mass, electric charge, and spin of these infinitesimal particles underlies at the physical world of our everyday experience. These physical properties dictate how the fundamental particles themselves compose more complex particles and atoms. The properties of the fundamental particles then govern how those atoms in turn build molecules, cells, organisms and all bulk matter.

The fundamental particles currently known to physicists are the quarks, leptons, and gauge bosons. The gauge bosons (integer spin) mediate the interactions between the quarks (q) and leptons (l), which have 1/2-integer spin. One or more gauge bosons have been observed for each of the fundamental forces currently described by physicists with a working quantum field theory (QFT). The QFT describing the electromagnetic and nuclear interactions between quarks, leptons, and gauge bosons is called the Standard Model (SM) of particle physics.

The force carriers, such as photon and gluon, do not have mass, but the weak force carriers W^+ , W^- and Z^0 do. For symmetry reasons, the SM requires massless particles, unless some mechanism is incorporated that (partially) distorts the symmetry. The favored mechanism is that of “spontaneous gauge-symmetry breaking”, caused by a field that is associated to the Higgs particle (Higgs 1964, Englert & Brout 1964). This is the only particle of the Standard Model that has not yet been observed.

In the year 2007 the international scientific community will welcome a new era of experimental particle physics at the European Organization for Nuclear Research (Le Centre Européen de Recherche Nucléaire: CERN) in Geneva. Productive researches have been carried out for more than ten years at the Large Electron-Positron Collider (LEP) in CERN and TEVATRON in Fermi National Accelerator Laboratory in USA. Their highlights were the verification of the Standard Model up to an energy scale of about 200 GeV, the precision measurement of the W and Z masses and finally the discovery of the top quark.

After these successful researches, the Large Hadron Collider (LHC) will open up an unprecedented range of collision energies. The acceleration of electrons and positrons in ring colliders like LEP is practically limited by energy loss through synchrotron radiation which increases with γ^4/r , where γ is the Lorentz factor and r the radius of the storage ring. This effect is less important for hadrons which - due to their larger mass - acquire much more energy than electrons with the same γ . Thus the LHC, which will be installed in the same 27 km long ring tunnel as LEP, will be able to reach center-of-mass energies up to 14 TeV in proton-proton. This is an increase of a factor 7 in center-of-mass energy with respect to the TEVATRON, today’s most powerful hadron collider, and a factor 70 compared to LEP2. At the TeV energy scale which will now be accessible, a large potential for new physics is expected by theorists. The cross section of Higgs boson is quite less than that of the other particles, so a high luminosity is required. LHC is designed so as to increase the luminosity up

to is $1.0 \times 10^{34} \text{cm}^{-2} \text{m}^{-1}$. In order to realize such high luminosity, the interval of the proton bunch crossing is required to be 25nsec (corresponds to 40MHz collision rate).

Since the LHC opens up an unexplored energy region, the general-purpose detectors also have to be able to deal with the unexpected. The ATLAS detector (A Toroidal LHC ApparatuS) is one of the general-purpose detectors designed for an experiment with the LHC. The aim of this experiment is to probe further into the fundamental forces of nature than has been currently possible. In order to get there, lots of research has been undertaken to prove that the detectors can cope at least with a broad variety of expected physics processes. It is presently the most important phenomenon to be investigated and, henceforth, its discovery of prime importance to the LHC experimental programme.

In any experiment, it is important to separate " interested signals " from all signals. This separation is performed by using a characteristic signal; this technique is called " trigger ". In other words, the trigger signal decides whether the event should be acquired. The Higgs production cross section is quite smaller (about 10^{-9}) than the other event. In order to acquire the low S/N event by computer algorithm of data reduction, multi level trigger should be equipped. The ATLAS trigger is organized in three trigger levels (LVL1, LVL2 and LVL3). The LVL1 trigger uses reduced-granularity data from a subset of detectors. The LVL2 trigger uses full-granularity, full-precision data from most of the detectors, but examines only regions of the detector flagged at LVL1 as containing interesting information. The LVL3 trigger uses the full event data for the final selection of events for off-line analysis. In the LHC experiment, if all events are stored, the data size becomes huge due to the high luminosity. Therefore the trigger signal is also used to reduce the data size in high rate experiment. The rate of selected events is reduced to $\sim 100\text{Hz}$ for permanent storage.

The Muon is a just heavy electron (200 times heavier than an electron), but, because of its larger mass, produces much less synchrotron radiation. Therefore muons can reach outside of the detector hardly losing energy, and the muon spectrometers are aligned at the most outside of the detector. The muons with high momentum created at collision point are traveled to outside the detector. Their trajectory is bent by the toroidal magnet aligned inside of the muon spectrometer. By measuring the curvature, their momentum is measured. Muon trigger signal are created using the momentum. There are two detectors for muon trigger; Resistive Plate Chamber in barrel part and Thin Gap Chamber in endcap part. They also provided a fast digital signal within 25nsec gate defined by the interval between beam crossings. This thesis is mainly described Thin Gap Chamber.

The high luminosity imposes rather stringent requirements on the trigger detector performance. Thin gap chamber is designed in a way similar to MultiWire Proportional Chamber (MWPC), with the difference that the anode wire pitch is larger than the cathode-anode distance. Signals from the anode wires provide the trigger information together with readout strips arranged orthogonal to the wires. The gas is selected to $\text{CO}_2 : \text{n-C}_5\text{H}_{12} (\text{n-pentane}) = 55 : 45$. CO_2 plays role as a working gas and n-pentane as a quencher. The characteristic of the TGC is narrow timing spread of the signals. The following two performances are required for TGC; (1) High detection efficiency is required for trigger chamber; to be more than 99%, (2) Fast signal response is required for the bunch crossing identification; to be less than 25nsec. In order to cover the whole area on endcap region of ATLAS Detector (about 6000m^2), about 3600 TGCs is required.

They were produced in Japan, Israel, and China in parallel. In Japan, about 1200 TGCs were produced at High Energy Accelerator Research Organization (KEK). The production was started from 2001 and was finished in 2005.

All TGCs should be checked for their performance before installed to the ATLAS detector. In April 2001, the facility was constructed at Kobe University. The inspection of all TGC had to be

performed for three years. Therefore, it is indispensable to construct a large-scale facility to inspect TGC continuously for a long time.

In general, it is difficult to operate stably a large-scale facility for a long time. As the example, the operation of the nuclear reactor is the similar case. In the development of such system, it should be prepared to have a safety, flexibility, solidity, and efficient and easy operation. For safety, the system should be considered how to cope with emergency situations (e.g. power failure or miss operation). The system should be equipped with monitor and control systems to know what happen and not to expand the trouble. Flexibility and solidity is important in case of a maintenance and modification of the system. A lot of people are related to the system, so efficient and easy operation is significant.

There are four requirements for the quality assurance of TGCs. Firstly, the position-by-position detection efficiency should be measured at the whole detection area of TGC so as to detect the muons surely. Secondly, the stability of TGC should be checked for long-term operation. Thirdly, the gas tightness of TGC should be checked because n-pentane is flammable gas. Lastly, a lot of TGCs should be inspected at the same time because the schedule of the installation of TGC to ATLAS detector was already decided.

Cosmic ray muon is used as the source for efficiency measurement because of its uniform flux. We need to know when it came and where it passed through; i.e. the incoming muon trajectory should be reconstructed with adequate spatial resolution. For the solution of this, scintillation counters and drift tubes were used; the former is for the trigger and the latter is for the reconstruction of the muon trajectory. In order to check the stability, we should know the value of a current flowing between anode and cathode of TGC by applying adequate high voltage. If a TGC had some problems, however, the current become larger than a stable one. Therefore we developed a monitoring system of current. In addition, we need to increase the applied high voltage gradually because TGC may be broken off by applying a nominal operation voltage at the beginning of the inspection. So we developed the automatic control system of high voltage. In order to check the gas tightness, we applied a pressure to TGC. The pressure was decreased if there were some leakage, so we should measure this pressure drop. The applied pressure was allowed up to 600Pa because TGC was manufactured by only gluing their parts (not using any screw). For the solution of this, the measurement system with low differential pressure gauge was developed.

All TGCs were finished to inspect their performance in July 2005. We could find some problems of some chambers and classify all chambers into five grades. By this research, the performance of the trigger chambers for ATLAS experiment could be guaranteed.

In this thesis, I describe the development of the inspection station for Japanese TGC. The structure of the thesis is as follows. Chapter 2 contains a brief overview of the physics motivation together with the experimental method of Higgs boson search. Chapter 3 describes the experimental apparatus; the LHC accelerator and the ATLAS detector. In Chapter 4, the description is given on the Thin Gap Chamber. The details of the inspection system and method are presented in Chapter 5. In Chapter 6, the analysis method of the cosmic ray test. Chapter 7 describes the performance of the cosmic ray test station. The performance of TGC is described in Chapter 8. Finally, I present the summary and conclusion in Chapter 9.

2 Physics Motivation

2.1 Standard Model

The so-called 'Standard Model' of the electroweak theory[1][2][3] is a quantum field theory based on the gauge group $SU(2) \times U(1)$. The $SU(2)$ part represents the weak isospin symmetry, and the $U(1)$ part is for the weak hyper-charge. The symmetry is spontaneously broken by the Higgs mechanism, which gives masses to weak gauge bosons.

The model includes three generations of spin-1/2 fermions and corresponding anti-fermions as sources of the electroweak force:

- neutral leptons (neutrinos): $\nu_e(\bar{\nu}_e), \nu_\mu(\bar{\nu}_\mu), \nu_\tau(\bar{\nu}_\tau)$
- charged leptons: $e^- (e^+), \mu^- (\mu^+), \tau^- (\tau^+)$
- charge +2/3 quarks: $u(\bar{u}), c(\bar{c}), t(\bar{t})$
- charge -1/3 quarks: $d(\bar{d}), s(\bar{s}), b(\bar{b})$

They are listed above in the ascending order of their masses, whereas the neutrinos are assumed to be massless. The Standard Model does not restrict the number of generations to be three; it has been experimentally confirmed for the case of light neutrinos.

The boson fields mediating the interactions can be derived by the local gauge invariance of the Lagrangian. Requiring the Lagrangian density to be invariant under local $SU(2)$ transformations in the isospin space, the minimum interaction Lagrangian including an isospin triplet of gauge fields, $W_\mu^{1,2,3}$, is obtained. Similarly, requirement of the local $U(1)$ invariance results in a gauge field B_μ . The four gauge fields represent massless vector bosons, which do not directly correspond to physically observed electroweak bosons. The physically observed gauge bosons correspond to linear combinations of the $SU(2)$ and $U(1)$ gauge bosons:

$$W_\mu^+ = \frac{1}{\sqrt{2}}(W_\mu^1 - iW_\mu^2) \quad (2.1)$$

$$W_\mu^- = \frac{1}{\sqrt{2}}(W_\mu^1 + iW_\mu^2) \quad (2.2)$$

$$Z_\mu = \cos \theta_W W_\mu^3 - \sin \theta_W B_\mu \quad (2.3)$$

$$A_\mu = \sin \theta_W W_\mu^3 + \cos \theta_W B_\mu \quad (2.4)$$

where θ_W is an adjustable parameter called the Weinberg angle or weak mixing angle.

The couplings of the fermions to the gauge fields are obtained from the gauge invariance and the known electromagnetic and weak couplings at low energies. The experimental fact that the charged current interaction takes place in left-handed forms must also be taken into account. This fact is included into the model by hand: the Standard Model doesn't explain why the charged current has a $V - A$ form. Left-handed fermions are written as the isospin doublets

$$\begin{pmatrix} \nu_{eL} \\ e_L \end{pmatrix} \quad \begin{pmatrix} \nu_{\mu L} \\ \mu_L \end{pmatrix} \quad \begin{pmatrix} \nu_{\tau L} \\ \tau_L \end{pmatrix}$$

$$\begin{pmatrix} u_L \\ d_L \end{pmatrix} \quad \begin{pmatrix} c_L \\ s_L \end{pmatrix} \quad \begin{pmatrix} t_L \\ b_L \end{pmatrix},$$

while right-handed fermions stay SU(2) singlets

$$\begin{array}{cccccc} e_R & \mu_R & \tau_R & & & \\ u_R & c_R & t_R & d_R & s_R & b_R. \end{array}$$

The left-handed and right-handed fields for a fermion f are defined by

$$f_L = \frac{1}{2}(1 - \gamma_5)f, \quad (2.5)$$

$$f_R = \frac{1}{2}(1 + \gamma_5)f. \quad (2.6)$$

There are no right-handed neutrinos in the minimal Standard Model.

The Lagrangian describing the interactions between fermions and gauge bosons has three terms. The first, the charged current term is

$$\mathcal{L}_{cc} = \frac{g}{2\sqrt{2}}(J_{cc}^\mu W_\mu^- + h.c.), \quad (2.7)$$

where the charged current J_{cc}^μ is given by

$$J_{cc}^\mu = \begin{pmatrix} \bar{\nu}_{eL} & \bar{e}_L \end{pmatrix} \gamma^\mu \begin{pmatrix} \nu_{eL} \\ e_L \end{pmatrix} \quad (2.8)$$

for electrons and other leptons, and by

$$J_{cc}^\mu = \begin{pmatrix} \bar{u}_L & \bar{c}_L & \bar{t}_L \end{pmatrix} \gamma^\mu U \begin{pmatrix} d_L \\ s_L \\ b_L \end{pmatrix} \quad (2.9)$$

for quarks. The unitary matrix U describes the mixing of the weak couplings of quarks, and is often called as the Cabibbo-Kobayashi-Maskawa matrix. Comparing the coupling constant in equation (2.7) with the Fermi-type four point vertex Lagrangian for muon decays, a relationship

$$\frac{g^2}{8m_W^2} = \frac{G_F}{\sqrt{2}} \quad (2.10)$$

is obtained, where G_F is the Fermi constant,

$$G_F = 1.16637(2) \times 10^{-5} GeV^{-2} \quad (2.11)$$

The second, the electromagnetic term is

$$\mathcal{L}_{em} = g \sin \theta_W (J_{em}^\mu A_\mu + h.c.), \quad (2.12)$$

where the electromagnetic current J_{em}^μ is given by

$$J_{em}^\mu = q_f \bar{f} \gamma^\mu f \quad (2.13)$$

for any fermion f with charge q_f . Comparing equation (2.12) with the usual electromagnetic interaction Lagrangian, the relation

$$e = g \sin \theta_W = g' \cos \theta_W \quad (2.14)$$

is obtained. It follows from equations (2.10) and (2.14) that the mass of W^\pm is given by

$$m_W = \sqrt{\frac{\pi\alpha}{\sqrt{2}G_F \sin^2 \theta_W}} \quad (2.15)$$

$$= \frac{37.280 \text{ GeV}}{\sin \theta_W} \quad (2.16)$$

The Z^0 mass is related to m_W as

$$m_Z = \frac{m_W}{\cos \theta_W} \quad (2.17)$$

The third, the neutral current term is

$$\mathcal{L}_{nc} = \frac{e}{\sin \theta_W \cos \theta_W} (J_{nc}^\mu Z_\mu + h.c.), \quad (2.18)$$

where the neutral current J_{nc}^μ is given by

$$J_{nc}^\mu = g_V^f \bar{f} \gamma^\mu f + g_A^f \bar{f} \gamma^\mu \gamma_5 f \quad (2.19)$$

for any fermion f . The vector and axial-vector coupling constants g_V^f and g_A^f are given by

$$g_V^f = I_3 - 2q_f \sin^2 \theta_W, \quad (2.20)$$

$$g_A^f = I_3, \quad (2.21)$$

where I_3 is the third component of the weak isospin. The coupling constants g_f , g_V^f and g_A^f are summarized in Table 2.1.

Fermion	q	g_V	g_A
ν	0	$\frac{1}{2}$	$\frac{1}{2}$
e, μ, τ	-1	$-\frac{1}{2} + 2 \sin^2 \theta_W$	$-\frac{1}{2}$
u, c, t	$\frac{2}{3}$	$\frac{1}{2} - \frac{4}{3} \sin^2 \theta_W$	$\frac{1}{2}$
d, s, b	$-\frac{1}{3}$	$-\frac{1}{2} + \frac{2}{3} \sin^2 \theta_W$	$-\frac{1}{2}$

Table 2.1: Electroweak coupling constants of fermions

2.2 Standard Model Higgs

Electroweak theory predicts the existence of four gauge bosons, γ , W^\pm , and Z^0 . These are necessarily massless in order to preserve the local gauge invariance of the theory. However, it is known that W^\pm and Z^0 bosons of the weak interaction have mass. The Higgs mechanism[4][5][6] provides a possible explanation of the origin of the masses through gauge invariant spontaneous symmetry breaking of the electroweak sector. It is an extension of the Goldstone Theorem which states that if a Lagrangian has a global symmetry which is not a symmetry of the vacuum (i.e. the ground state) then there must exist one massless boson, scalar or pseudo-scalar, associated to each generator which does not annihilate the vacuum. These modes are known as the Goldstone Bosons. In the Higgs mechanism a weak isospin doublet of complex scalar fields $\phi^0(x)$ and $\phi^+(x)$ is introduced which must belong to the $SU(2)_L \otimes U(1)_Y$ multiplets and along with the scalar potential $V(\phi)$

$$\phi(x) = \begin{pmatrix} \phi^+(x) \\ \phi^0(x) \end{pmatrix} = \frac{1}{\sqrt{2}} \begin{pmatrix} \phi_1(x) + i\phi_2(x) \\ \phi_3(x) + i\phi_4(x) \end{pmatrix} \quad (2.22)$$

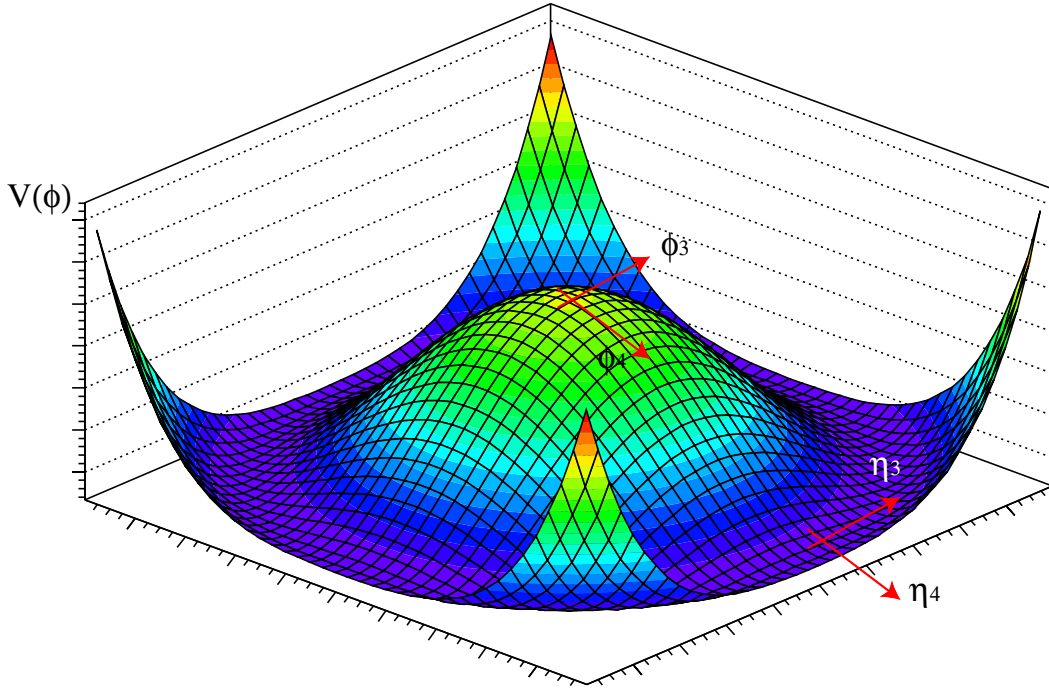


Fig. 2.1: The Higgs potential V (2.23) for a complex scalar field with $\mu^2 < 0$ and $\lambda > 0$.

$$V(x) = \mu^2 \phi^\dagger \phi + \lambda (\phi^\dagger \phi)^2, \quad \lambda > 0. \quad (2.23)$$

This gives a contribution to the electroweak Lagrangian, L_{Higgs} , where D_μ is the covariant derivative:

$$\mathcal{L}_{Higgs} = (D_\mu \phi)^\dagger (D_\mu \phi) - V(\phi), \quad D^\mu = \partial^\mu - i \frac{g}{2} \sigma \cdot \mathbf{W}^\mu - i \frac{g'}{2} Y B^\mu. \quad (2.24)$$

The minimum of V corresponds to the ground state of the system or vacuum which is at $|\phi| = 0$ for $\mu^2 > 0$, but for the choice $\mu^2 < 0$ the minimum shifts to

$$|\phi^2| = \phi \phi^\dagger = \frac{1}{2} (\phi_1^2 + \phi_2^2 + \phi_3^2 + \phi_4^2) = -\frac{\mu}{2\lambda} = \frac{v^2}{2}, \quad (2.25)$$

where v is the vacuum expectation value. The above solutions are now degenerate and any point satisfying the equation of a circle is a ground state. The perturbation procedure of Feynman calculus starts with fields which are fluctuations from the vacuum ground state. This leads to the definition of two new field variables η_1 and η_2 , so that the potential is of the form in Fig2.1. They have their origin at an arbitrarily chosen minimum

$$| \langle 0 | \phi | 0 \rangle | = \frac{1}{\sqrt{2}} \begin{pmatrix} 0 \\ v \end{pmatrix}, \quad \text{where } \phi_1 = \phi_2 = \phi_4 = 0, \quad \phi_3^2 = v^2, \quad (2.26)$$

$$\eta_3 = \phi_3 - v \quad \text{and} \quad \eta_4 = \phi_4.$$

The symmetry of the Lagrangian becomes hidden by the choice of a particular minimum. The Lagrangian expressed in terms of the new fields reveals a massive scalar particle η_3 of mass

$$M_{Higgs} = \sqrt{2\lambda v^2}, \quad (2.27)$$

the Higgs boson H , and three massless Goldstone bosons ϕ_1 , ϕ_2 , and η_4 . These unwanted Goldstone bosons can be removed by applying a unitary gauge transformation to $\phi(x)$ such that only the real Higgs field remains,

$$\phi(x) = U\phi(x) = \frac{1}{\sqrt{2}} \begin{pmatrix} 0 \\ v + H(x) \end{pmatrix}. \quad (2.28)$$

Electroweak Boson Masses

In doing so, the three Goldstone bosons disappear from the theory: their corresponding degrees of freedom are eaten by the W^\pm and Z^0 fields which acquire mass and a third, longitudinal, polarization state. By invoking the Higgs mechanism, expanding the fields about the chosen vacuum ϕ^0 and gauging away the Goldstone bosons, the gauge boson masses are generated:

$$M_W = \frac{gv}{2}, \quad M_Z = \frac{gv}{2 \cos \theta_W}, \quad M_\gamma = 0. \quad (2.29)$$

Fermions Masses

As well as coupling to the gauge fields W_μ and B_μ , the Higgs field couples to the fermion matter fields to generate their masses. The coupling of the Higgs field to a fermion pair is parameterized by an arbitrary Yukawa coupling constant $\lambda_f = m_f \sqrt{2}/v$, different for each fermion and proportional to its mass m_f . Lepton number conservation is assumed within the SM, giving a diagonal lepton mass matrix. The lack of quark generation number conservation in electroweak interactions means that the observed physical mass eigenstates of quarks are not eigenstates of weak isospin. The level of quark mixing is parameterized in terms of the Cabibbo-Kobayashi-Maskawa mixing matrix.

2.2.1 Experimental Constraint of Higgs Mass

Of particular interest is the constraint on the mass of the Higgs boson, because this fundamental ingredient of the Standard Model has not been observed yet. Fig.2.2[7] shows the $\Delta\chi^2$ curve derived from high- Q^2 precision electroweak measurements, performed at LEP as a function of the Higgs-boson mass, assuming the Standard Model to be the correct theory of nature. The preferred value for its mass, corresponding to the minimum of the curve, is at 91GeV, with an experimental uncertainty of +45 and -32GeV (at 68 percent confidence level derived from $\Delta\chi^2 = 1$ for the black line, thus not taking the theoretical uncertainty shown as the blue band into account).

While this is not a proof that the Standard-Model Higgs boson actually exists, it does serve as a guideline in what mass range to look for it. The precision electroweak measurements tell us that the mass of the Standard-Model Higgs boson is lower than about 186GeV (one-sided 95 percent confidence level upper limit derived from $\Delta\chi^2 = 2.7$ for the blue band, thus including both the experimental and the theoretical uncertainty). This limit increases to 219GeV when including the LEP-2 direct search limit of 114GeV shown in yellow.

2.2.2 Higgs Production

This section describes the most important Higgs boson production processes. Fig.2.3 shows typical Feynman diagrams of Higgs production for proton collider. The relevant cross sections are depicted in Fig.2.4 [16].

$gg \rightarrow H$

The gluon fusion processes (Fig.2.3 (a)) proceed primarily through a top quark triangle loop[8][9][10],

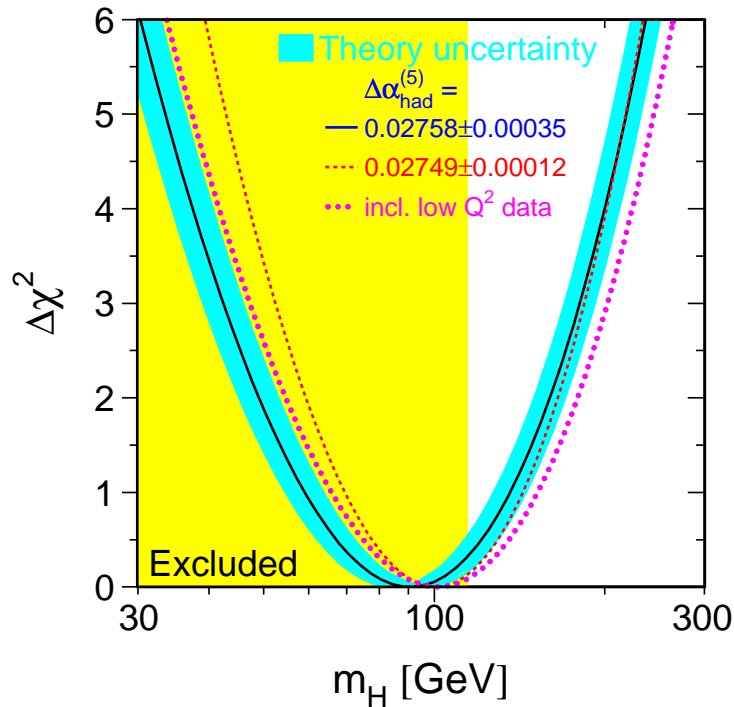


Fig. 2.2: $\Delta\chi^2 = \chi^2 - \chi_m^2$ in vs. m_H curve. The line is the result of the fit using all LEP data [7]; the band represents an estimate of the theoretical error due to missing higher order corrections. The vertical band shows the 95% CL exclusion limit on m_H from the direct search. The dashed curve is the result obtained using the evaluation of $\Delta\alpha_{had}^{(5)}(m_Z^2)$ from [17].

and is the dominant neutral Higgs boson production mechanism at LHC, with cross-sections of roughly 200 - 0.1 pb for $M_{Higgs} = 100 - 1000 \text{ GeV}/c^2$. The dependence of the gluon fusion cross-section on different parton densities yields roughly an additional 15% uncertainty in the theoretical prediction.

$qq \rightarrow qqV^*V^* \rightarrow qqH$

The vector boson fusion (VBF, Fig.2.3 (b)) is a shorthand notation for the full $qq \rightarrow qqH$ process, where both quarks radiate virtual vector bosons which then annihilate to produce the Higgs boson. The resulting Standard Model cross-sections are in the range 5 - 0.01 pb for $M_{Higgs} = 100 - 1000 \text{ GeV}/c^2$.

$gg, qq \rightarrow t\bar{t}H$

Also the process $gg, q\bar{q} \rightarrow t\bar{t}H$ (Fig.2.3 (c)) is relevant only for small Higgs masses, Fig.2.4. The analytical expression for the parton cross section, even at lowest order, is quite involved, so that just the final results for the LHC cross section are shown in Fig.2.4.

Associated production with top quarks is also an interesting process for measurements of the fundamental Htt Yukawa coupling. The cross section $\sigma(pp \rightarrow t\bar{t}H)$ is directly proportional to the square of this fundamental coupling. If $m_{Higgs} > 130 \text{ GeV}$, Yukawa coupling can be measure using $t\bar{t}H \rightarrow WW$ channel with cross-section of $> 125 \text{ fb}$. Main background of this channel is $t\bar{t}$ and $t\bar{t}W/Z$.

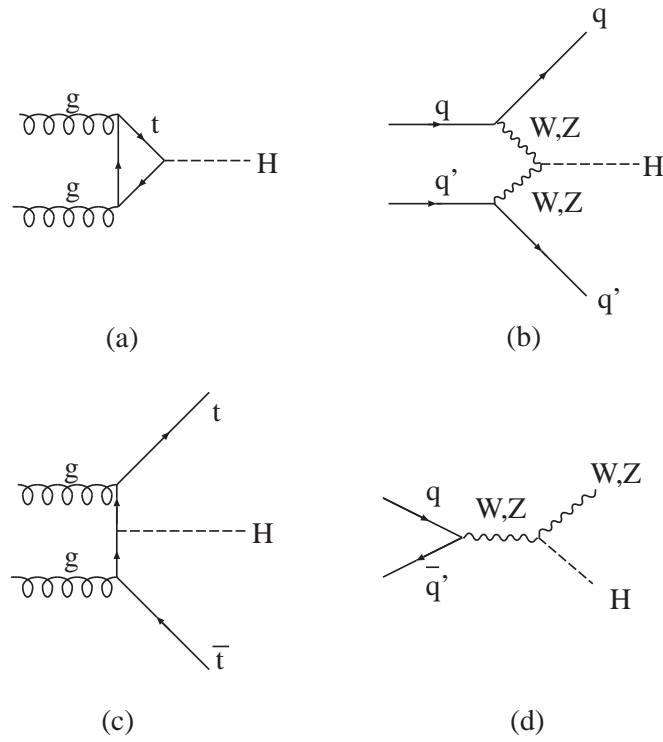


Fig. 2.3: Higgs Production diagram: (a)gluon fusion process, (b)Vector Boson Fusion process, (c) $t\bar{t}H$ production process, (d)W/Z associate production

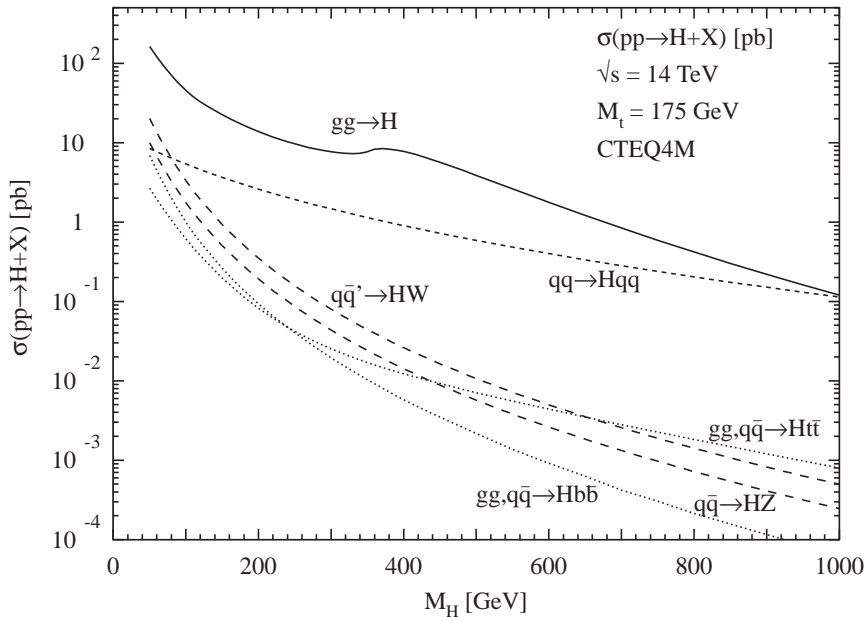


Fig. 2.4: Production cross section of Higgs[16]

$$q\bar{q} \rightarrow V^* \rightarrow VH$$

The cross-section for $q\bar{q} \rightarrow W^\pm H$ (Fig.2.3 (d), summed over both W charge states) reaches values of $2 - 0.001$ pb for $M_{Higgs} = 100 - 1000 \text{ GeV}/c^2$. The corresponding $q\bar{q} \rightarrow ZH$ cross-section is roughly a factor of two lower over the same Higgs boson mass range. The theoretical uncertainty is estimated to be about 15% from the remaining scale dependence. The dependence on different sets of parton densities is rather weak and also leads to a variation of the production cross-sections by about 15%. The signature of Higgs boson production in the VH channel are governed by the corresponding decays of the Higgs boson and vector boson.

2.2.3 Higgs Decay

Like most other elementary particles, the Higgs boson is not stable, which means that it will decay immediately after having been produced. Again, the largest coupling is to decay products with the highest possible mass. This is shown in Fig.2.5, where the branching ratios to particular decay products are given as a function of the nominal Higgs mass.

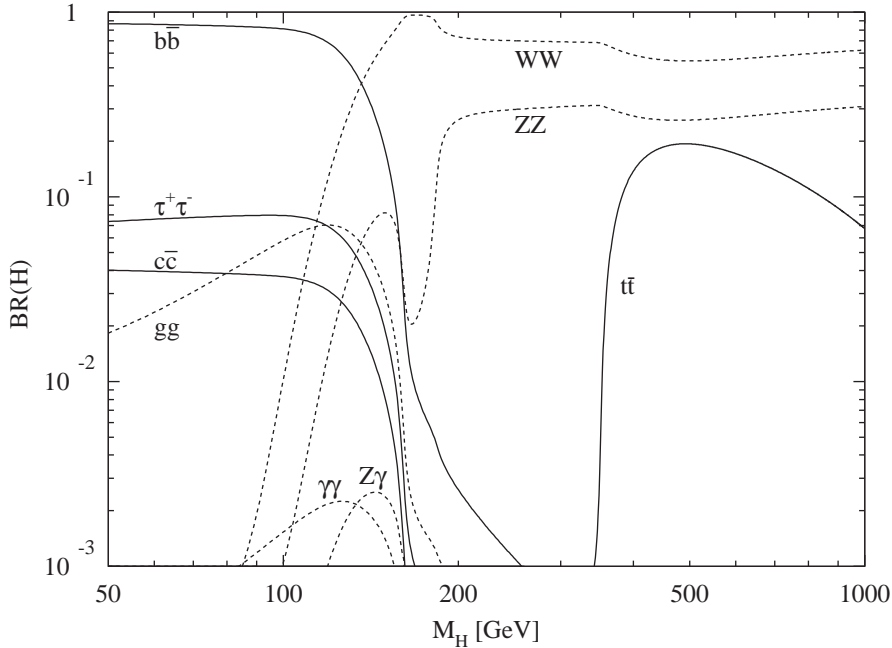


Fig. 2.5: Decay Width of Higgs boson as a function of Higgs Mass (M_H)[16].

The decay $H \rightarrow b\bar{b}$ dominates up to $m_{Higgs} \approx 140 \text{ GeV}/c^2$, from where the decay $H \rightarrow W^+W^-$ is taking over to dominate up to the theoretical limit of $m_{Higgs} \leq 1 \text{ TeV}/c^2$. Other decays of importance, i.e. accounting for more than ten percent of the Higgs decay, are $H \rightarrow ZZ^{(*)}/\gamma$, especially when both Z bosons are real, and $H \rightarrow t\bar{t}$ as soon as the threshold $m_{Higgs} \geq 2m_t$ has been passed. Some decays can possibly lead to clear event topologies, i.e. decays into relatively stable particles that lead to easily recognizable event topologies. However, most of the decays lead to multiple jets of particles. These particle jets are caused by cascade decays, where a decay product almost immediately decays itself.

A particularly clear event topology is the "golden" Higgs decay channel: four high energy muons form two pairs originating from the decay of real Z bosons from the Higgs decay, i.e. $H \rightarrow ZZ \rightarrow \mu^+\mu^-\mu^+\mu^-$. The chance for this particular decay channel to occur is not very large, as three small branching ratios are involved: $\text{BR}(H \rightarrow ZZ) \sim 30\%$ for $m_{Higgs} > 200\text{GeV}/c^2$ and $\text{BR}(ZZ \rightarrow \mu^+\mu^-) = 3.36\%$ independently of m_{Higgs} , which yields $\text{BR}(H \rightarrow 4\mu^\pm) \approx 3.4 \times 10^{-4}$ for $m_{Higgs} > 200\text{GeV}/c^2$. Ironically enough, this is comparable to the direct decay probability $H \rightarrow \mu^+\mu^-$, which has a branching ratio of $\approx 2 \times 10^{-4}$ for $m_{Higgs} < 125\text{GeV}/c^2$. However, events with just two high energy muons do not provide a clear, or better yet, distinct enough event topology. There are too many QCD background processes in which two high energy muons are produced, e.g. $pp \rightarrow Z + X \rightarrow \mu^+\mu^- + X$ where the Z is produced directly.

The four-muon event topology is of interest as well when one of the Z bosons is not real. This happens when the Higgs mass is below the $2m_Z \approx 180\text{GeV}/c^2$ threshold. The virtual Z or massive photon, denoted as γ^*/Z^* has the same properties as a real Z boson except for the lower mass. However, there are now other QCD processes that yield a comparable four-muon event topology.

2.3 Higgs Search in ATLAS Detector

2.3.1 Major Search Mode

In Fig.2.5 the branching ratios are shown for Higgs masses between 50 and $1\text{TeV}/c^2$. Only a few decay channels of the Higgs boson are accessible to experimental observation since the decay channels have either small branching ratios, or they are obscured by a large background of events. Statistics will be the limiting factor in the detection of the Higgs boson, in particular for Higgs masses approaching $1\text{TeV}/c^2$.

- **Low-Mass Higgs Boson ($M_H < 120\text{GeV}/c^2$):**

Below the WW or ZZ threshold ($M_H < 2M_Z$), the dominant decay into the heaviest accessible pair of quarks

$$H \rightarrow b\bar{b} \tag{2.30}$$

is swamped by the QCD background (the direct $b\bar{b}$ cross-section is very high, see Fig.2.5).

The decay channel

$$H \rightarrow \gamma\gamma \tag{2.31}$$

suffers an enormous background from $q\bar{p} \rightarrow \gamma\gamma$, $gg \rightarrow \gamma\gamma$, $gq \rightarrow q\gamma\gamma$ and $Z \rightarrow e^+e^-$ processes, where the jets or e^\pm fake a γ . These backgrounds can be reduced with excellent photon resolution and excellent γ/jet and γ/e^\pm separation. Hence an electromagnetic calorimetry with excellent performance is required.

- **Search for VBF $H \rightarrow \tau\tau$ mode**

When the mass of Higgs is relatively small ($115 < m_{Higgs} < 140\text{ GeV}$), a vector boson fusion process with

$$H \rightarrow \tau^+\tau^- \tag{2.32}$$

plays a important role for this discovery [18]. In this channel, $\tau\tau \rightarrow$ leptonic decay + hadronic decay (lepton-hadron mode) is as important as leptonic + leptonic (lepton-lepton mode) because a branching ratio of hadronic tau decay is larger than that of leptonic tau decay by a factor of ~ 2 . It leads this channel to the first discovery of Higgs.

Since W and Z bosons are heavy, the out-going quarks have larger transverse momenta (p_T) than the QCD background processes. They will be observed in a forward region with high- p_T . Tagging these forward jets help us to suppress the background processes. Furthermore, there is no color exchange between two out-going quarks, the Higgs boson will be observed in large rapidity gap, where activities of QCD jets are small.

$H \rightarrow \tau\tau$ provides high- p_T lepton from a leptonic tau decay and it can be used as a trigger of this event. Momenta carried by ν 's emitted from τ decays can be estimated using the \cancel{E}_T information.

Dominant background process is Drell-Yan with two high- p_T jets and the invariant mass distribution makes a peak at Z_0 mass.

- **Intermediate-Mass Higgs Boson** ($120\text{GeV}/c^2 < M_H < 800\text{GeV}/c^2$):

In this mass region the decay

$$H \rightarrow ZZ^{(*)} \rightarrow l^+l^-l^+l^- \quad (2.33)$$

provides a very clean signature of the Higgs boson. For the range $M_H < 2M_Z$ one of the two Z bosons is virtual (off-shell). For a Higgs mass of $150\text{GeV}/c^2$ one expects ~ 550 such events per year. The four leptons have a high transverse momentum ($5\text{GeV}/c < p_T < 50\text{GeV}/c$). The background is mainly coming from prompt muons, decay muons, hadronic punch-through, neutrons and muon induced electromagnetic secondaries. To achieve a good acceptance for such kind of events, the geometrical and kinematic acceptance for leptons has to be maximized, the significance of the signal will depend on the four-lepton mass resolution. Hence a good lepton energy and momentum resolution at the level of 1% is necessary. For large Higgs boson masses the Higgs width increases rapidly and the signal will be rate limited, hence the accelerator luminosity becomes more important than the detector performance.

- **Heavy-Mass Higgs Boson** ($M_H > 800\text{GeV}/c^2$):

For a heavy Higgs boson the channel

$$H \rightarrow ZZ \rightarrow l^+l^-\nu\bar{\nu} \quad (2.34)$$

becomes six times more frequent than $H \rightarrow ZZ \rightarrow l^+l^-l^+l^-$ and can be detected with the measurements of two high- p_T leptons and a high missing E_T due to the escaping neutrinos. Also the channels

$$H \rightarrow WW, ZZ \rightarrow l^\pm + \nu + 2jets, 2l^\pm + 2jets \quad (2.35)$$

provide promising signatures for a heavy Higgs boson.

2.3.2 Higgs Discovery Potential

In the search for the Higgs boson it could be convincingly demonstrated that the ATLAS experiment is capable of detecting a Standard Model Higgs boson with a high significance ($> 5\sigma$) in the mass range allowed, which extends from $\sim 100\text{GeV}$ (present LEP limit) to $\sim 1\text{TeV}$.

A discovery potential of Higgs at ATLAS is shown as a function of the Higgs boson mass for individual channels as well as for the combination of all channels in Fig.2.6. Over a large fraction of the mass range considered the Higgs boson can be discovered in at least two independent channels. In comparison to studies performed previously, the ATLAS sensitivity in additional, new channels could

be established. For heavy case ($m_{Higgs} > 200\text{GeV}$), a decay into $ZZ \rightarrow l^+l^-l^+l^-$ has an excellent performance of much higher than 10σ .

The potential in the intermediate range of Higgs mass is shown in Fig.2.6 of right with an integrated luminosity of 30fb^{-1} . The vector boson fusion process with $H \rightarrow \tau\tau$ and $H \rightarrow W^+W^-$ provides an excellent sensitivity in the mass region of 115-140GeV and 125-190GeV respectively. A significance combined with 6 promising channels is larger than 8σ . This corresponds to the fact that we can perform 5σ discovery of the Higgs boson (114-200GeV) within the first year run (10fb^{-1}).

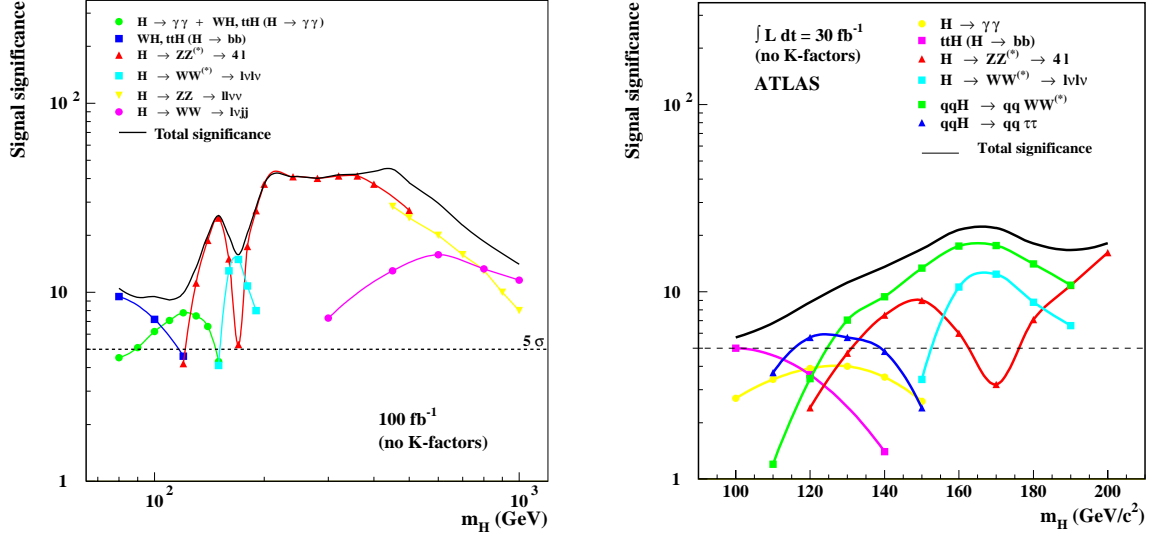


Fig. 2.6: Left: ATLAS sensitivity for the discovery of a Standard Model Higgs boson with full range (100-1000 GeV). The statistical significances are plotted for individual channels, as well as for the combination of all channels, assuming an integrated luminosity of 100fb^{-1} [15]. Right: Intermediate mass range (100-200GeV) with an integrated luminosity of 30fb^{-1} [18]. The blue line indicate the significance of the VBF process.

3 Experimental Setup

This chapter gives an introduction to the Large Hadron Collider (LHC). This accelerator will allow to explore particle physics up to energies that dominated the universe just 10^{-12} sec after the "Big Bang" when the temperature was about 10^{16} K. We will discuss the design of the ATLAS experiment and - in greater detail - its Muon System.

3.1 LHC Accelerator

LHC is a proton-proton collider with world largest center-of-energy $\sqrt{s} = 2 \times 7 = 14$ TeV at CERN. It is planned to be operational in the year 2007. Owing to the composite nature of the proton, only a fraction of the beam energy will be available for an elementary parton interaction. To enhance the observability of heavy particles originating from infrequent hard encounters where the colliding constituents take a large fraction of the total momentum, the LHC designers aim for a maximum luminosity as high as $10^{34} \text{cm}^{-2} \text{s}^{-1}$. This design luminosity will be achieved by having a bunch of 10^{11} protons every 25nsec in both colliding beams whose transverse radii will be $16\mu\text{m}$. The parameter of LHC is listed in Table 3.1.

Main Ring	26,658.87m	Bunch Interval	24.95nsec
Injector Energy	450GeV	Number of proton	1.1×10^{11} /bunch
Proton Energy	7.0TeV	Bunch Length	77mm
High Luminosity(7years)	$10^{34} \text{cm}^{-2} \text{s}^{-1}$	beam radius	$15.9 \mu\text{m}$
Low Luminosity(3years)	$10^{33} \text{cm}^{-2} \text{s}^{-1}$	beam crossing angle	$300 \mu\text{rad}$
Luminosity Lifetime	10hours		

Table 3.1: The parameter list for the LHC Accelerator. [19]

The LHC will make maximum use of the existing accelerator infrastructure at CERN (Fig.3.1) before injecting them into the LHC. The Super Proton Synchrotron (SPS) will be the final pre-injector for the LHC, accelerating $26\text{GeV}/c$ protons from the PS to $450\text{GeV}/c$ before extraction to LHC. The beam line will be occupied with super-conducting NbTi bending magnets, quadrupoles for the beam optics and accelerating cavities. These magnets will house two separated beam lines with opposite magnetic fields of 8.4T strength. The 1232 dipole magnets along the beam line will be $\sim 14.6\text{m}$ long. There are 4 interaction points in LHC, and the following detector is arranged at each points.

1. ATLAS (A Troidal LHC ApparatuS)
2. CMS (The Compact Muon Solenoid)
3. LHC-B
4. ALICE (A Large Ion Collider Experiment)

ATLAS and CMS are the general-purpose detectors, LHC-B is the specialized detector for B Physics and ALICE is one for heavy ion collision (1PeV Pb-Pb collision at maximum).

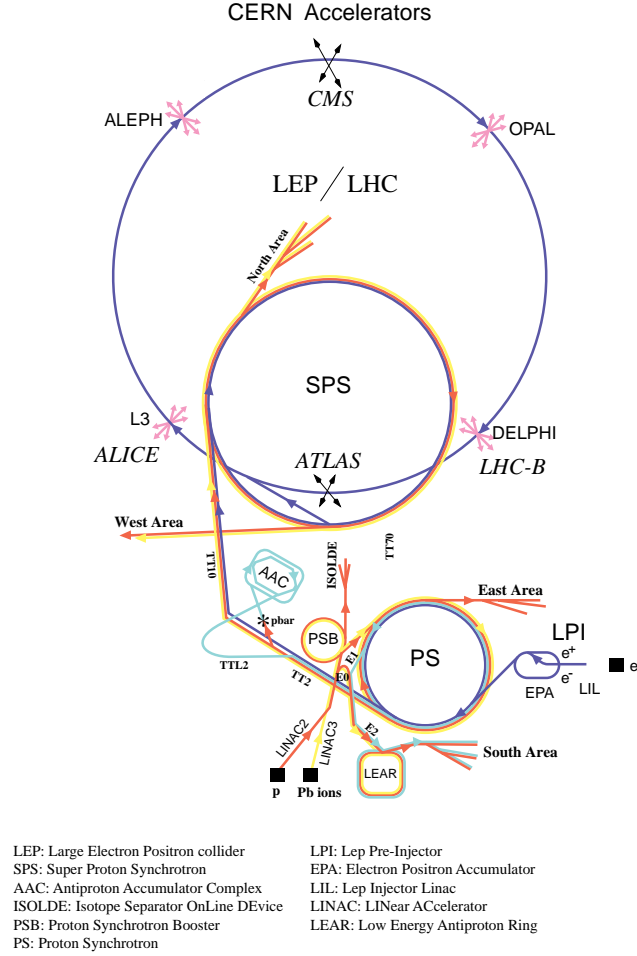


Fig. 3.1: Schematic view of the CERN accelerator complex.

3.1.1 Luminosity

One of parameters of a colliding-type accelerator is the luminosity \mathcal{L} . For a physical process of cross-section σ , the event rate is given by

$$\frac{dN}{dt} = \sigma \mathcal{L}. \quad (3.1)$$

in the case of a head-on collider like LHC, the luminosity is given by

$$\mathcal{L} = \frac{N_{p1} N_{p2} f_{cross}}{4\pi \sigma_x^* \sigma_y^*}, \quad (3.2)$$

where N_{p1} and N_{p2} are the number of proton per each bunch respectively, f_{cross} is the bunch crossing frequency, and $\sigma_x^* \sigma_y^*$ is the cross-section of the bunches at the interaction point. It is obvious from equation (3.2) that better luminosity is attained by:

- increasing N_{p_1} and N_{p_2} ,
- increasing f_{cross} ,
- decreasing $\sigma_x^*\sigma_y^*$, i.e., focusing the beam to a smaller spot at the interaction point.

The design luminosity of LHC is $1.0 \times 10^{34} \text{cm}^{-2} \text{m}^{-1}$ for each interaction point. For rough estimation, each parameter follows the following calculation:

$$\mathcal{L} = \frac{N_{p_1} N_{p_2} f_{cross}}{4\pi\sigma_x^*\sigma_y^*} \quad (3.3)$$

$$= \frac{(10^{11}[\text{proton/bunch}])^2 \times 40[\text{MHz}]}{4\pi(16[\mu\text{m}])^2} \quad (3.4)$$

$$\sim 10^{34}[\text{cm}^{-2}\text{s}^{-1}] = 10[\text{nb}^{-1}\text{s}^{-1}]. \quad (3.5)$$

There are two operation modes of luminosity at the LHC; one is called "high-luminosity mode" and another is called "low-luminosity mode". The later mode is $10^{33} \text{cm}^{-2} \text{s}^{-1}$ for the first 3 years.

At high luminosity, each bunch crossing contains an average of 23 proton-proton collisions. These events are called "minimum-bias event".

3.1.2 Particle Production Rates

LHC will collide protons onto protons, with a centre-of-mass (total collision) energy of 14 TeV. At these energies not only can the valence-quarks collide, but also the gluons holding them together, and a whole sea of quark-antiquark pairs that are allowed a fleeting existence under the laws of quantum mechanics. The partons that collide carry only a part of the total energy of the proton. Effectively, mass states up to a few TeV can be created.

Fig.3.2 shows the prediction of particle-production cross-sections for the particles of most interest at the LHC, compared to those of the Tevatron, which collides protons onto antiprotons. Also shown is the expected production rate at the LHC for " high-luminosity mode ". The total cross-section is very large (10^8nb) compared to the cross-section of the Higgs (around 0.1nb , depending on its mass). A detector is needed that can handle the enormous total collision rate and still can separate the signals of interest from the other events ('background').

3.2 ATLAS Detector

Fig.3.3 shows the interaction of various particles with the different components of a detector. In order to test each component for a special set of particle properties, detectors are divided into many components. These components are stacked so that all particles will go through the different layers sequentially. A particle will not be evident until it either interacts with the detector in a measurable fashion, or decays into detectable particles.

A few important things to note:

- Charged particles, like electrons and protons, are detected both in the tracking chamber and the electromagnetic calorimeter.
- Only muons can penetrate to all components, so it can arrive to the muon detector.
- Neutral particles, like neutrons and photons, are not detectable in the tracking chamber; they are only evident when they interact with the detector. Photons are detected by the electromagnetic calorimeter, while neutrons are evidenced by the energy they deposit in the hadron calorimeter.

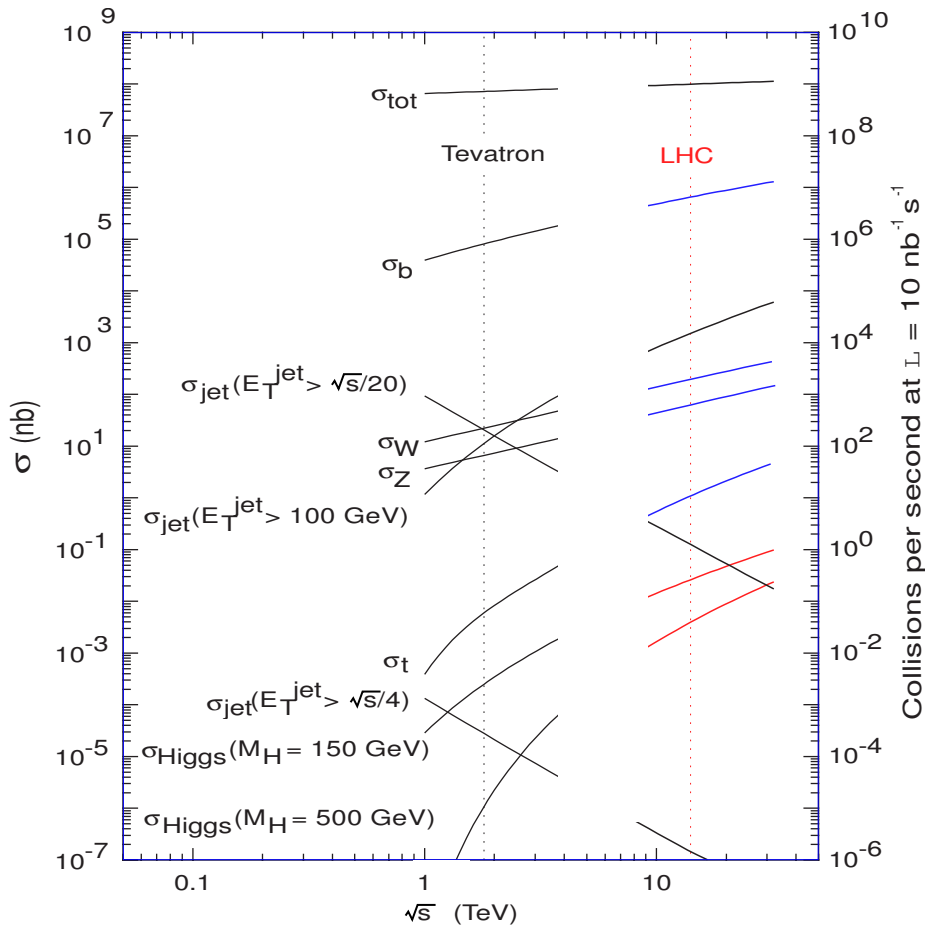


Fig. 3.2: A selection of proton-(anti)proton cross-sections as function of interaction energy. The Tevatron collides protons onto antiprotons, whereas the LHC collides protons onto protons. The right-axis indicates the resulting number of events per second expected at the LHC, operated at high luminosity[21].

- Each particle type has its own "signature" in the detector. For example, if a physicist detects a particle only in the electromagnetic calorimeter, then he is fairly certain that he observed a photon.

The ATLAS collaboration proposes to build a general-purpose detector which is designed to exploit the full discovery potential of LHC [14]. Fig.3.4 shows a 3D view of the final design of the whole ATLAS Detector. The ATLAS experiment is characterized by the following magnet configuration: A super-conducting solenoid will be installed around the Inner-Detector cavity and large super-conducting air-core toroids consisting of independent coils will be arranged with an eight-fold symmetry outside the calorimetries. ATLAS will be 22m high, 44m long, and will have a weight of ~ 7000 tons. This enormous size is a direct consequence of both the high luminosity and the large center-of-mass energy of the LHC beams.

A variety of signatures are important to achieve robust and redundant physics measurements with the ability of internal crosschecks. The goal to exploit the full physics potential of LHC and the requirements lead to the following basic design considerations:

- very good electromagnetic calorimetry for electron and photon identification and measure-

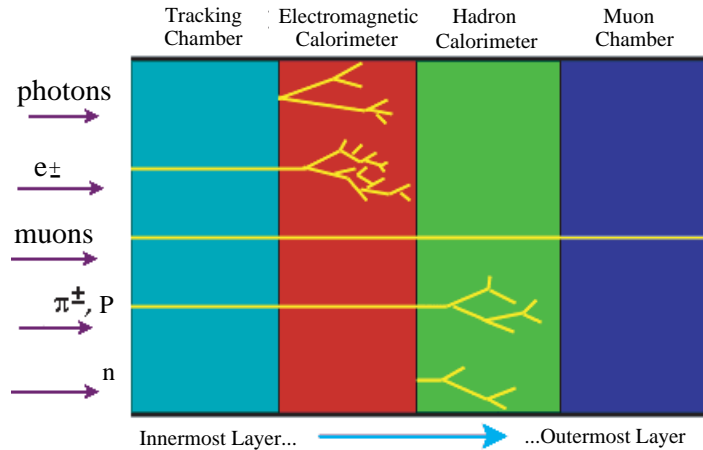


Fig. 3.3: The interaction of various particles with the different components of a detector. Neutrinos are not shown on this chart because they rarely interact with matter, and can only be detected by missing matter and energy.

ments, complemented by hermetic jet and missing E_T calorimetry;

- efficient tracking at high luminosity for lepton-momentum measurements, for b-quark tagging, and for enhanced electron and photon identification, as well as τ and heavy-flavor vertexing and reconstruction capability of some B-decay final-states at lower luminosity;
- stand-alone, precision muon-momentum measurements up to highest luminosity, and very low- p_T trigger capability at low luminosity;
- large acceptance and maximum η coverage.

The coordinates are defined to form a right-handed Cartesian coordinate system. The beam line defines the z-axis. The positive z-direction points in the direction of LHCb (see Fig.3.1). The x-axis points in the direction towards the center of the LHC ring. The positive y-direction points (almost) upwards. Note that, due to the geological conditions around Geneva, the tunnel does not lie in a horizontal plane and therefore the y-axis has a small angle with the vertical (0.704°). The symmetry of the detectors is cylindrical, making cylindrical coordinates useful with the usual definition: the z-axis is the same as for the Cartesian coordinate system, the azimuthal angle symbol is ϕ and the radial symbol is R . When using polar coordinates, the radial-coordinate symbol is r and the polar angle symbol is θ . For hadron colliders one often uses the pseudorapidity instead of θ :

$$\eta \equiv -\ln\left(\tan\frac{\theta}{2}\right) \quad (3.6)$$

because the particle multiplicity-distribution in pseudorapidity ($dN/d\eta$) is basically flat.

3.2.1 Inner Detector

The ATLAS Inner Detector is shown in Fig.3.5. It combines high-resolution detectors at inner radii with continuous tracking elements at outer radii, all contained in a solenoidal magnet with a central field of 2T.

The silicon-pixel vertex-detector consists of three barrel layers of 140 million pixels (each $50\mu\text{m}$ in r - ϕ direction and $400\mu\text{m}$ in the direction along the beam line) and four disks on each side between

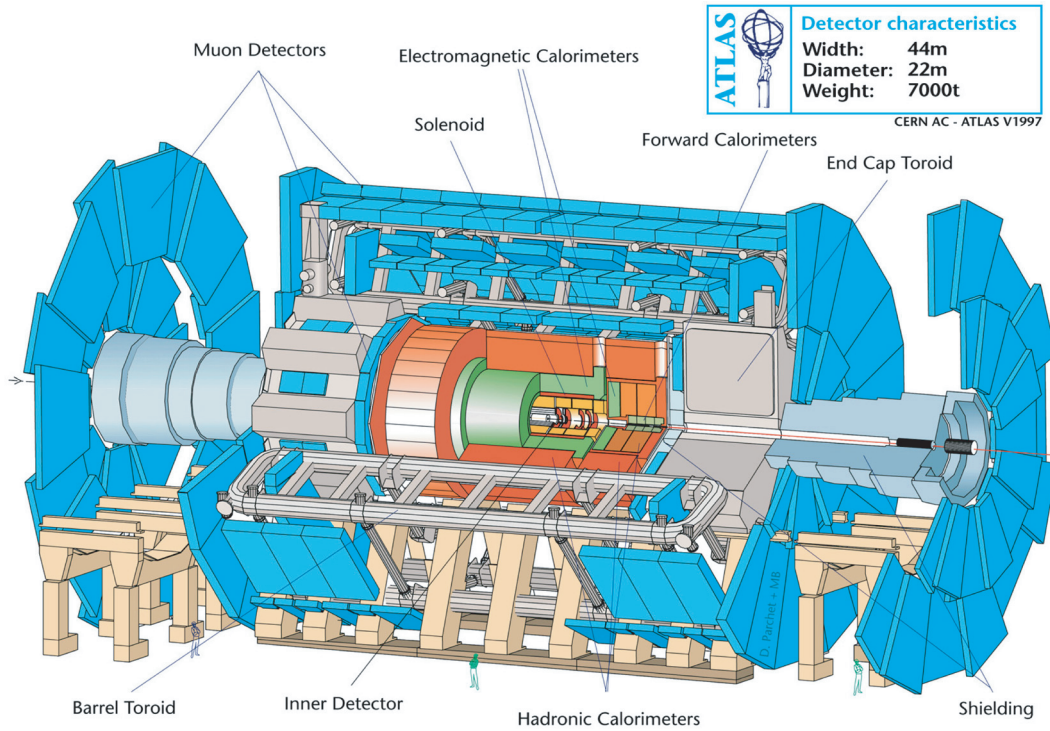


Fig. 3.4: ATLAS Detector [11]

radii of 11cm and 14cm aiming for a point resolution of $\sigma_{r,\phi} = 12\mu\text{m}$ and $\sigma_z = 60\mu\text{m}$. This high resolution allows reconstructing the track origin to find secondary decay vertices. The readout chips must withstand over 300kGy of ionizing radiation and over 5×10^{14} [neutrons/cm²] in ten years of operation.

The silicon strip detectors - Semi Conductor Tracker (SCT) - with a pitch of $80\mu\text{m}$ are mounted in four barrel layers and nine forward double disks in order to provide four precision measurements per track in the radial range between 30 and 55cm, contributing to the measurement of momentum, impact parameter and vertex position. The spatial resolution in the azimuthal direction (perpendicular to the strips) will be $\sigma_{r,\phi} = 18\mu\text{m}$. A second coordinate resolution of $\sigma_z = 580\mu\text{m}$ is obtained by tilting the two detector planes of each double layer by 40mrad with respect to each other.

The Transition Radiation Tracker (TRT) consists of 420,000 proportional drift tubes with a diameter of 4mm. It is divided into a barrel part and several forward wheels. The detector is operated with a Xe/CF₄/CO₂ gas mixture optimized for the detection of X-rays created as transition radiation in stacks of thin radiators between the tubes. The single-wire resolution will be $170\mu\text{m}$ and the efficiency will be $> 50\%$ even for the highest rates (15MHz). Two different discriminator thresholds will be used to distinguish between tracking hits (only lower threshold) and transition-radiation hits (both thresholds).

3.2.2 Calorimetry

The ATLAS calorimetry is shown in Fig.3.6. It consists of electromagnetic calorimeters and hadronic calorimeters. A barrel cryostat around the inner cavity contains the barrel electromagnetic

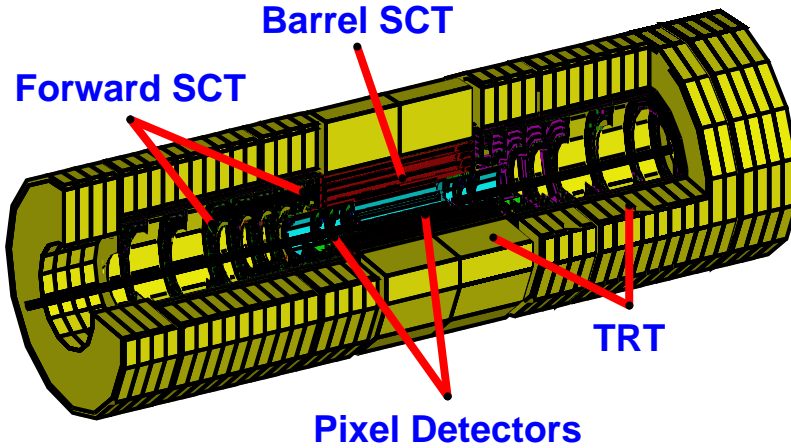


Fig. 3.5: Atlas Inner Detector consisting of a pixel detector system, the SCT and the TRT. The whole Inner Detector has a length of 6.8m and a radius of 1.15m [14].

Liquid Argon (LAr) calorimeter and the coil of the solenoid magnet. Two end-cap cryostats enclose the electromagnetic and hadronic end-cap calorimeters as well as the integrated forward calorimeter.

3.2.2.1 Electromagnetic Calorimeter

The electromagnetic calorimeter is a lead-LAr detector with accordion shaped Kapton electrodes and lead absorber plates over its full coverage (Barrel part: $|\eta| < 1.475$, end-cap parts: $1.375 < |\eta| < 3.2$). The LAr sampling technique is radiation resistant and provides long-term stability of the detector response, excellent hermeticity, good energy resolutions, and relatively easy detector calibration. The total thickness of the electromagnetic calorimeter is $> 24X_0$ in the barrel part and $> 26X_0$ in the forward region. The segmentation of the calorimeter will be $\Delta\eta \times \Delta\phi \approx 0.025 \times 0.025$, aiming for an energy resolution of

$$\frac{\Delta E}{E} = \frac{10\%}{\sqrt{E}} \oplus 1\% \quad (E \text{ in GeV}). \quad (3.7)$$

The energy-scale precision will be 0.1% and the measurement resolution of the shower direction in θ will be $\sim 50\text{mrad}/\sqrt{E}$ (E in GeV).

3.2.2.2 Hadron Calorimeter

The hadronic calorimeter uses different techniques and devices as best suited for the different requirements and the radiation environment.

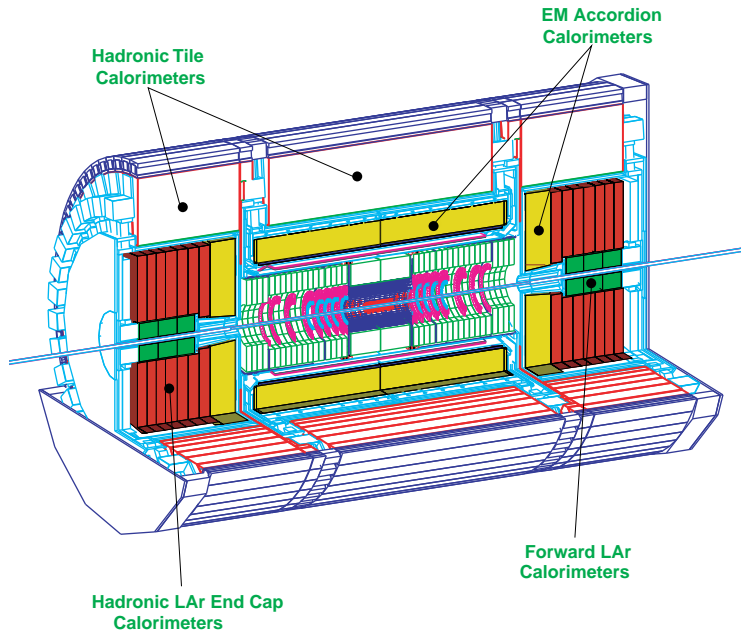


Fig. 3.6: Layout of the ATLAS Calorimetry [14]

In the range of $|\eta| < 1.6$ a sampling calorimeter is used with iron as absorber material and scintillating tiles (3mm thick) as active material (TILE Calorimeter). The signals produced on both sides of the scintillating tiles are read out by wavelength-shifting fibers into two separate photo-multipliers. The barrel hadronic calorimeter will have an inner radius of 2.28m and an outer radius of 4.23m. The resulting granularity of the hadronic calorimeter will be $\Delta\eta \times \Delta\phi \approx 0.1 \times 0.1$. The total thickness is 11 interaction lengths λ at $\eta = 0$, including 1.5λ of the outer support.

In the forward range of $1.5 < |\eta| < 4.9$, a hadronic LAr calorimeter is used. The end-cap hadronic calorimeter extends up to $|\eta| < 3.2$ and is a copper-LAr detector with parallel plate geometry. The expected energy resolution is

$$\frac{\Delta E}{E} = \frac{50\%}{\sqrt{E}} \oplus 3\% \quad (|\eta| < 3). \quad (3.8)$$

The high-density forward calorimeter (FCAL) covers the region of $3.2 < |\eta| < 4.9$ with the front face about 5m from the interaction point (high level of radiation). The detector is based on rods filled with LAr in a copper and tungsten matrix. The FCAL is tagging forward jet and measuring missing E_T . The energy resolution is required as

$$\frac{\Delta E_T}{E_T} = \frac{100\%}{\sqrt{E_T}} \oplus 10\% \quad (3 < |\eta| < 4.9). \quad (3.9)$$

3.2.3 Muon Spectrometer

The Muon is a just heavy electron (200 times heavier than an electron), but, because of its larger mass, produces much less synchrotron radiation. Therefore muons can reach outside of the calorimeter hardly losing energy, so the muon spectrometers are aligned at the most outside of the detector (see Fig.3.3).

The Muon Spectrometer dominates the size of the ATLAS experiment with its outer diameter of $\sim 22\text{m}$. Fig.3.7 shows the Muon Spectrometer. The ATLAS Muon Spectrometer is based on the magnetic deflection of muon tracks in a system of three large super-conducting air-core toroid magnets instrumented with separate function trigger and high-precision tracking chambers.

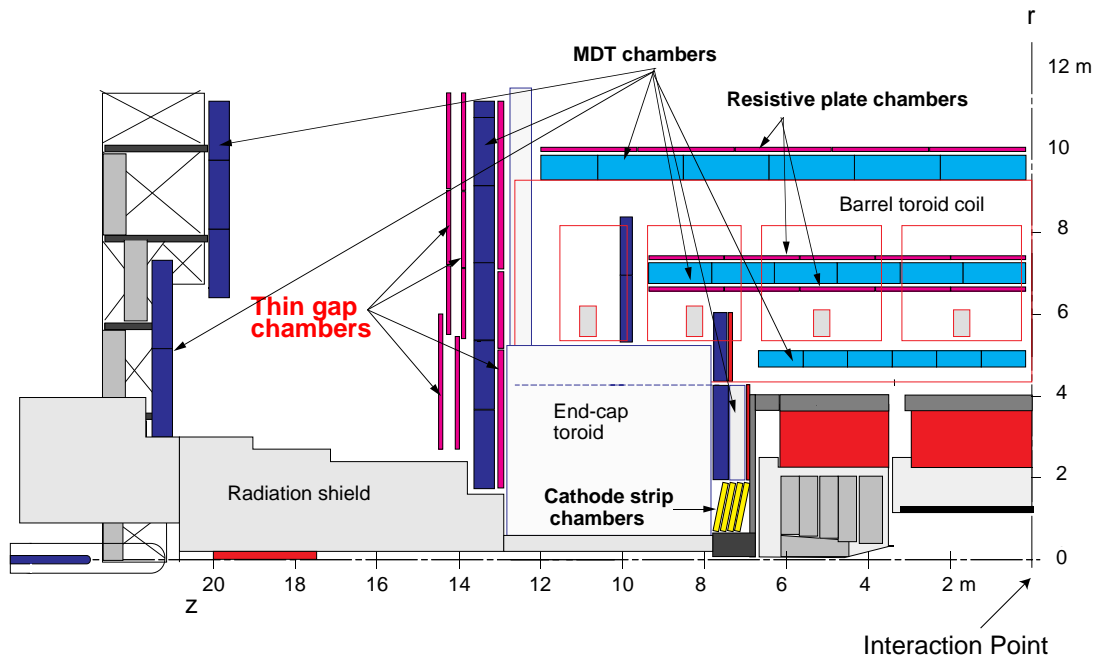


Fig. 3.7: Side view of one quadrant of the ATLAS Detector[13].

The design and performance of the Muon Spectrometer must satisfy the following requirements:

- the largest possible discovery reach for expected and unexpected new physics, with minimal systematic biases;
- good discrimination against high levels of charged and neutral particle background from minimum-bias events and radiation;
- safe and reliable operation in difficult environmental conditions for the anticipated lifetime of the LHC.

The discovery potential of the spectrometer has been optimized on the basis of selected benchmark processes ($H \rightarrow ZZ \rightarrow 4l$). The important parameters that need to be optimized for maximum physics reach are:

- Resolution: momentum and mass resolutions at the level of 1% are essential for the reconstruction of narrow two- or four-muon final states on top of high background levels, such as the intermediate-mass

Higgs, and for reliable charge identification. A transverse momentum resolution that is constant over the full rapidity range is desirable.

- “ Second coordinate ” measurement:
a measurement of muon tracks in the non-bending projections with an r.m.s spatial resolution of $5 \sim 10\text{mm}$ is required for safe track reconstruction and reliable momentum determination.
- Rapidity coverage of track reconstruction:
all physics channels profit from a pseudorapidity coverage up to $|\eta| \approx 3$ ($dN/d\eta$ is constant) and good hermeticity, in particular rare high-mass processes.
- Trigger selectivity:
transverse momentum thresholds of $10 \sim 20\text{GeV}/c$ are adequate for high-mass states, which will be in the focus of LHC physics at nominal luminosity. Lower thresholds of $p_T \approx 5\text{GeV}/c$ are required for CP violation and beauty physics.
- Trigger coverage:
adequate trigger efficiencies can be obtained with a pseudo-rapidity coverage smaller than that of the precision chambers.
- The actual requirements are mostly determined by processes at the opposite ends of the LHC mass scale:
the need for good acceptance for rare high-mass Higgs particles, and the need for very high statistics to study small rate asymmetries due to CP violation in the B sector. A trigger coverage of $|\eta| < 2.4$ is found to be sufficient.
- Bunch-crossing identification:
the LHC bunch-crossing interval of 25nsec sets the scale for the required time resolution of the first-level trigger system. Achieving a resolution $\Delta p_T/p_T \approx 10\%$ for $p_T = 1\text{TeV}/c$ dictates the combination of the bending power in the central rapidity region, and of the precision with which the muon instrumentation must measure the sagitta of the particles.

3.2.3.1 Momentum Measurement

Magnetic fields are applied to bend the trajectory of a charged particle, and so determine its momentum. If the position of a muon in an air-core magnet of length L is measured at three equidistant points along the track, the sagitta s of the circular orbit is (see Fig.3.8):

$$s = R(1 - \cos \frac{\alpha}{2}) \approx \frac{R\alpha^2}{8} \quad (3.10)$$

The momentum $P[\text{GeV}/c]$ of the particle is obtained according to the following equation:

$$P = 0.3BR, \quad (3.11)$$

where $R[\text{m}]$ is the measured radius of curvature, and $B[\text{T}]$ is the strength of the magnetic field. Then $R = P/(0.3B)$ and $\alpha \approx 0.3BL/P$. For small deflection angles we have

$$s = 0.3 \frac{BL^2}{8P} \quad (3.12)$$

Therefore, the momentum P can be measured by measuring s .

In order to estimate the momentum error, a position resolution on each point x_i is defined as $\sigma(x)$. s is also represented as following:

$$s = x_2 - \frac{x_1 + x_3}{2}, \quad (3.13)$$

and a precision of s is $\sigma(s) = \sqrt{3/2}\sigma(x)$. Therefore, the momentum error is obtained

$$\frac{\sigma(P)}{P} = \frac{\sigma(s)}{s} = \sqrt{\frac{3}{2}}\sigma(x)\frac{8P}{0.3BL^2}. \quad (3.14)$$

If the track is measured at N equidistant points, the corresponding relation is [23]:

$$\frac{\sigma(P)}{P} = \frac{\sigma(x)P}{0.3BL^2}\sqrt{\frac{720}{N+4}} \quad (3.15)$$

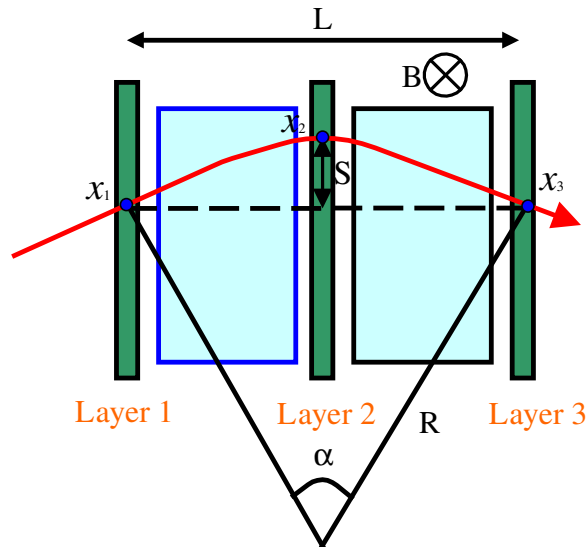


Fig. 3.8: Measurement of sagitta.

3.2.3.2 Muon Detector

The ATLAS Muon Spectrometer will measure the trajectories of muons at three stations of chambers. In the barrel ($|\eta| < 1$) they will be arranged in three cylinders concentric with the beam axis at radii of about 5m, 7.5m and 10m. In this η -region the particles are measured near the inner and outer field boundaries, and inside the field volume, in order to determine the momentum from the sagitta. The end-cap chambers will cover the pseudo-rapidity range $1 < |\eta| < 2.7$ and are arranged in four disks at distances of 7m, 10m, 14m and 21 ~ 23m from the interaction point. In the forward region, for $|\eta| > 1.4$, the magnet cryostats do not allow the positioning of chambers inside the field volume.

The ATLAS Muon Spectrometer consists of two parts; Precision Chambers and Trigger Chambers, using four different chamber technologies:

Precision Chambers:

For the precision measurement of muon tracks in the principal bending direction of the magnetic field, Monitored Drift Tube (MDT) chambers are used except in the innermost ring of the end-cap inner-station ($2 < |\eta| < 2.7$), where particle fluxes are highest. In the innermost ring of the end-cap inner-station Cathode Strip Chambers (CSCs) are employed. The CSCs are multi-wire proportional chambers with cathode strip readout.

Trigger Chambers:

These chambers will provide the trigger function, the bunch-crossing identification and the measurement of the “ second coordinate ” (coordinate along the magnetic field line).

In the barrel ($|\eta| < 1.05$), this information is provided by three stations of Resistive Plate Chambers (RPCs). They are located on both sides of the middle MDT station, and either directly above or directly below the outer MDT station. In the end-caps ($1.05 < |\eta| < 2.4$), three stations of Thin Gap Chambers (TGCs), located near the middle MDT station will be installed. This thesis is devoted to a detailed study of the performance of the ATLAS Muon Spectrometer with the main focus on the TGC system.

3.2.3.3 Magnet System

The magnet system of the ATLAS Muon Spectrometer consists of three air-core super-conducting toroids with an open structure to minimize the contribution of multiple scattering to the momentum resolution. The toroidal design of the magnet system made it possible to provide a high-resolution, large acceptance and robust stand-alone Muon Spectrometer.

The barrel toroid extends over a length of 25m, with an inner bore of 9.4m and an outer diameter of 20.1m. The two end-cap toroids are inserted at each end. They have a length of 5m, an inner bore of 1.64m and an outer diameter of 10.7m. Each toroid consists of eight flat coils assembled radially and symmetrically around the beam axis. The barrel-toroid coils are contained in individual cryostats, whereas the eight end-cap toroid coils are assembled in a single, large cryostat. Fig.3.9 shows a 3D view of the muon magnet system. A combined optimization of the magnet-field strength and its radius, constrained by magnet-fabrication costs and by space limitations in the experimental cavern, led to the air-core toroid magnet configuration providing a bending power at $\phi = 0$ of $\int Bdl = 2\text{Tm}$ at $\eta = 0$ up to $\int Bdl = 9\text{Tm}$ at $\eta = 2.8$. The average toroidal magnetic field will be $\sim 0.5\text{T}$. A big advantage of the toroidal magnetic field is the fact that the bending power increases with higher pseudo-rapidities. Fig.3.10 shows the photograph of 8 barrel toroid magnets installed in ATLAS detector.

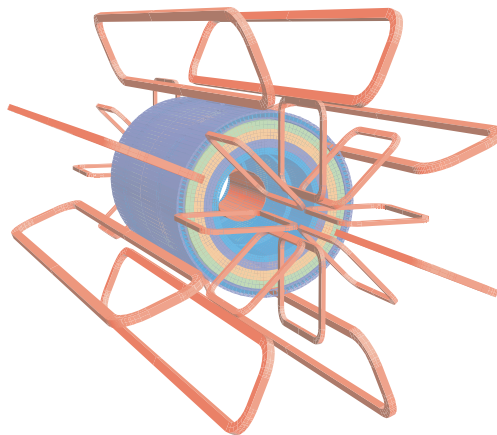


Fig. 3.9: Geometry of magnet windings and magnetic masses. Visible are the eight barrels toroid coils, with the end-cap coils interleaved. The solenoid winding lies inside the calorimeter volume. The tile calorimeter is modeled by four layers with different magnetic properties, plus an outside return yoke; the forward shielding disk is not displayed, for the sake of clarity. [14]

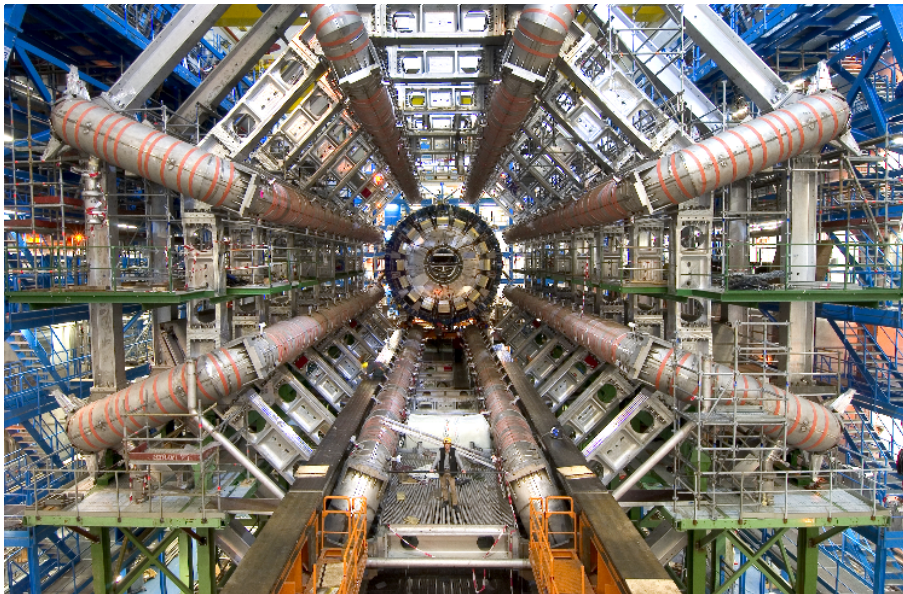


Fig. 3.10: Photo of barrel toroid magnet[24].

3.2.3.4 MDT(Monitored Drift Tube)

The basic detection elements of the MDT chambers are aluminum tubes of 30mm diameter and 400 μ m wall thickness, with a 50 μ m diameter central W-Re wire. The standard operating conditions is a gas mixture of 93% Ar and 7% CO₂ at 3bar absolute pressure and a low gas gain of 2×10^4 to minimize the fraction of streamers. The corresponding high voltage setting is 3080V: The choice of high pressure is driven by the need to improve the spatial resolution by minimizing the longitudinal diffusion and the fluctuations of the number of primary electrons. According to Ref. [25] [26], the baseline gas shows no aging but is highly non-linear dependence of the drift velocity on the electric field and greater drift time (a maximum drift time of ~ 700 nsec), compared with the more frequently used gas mixtures containing hydrocarbons. The single-wire resolution is $\sim 50\mu$ m without background rate and stay below the 80 μ m-limit for the highest background rate (1500 Hz/cm including an uncertainty factor of 5 for safety). The most important parameters of the MDT chambers are summarized in Table3.2.

The tubes are produced by extrusion from a hard aluminum alloy, and are available commercially. They are closed by endplugs which provide for accurate positioning of the anode wires, wire tension, gas tightness, and electrical and gas connections. The drift tubes can be manufactured to tight mechanical tolerances which are well matched to their intrinsic resolution properties, mostly using automated assembly procedures. The tube lengths vary from 70cm to 630cm.

To improve the resolution of a chamber beyond the single-wire limit and to achieve adequate redundancy for pattern recognition, the MDT chambers are constructed from 2×4 monolayers of drift tubes for the inner and 2×3 monolayers for the middle and outer stations. The tubes are arranged in multilayers of three or four monolayers, respectively, on either side of a rigid support structure (Fig.3.11). The support structures (' spacer frames ') provide for accurate positioning of the drift tubes with respect to each other, and for mechanical integrity under effects of temperature and gravity; for the barrel chambers which are not mounted in a vertical plane, they are designed to bend the drift tubes slightly in order to match them to the gravitational sag of the wires. The spacer

frames also support most of the components of the alignment system.

The structural components of the spacer frames are three 'cross-plates', to which the drift tube multilayers are attached, and two 'long beams' connecting the cross-plates. The frames need to be constructed to a moderate mechanical accuracy of $\pm 0.5\text{mm}$ only; accurate positioning of the drift tubes is provided by the assembly procedure. They will be attached to the rail structures of the spectrometer by three-point kinematic supports. Once a chamber is installed in its final location in the spectrometer, mechanical deformations are monitored by an in-plane optical system; hence the name " monitored drift tube chambers ".

Parameter	Design Value
Gas	Ar : CO ₂ = 93 : 7
Gas Pressure	3bar(absolute)
High Voltage	3080V
Gas Gain	2×10^4
Position Resolution	$81\mu\text{m}$

Table 3.2: MDT Parameter [25] [26]

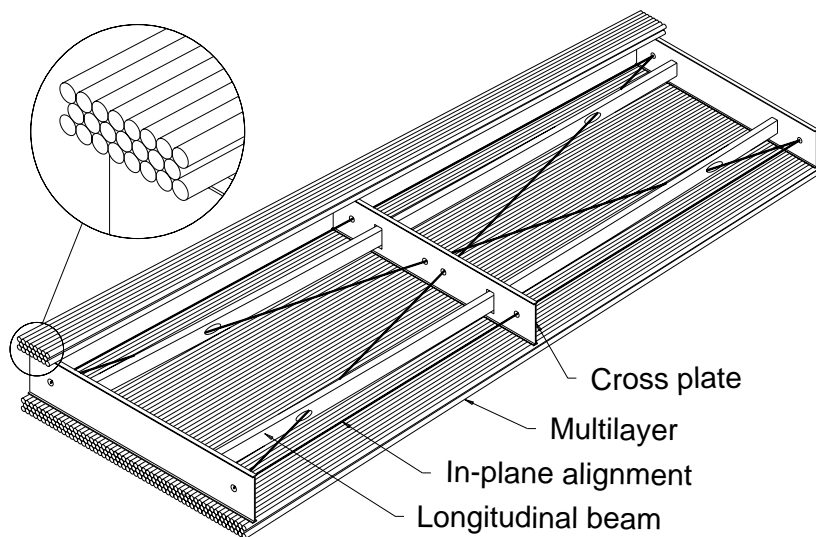


Fig. 3.11: Monitored Drift Tube [14]

The momentum resolution of MDT could be estimated using Eq.(3.15). For the muon with $P_T = 100\text{GeV}$, $N=3$, $L = 6\text{m}$, $\sigma(x) = 80 \mu\text{m}$, $BL = 4\text{Tm}$ is substituted in Eq.(3.15),

$$\frac{\sigma(P_T)}{P_T} = 0.82\% \quad (3.16)$$

The stand-alone muon momentum resolution of the spectrometer is shown in Fig.3.12 for the barrel (Left) and end-cap (Right) part. The different contributions to the resolution are indicated: multiple scattering, relative chamber alignment uncertainties, the drift tube measurement uncertainty, as well as the energy loss fluctuations in the calorimeter. Only for muon momenta above 250GeV can the excellent precision of the MDTs be fully exploited.

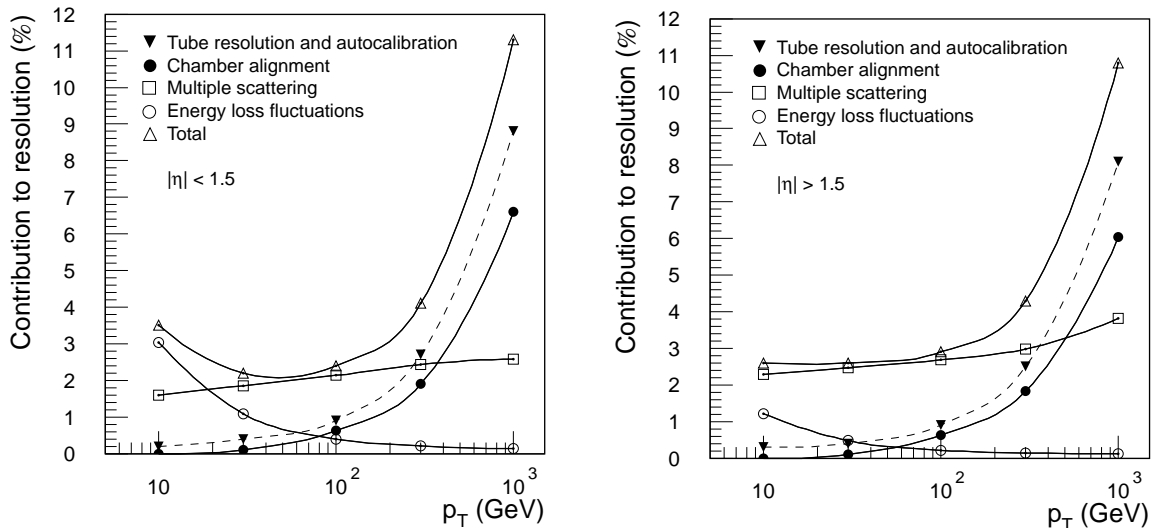


Fig. 3.12: Momentum Resolution for ATLAS MDT Chamber [14]. Left shows the barrel region ($|\eta| < 1.5$) and right shows the end-cap region ($|\eta| > 1.5$).

3.2.3.5 CSC(Cathode Strip Chamber)

The CSCs are multiwire proportional chambers with cathode strip readout and with a symmetric cell in which the anode-cathode spacing is equal to the anode wire pitch. The precision coordinate is obtained by measuring the charge induced on the segmented cathode by the avalanche formed on the anode wire. Good spatial resolution is achieved by segmentation of the readout cathode and by charge interpolation between neighboring strips. The cathode strips for the precision measurement are oriented orthogonal to the anode wires. The anode wire pitch is 2.54mm and the cathode readout pitch is 5.08mm; r.m.s. resolutions of better than $60\mu\text{m}$ have been measured in several prototypes. Other important characteristics are small electron drift times ($\leq 30\text{nsec}$), good time resolution (7nsec), good two-track resolution, and low neutron sensitivity. A measurement of the transverse coordinate is obtained from orthogonal strips, i.e. oriented parallel to the anode wires, which form the second cathode of the chamber. A cutout view of one gap is shown in Fig.3.13. The most important parameters of the CSC chambers are summarized in Table 3.3.

Parameter	Value
Anode wire	W-Re $30\mu\text{m}$ wire
Wire Pitch	2.54mm
Anode-Cathode	2.54mm
High Voltage	2600V
Gas	Ar : CO ₂ : CF ₄ = 30 : 50 : 20
Gas Gain	4×10^4

Table 3.3: CSC Parameter [14]

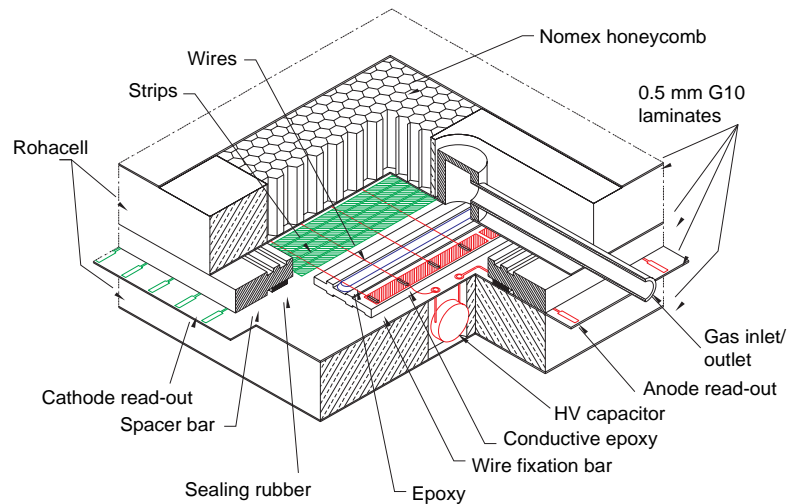


Fig. 3.13: Cathode Strip Chamber [14]

3.2.3.6 RPC(Resistive Plate Chamber)

The RPC is a gaseous detector providing a typical space-time resolution of $1\text{cm} \times 1\text{nsec}$ with digital readout. The basic RPC unit is a narrow gas gap formed by two parallel resistive bakelite plates, separated by insulating spacers. The primary ionization electrons are multiplied into avalanches by a high, uniform electric field of typically $4.5\text{kV}/\text{mm}$. Amplification in avalanche mode produces pulses of typically 0.5pC . The RPCs will be operated with a gas mixture of 97% tetrafluoroethane ($\text{C}_2\text{H}_2\text{F}_4$) and 3% isobutane (C_4H_{10}), a non-flammable and environmentally safe gas that allows for a relatively low operating voltage. The signal is read out via capacitive coupling by metal strips on both sides of the detector. A trigger chamber is made from two rectangular detector layers, each one read out by two orthogonal series of pick-up strips: the ' η strips' are parallel to the MDT wires and provide the bending view of the trigger detector; the ' ϕ strips', orthogonal to the MDT wires, provide the second-coordinate measurement which is also required for the offline pattern recognition.

RPCs have a simple mechanical structure, use no wires and are therefore simple to manufacture. The 2mm thick Bakelite plates are separated by polycarbonate spacers of 2mm thickness which define the size of the gas gap. The spacers are glued on both plates at 10cm intervals. A 7mm wide frame of the same material and thickness as the spacers is used to seal the gas gap at all four edges. The mechanical structure of an RPC is shown in Fig.3.14. The outside surfaces of the resistive plates are coated with thin layers of graphite paint which are connected to the high voltage supply. These graphite electrodes are separated from the pick-up strips by $200\mu\text{m}$ thick insulating films which are glued on both graphite layers. The readout strips are arranged with a pitch varying from 30.0 to 39.5mm.

Each chamber is made from two detector layers and four readout strip panels. These elements are rigidly held together by two support panels which provide the required mechanical stiffness of the chambers. The panels are made of polystyrene sandwiched between two aluminum sheets. One panel is flat, 50mm thick, with 0.5mm thick aluminum coatings; the other panel is 10mm thick with 0.3mm coatings and is preloaded with a 1cm sagitta. The two panels are rigidly connected by 2mm thick

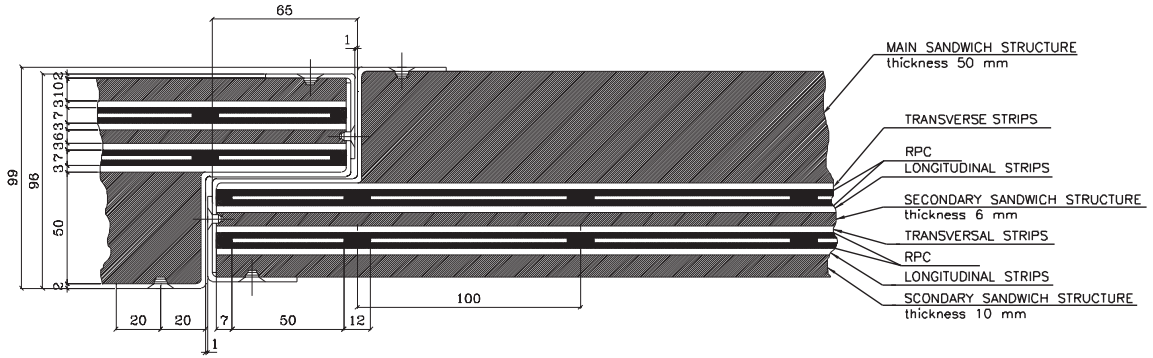


Fig. 3.14: Resistive Plate Chamber [14]

aluminum profiles, such that the preloaded support panel provides uniform pressure over the whole surface of an RPC module. The principal RPC parameters are summarized in Table 3.4.

Parameter	Value
Gas Gap	$2.00 \pm 0.22\text{mm}$
High Voltage	$8.90 \pm 0.15\text{kV}$
Bakelite Volume Resistivity	$(1 \sim 5) \times 10^{10}\Omega \text{ cm}$
Carbon Resistivity	$100 \pm 40\text{k}\Omega$
Gas	$\text{C}_2\text{H}_2\text{F}_4 : \text{C}_4\text{H}_{10} = 97 : 3$
Gas Pressure	$(1.0 \pm 0.5)\text{mbar}$

Table 3.4: RPC Parameter [14]

To preserve the excellent intrinsic time resolution of the RPCs, the readout strips are optimized for good transmission properties and are terminated at both ends to avoid signal reflections. The front-end electronics are based on a three-stage voltage amplifier followed by a variable-threshold comparator. The amplifier frequency response is optimized for the typical time structure of RPC avalanches. Eight amplifier-comparator channels are implemented in a VLSI chip in GaAs technology. The chips are mounted on printed circuit boards attached to the edges of the readout panels.

3.2.3.7 TGC(Thin Gap Chamber)

Thin gap chambers are designed in a way similar to multiwire proportional chambers, with the difference that the anode wire pitch is larger than the cathode-anode distance. Signals from the anode wires provide the trigger information together with readout strips arranged orthogonal to the wires. The readout strips also serve to measure the second coordinate. The detail features of TGCs will be described in chapter 4.

3.2.4 Experimental Environment

The high level of particle fluxes in the Muon Spectrometer has a major impact on the design of the whole system. They define parameters such as the rate capability of single tubes and the aging properties, and are one important input for the choice of the baseline gas and the front-end electronics.

The background sources in the Muon Spectrometer can be classified into two categories:

Primary background:

Primary collision products penetrating into the Muon Spectrometer through the calorimeters, which are correlated in time with the p-p interaction. Conventional sources of primary background are semileptonic decays of light ($\pi, K \rightarrow \mu X$) and heavy ($c, b, t \rightarrow \mu X$) flavors, gauge Boson decays ($W, Z, \gamma^* \rightarrow \mu X$), shower muons and hadronic punch-through. At small $p_T < 10\text{GeV}/c$, the largest source of background are muons from π/K decays in flight; depending on pseudo-rapidity, muons with momenta of 3-6GeV/c will be absorbed in the calorimeters. At moderate $p_T > 10\text{GeV}/c$, top and Z decays also give a sizeable contribution.

Radiation background:

Background consisting mostly of neutrons and photons in the 1MeV range, produced by secondary interactions in the forward calorimeter, shielding material, and the beam pipe and machine elements. Low-energy neutrons, which are an important component of the hadronic absorption process, escape the absorber and produce a gas of low-energy photon background through nuclear n- γ processes. This background enters into the spectrometer from all directions and is not any longer correlated in time to the primary p-p interaction. Using the MDTs as an example, typical detection efficiencies for photons are at the level of 1%, and those for neutrons one order of magnitude smaller. Notwithstanding these low sensitivities, the low energy neutral particle background will dominate the counting rates in most areas of the spectrometer (see Fig.3.15).

The neutron and photon fluxes have been computed [56] taking into account the material distribution and the magnetic field in the ATLAS detector and the experimental hall. To obtain actual detection efficiencies, two approaches were used: Prototypes were exposed to neutron and photon sources, and the detection efficiency measured at several known particle energies [55] [50]. According to these studies, the neutron sensitivity of one TGC is $\sim 0.048\%$ for 2.5MeV and $\sim 0.13\%$ for 14MeV, and the γ sensitivity in average over our expected photon-energy distribution is measured to be less than 1% in the whole energy range and less than 0.1% under 100keV.

The uncertainties of the count-rate calculations have been quantified and the following contributions have been identified:

- the combination of the uncertainties attached to the total p-p cross-section and to the multiplicity produced in the primary collisions, is estimated at $\pm 30\%$;
- limited knowledge of the showering process in the absorber, and of the (n, γ) cross sections could conspire to modify the fluencies by a factor of up to 2.5;
- the comparison of simulation results and laboratory measurements on chamber sensitivities conservatively suggests that the numbers assumed could be in error by a factor of up to 1.5.

A conservative linear superposition of these uncertainties yields a factor of five. The ATLAS muon instrumentation is therefore designed to operate at a nominal luminosity of $\mathcal{L} = 10^{34}\text{cm}^{-2}\text{s}^{-1}$, allowing for a safety factor of five on the background rate.

The fluences of the most important particle types in the muon spectrometer are summarized in Fig.3.15[56]. According to Ref.[56], the counting rate on each detector was estimated as $\sim 30\text{Hz}/\text{cm}^2$ at high luminosity by considering the detection efficiency of detectors and the sensitivity for each particle.

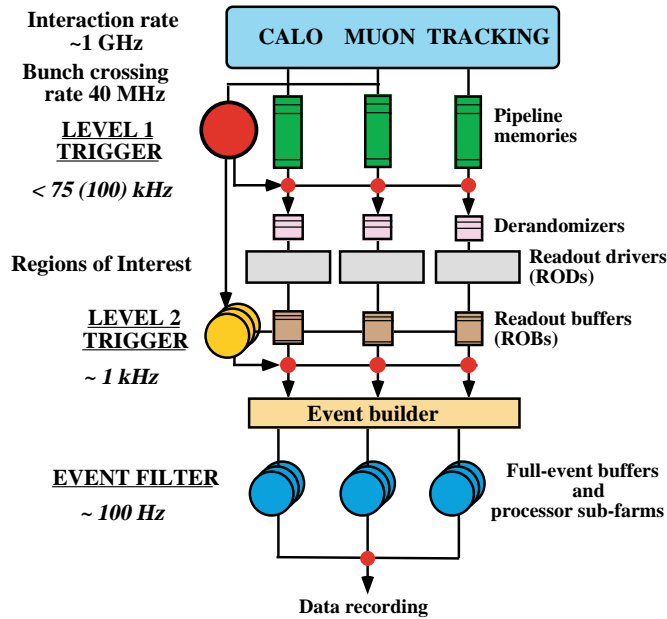


Fig. 3.16: Block diagram of the Trigger/DAQ system. [20]

for the physics programme, for example by increasing the thresholds on some of the inclusive (single-object) triggers when operating at the highest luminosities, and by relying more heavily on multi-object triggers.

An essential requirement on the LVL1 trigger is that it should uniquely identify the bunch crossing of interest. Given the short (25nsec) bunch-crossing interval, this is a non-trivial consideration. In the case of the muon trigger, the physical size of the muon spectrometer implies times-of-flight comparable to the bunch-crossing period. For the calorimeter trigger, a serious challenge is that the pulse shape of the calorimeter signals extends over many bunch crossings.

Events selected by LVL1 are read out from the front-end electronics systems of the detectors into readout buffers (ROBs). A large number of front-end electronics channels are multiplexed into each ROB. Intermediate buffers, labeled 'derandomizers' in Fig.3.16, average out the high instantaneous data rate at the output of the pipeline memories to match the available input bandwidth of the readout drivers (RODs).

All of the data for the selected bunch crossing from all of the detectors are held in the ROBs either until the event is rejected by the level-2 (LVL2) trigger (in which case the data are discarded) or, in case the event is accepted by LVL2, until the data have been successfully transferred by the DAQ system to storage associated with the Event Filter (which makes the third level of event selection). The process of moving data from the ROBs to the Event Filter (EF) is called event building. Whereas before event building each event is composed of many fragments, with one fragment in each ROB, after event building the full event is stored in a single memory accessible by an EF processor.

The LVL2 trigger makes use of 'region-of-interest' (RoI) information provided by the LVL1 trigger. This includes information on the position (η and ϕ , where η is pseudorapidity and ϕ is azimuthal angle) and p_T range of candidate objects (high- p_T muons, electrons/photons, hadrons/taus, jets), and energy sums (missing- E_T vector and scalar E_T value, where E_T is transverse energy). The RoI data are sent by LVL1 to LVL2, for all events selected by the LVL1 trigger, using a dedicated data path. Using the RoI information, the LVL2 trigger selectively accesses data from the ROBs, moving

only the data that are required in order to make the LVL2 decision. The LVL2 trigger has access to all of the event data, if necessary with the full precision and granularity. However, typically the LVL2 trigger needs only data from a small fraction of the detector, corresponding to limited regions centred on the objects indicated by the LVL1 trigger. Hence, usually only a few percent of the full event data are required thanks to the RoI mechanism.

LVL2 will reduce the rate to $\sim 1\text{kHz}$. However, in contrast to the 75kHz (upgradeable to 100kHz) limit for LVL1 that comes from the design of the detector front-end electronics, this is not a hard number. The latency of the LVL2 trigger is variable from event to event; it is expected to be $\sim 1\text{-}10\text{ms}$.

In the case of muon triggers, rejection power at LVL2 comes from sharpening (and where necessary raising) the p_T threshold compared to LVL1, and from applying isolation requirements. Sharper p_T thresholds are possible by using the precision muon chambers (MDTs and CSCs) and also the inner detector. The isolation requirements use calorimeter information, demanding little E_T in a region around the muon candidate.

After an event is accepted, the full data are sent to the LVL3 (Event Filter) processors via the event builder. At LVL3 a complete event reconstruction is possible with decision times up to about 1sec . The LVL3 system must achieve a data storage of $10\text{-}100\text{MB/s}$ by reducing the event rate and the event size. For some triggers, such as Higgs boson candidates, the full event size of about 1MB will be recorded.

3.2.6 LVL1 Endcap Muon Trigger

Fig.3.17 shows the LVL1 muon trigger scheme in the end-cap region. The low- p_T and high- p_T trigger utilizes information from all seven planes, two doublets and one triplet. Typical value for the trigger threshold is 6GeV , and this is the value for which the layout has been optimized. In order to have good trigger efficiency and an efficient background reduction, a 3-out-of-4 coincidence is required for the doublet pair planes of M2 and M3, for both wires and strips, a 2-out-of-3 coincidence for the triplet wire planes, and a 1-out-of-2 coincidence for the triplet strip planes is required. Then the trigger windows are formed in $r - \phi$ space, with the wire signals determining the r -coordinate and strips the ϕ . The trigger algorithm uses pivot plane hits and extrapolates to the interaction point to construct the apparent infinite-momentum path of the track. The deviation from this path of hits found in the preceding confirming trigger planes is related to the track momentum. A window is constructed for each trigger region in the r and ϕ directions around the infinite momentum path. A coincidence is signaled if there is a hit in the window corresponding to the hit location in the pivot plane. Independent signals are generated for r and ϕ . The p_T threshold applied is determined by the size of the two-dimensional window, called coincidence window, and for any single threshold this window is optimized to provide 90% efficiency. The trigger-logic can concurrently generate three different high- p_T plus three different low- p_T threshold triggers by being configured with six sets of window sizes. Tracks are flagged according to the highest threshold they cross. This selection of tracks is performed for every bunch for every trigger sector, a ϕ -slice is both ends. The final trigger decision in the end-cap system is done by merging the results from all sectors.

It is important to keep the latency (time taken to form and distribute the trigger decision) to a minimum. During this time information for all detector channels has to be retained in ‘ pipeline ’ memories. These memories are generally contained in custom integrated circuits, placed on the detector, in inaccessible regions and in a high-radiation environment. The total number of TGC

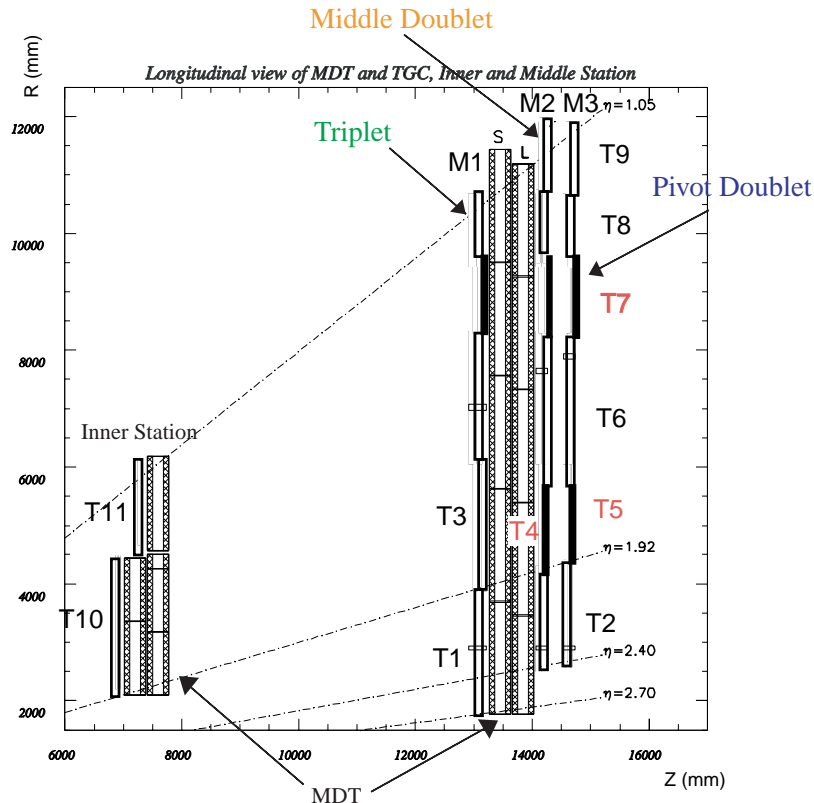


Fig. 3.17: Longitudinal view of the TGC system, showing trajectories of high- and low- p_T muons and their trigger windows. M1 is the TGC triplet, M2, M3 are the TGC doublets, S and L are the small and large MDTs, I is the inner-station TGC. To allow overlapping of the physical chambers, doublets and triplets at adjacent ϕ are at slightly different z ; the bold lines show a doublet/triplet at two adjacent ϕ 's. [14]

channels exceeds 3×10^5 . For reasons of cost and reliability, it is desirable to keep the pipeline lengths as short as possible. The LVL1 latency, measured from the time of the proton-proton collision until the trigger decision is available to the front-end electronics, is required to be $2.0 \mu\text{s}$ (leaving 500nsec contingency).

The trigger efficiency was evaluated by simulating the trigger logic using the coincidence windows [14]. The lower momentum limit for detecting a muon in the Muon System is set by the energy loss in the calorimeter and corresponds to $p_T \sim 3 \text{ GeV}$ in the barrel, but can be as low as $p_T \sim 1 \text{ GeV}$ in the end-cap. In order to evaluate the level of rejection of muons by the trigger system below a given trigger threshold, single muons over a wide range of momenta were generated in a Monte Carlo program and passed through the detector and trigger simulation programs. The trigger efficiency was evaluated as a function of p_T both for single muons and for muons in physics events, for the combined barrel and end-cap LVL1 trigger system. Since in some regions of the detector (notably in the end-cap) window size and trigger efficiency have some η dependence, the efficiency was evaluated as a function of η (integrated over ϕ). These calculations were performed for pseudorapidities covering the geometrical acceptance of the trigger system. The total trigger efficiency in the region $|\eta| < 2.4$, including geometrical losses, is 79% for 6GeV muons in the low- p_T trigger with 6GeV threshold, and 81% for 20GeV muons in the high- p_T trigger with 20 GeV threshold.

4 Thin Gap Chamber (TGC)

The detection of a charged lepton is the primary trigger for many LHC processes. The high luminosity imposes rather stringent requirements on the trigger detector performance. The muon trigger system has to provide a fast digital signal within 25nsec gate defined by the interval between beam crossings. Thin gap chambers (TGCs) operating with n-pentane and CO₂ mixture, have given very good results in long-term operation in the OPAL experiment of the CERN Large Electron Positron Collider (LEP) and were subsequently chosen for muon trigger chambers in the endcap region of the LHC experiment ATLAS. TGCs have a structure similar to that of Multiwire Proportional Chamber (MWPC), except that the anode-to-anode distance is larger than that of the anode-to-cathode. This detail is described in this chapter.

4.1 Operation Principle

4.1.1 Gas ionization by charged particles

Detection of an ionizing particle in a wire chamber is based on ionization produced by the particle in the fill gas of the detector. For energetic charged particles, it is thus sufficient to enter the gas volume in order to be detected. The amount of ionization produced per unit length of gas traversed can be estimated from the linear energy loss given by the well known Bethe-Bloch formula [27] [28] [29].

$$-\frac{dE}{dx} = \frac{4\pi r_e^2 m_e c^2 N_0 Z z^2}{A\beta^2} \left[\ln\left(\frac{2m_e c^2 \beta^2}{(1-\beta^2)I}\right) - \beta^2 \right] \quad (4.1)$$

where r_e is the classical electron radius; Z and A are the atomic number and mass number of the material transversed; z and β are the charge in elementary charges and velocity as a fraction of velocity of light of the ionizing particle; and I is the effective ionization potential of the material transversed. The energy loss given by the Bethe-Bloch formula exhibits a minimum at energies typically roughly 4 times the rest energy of the particle, after which the energy loss remains constant. The regime above the minimum energy loss is known as minimum ionizing regime, where all the particles ionize at an approximately constant rate, regardless of their energy. Particles in the minimum-ionizing regime are frequently called minimum ionizing particle (MIP), and they are encountered constantly in detector applications in high energy and cosmic ray physics. Another quantity of interest is the mean energy loss per ion pair produced in the gas, which combined with the energy loss gives the mean number of ion pairs per unit track length.

For particles whose energy loss in traversing the detector is small compared with their energy upon entering the detector, the particle track in the gas can be assumed straight in first approximation, and the most probable deposited energy can be estimated by multiplying the linear energy loss by the length of the track within the gas volume. On closer analysis the distribution of deposited energy to a thin traversed layer of material is described by the Landau distribution [30]. For lower energy charged particles the effect of scattering inside the detector may cause much larger energy losses and

also cause the charge cloud created by the particle to spread to a larger volume, which may worsen the position measurement accuracy.

4.1.2 Drift of electrons and ions in gases

As the electrons and ions drift in an electric field in the gas they gain energy from the electric field and lose energy through scattering from the gas molecules. For ions the average drift velocity depends up to very high fields linearly on the reduced field $\bar{E} = E/P$ where P is the gas pressure.

For electrons the mobility, defined as the ratio of the reduced field and the drift velocity, is constant only for very low electric fields, and depends strongly on the electric field in larger fields [34]. Therefore, the drift velocities for electrons are generally determined experimentally. A typical drift velocity at high fields is of the order of $5\text{cm}/\mu\text{sec}$, which means that electrons are roughly 1000 times faster than the drifting ions. Hence, in some cases, the ions can be assumed to remain immobile and only the electron drift can be taken into account in calculations. On the other hand, the ion contribution to the output pulse from a wire chamber generally dominates over the electron contribution because of the radial potential distribution around the wire. Furthermore, the long-term development of a pulse from a wire chamber is dictated by the motion of the ions in the detector.

In addition to drift motion caused by the electric field, diffusion also affects the time development of a charge cloud created by an ionizing particle. The diffusion of charges is especially important in such position sensing applications where the charge cloud drifts large distances (several cm or more) before it reaches the readout electrodes. In some cases the position sensing is determined by the arrival time of the electron cloud to the anode (gaseous drift chamber), and the time measurement accuracy may deteriorate because of the diffusion.

4.1.3 Gas Amplification

The main process of gas detectors is a gas multiplication of an electron in the strong electric field around the anode. This process is theoretically explained based on Townsend theory [31].

At first, primary electrons produced by an incident particle in the gas volume are forced by the applied electric field in the chamber. In the moderate electric field of $\sim 1\text{kV}/\text{cm}$ in the drift region, the primary energy of the drifting electrons in the cloud is immediately lost by collisions with the gas atoms, and drifted toward the anode electrodes without any additional ionization.

A small amount of electrons is lost by recombination or attachment. When a low energy electron collides with a positive ion, the electron is sometimes combined with the ion. This is called "recombination", which appears in extremely weak electric field ($\ll 100\text{V}/\text{cm}$). If an electron is captured by a neutral atom, the electron and atom form a negative ion. This phenomenon is called "attachment". In the noble gas, this effect is almost negligible.

The electric field near the anode electrode increases. Then as an electron goes near the anode electrode, the energy of an electron increases. When the energy exceeds the first ionization potential of the gas, the secondary ionization are occurred. These secondary electrons are accelerated again, and they ionize gas atoms one after another. Hence, the number of the secondary electron exponentially increases in the proximity of the anode electrode, which is called an electron avalanche. If λ is the mean free path of an electron for the secondary ionization, the number of ionization through the unit path of an electron is expressed as $\alpha = 1/\lambda$. This α is the first ionization coefficient or the

first Townsend coefficient. The increase rate of the electron dn/n is proportional to unit length dx

$$\frac{dn}{n} = \alpha dx. \quad (4.2)$$

This function is called Townsend Equation. Consequently, the number of the total electron n after the path length of x becomes

$$n = n_0 \exp(\alpha x) \quad (4.3)$$

where n_0 is the initial number of the primary electrons. The number of the total electron rapidly increases. Thus the α is an intrinsic value to the gas, and depends on the electric field strength, gas pressure and gas type. Because the electric field depends on the position, α is also a function of the path length of an electron. Therefore, the multiplication factor M of a detector is expected as an exponentiated integral of the first Townsend coefficient along the drift path,

$$M = \frac{n}{n_0} = \exp\left(\int \alpha dx\right). \quad (4.4)$$

M depends on the strength of the electric field through the dependence of α . Therefore, M is a function of the applied voltage through the dependence of α on the electric field. Here, this multiplication factor does not include the losses of the electrons during the electron drift via attachment or recombination. Since the operation of wire chambers is based on the drift and multiplication of electrons in the fill gas, a primary requirement for the gas filling is that its electron attachment coefficient is low. This is generally true for noble gases, and therefore most of the wire chamber fill gases are based on noble gases such as argon, xenon or neon.

In the multiplication process, large number of positive ions is generated. When these ions return to the neutral state via recombination, a photon of UV energy region ($\sim 10eV$) is emitted. Once the UV photon irradiates the electrode material, secondary electron(s) are emitted via the photoelectric effect. These secondary electrons are also multiplied near the anode electrodes. If the average number of the secondary electrons due to a positive ion exceeds 1, this process occurs endlessly and causes discharges. Photons are also emitted as the argon ions reached the detector cathode and are neutralized by extracting an electron from the cathode. In order to suppress this effect, some additional gases, which absorb the UV photons, are mixed with the base gas. Organic gases such as methane or ethane is normally used as the additional gas, which is called "quenching gas" or "quencher". These organic gases absorb the UV photons and change the energy into the rotation or vibration of the molecule.

Fig.4.1 shows the Time development of an avalanche near to an anode wire in a proportional chamber [33] [34]. (a) shows a primary electron moving towards anode wire, (b) the electron gains kinematic energy in the electric field and ionizes further atoms; multiplications starts. (c) shows the electron and ion clouds drift apart. (d) and (e) shows the electron cloud drifts towards the wire and surrounds it; the ion cloud withdraws radially from the wire.

4.1.4 Operation Mode

In the case of a thin anode wire, the critical electric field value is normally exceeded only near the anode wire, where the avalanche is initiated. The total multiplication factor depends on the voltage applied to the anode wire. Fig.4.2 depicts qualitatively the development of the output signal with increasing anode voltage and the different modes of operation of a wire chamber.

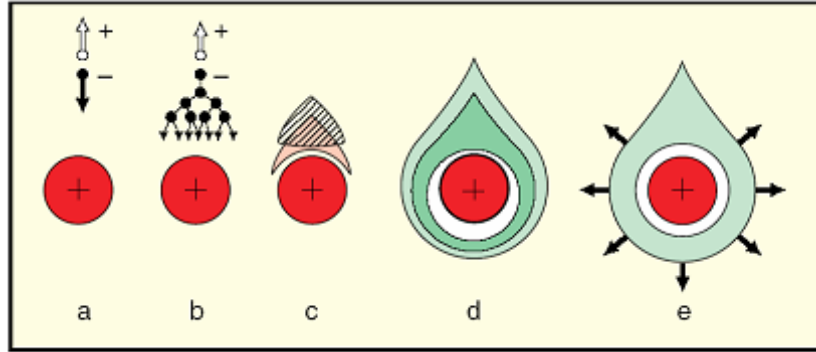


Fig. 4.1: Time development of an avalanche near to an anode wire in a proportional chamber. [33]

In the recombination region, the electric field separates the electron and ion charges so slowly that significant recombination occurs and not all created charges are collected. With sufficiently high electric field, all the charges are collected from the detector, but no charge multiplication occurs. This is the ion saturation region. When the electric field close to the wire reaches the threshold value for charge multiplication, the detector starts to operate in the proportional region, where multiplication takes place in a manner where the output signal is proportional to the amount of charge initially created.

Strict proportionality assumes that space charge (due to the longer-lived positive ions) and induced effects remain negligible, compared to the external field. At higher gas multiplication, or in a high flux of charged particles, the space charge effects alter the effective electric field; the chamber works in the mode of limited proportionality: the signal is no longer strictly proportional to the energy loss of the particle; the relation between collected charge and dE/dx can still be put to use, though.

Further increase of the electric field eventually leads to electric breakdown of the gas. This takes place when the space charge inside the avalanche is strong enough to shield the external field. A recombination of ions then occurs, resulting in photon emission and in secondary ionization with new avalanches beyond the initial one. If the process propagates (backwards, from the avalanche tail) until an ion column links anode and cathode, a spark discharge will eventually occur, and a chamber or counter is said to operate in the Geiger-Muller mode.

By using gas mixtures that strongly absorb the UV photons, the formation of additional avalanches far from the original site is prevented. Instead, new avalanches are limited to the immediate vicinity of the original. This mode is called the limited streamer or self-quenched streamer mode. In this mode, the new avalanches will grow in the form of a narrow "streamer" that extends radially away from the anode wire surface[57][58]. These streamers are 150 - 200 μm thick and extend a few millimeters from the anode. They are self-limiting and terminate with a final length that increases with applied voltage. If the original ion pairs are formed over a limited axial distance, only a single streamer is formed. For more extended tracks, multiple streamers are observed. At sufficiently high values of the voltage, a single electron can trigger a streamer. The rise time of typical output pulses has been measured as 30 - 40nsec[57], so the limited streamer mode can result in good timing precision as well.

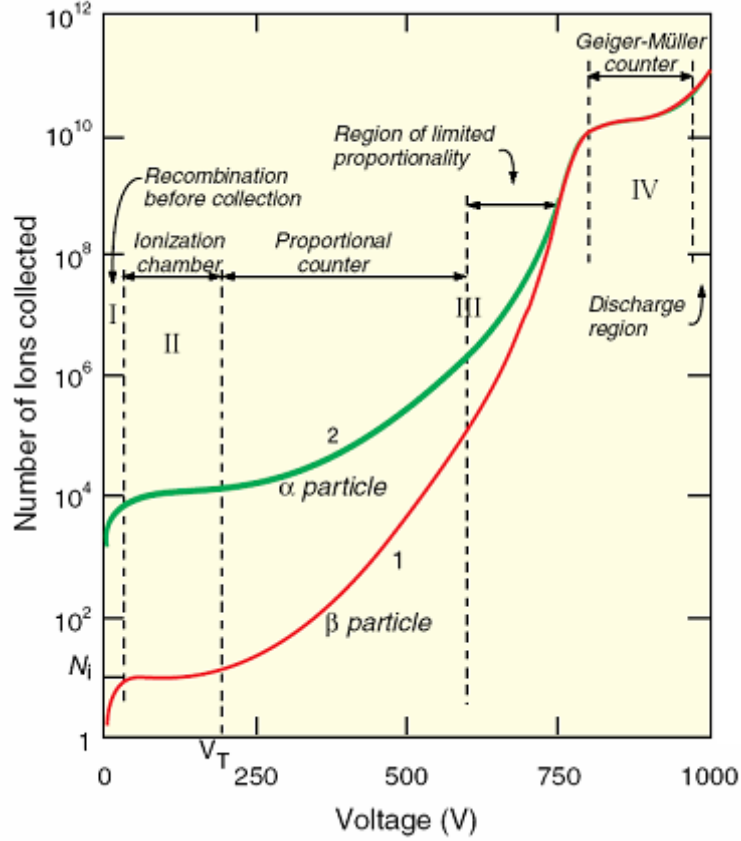


Fig. 4.2: Output signal from a wire chamber as a function of anode voltage with two different energy deposition, α particle and β particle. Different operation modes are indicated. [40]

4.1.5 Multiwire Proportional Chamber (MWPC)

Multiwire proportional chamber (MWPC) [32] is a plane of anode wires positioned between two cathode planes. Fig.4.3 shows a sketch of the first MWPC. It consists of a plane of parallel sense wires with spacing s and length L inserted in a gap of thickness Δ . The potential distributions and fields can be calculated with good accuracy from the exact formula for the potential and field strength around an array of parallel wire (diameter a) along z and located at $y = 0, x = 0, \pm s, \pm 2s, \dots$,

$$E(x, y) = \frac{CV_0}{2\epsilon_0 s} \left\{ \left[1 + \tan^2 \left(\frac{\pi x}{s} \right) \tanh^2 \left(\frac{\pi y}{s} \right) \right]^{\frac{1}{2}} \left[\tan^2 \left(\frac{\pi x}{s} \right) + \tanh^2 \left(\frac{\pi y}{s} \right) \right]^{-\frac{1}{2}} \right\} \quad (4.5)$$

$$V(x, y) = \frac{CV_0}{4\pi\epsilon_0} \left\{ \frac{2\pi l}{s} - \ln \left[4 \left(\sin^2 \left(\frac{\pi x}{s} \right) + \sinh^2 \left(\frac{\pi y}{s} \right) \right) \right] \right\} \quad (4.6)$$

$$C = \frac{2\pi\epsilon_0}{\left(\frac{\pi l}{s} \right) - \ln \left(\frac{2\pi a}{s} \right)}, \quad (4.7)$$

where V_0 is the potential of wire surface, C is the capacitance between anode and cathode, l is the distance between anode and cathode. Therefore, each wire is worked as drift tube in the vicinity of the wire.

The spatial resolution is limited by the diffusion of ionization electrons during the drift and by the fluctuations of the ionization process. Depending on the gas mixture, the width of the diffusion cloud after 1cm of drift is typically between 50 and 300 μm ; small diffusion implies low drift velocity.

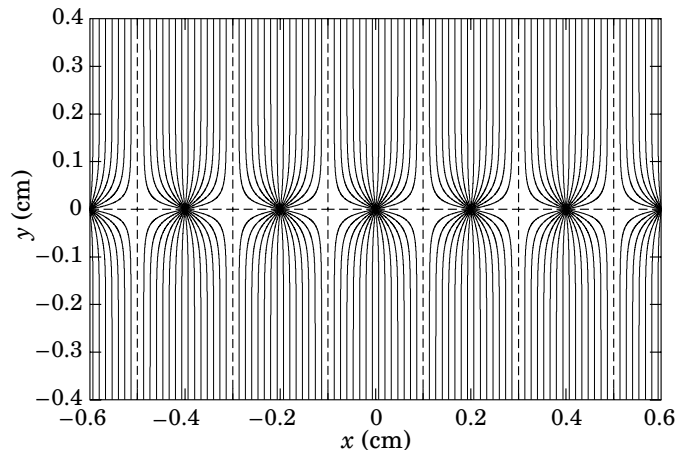


Fig. 4.3: Electric field lines in a MWPC with an anode pitch of 2mm as calculated with GARFIELD programm [36].

4.2 Requirements for the Performance

TGC has been chosen as a trigger detector of the ATLAS end cap muon spectrometer. The basic five requirements on the performance of the chamber are:

1. High detection efficiency: In order to create the trigger signal, the detection efficiency has to be more than 99% at all detection area.
2. Good time resolution: At LHC the bunch-crossing spacing is 25nsec. The time jitter of the detector has to be smaller. This means assigning more than 99% of the triggered muons to the correct bunch-crossing.
3. Fine granularity: This is needed since the trigger chambers is located outside the magnetic field and can have only a relatively short lever arm of approximately 1m. To match the geometric granularity to needed high p_T threshold ($> 20\text{GeV}$), the number of wires in a segmentation varies as a function of η .
4. Good performance under high background rate which is estimated to be smaller than $1\text{kHz}/\text{cm}^2$.
5. two-dimensional readout

A small time jitter was obtained by optimizing the cell geometry and the gas mixture [43]. Small segmentation was obtained by ganging together adjacent wires (typically five wires spaced by 1.8mm) and reading the anodes for the polar coordinate, which are important because of the toroidal structure of the magnetic field.

4.3 Structure of TGC

Fig.4.4 shows the cross-section of TGC. TGC have an anode plane made of $50\ \mu\text{m}$ in diameter gold-plated tungsten wires with 1.8 mm pitch. The wire plane is sandwiched between the graphite cathodes 1.4 mm from the wires. In order to induce the positive charge on strip, the surface resistivity of the graphite is adjusted around ($0.5M\Omega \sim 1.5M\Omega$)

The copper strips with several mm pitch provide a capacitively coupled readout. The mechanical support is provided by 1.6 mm thick G-10 plates that carry the strips. There are about 1000 wires in one chamber, and several wires are grouped together.

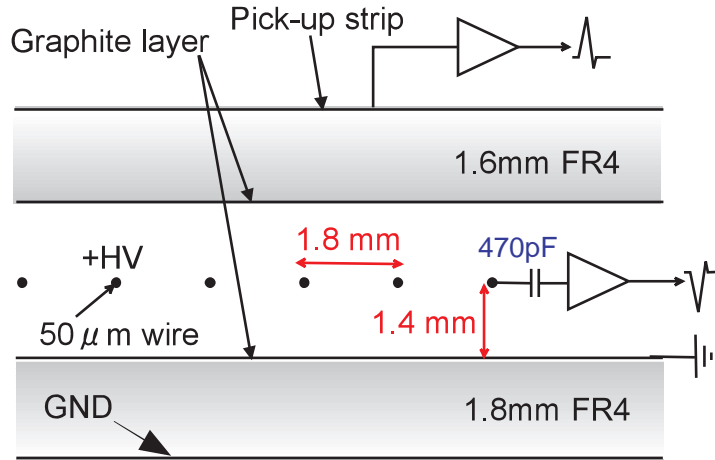


Fig. 4.4: Cross section of TGC [14]

TGC is operated with 3.0kV applied high voltage on the anode wire. Fig.4.5 shows the electric field line of TGC (left) and the equipotential line (right) at this operation voltage[37]. The field strength is about 40kV/cm at a position away from the anode wire by 0.2cm and 10kV/cm by 1.3mm (vicinity of the cathode plane). Therefore, the avalanche can be started to grow from the vicinity of the strip plane.

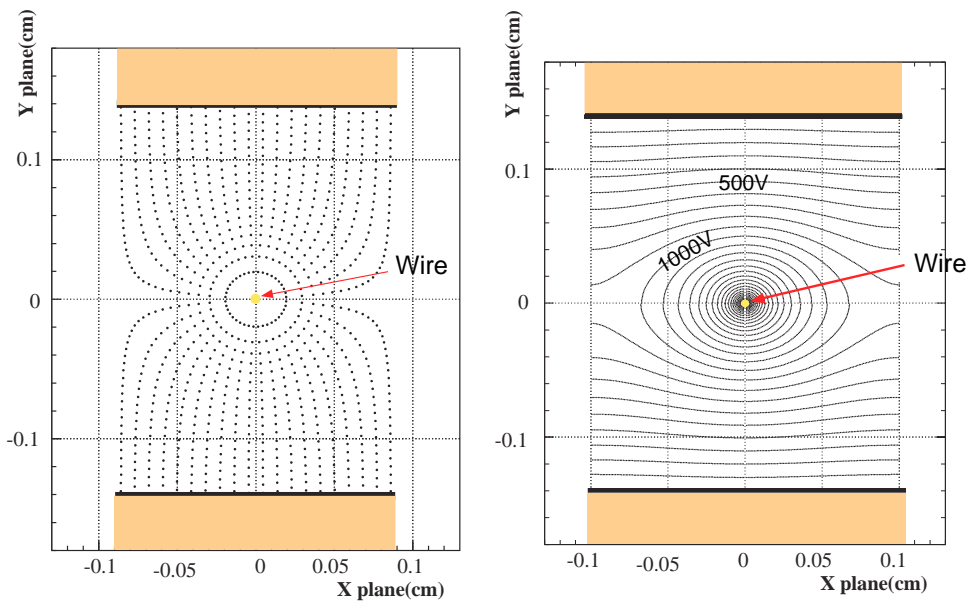


Fig. 4.5: Left is the electric field lines in a TGC and right is the equipotential line (both were calculated with TARFIELD program [37]).

The gas is selected CO_2 : n- C_5H_{12} (n-pentane)=55:45. CO_2 plays role as a working gas and n-

pentane as a quencher. TGCs are operated in the limited proportional mode in this condition. In order to identify the fast bunch crossing of LHC, TGC should have a narrow timing spread of signals. For CO₂-based gases, the drift velocity of electrons does not reach saturation at such a high electric field due to the low electron capture cross section of CO₂ (see Table.4.1). Therefore, the drift time is short, and a typical rise time of TGC is measured below 5nsec. Fig.4.6 shows the ionization and ion-fragmentation cross-section of hydrocarbon vapors under vacuum-ultraviolet radiation[38]. As shown in this figure, n-pentane has the largest cross section in the hydrocarbon which is a gas in the room temperature (boiling point = 36°C).

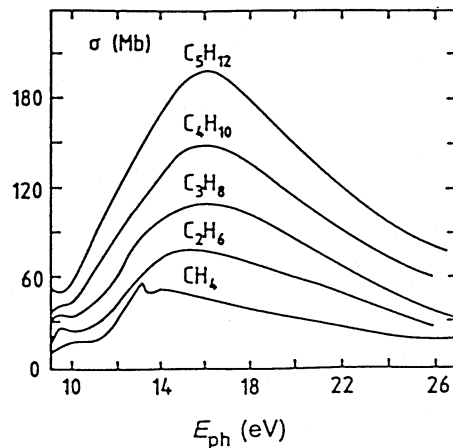


Fig. 4.6: Ionization and ion-fragmentation cross-section of hydrocarbon vapors under vacuum-ultraviolet radiation. n-pentane has largest cross section[38].

gas	cross section
CO ₂	6.2×10^{-9}
O ₂	2.5×10^{-5}
H ₂ O	2.5×10^{-5}
Cl	4.8×10^{-4}

Table 4.1: The electron capture cross section for various gas.

In order to prevent the wire from sagging and to keep the anode-cathode distance constant, two types of the mechanical support parts are used; called “ wire-support ” and “ button support ”. Fig.4.7 shows the schematic view of support structures. Each support part is intrinsically inefficient.

The signal arrival time in the TGC is dominated by the drift of electrons. It has been observed [43] that the usual tail in the signal arrival time distribution in TGCs originates from those particles that pass through the region close to the boundary between two wires, where the electric field, and consequently the electron drift velocity, are very low. This motivated the decrease in size of the elementary cell in the present prototype, compared to that used in the OPAL experiment [44] [45].

The electric field configuration and the small wire distance provide for a short drift time and thus a good time resolution. As an example, the distribution of avalanche arrival times with respect to an external trigger is shown in Fig.4.8 for minimum-ionizing particles incident normal to the chamber surface. The tails of the timing distribution are mostly due to particles traversing the chamber

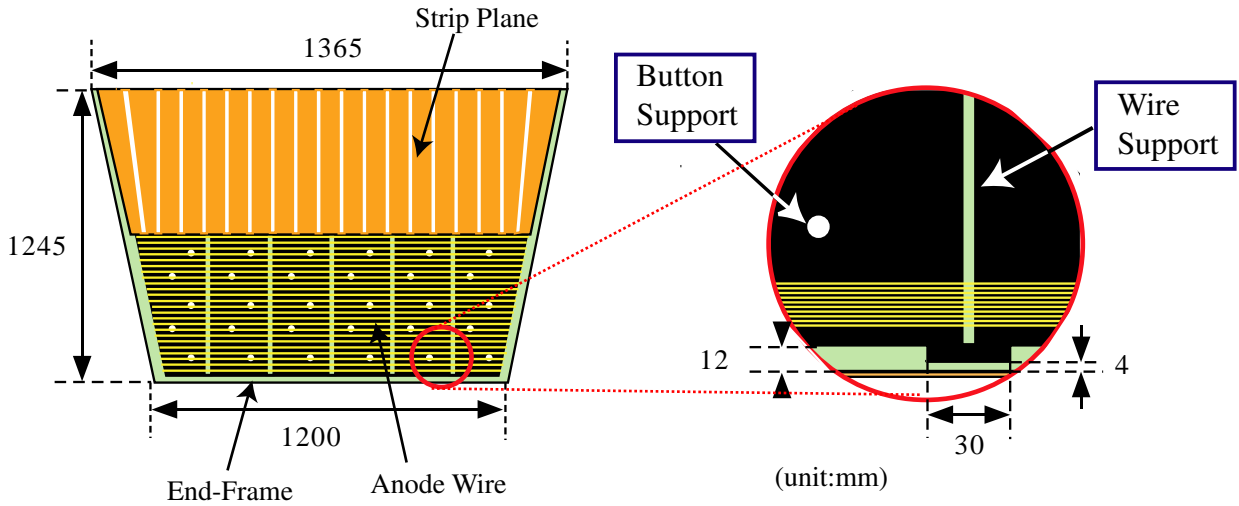


Fig. 4.7: Support structure of TGC

in the low-field region halfway between two anode wires. As the angle increases, the tracks pass closer to the wire, thus reducing the maximum drift distance and improving the time resolution. In the ATLAS chamber layout, all muons passing through TGCs with transverse momenta above the required threshold have incident angles greater than $\sim 10^\circ$.

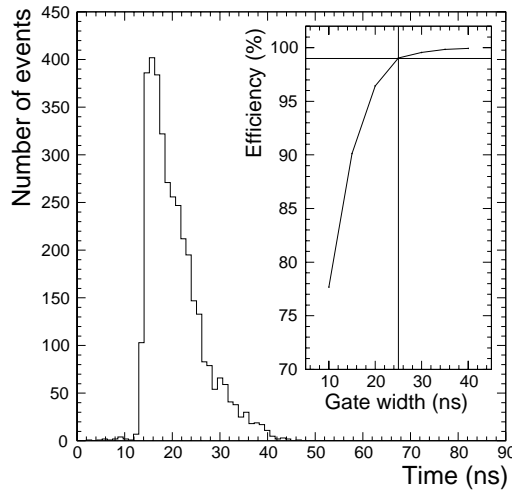


Fig. 4.8: Measured arrival time distribution for a minimum-ionizing particle and the fraction of the arrival times within a given time width. There is 99% efficiency for a gate width of 25ns, at 0° incident angle [13].

If the chamber was distorted, the gap becomes wide and the field becomes weak. Fig.4.9 shows the output pulse height as a function of the gap interval. The distortion of 0.1mm corresponds to the 5% change in pulse height. This corresponds to the decreasing of 100V applied high voltage.

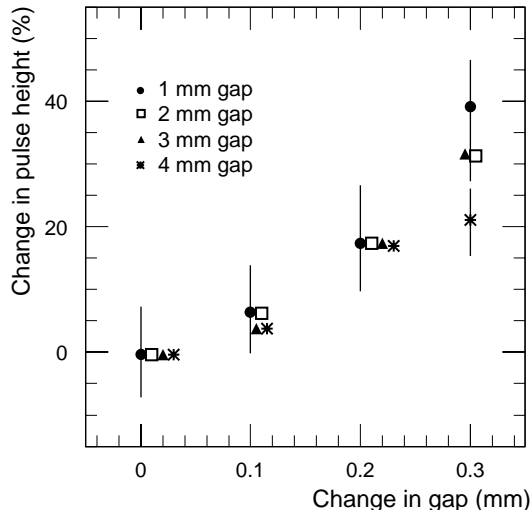


Fig. 4.9: The relation between gas gap and output pulse height. [14]

4.4 TGC Module

In the ATLAS detector, three trigger stations will be installed 14 m from the interaction point; consisting of 3, 2 and 2 TGC layers, respectively, looking from the interaction point. The combination of three stations will allow the trigger of particles with $p_T > 6\text{GeV}/c$. TGCs are constructed in doublets and in triplets to increase the mechanical strength and to prevent the inefficient support structure from overlapping. Fig.4.10 shows cross-sections of a TGC triplet and of a doublet. The anode plane is sandwiched between two cathode planes made of 1.6 mm G-10 plates on which the graphite cathode is deposited. The TGC layers are separated by 20 mm thick paper honeycomb panels, which provide a rigid mechanical structure for the chambers. On the outside, the gas pressure is sustained by 5 mm thick paper honeycomb panels. These are covered in turn by 0.5 mm G-10 plates.

The seven layers in the middle station are arranged in one triplet (M1 station) and two doublets (M2 and M3 station). On the backside of the cathode plates facing the center plane of the chamber, etched copper strips provide the readout of the azimuthal coordinate; no readout strips are foreseen for the central layer of a triplet.

Fig.4.11 shows the R - ϕ view of the endcap trigger plane; left shows M1 plane, right shows M3 plane. Each cell shown represents a TGC module (doublet or triplet). Chamber boundaries are shown. A single octant has been shaded and the chamber type at each radius indicated. There are 3792 singlets in total; 1296 singlets for M1 sector, 2496 singlets for M2 and M3. Each type is classified from T1 to T11 and summarized in Table.4.2.

sector	module	type name
M1	Triplet	T1,T3,T6,T7,T8
M2	Doublet	T2,T4,T5,T6,T7,T8,T9
M3	Doublet	T2,T4,T5,T6,T7,T8,T9

Table 4.2: TGC type name in each sector.

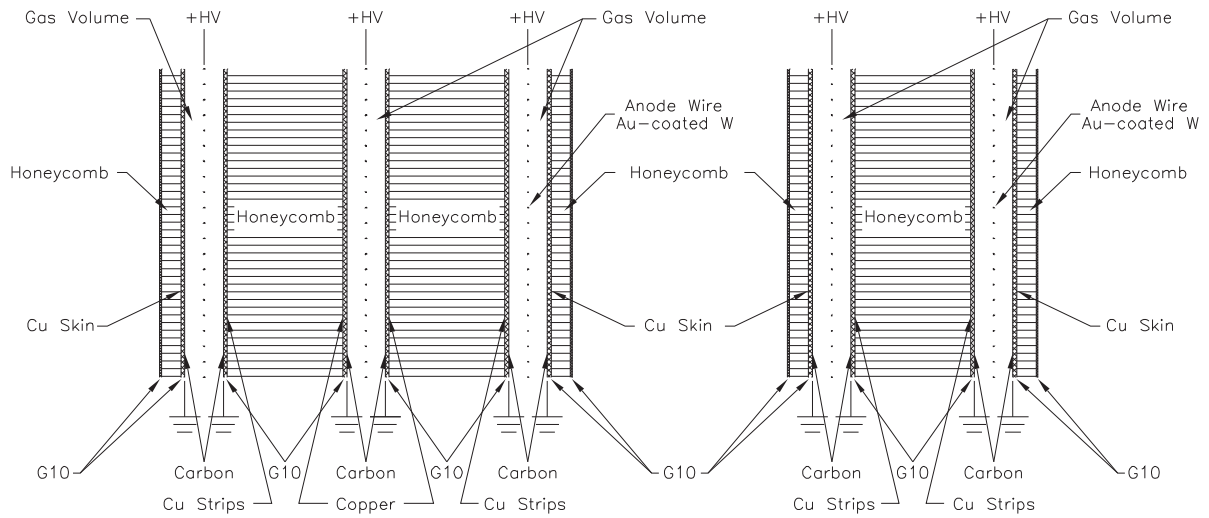


Fig. 4.10: Cross section of TGC Module. Left indicates Doublet and Right indicates Triplet. [14]

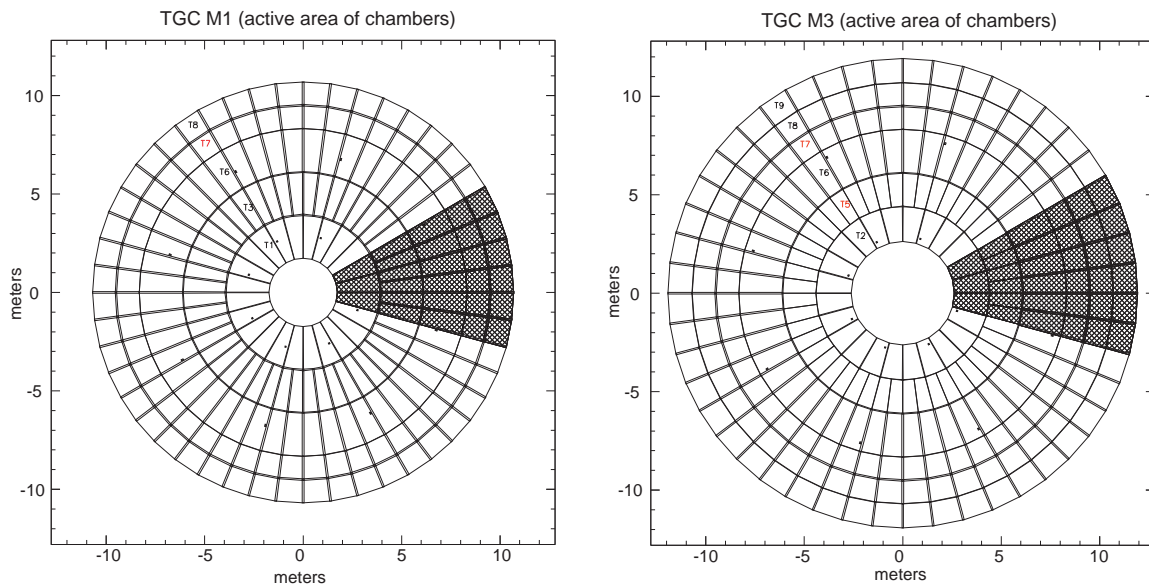


Fig. 4.11: Left: R- ϕ view of the first trigger plane (triplet). Right R- ϕ view of the third trigger plane (pivot plane doublet). Each cell shown represents a single TGC unit (doublet or triplet). Chamber boundaries are shown. A single octant has been shaded and the chamber type at each radius indicated [14].

4.5 ASD(Amp Shaper Discriminator)

To form a trigger signal, several anode wires are grouped together and fed to a common readout channel. The number of wires per group varies between 4 and 20, depending on the desired granularity as a function of pseudorapidity. The ganged signals are fed into a low-impedance two-stage amplifier. The combination of chamber and amplifier yields a rise time of the amplifier output into the discriminator of $10 \sim 20$ nsec.

The amplifier-shaper-discriminator (ASD) chip was developed in KEK [61]. A block diagram of the ASD chip is shown in Fig.4.12. Its first stage (preamplifier) is a common emitter cascade charge amplifier. The gain of it is approximately $0.8\text{V}/\text{pC}$. An emitter follower output of this preamplifier stage is provided for monitoring. The second stage (shaper) consists of a main-amplifier with differential outputs and a baseline restorer. The main-amplifier section has a gain of 7. The shaper circuit has pole-zero cancellation circuit to cancel $1/t$ tail.

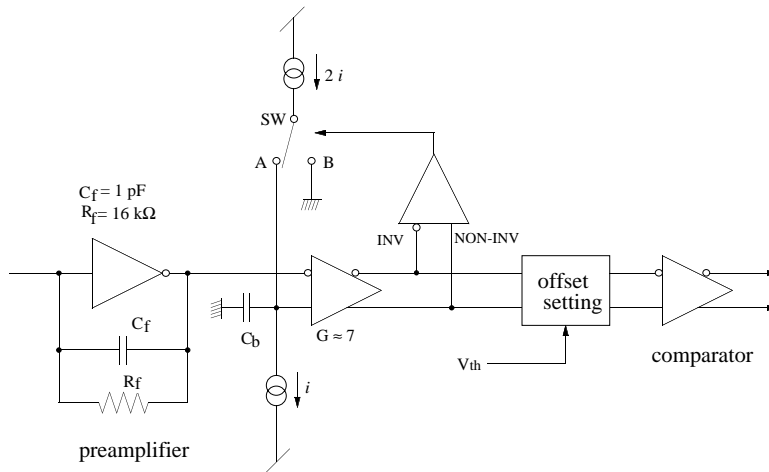


Fig. 4.12: Block diagram of the ASD chip [61].

Depending upon the output differential signal level seen by the switch control section, the switch connects to the “ A ” side or to the “ B ” side of Fig.4.12. When the switch is connected to the “ A ” side, the capacitor C_b will be charged from the current source by the amount of ‘ i ’. When the switch is connected to the “ B ” side, the capacitor will be discharged by the amount ‘ i ’, resulting in stabilized DC output levels, or a baseline restoration. In other words, the circuit makes the baseline level of the differential outputs from the main-amplifier to be equal. The pile-up is suppressed under the high rate environment due to this circuit.

Following the main-amplifier is an offset setting (discriminator) which transforms the main-amplifier outputs to the levels required at the inputs to the comparator, where offset voltage is controlled by DC voltage (threshold voltage, V_{th}) supplied from outside of the chip. The IC contains 4 channels in one package, and V_{th} is common to the 4 channels. Its outputs conform to the Low Voltage Differential Signaling standard, LVDS, to assure drivability and immunity against noise and minimizing power. By design, this circuit can be used for both wire and strip signals by setting an appropriate threshold level.

We can read 16ch simultaneously with 4chips in one card (see Fig.4.13). Since a layer of T7 type has 32ch output for wire and strip respectively, 4 ASDs are equipped on one chamber and 10ASDs on a triplet. ASD cards were covered with the Tin-plated copper shield to protect from external noise (see Fig.4.14).

Fig.4.15 shows the structure of the wire readout part. Each wire group is connected with a HV capacitor and print-circuit board. This board called adaptor board transmits the wire signal to ASD. The board was also covered with the copper shield.



Fig. 4.13: Picture of ASD card (without shield)



Fig. 4.14: Picture of ASD (with shield)

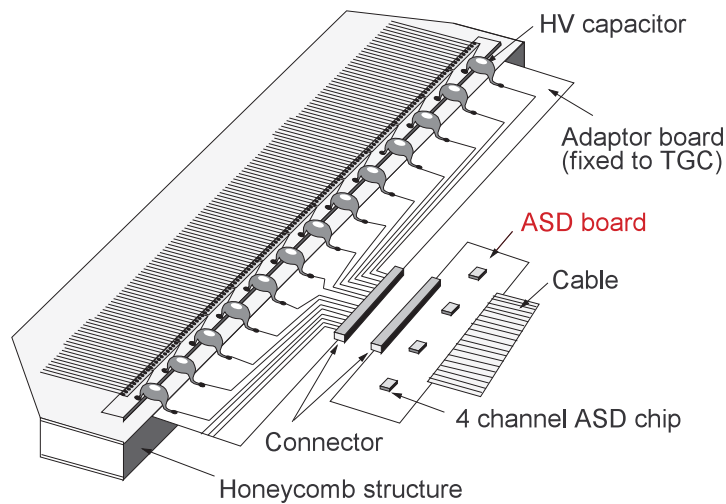


Fig. 4.15: The schematic view of the structure for wire readout part [14].

4.6 Production and Inspection

4.6.1 TGC Production

ATLAS TGC chambers are produced in parallel in Japan, Israel, and China. Basic performances of materials used in gas volumes were studied at KEK (Japan) in small prototype chambers[49]. Production procedures of real-size TGCs were developed from March 1998 to the end of 2000[54]. TGC was produced by gluing their parts (not using any screw). The TGC series production started in January 2001. A production of about 1100 TGCs was to be completed in Japan by the middle of 2004. In order to meet this schedule, the KEK production facility was designed to produce two TGCs per day with about 12 workers and 3 physicists as supervisors.

Fig.4.16 shows the size and type of TGC manufactured in Japan. As this figure shows, 3 types of chamber, called T7, T4 and T5 type, had been made. Total numbers of the chambers are 1211 summarized in Table.4.3. It was necessary to inspect the performance of TGCs before installing them to ATLAS detector. Hence, following points need to be checked;

- Detection efficiency is more than 99% by excluding the inefficient area with fine granularity.
- Signal response is less than 25nsec for bunch identification.

TGC Type	TGC Wheel	Need for ATLAS	# of TGCs	# of Modules
T7 Triplet	M1	96	356	113
T7 Doublet	M2	96	218	106
T7 Doublet	M3	96	221	109
T4 Doublet	M2	96	215	107
T5 Doublet	M3	96	214	107
SUM		480	1224	542

Table 4.3: Summary of the production of TGC Units at KEK.

4.6.2 Inspection Schedules

Because the installation schedule to ATLAS was decided, we must finish the inspection by August 2005. To inspect 542 modules in 45 months from November 2002 to August 2005, 5 modules/week on average is required. The schedule was designed taking the periods for system modification, year-end and New Year shutdown into consideration. We perform this inspection every day in three years until finishing. The system that is stable during the test period is required.

	inspection	system modification
T7 Triplet	2002/11/1 ~ 2003/4/18	2003/4/18 ~ 2003/5/30
T7 Doublet	2003/5/30 ~ 2004/4/16	2004/4/16 ~ 2004/5/28
T4 Doublet	2004/5/28 ~ 2004/10/29	2004/10/29 ~ 2004/12/24
T5 Doublet	2005/1/7 ~ 2005/6/10	

Table 4.4: The goal of inspection and system modification.

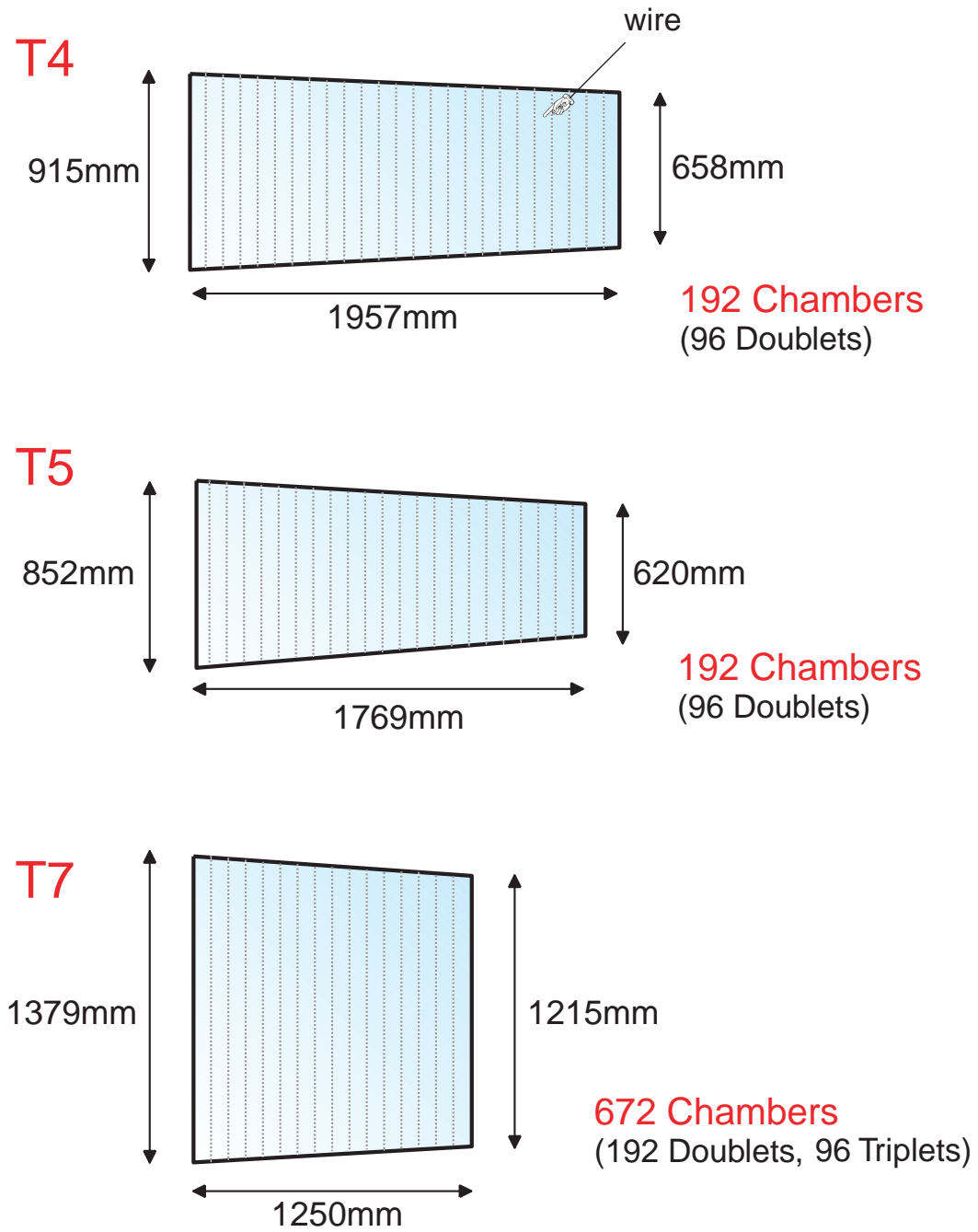


Fig. 4.16: The size of the TGC produced in Japan.

5 Test Facility

In order to detect all muons generated at the collision point, it is necessary to inspect the uniformity of efficiency over all detection area. These characteristics are confirmed by using the cosmic rays muon. All TGCs produced in KEK are checked. Because the areas of TGC inspected as shown in Fig.4.16 are around 2m^2 , it was necessary to construct a large-scale leased facility.

Requirement for the test system is;

- It can examine the chamber efficiency as many as possible at the same time.
- It has sufficient fiducial volume (or acceptance, detection area) in order to check whole detection area of TGC.
- It has long term stability.
- It has enough accuracy for efficiency measurements.

There are the following three stages to inspect the performance of TGC;

1. Cosmic ray test; the measurement of the detection efficiency and timing response,
2. High voltage test; the check of the long term stability,
3. Leak test; the check of the gas tightness.

5.1 Leak Test

In this section, the procedure of the Leak Test is described. The n-pentane is a flammable and poisonous gas. In addition, the gas-gain maybe degraded due to contamination of oxygen, since oxygen is a high electronegative gas and can be recombined with the ionized electron. Thus, it is very serious if chamber has some leakage.

5.1.1 Chamber Leakage

In order to measure leakage from a chamber, we applied pressure to the gas volume. However the chamber can be damaged due to over-pressure because the chamber is manufactured only by gluing its parts and is fragile with respect to inner pressure. We set, therefore, the maximum pressure allowed to 600Pa.

Gas tightness of chamber is checked as follows;

1. Pressure is applied up to 600Pa.
2. Shutoff the gas inlet and outlet.
3. After 5 minutes, pressure drop ΔP is measured.

A chamber is accepted as passed one against the gas tightness check if the ΔP is less than 50Pa. Because the volume of the chamber is about 4000cc, the leakage volume of the chamber for $\Delta P = 50\text{Pa}/5\text{min}$ is corresponding to $\Delta V \sim 2\text{cc}$.

5.1.2 CO₂ Channel

There is the volume around the chamber to prevent n-pentane from leaking to outside the modules. It is called 'CO₂ Channel'. Even if a chamber have some leakage, n-pentane is collected by flowing CO₂ in the 'CO₂ Channel'. The gas tightness check for CO₂ Channel should be carried out as well as the chamber.

Fig.5.1 shows the schematic view of the CO₂ Channel for the T7 type. Green and red area indicates the CO₂ Channel.

For CO₂ channel, the criteria is set to be $\Delta P < 100\text{Pa}/5\text{min}$. T7 type modules have 2 types of CO₂ channel. This is because they have different a path for CO₂ channel after installed in ATLAS detector. One path called 'Main', and other called 'Side' (see Fig.5.1). In T4 and T5 type, Main and Side are connected to the series.

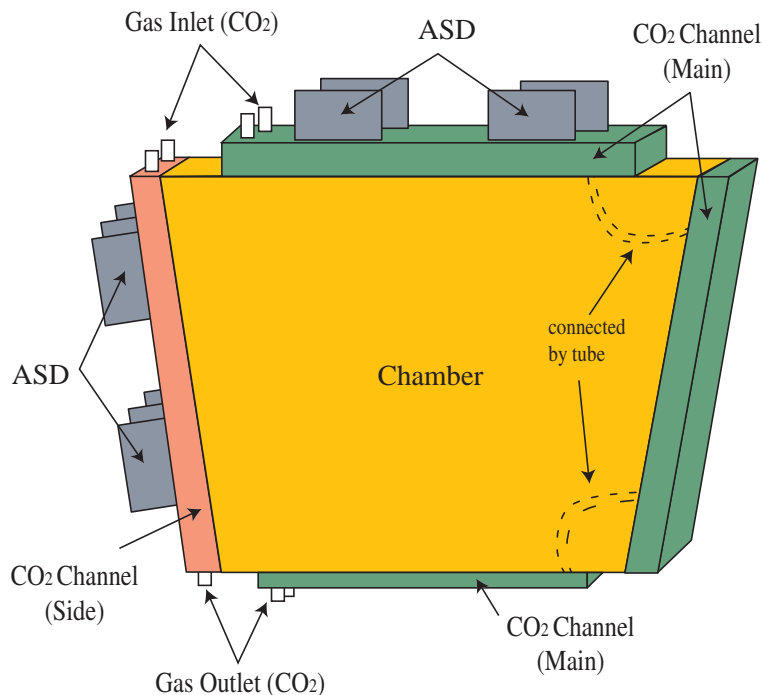


Fig. 5.1: The schematic view of CO₂ Channel for T7 type. CO₂ is flowed in the green and red volume to collect the n-pentane if there are some leakage.

5.1.3 System Setup

In this process, the gas-tightness is checked by applying the pressure to chamber, and/or CO₂ Channel, Fig.5.2 shows the image of the test setup. Fig.5.3 shows the gas piping diagram. In order to avoid the overpressure, a safety system, a water bubbler is mounted on the system. Its water level is adjusted to the maximum pressure of the system. The pressure is measured using a manometer, which can measure the difference from the atmospheric pressure up to 1kPa. In addition, a differential pressure sensor (OMRON E8Y series), by which the pressure up to 10kPa is transduced to the current, is used to record variance of pressure during gas tight check. The output current is converted to the voltage and fed to AD converter (Analog to Digital converter) connected to computer through the PCMCIA bus (AD12-8(PM) manufactured by CONTEC Co. Ltd. [59]). The resolution of the

pressure measurement is about 2.4Pa. The sampling rate was designed as 1Hz to measure the slow variation of the pressure and reduce the data size.

Since the difference of pressure is small, it is necessary to distinguish whether variation of the pressure is due to leakage of gas volume or the change of environment temperature. As for the chamber, the temperature change of 1°C is corresponding to the pressure change of 300Pa. In order to evaluate the environmental effect, the pressure of a 100m-long tube, which has same volume size as a chamber, was measured as a reference. Fig.5.4 shows an example of pressure change during the test. Blue line shows the reference pressure and red line shows the chamber pressure. Since the reference is dropped as well as the chamber, these change of pressure are due to change of temperature and it was found that this chamber has negligible leak.

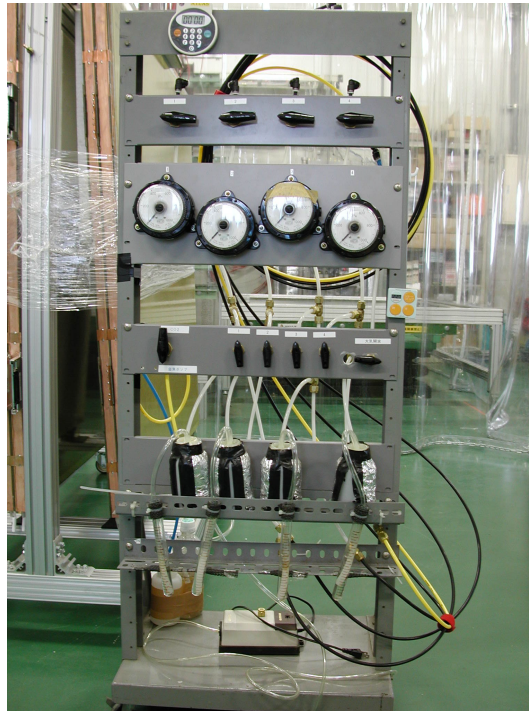


Fig. 5.2: Gas Leak Test Machine. There are 4 lines. The gas piping diagram is also shown in Fig.5.3.

5.1.4 Repair

If there is some leakage, the point of the leakage should be searched and repaired. Two detection methods were developed. These are called “ Pressurizing Method ” and “ Decompression Method ”. Fig.5.5 shows the jig for these methods. In the Decompression Method, the point is searched by using a formed rubber jig shown as Fig.5.5(a). It is attached to a vacuum cleaner and decompress the chamber (or CO₂ channel) if leakage point is in covered area. Because this jig can cover about 10cm region, this method is very useful so as to search wide area. In the Pressurizing Method, the point is searched by using compressed air. When compressed air is sprayed toward the leakage point, the pressure of chamber (or CO₂ channel) rises. Because the air gun can spray at a pinpoint, this method is used to detect precise position of the leakage.

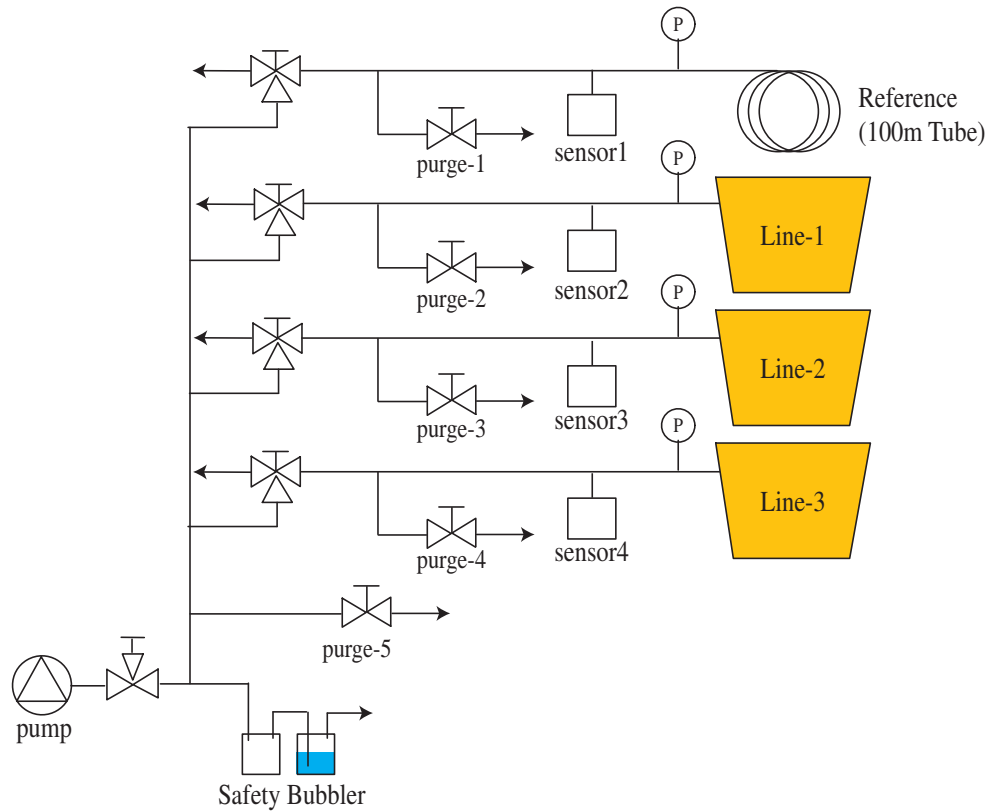


Fig. 5.3: The gas piping diagram for leak test. One line is the reference to check the change of the environment. Other three lines are used for the test. The pressure of each line is monitored by a manometer and a pressure sensor. The safety bubbler to avoid the overpressure is mounted on main line. The pressure is applied by the small pump. The flow rate is adjusted by a needle valve.

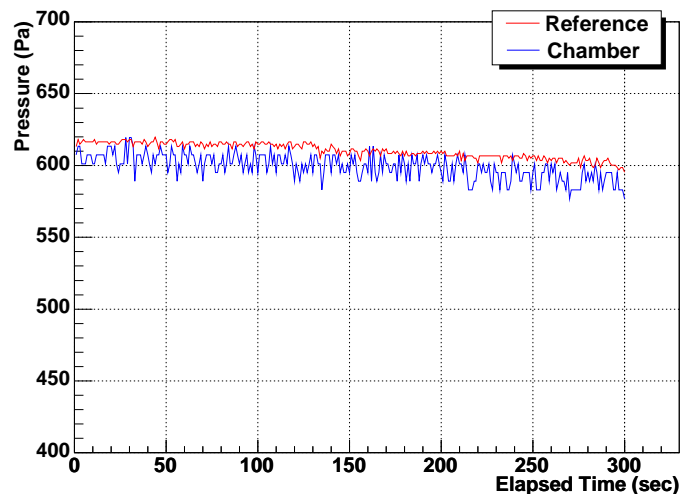
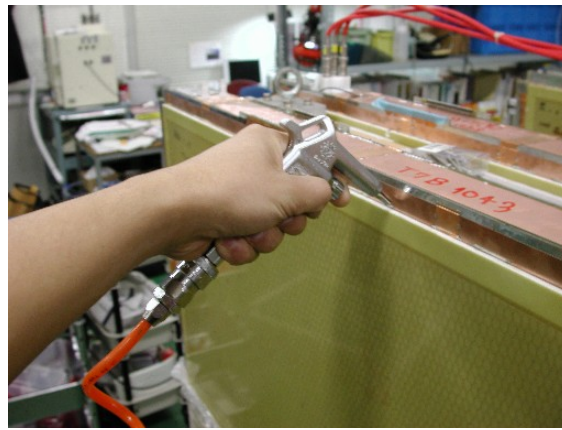


Fig. 5.4: An example of the test result of gas tightness check. The pressure is shown as the function of the elapsed time of the test. Red line and blue line indicate the pressure of the reference and chamber, respectively.



(a)

(b)



(c)

Fig. 5.5: There are 2 types of the repairing method. (a) a jig attached to a cleaner. (b) decompressing by the cleaner. (c) applying the pressure by compressed air-gun.

5.1.5 Inner Leak

If the CO₂ Channel had some leakage, the point of the leakage was not only on the surface of the chamber but also in the volume of the paper-honeycomb. In the production stage, the paper-honeycomb was glued between two chambers by painting the adhesive. There was some pinhole somewhere in the volume of the paper-honeycomb and it was connected to the CO₂ Channel, the pressure of it was transmitted toward the paper-honeycomb through the pinhole. This type of leakage is called “ Inner Leak ”. Fig.5.6 shows the schematic view. Then the pressure of the paper-honeycomb (P') is increased as well as the CO₂ Channel (P). The time to transmit the pressure is depended on the time constant C/R , where C is the volume of the paper-honeycomb and R is the size of the pinhole. It takes some minutes to increase P' until up to P for the chamber with large R and small C . It takes 1 day for one with very small R and large C . The valve connected to the gas inlet was closed after $P' \sim P$. If the valve was opened shortly to release the pressure P , P is fall to zero at once. The pressure P' is, however, decrease slowly depending on the time constant. If the valve was closed again after $P = 0$, P was increased because of the pressure return from the paper-honeycomb P' . Fig.5.7 shows an example of the Inner Leak. The pressure return and its time constant are clearly seen.

The Inner Leak is examined for the CO₂ channel judged as the defective tightness. When the

pressure was return up to 600Pa and was not decreased for 5 minutes, the CO₂ channel has the Inner Leak but no leakage outside. In such case, the CO₂ channel passed the criteria. If the returned pressure, however, was decreased, there were some holes outside the paper-honeycomb. In most case, there are one or more holes at a groove of the strip pattern.

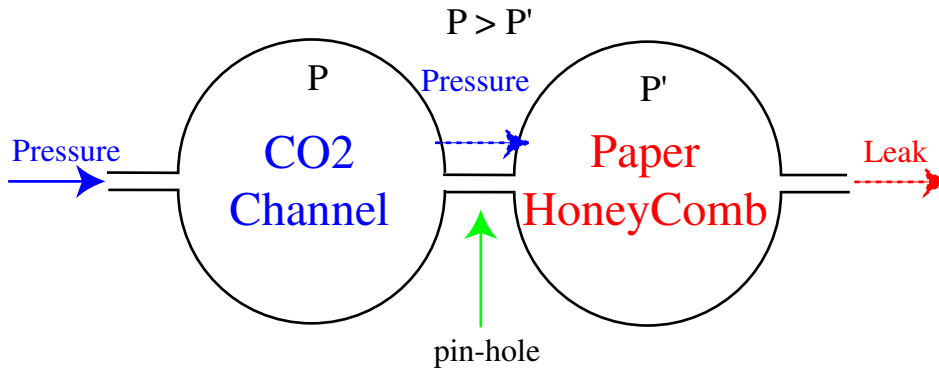


Fig. 5.6: The schematic view of the Inner Leak. CO₂ Channel and the paper-honeycomb are connected together through the pinhole. Since the pressure of the CO₂ Channel (P) comes off to the paper-honeycomb, the pressure of the paper-honeycomb (P') rises up to P . In most case, there are some holes outside in the paper-honeycomb.

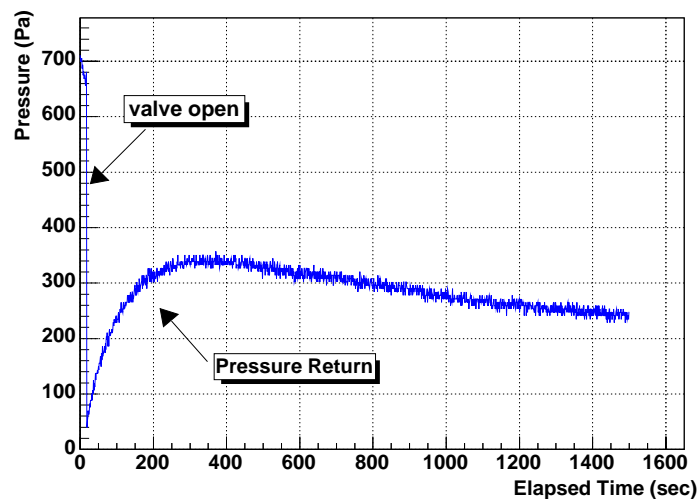


Fig. 5.7: The pressure variation of the Inner Leak. After applying the pressure for appropriate period, it is released by opening a shutoff valve for the outlet of the CO₂ channel. When $P = 0$, the valve is closed again and the pressure is returned from the paper-honeycomb. This graph shows the pressure return and its time constant clearly.

5.2 Results

The results of Leak Test are summarized in Table.5.1. Rank “ A ” means the chamber judged no leakage on both chamber and CO₂ channel. There are 357 modules in rank “ A ” (65.6% of all modules). The modules categorized in other ranks have some leakage. Rank “ B ” and “ C ” means the some leakage on CO₂ channel. There is no Inner Leak on rank “ B ” and some Inner Leak on

rank “ C ”. From rank “ D ” to “ F ”, the chamber was judged as no gas tightness. In total, 15 chambers had some leakage at the beginning of the test.

Fig.5.8, Fig.5.9 and Fig5.10 show the distribution of the pressure drop ΔP for Chamber, CO₂ channel Main and Side respectively. We could repaired almost all leakage exceeded 4 chambers, 6 CO₂ channels for Main and 1 for Side.

Rank	Chamber	CO ₂ Channel	Inner Leak	# of module
A	OK	OK	OK	357
B	OK	NG	OK	46
C	OK	NG	NG	106
D	NG	OK	OK	10
E	NG	NG	OK	3
F	NG	NG	NG	2
G	OK	Unknown	Unkown	18
				542

Table 5.1: Summary of Leak Test

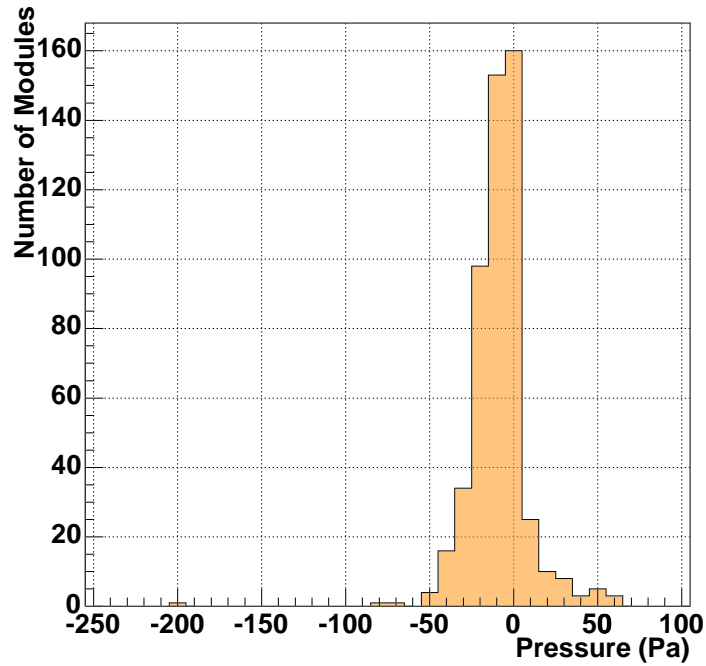
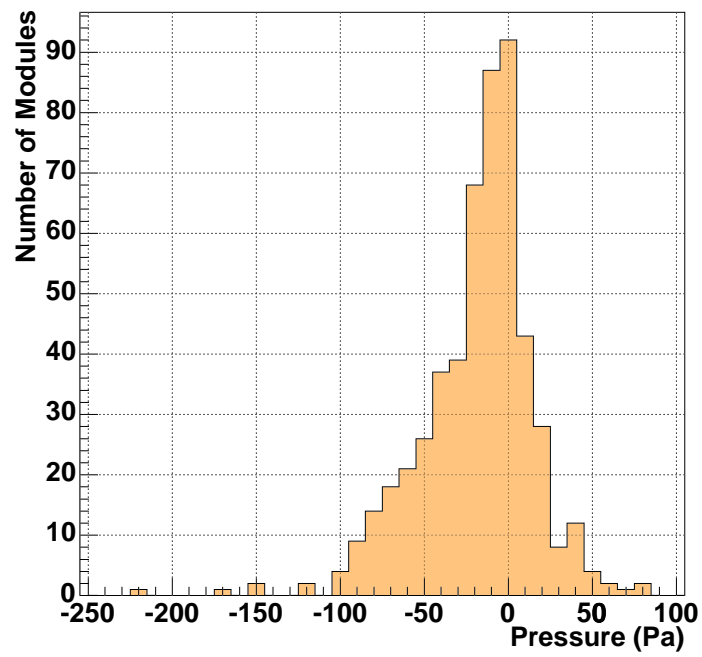
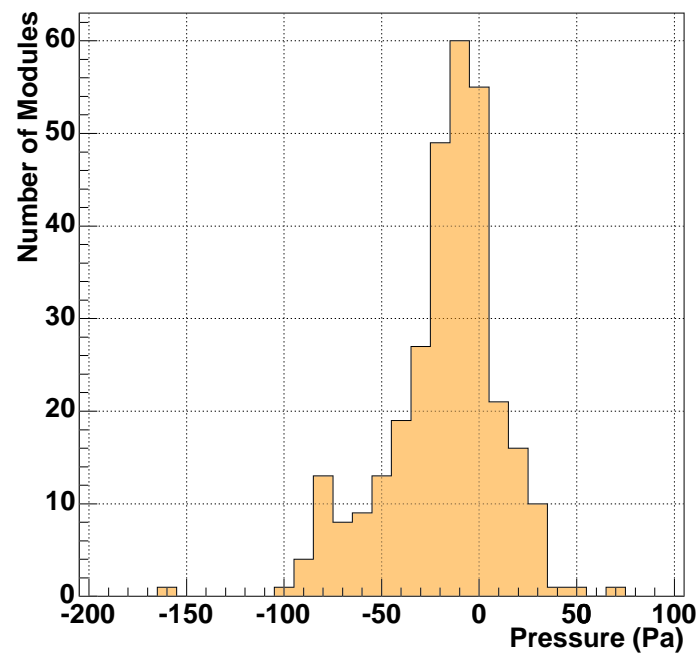


Fig. 5.8: Histogram of Chamber Leak

Fig. 5.9: Histogram of CO₂ channel (Main)Fig. 5.10: Histogram of CO₂ channel (Side)

5.3 High Voltage Test

In this section, the high voltage test (HV Test) procedure and test system was explained. This process was the first test for TGC modules to flow the mixed gas ($\text{CO}_2 + \text{n-pentane} = 55 : 45$) and apply the positive high voltage (HV) of 3.1kV. The stability of the chamber was checked by measuring current of chamber with mixed gas. In addition, unstable chambers can be found by applying HV for a long time and monitoring the current. Therefore we have developed the system for monitoring, recording the current data, and analysis.

Though anode wires are insulated for the cathode plane, small leakage current flows on the inner surface of the chamber. In usual, this was about 100nA. However, the adhesive leaking at the bonding part (the wire support and button support) may become an electric path which causes the current increase. The flux of the solder also may become a path if it remains on the carbon plane and solder. As for such a chamber, leak current was large, and operation became unstable.

In some cases, the large leak current indicated the bad condition of anode and/or cathode. If some powder of carbon or some dust had remained on the surface of the cathode plane at the TGC production stage, it caused sparks. The sparks were measured as an outbreak of large current. Fig.5.11 shows the example of such sparking. Red solid line indicates the current. The large current, approximately $1\mu\text{A}$, started suddenly, and continued for nearly 30 minutes. Such current was not caused by streamer but by micro discharge because the current came to stabilize after a while. In addition, if there was a thorn on the anode wire, the electric field concentrates at this point, and discharge might be caused. After repeating the sparks, the anode wire and cathode plane became smoother. Thus, this process helps chambers more stable.

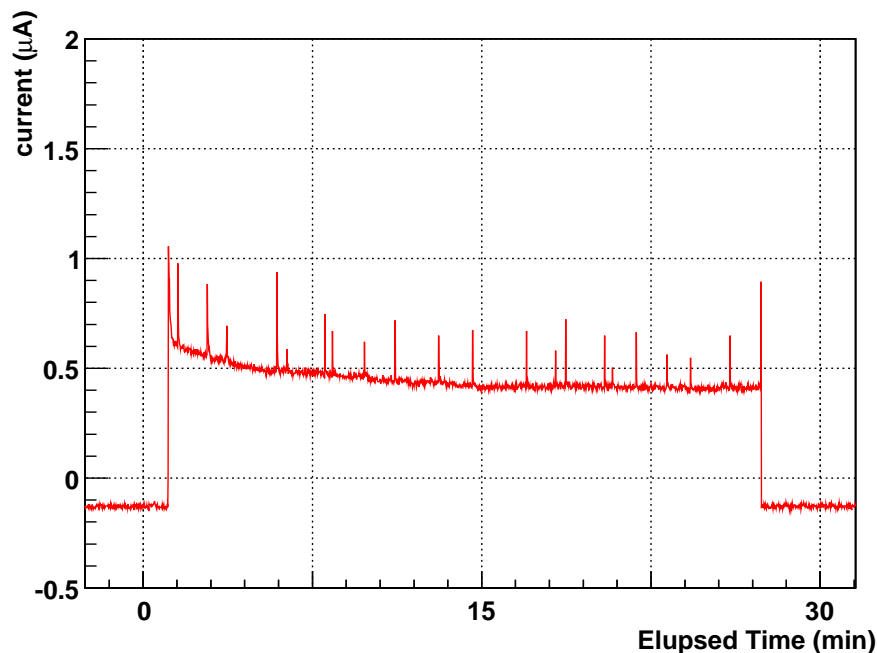


Fig. 5.11: Example of the large continuous current. Red line indicates the current and blue line indicates the high voltage. The large current, about $1\mu\text{A}$, started to flow suddenly, and continued to flow for 30 minutes. The gradual decreasing of the current indicates that the dust or the thorn was burnt off by spark, and the anode wire and cathode plane became smoother.

5.3.1 Test Procedure

1. Preliminary Test

Before testing with mixed gas, preliminary check was performed. In this procedure, the chamber was filled with CO₂ and applied positive HV of 2.9kV. CO₂ flow rate was about 20cc per minute. The volume of the chamber is about 4000cc, so that it took 40 minutes to replace the air to CO₂. To fill with the gas completely, 8 hours circulation was required. Total amount of the gas is corresponding to 10 times of the chamber volume. After 8 hours, 2.9kV was applied to the anode wire. If no sparks was observed at 2.9kV and the current was less than 1 μ A for 8 hours, then 3.0kV was applied for 1 hour. After 1 hour with a current not exceeding 1 μ A, the preliminary test finished. In addition, we confirmed the consistency by comparing the value of the stationary current in this procedure with one taken in the production procedure.

2. Test with Mixed Gas

The chamber was filled with the mixed gas after preliminary test. As well as the previous procedure, it took 8 hours to replace the gas. 2.5kV was applied during the gas replacement. After 8 hours, the HV was raised gradually up to 3.1kV, nominal operation high voltage. The time table of the test is listed in Table.5.2. With the mixed gas, 3.1kV could not be applied immediately. This is because the chamber may become unstable with n-pentane. This phenomenon will be discussed in section 5.3.2. The criterion of this test was the stable operation for 8 hours. The stable operation means that no Trip¹ was observed during 3.1kV. If there have been Trip, the test restarted after applying 3.1kV again.

3. 3.3kV Test

After 3.1kV test, the high voltage was applied up to 3.3kV in order to examine the margin of chamber operation. As mention in section 4.3, TGC is designed to operate in Limited Proportional Mode. However, operation with 3.3kV may become Streamer Mode. If the chamber started to discharge continuously, the chamber might be broken off. The chamber with no trip more than 20 minutes was judged as one with sufficient margins. We found no chamber had broken off by transition to Streamer Mode.

	Gas	Voltage	Elapsed Time	criterion
1	CO ₂	2.9kV	6 hours	not exceeded 1 μ A
2	CO ₂	3.0kV	1 hour	not exceeded 1 μ A
3	Mix	2.5kV	8 hours	
4	Mix	2.7kV	1 hours	
5	Mix	2.9kV	1 hours	
6	Mix	3.0kV	4 hours	
7	Mix	3.1kV	8 hours	No Trip for 8 hours
8	Mix	3.2kV	1 hour	
9	Mix	3.3kV	1 hour	No Trip for 20min

Table 5.2: The list of HV Test Procedure.

¹Trip is the function of the HV module. This is the safety system that the HV module cut the HV automatically when the current that the 80% of the limit value is flow for more than 1 second. We can set the limit value from 0.1 μ A to 1mA. In this procedure, we set this value to 10 μ A.

5.3.2 Short-circuit of the anode wire

As mentioned above, the large current such as shown in Fig.5.11 was observed. Even worse, short-circuit by formed electrical paths between anode wire and cathode plane was observed. The resistance between anode and cathode was usually several $G\Omega$ or more. In contrast, the resistance of these paths (R_{short}) was only several $M\Omega$. Fig.5.12 shows the schematic view of this phenomenon. The mechanism is as follows;

1. n-pentane is liquefied locally, especially near the support structure.
2. n-pentane dissolves the carbon on the cathode plane.
3. The carbon forms the electrical path.
4. Discharges play an important role to grow the carbon path.

Consequently, the high voltage could not be applied any longer.

In order to repair this trouble, the liquefying n-pentane should be evaporated and the carbon path should be burnt off. Such n-pentane could be evaporated by circulating dry and pure CO_2 . After evaporating n-pentane, the current was applied to burn off the path using Joule Heat. The anode wire is connected, however, in AC coupling through decoupling capacitor (see Fig.5.13). For this reason, only pulsed current can be applied. By turning on and off the switch of the HV module (set $\sim 2kV$) immediately, the pulsed current was generated.

Two ways of applying pulsed current were developed. One is that the current was applied to the whole wire groups, and another is to the local wire group. The former was effective for the chamber with $R_{short} > 30 M\Omega$, and the latter with $R_{short} < 10 M\Omega$. This is because only a little current could be applied by the HV module. In order to apply the current locally, a shorted wire group should be identified. It was searched for by measuring the capacity between the signal read-out pin and GND. This capacity C_{total} is equaled to the synthetic capacity of C_{HV} and C_{wc} , where C_{HV} is decoupling capacitor (470pF) and C_{wc} is the capacity between anode wire group and cathode plane. Because C_{wc} became lower due to the R_{short} , C_{total} became lower as well.

Out of 542 modules, 103 module experienced this short-circuit or large current one time or more. Most of all could be repair, but three modules could not repaired unfortunately. They were not inspected of the detection efficiency and were not shipped to CERN.

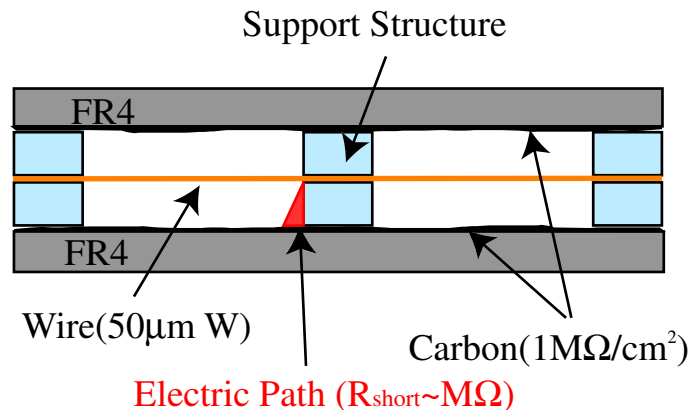


Fig. 5.12: The schematic view of Wire-Short phenomenon during the HV Test.

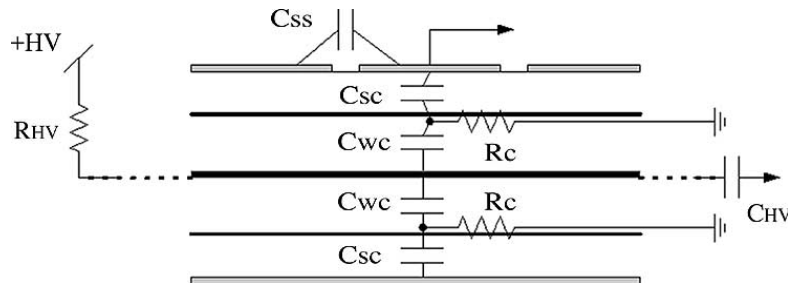


Fig. 5.13: The schematic view of the electrical circuit inside the TGC. R_{HV} is the input resistor, R_C the surface resistivity of the graphite paint, C_{SS} the capacitance of adjoining pickup strips, C_{WS} the capacitance between the anode wire and cathode plane, C_{SC} the capacitance between the cathode plane and the pickup strip and C_{HV} the coupling capacitor for the anode wire readout.

5.3.3 Gas System

The gas system for the HV Test has been developed. The photo of gas system is shown in Fig.5.14 and the gas piping diagram in Fig.5.16. Bubbling Method is adopted to feed CO_2 + n-pentane mixed gas for the HV Test. Vapor pressure of n-pentane is shown in Fig.5.15 as a function of temperature. N-pentane has the partial pressure of 0.45atm in 14°C . Flowing the CO_2 gas into the liquid n-pentane at 14°C , we could obtain the mixing rate of 55 : 45. The flow rate of the mixed gas is, therefore, two times as much as the rate of CO_2 . To control the gas flow, the precise flow controller with needle valve manufactured by KOFLOK Inc. (RK1250) is used. The maximum flow rate of the CO_2 is 100cc/min.

This system consists of the 4 systems for CO_2 and 4 systems for mixed gas. Thus, eight modules in total can be tested at the same time. The material for the gas piping is used PFA (PerFluoroAlkoxy) and SUS (Stainless Steel). These materials have the chemical tolerance against n-pentane (discussed in section 5.5.1). In order to prevent the chamber from overpressure, the pressure was always monitored by the low differential pressure switch (MS65H, manufactured by Yamamoto Electronic Works Co., Ltd.) that operated at 300Pa. When the pressure rose up to 300Pa, the switch turned on the electrical valve (AB42 series, manufactured by CKD corporation) to release the pressure. In addition, the water bubbler that operated at 300Pa is equipped if the electrical device did not work.

5.3.4 Current Monitoring System

The current monitoring system should satisfy the requirement as follows:

- The current of the chamber can always be monitored.
- In order to check the chamber status, the history of the current can be displayed.

To fulfill these demands, the system was developed.

5.3.4.1 Hardware

For the hardware applying high voltage to chambers, the following functions were required:

- The current, high voltage, and Trip status could be obtained.
- The high voltage could be controlled by a PC.

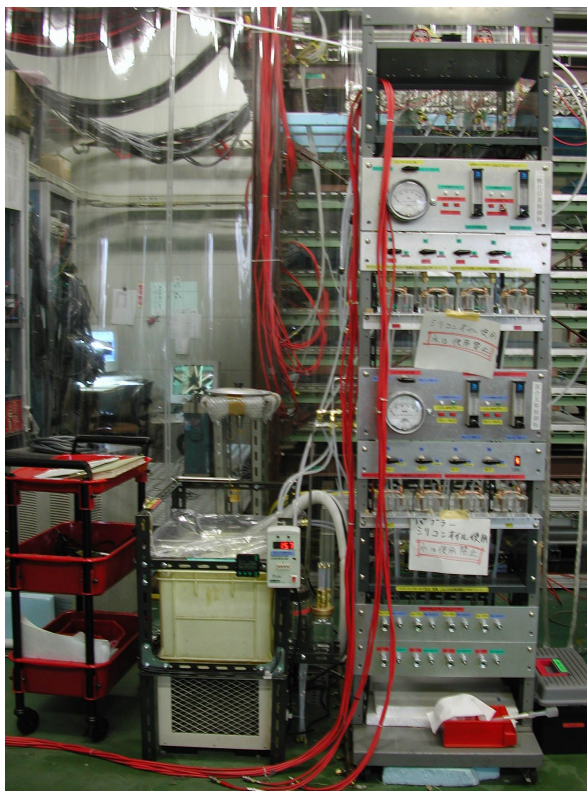


Fig. 5.14: Gas System for HV Test (using Bubbling Method)

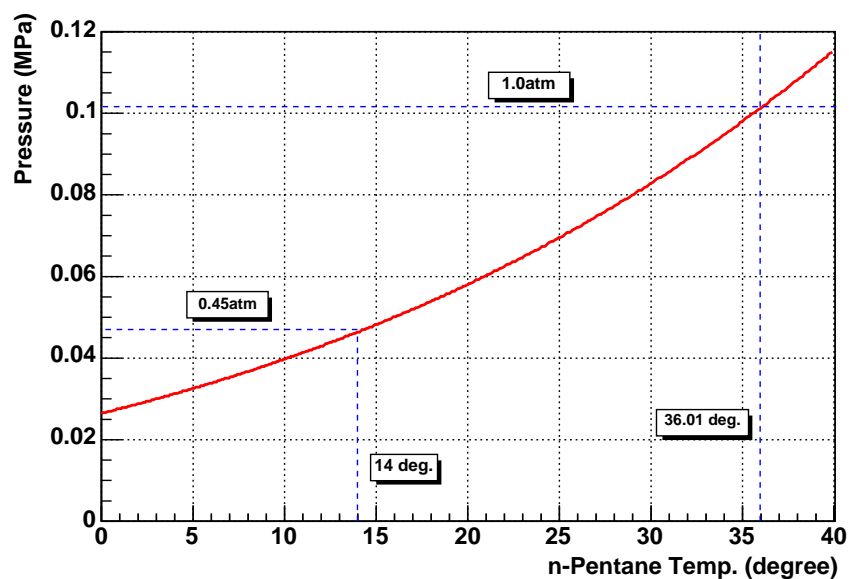


Fig. 5.15: The boiling point curve of n-pentane

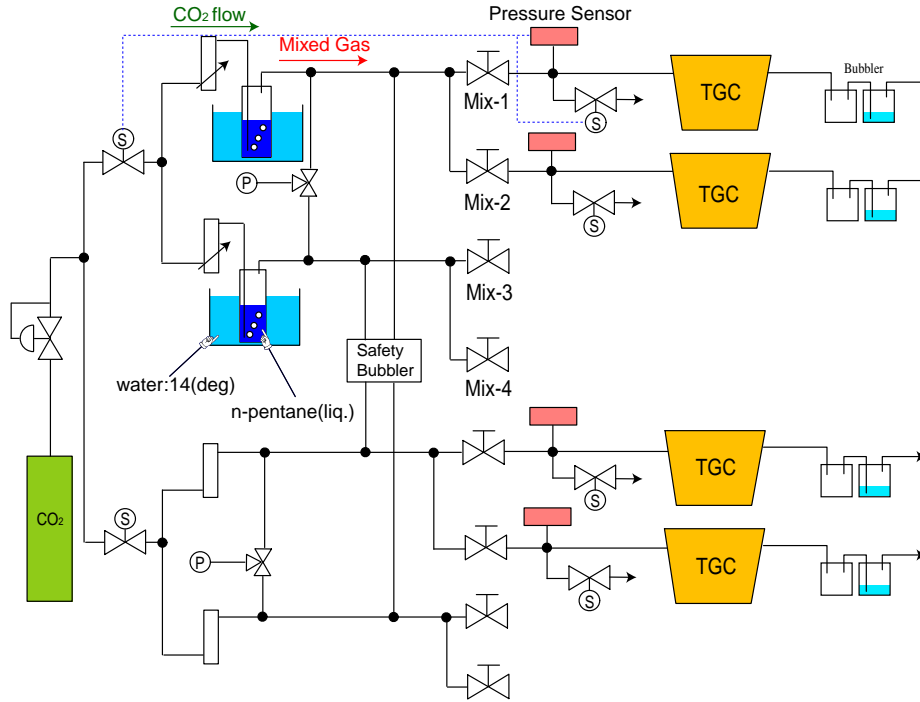


Fig. 5.16: The diagram of HV Test Gas Piping.

Therefore, we adopted the high voltage power supply (HV module) manufactured by SATO Electronics Co. Ltd. (F0922 HV NIM). The features of this module are as follows:

1. The current is shown on an analog meter.
2. The Trip status is on a front LEMO terminal.
3. The output voltage proportional to current is given on a front LEMO terminal.
4. The applied voltage to a chamber can be controlled by supplying the analog voltage to a terminal on the back panel.

The output voltage from each channel is summarized in Table.5.3. Fig.5.17 shows the system diagram. The leak current, HV, and Trip can be monitored using above function. The output voltage of each channel is fed to the AD (Analog to Digital) converter board installed on a PC. This board is AD12-64 PCI manufactured by CONTEC Co. Ltd. [59]. In total, 30 channels corresponding to 10 chambers readouts are used in this system. An amplifier circuit with the gain of 100 was developed (shown in Fig.5.18 (a)) so that the current up to $10\mu A$ can be measured.

The output for the Trip status is based on the open-corrector output of the transistor. Fig.5.18 (b) shows the circuit of the Trip output. The monitoring software detects the Trip state of each channel by monitoring this voltage. That is to say, the output voltage V_{cc} indicated normal state, zero indicates Trip state.

When the Trip is observed, it is necessary to alert to us and recover automatically in order to decrease the loss time. The applied high voltage could be controlled by the analog voltage supplied from the terminal on the back panel (from 0V to 10V). In order to control the high voltage power supply module from software, the DA (Digital to Analog) converter board is used (CONTEC, DA12-16 (PCI)). The resolution of the board is $10 [V]/4096 = 0.0024 [V]$. Thus, the minimum step of the applied high voltage is 2.4V.

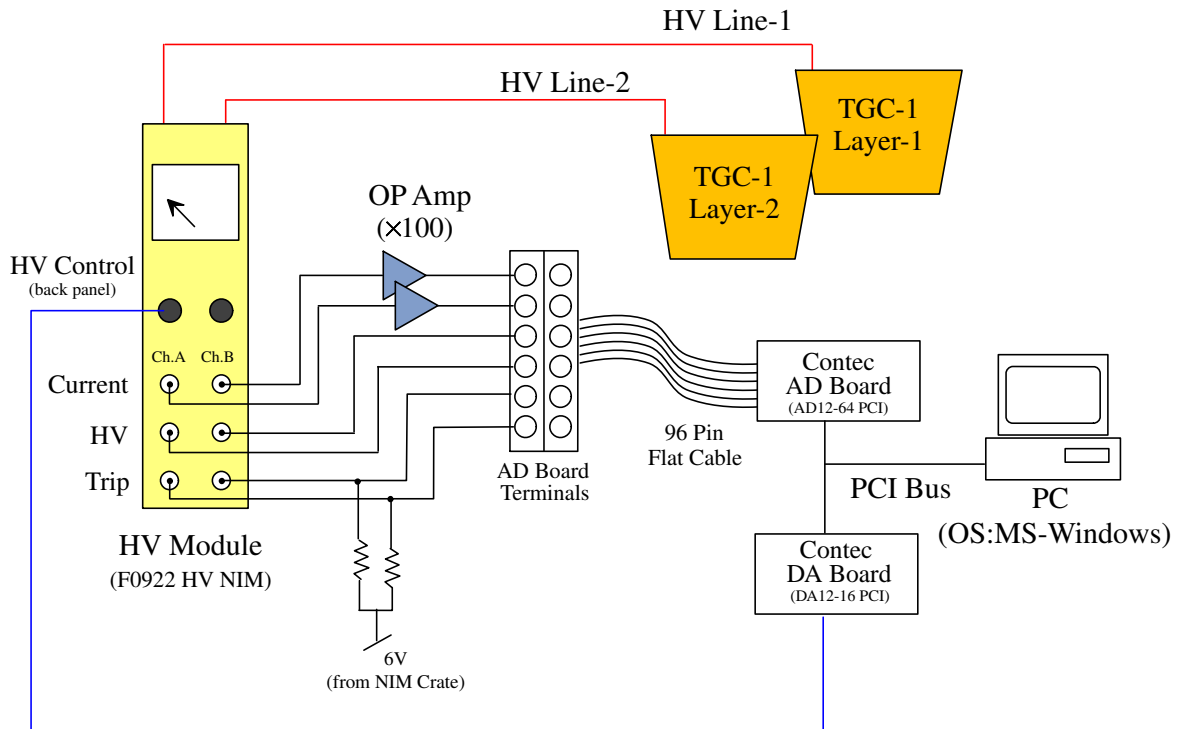


Fig. 5.17: The system diagram of the Current Monitor System

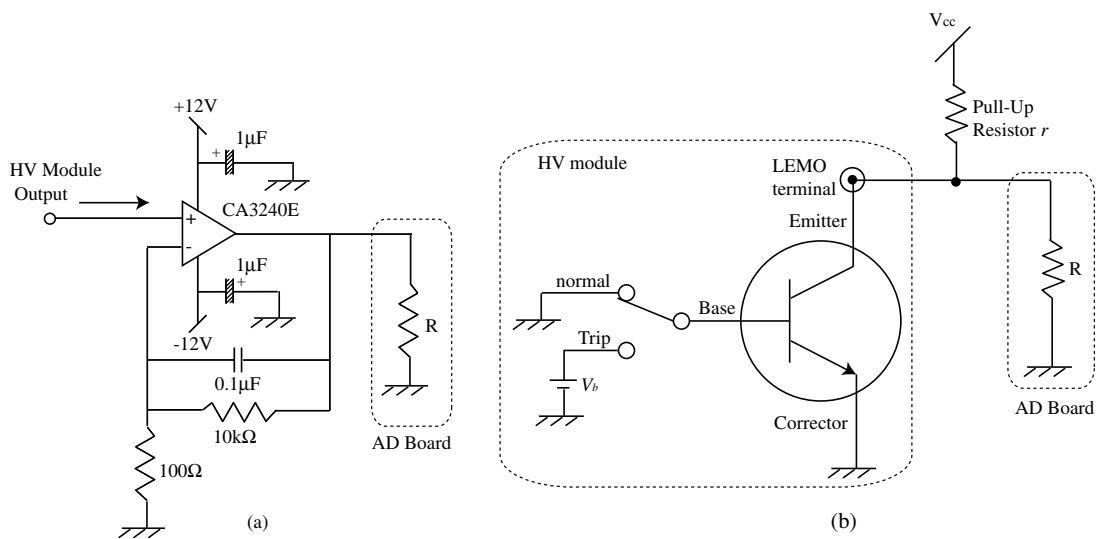


Fig. 5.18: (a) shows the amplifier circuit. (b) shows the schematic diagram of open-corrector output.

	real value	LEMO OutPut
Current	$1\mu A$	$10mV$
HV	1kV	-1V
Trip		open-corrector output

Table 5.3: HV Module OutPut

5.3.4.2 Software

In order to watch and perform the progress of the test process (described in Table 5.2), the monitoring and controlling software was developed. The data of current and high voltage are recorded to check the status. In addition, the applied high voltage is controlled to proceed the test automatically. So this software consists of three parts: monitoring, process management, and control. By utilizing these three system, the procedure of Table 5.2 was built in the program and the test could be proceeded automatically.

Monitoring

The monitoring part was the main part of the software. If an operator clicked the " START " button, the AD board started acquisition of the data of the current and the high voltage, and then the data was stored to the file. If the sampling rate of the data taking was too fast, the size of the data became huge. If it was too slow, however, the instantaneous discharge could not be monitored. Thus, the sampling rate of the data was chosen as 1Hz. Fig. 5.22 shows an example of the data. Red line indicates the current and blue line indicates the high voltage. As this example shows, the discharge can be recorded. In addition, this part managed the data of the monitoring channel, the type of the gas (CO₂ or mixed), the number of TGC ID, the current, the HV, Trip status, and data collection time.

Process Management

As shown in Table 5.2, each process continued for several hours. Therefore, it was important function to manage the progress of the test. A time keeper was equipped for each HV output to know how long it elapsed at the current stage. When the trip was observed, the signal was sent to the control part in order to recover from the Trip state. After the high voltage was recovered, the timer started again.

Control

By using the analog voltage obtained from DA board, the control part ramp up/down applied high voltage to the set value. Output voltage from DA board was determined by watching the monitored HV value. The Trip state could be recovered automatically thanks to this system. Of course, it helped saving labor.

In order to develop the algorithm of the automation, the short-circuit phenomenon described in section 5.3.2 should be taken into account. In order to prevent the chamber from long-term over current, the high voltage was lowered by 100V in the following cases;

1. The current flowed continuously more than $2\mu A$ for 5 seconds.
2. The Trip was observed in 6 times at same voltage.

If the Trip was given rise to in 6 times again after lowering the voltage by 100V, the HV was switched off. After investigating the causes of Trip by the operator, the HV was switched on at lower voltage than that before the Trip was observed.

Microsoft Visual Basic (VB) was adopted as programming language since it has good compatibility with CONTEC AD board. Fig. 5.19 shows the Monitoring Software panels written by VB. Fig. 5.19 shows the monitoring window, Fig. 5.20 shows the progress management window, and Fig. 5.21 shows the control window.

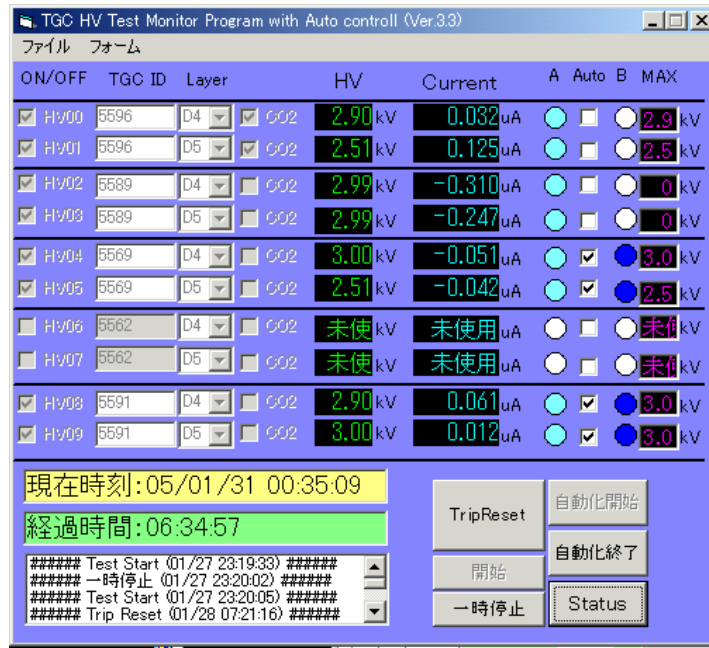


Fig. 5.19: Monitor Programs



Fig. 5.20: Timer Programs

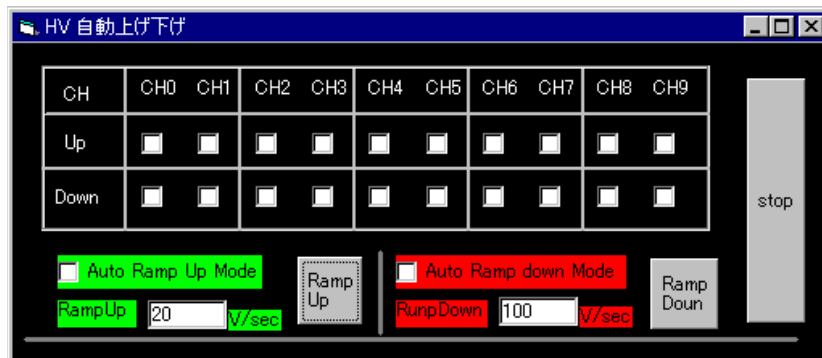


Fig. 5.21: Auto control Programs

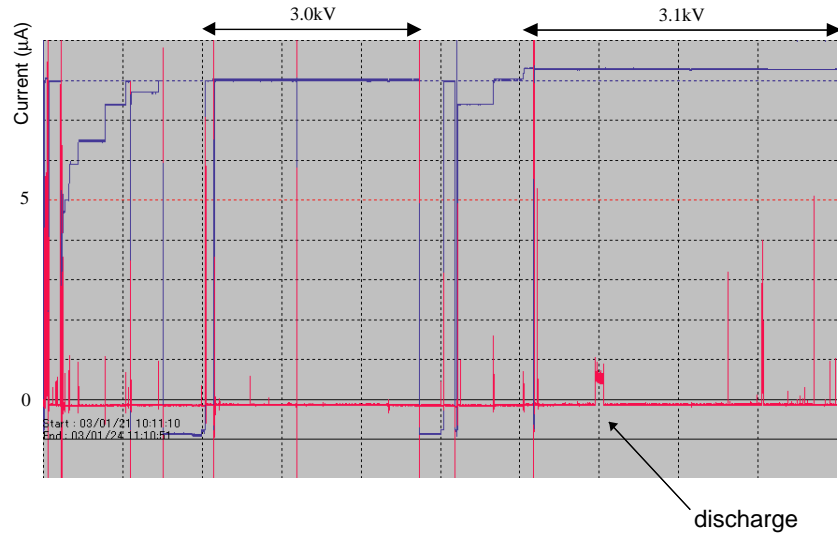


Fig. 5.22: The data sample of HV Test with mixed gas. Red line indicates the current and blue line indicates the high voltage.

5.3.5 Current Stability

In order to check the effect of the long-term high voltage application, the current data before 3.1kV test was compared with the data after 3.3kV test. Fig.5.23 shows the histograms, which were filled with the current data with applied high voltage of 3.0kV. Upper histogram (before) means the 1-hour data before 3.1kV Test. Lower histogram (after) means the 1-hour data after 3.3kV Test. As this histogram shows, high current caused by micro discharge was decreased and the current becomes stable by applying high voltage for this test period. Therefore, it can be concluded that the test procedure for showing in Table.5.2 is appropriate and helps stable operation of chambers.

5.3.6 Results

Fig.5.24 shows the distribution of $(N_{\text{before}} - N_{\text{after}})$, where N_{before} and N_{after} indicate the number of the data exceeding $2\mu\text{A}$ in Fig.5.23. If $(N_{\text{before}} - N_{\text{after}})$ is positive, it indicates the chamber become stable. As the result, most of chambers became stable by applying high voltage.

Table.5.4 shows the summary of the test day of HV test and the number of shorted module. If there were no trip or problems during the test period, it took two days to finish the test. About 70% chambers were passed HV Test within 10 days.

Rank	Test Day	# of module	Short
A	> 10 days	486	90
B	< 10 days	53	25
C	Test failed	3	3
	sum	542	118

Table 5.4: HV Test Summary

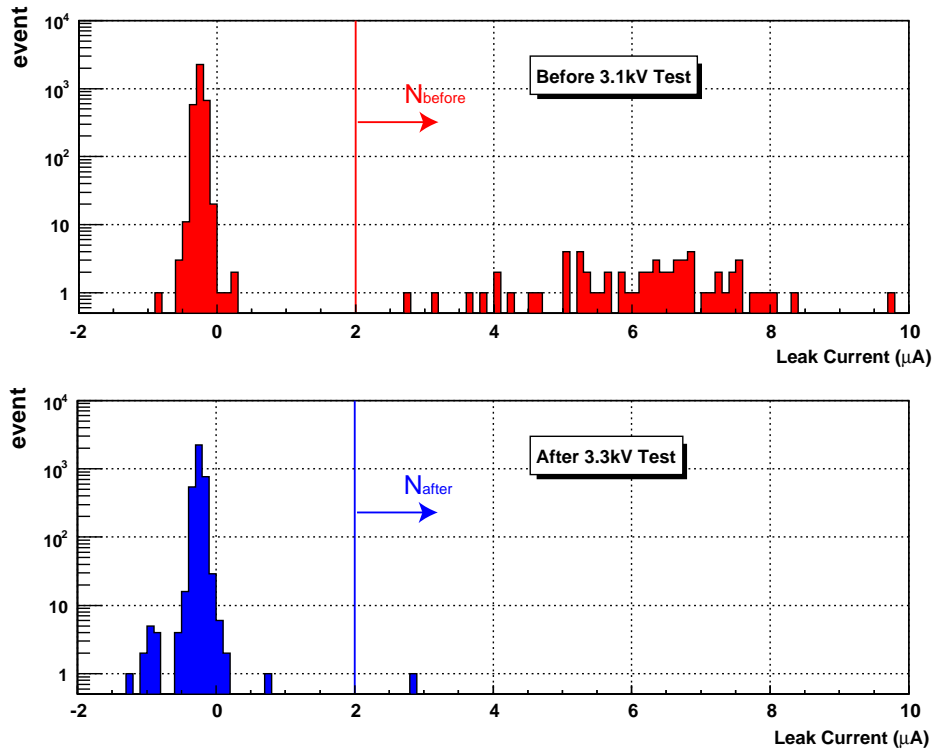


Fig. 5.23: The current distribution before and after HV Test. “ Before ” means the data before passing the 3.1kV Test. “ After ” means the data after passing the 3.3kV Test.

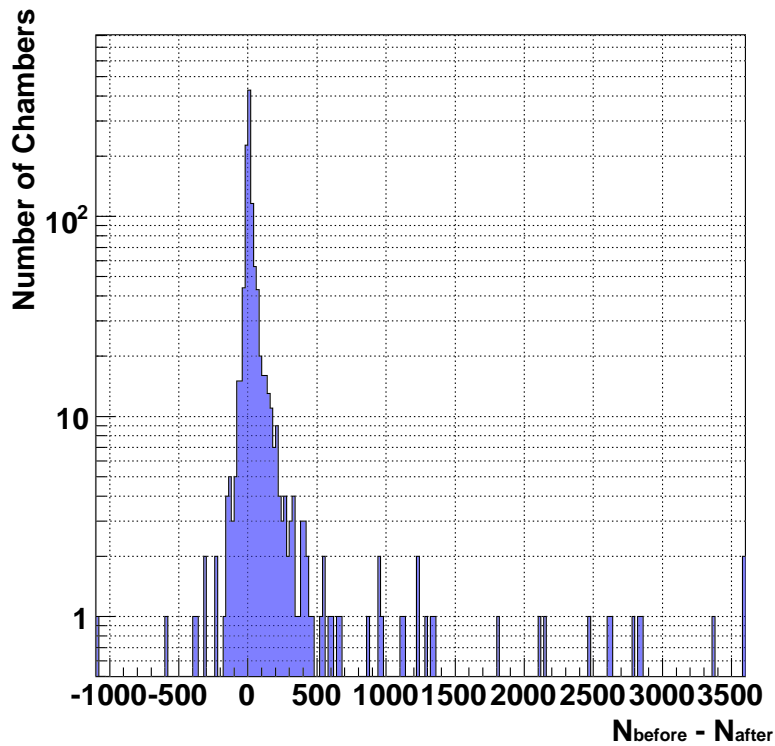


Fig. 5.24: The distribution of $(N_{\text{before}} - N_{\text{after}})$, where N_{before} and N_{after} indicate the number of the data exceeding $2\mu\text{A}$ in Fig.5.23.

5.4 Cosmic Ray Test

To measure the uniformity of the TGC efficiency and timing response, cosmic ray muons were used as the source for measurements over the whole detection area of TGC (around $2m^2$). To fulfill the requirements mentioned in the beginning of this chapter, a dedicated test station was developed at Kobe University. In this section, the system for T7 Triplet type was described, and system upgrade for other type was described in section 5.8.

Fig.5.25 (a) shows the schematic view of the test station, and (b) shows its picture. The mechanical structure of the test station consists of 1.5 m length, 2.5 m wide and 2.6 m height iron-made support frame. We define a left-handed coordinate system; Z coordinate is defined along vertical.

This station was equipped with two layers of scintillation counter hodoscopes for triggering cosmic-ray muon and 4 arrays of drift tubes for reconstructing the muon track. Plastic scintillation counters were arranged in two layers; on the top and on the bottom of the station. 12 layers of drift tubes in total were used for track reconstruction. The TGCs were inserted between the upper drift tube layers and the lower layers and these wires were parallel to the x coordinate. 8 TGC modules were operated simultaneously in the facility.

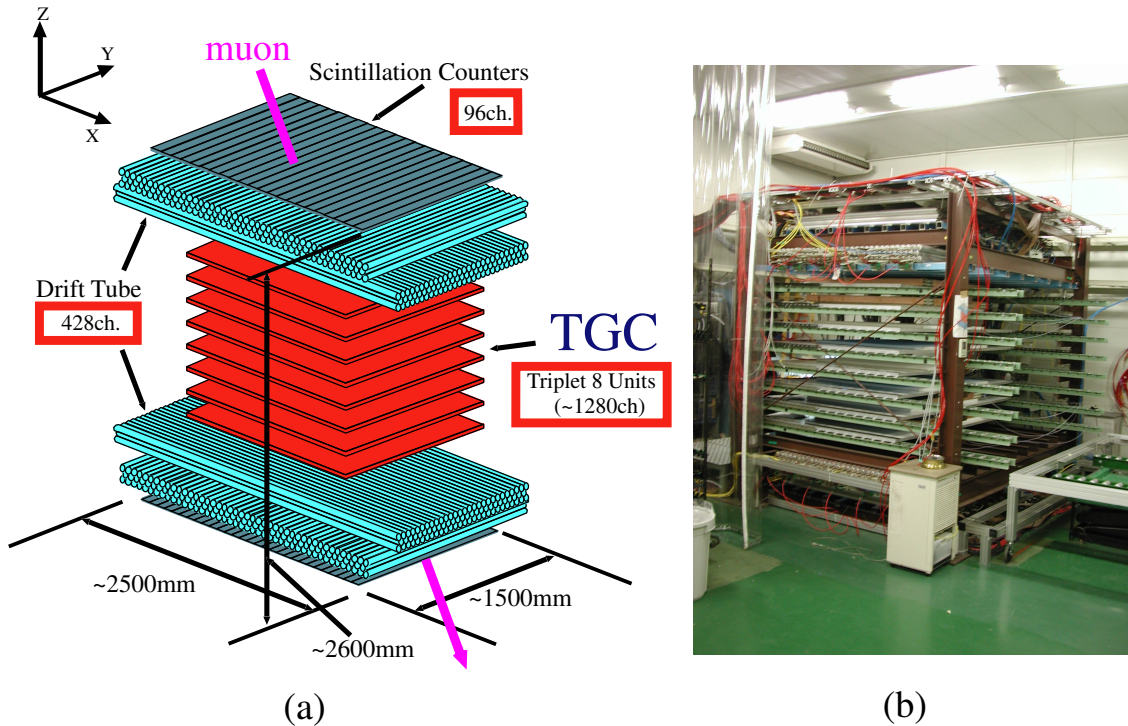


Fig. 5.25: (a) is the schematic view of the Cosmic Ray Test Stand and (b) is its picture.

In order to insert a chamber into the test station, it was laid at horizontal position. Since TGC module was heavy, about 80kg per module, the chamber may be distorted by its weight at horizontal position. In order to kept flatness to avoid deformation, the chamber was put on a flat pallet with high rigidity (shown in Fig.5.26 (a)). In addition, total amount of materials between the top and the bottom drift tube layer should be as low as possible to avoid multiple coulomb scattering. Aluminum-honeycomb panels were adopted to support TGC modules because of its lightweight, high rigidity, and high radiation length.

The test station is located in an air-conditioned area. In that area, special care is taken to hold temperature around 20°C to prevent the n-Pentane in the mixed gas from liquefying. In addition, humidity was kept below 50%, because high humidity causes discharge on the part of the HV connector of TGC and/or drift tube.

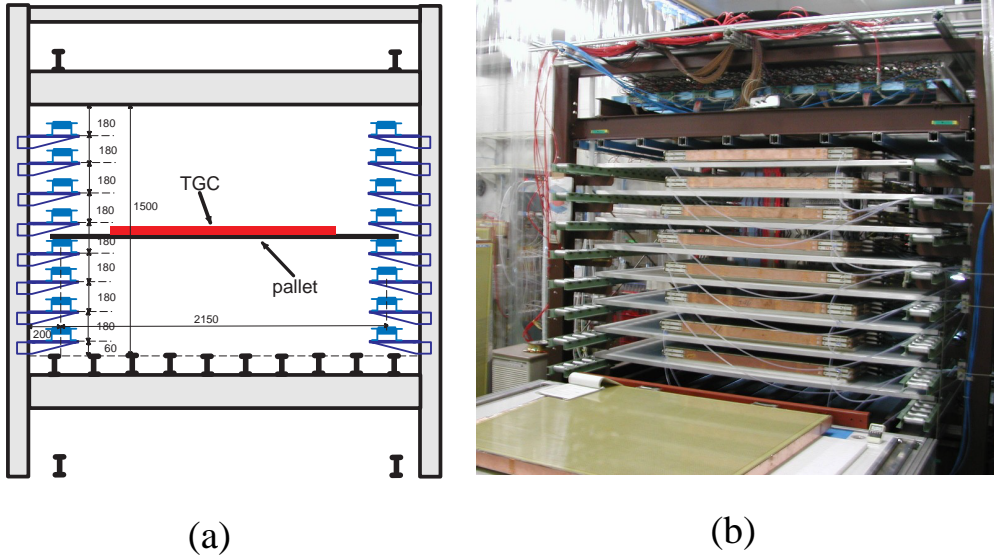


Fig. 5.26: (a) the side view of the Test Station. (b) picture of the station.

5.4.1 Scintillation counter

The trigger scintillation hodoscope set on both the top and the bottom of the test station. The size of 22 plastic scintillators on top are $70\text{mm} \times 1300\text{mm} \times 10\text{mm}$, and 22 are $90\text{mm} \times 1300\text{mm} \times 2.6\text{mm}$ on bottom. This scintillator system could cover the area of all type of the chamber produced in Japan. Each scintillator has photo multiplier tubes (PMT, R329-02 manufactured by HAMAMATSU) on both ends.

5.4.1.1 Trigger Scheme

Fig.5.28 shows the trigger scheme. The analog signals of PMT were digitized in NIM-Discriminator modules (RPN-110, manufactured by REPIC corporation). This digitized signal was processed in a dedicated module, called " trigger module ". At first, this module determined a valid scintillator hit by requiring signals from both ends of PMT. Then, ORed signal of 22 scintillator hits is defined as the hit of each layer. At last, the coincidence of the top and the bottom layer provided the trigger signal. Trigger rate was about 30Hz.

5.4.1.2 Efficiency of Scintillation counter

To measure the efficiency of each scintillation counter, cosmic rays were used. Trigger signal was created by two small plastic scintillation counters ($20\text{cm} \times 20\text{cm}$). The efficiency was studied using the number of the coincidence between the trigger and the test scintillation counter (coincidence from both ends were required). Fig.5.29 shows the number of coincidence as a function of the applied high voltage. The applied HV of each PMT were decided by investigating the plateau region, 1750V for this PMT.

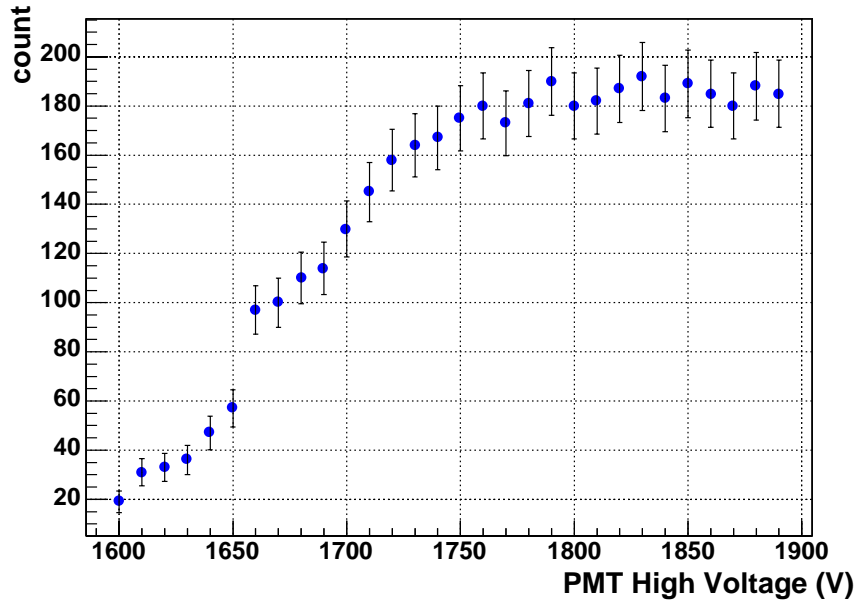


Fig. 5.29: The number of coincidence for a scintillation counter as a function of applied HV.

5.4.1.3 Timing Fluctuation

The timing of the scintillator was measured by Time-to-Digital Converter (TDC) modules². Fig.5.30 shows a distribution of timing difference between top and bottom scintillation counter. The peak value means the average time of flight (TOF) between top and bottom counter. The peak value agrees well with the distance between top and bottom of 2.6m. This distribution agrees well with this calculation.

As this graph shows, we found the fluctuation of TOF is $\sigma \sim 2.8\text{nsec}$. This is enough to measure the signal response of TGC with 25nsec or less. The width of the distribution corresponds to the timing fluctuation, which was derived mainly from the fluctuation of light propagation time in the scintillator and the jitter depending on the pulse height of the PMT.

²This detail will be described in section 5.4.3.3.

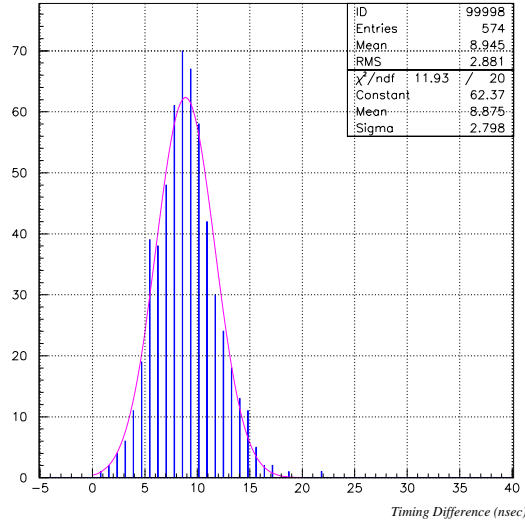


Fig. 5.30: Timing difference between top and bottom scintillation counters.

5.4.2 Drift Tube

Since it is necessary to identify the support structure of TGC in measuring the efficiency, the position resolution of the reconstructed track was required several mm. In addition, high track reconstruction efficiency without fake track was demanded as well in order to shorten the period of the inspection. The drift tube was chosen as tracking device because it was not so expensive and could be obtained sufficient position resolution for our purpose.

5.4.3 Operation Principle

A drift tube is a cylindrical proportional counter and a particle tracking detector that measure the drift time of ionization electrons in a gas to calculate the spatial position of ionizing particle.

$$E(r) = \frac{CV_0}{2\pi\epsilon_0} \frac{1}{r} \quad (5.1)$$

$$C = \frac{2\pi\epsilon_0}{\ln(b/a)}, \quad (5.2)$$

where V_0 is the voltage of anode wire, a is the diameter of anode wire, b is the distance between wire and tube, C is the capacity between the wire and tube. Electron cloud of primary electrons drifts with constant velocity, v , to the anode. Near thin anode wire, we get gas multiplication and register the signal. If the threshold of the boundary between the drift region and the avalanche region is assumed to $E(r) \sim 10$ [kV/cm], the corresponding radius is calculated as $r \sim 500$ [μm]. Thus, the avalanche is generated at the neighborhood of the anode wire. To determine the moment at which charge particle passes through, some other fast detectors, like scintillating counters are used.

The measured time is converted to the drift length using a conversion relation, called x-t relation. The track can be reconstructed using drift length information.

5.4.3.1 Structure of drift tube

The tubes are grouped into 4 super-layers; each consists of 3 staggered layers. Two super-layers, which were aligned orthogonal (x and y direction) for two-dimensional tracking, were located above the fiducial volume (up side drift tubes) and the other two super-layers were below the volume (down side drift tubes). Each super-layer was named as UpX, UpY, DownX, and DownY, respectively. The track in yz plane (xz plane) was reconstructed using UpX and DownX (UpY and DownY).

The cross-section of the tube is shown in Fig.5.31. The tube was made of aluminum with 2mm thickness. The diameter of each tube was 5 cm and the length was 250 cm for UpX and DownX, and 150 cm for UpY and DownY.

The gold-plated tungsten wire with $50\mu\text{m}$ diameter was used as an anode. In order to prevent the anode wire from sagging, the wire was strung with the tension of 280gw.

In order to obtain the constant drift velocity, we adopted the pre-mixed gas of Ar (50%) and ethane (50%). Fig.5.32 shows the drift velocity of various fraction of the argon and the ethane as a function of the electric field at two different pressure. In the drift region, the electric field was varied $0.22 < E(r) < 10\text{kV/cm}$ at the nominal operation voltage of 3.5kV. As shown Fig.5.32, the drift velocity was almost constant in this range with 50 : 50 mixture.

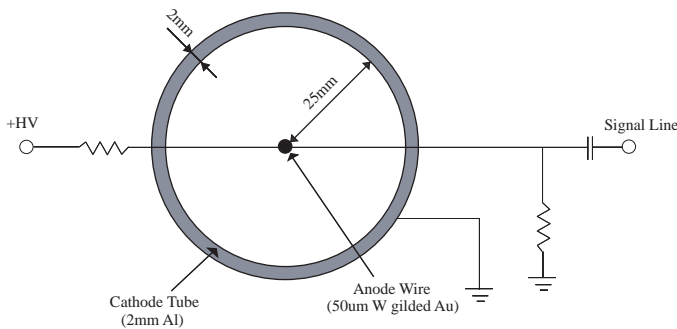


Fig. 5.31: Cross section of the Drift Tube

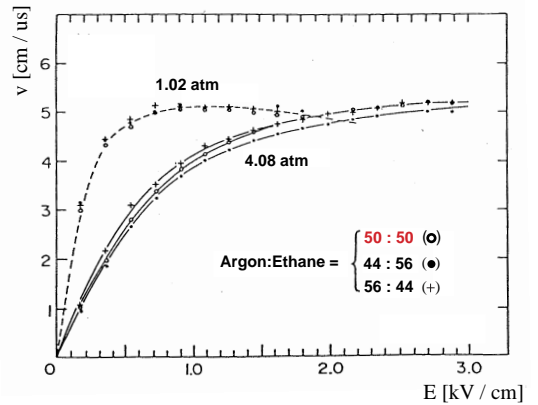


Fig. 5.32: The relation between the electric field strength E and the drift velocity v with several gas mixture ratio and pressure[35].

Because the gain of amplifier card was so low and the high gas gain was required, the drift tube was operated in limited streamer mode. In limited streamer mode, the output pulse height (i.e. the number of the collected electron) hardly depended on the number of primary cluster, so the position dependency of the incident muon was negligible. Fig.5.33 shows the samples of output pulse shape with two different HV. Fig.5.33 (a) shows HV = 3.2kV (limited proportional region) and (b) shows HV = 3.65kV (limited streamer region). The applied high voltage was finally decided as 3.5kV from the plateau of the HV vs efficiency curve.

5.4.3.2 Gas System

In this section, the gas system for drift tube was described. Fig.5.34 shows the gas piping diagram for drift tube. As mentioned previous section, the premixed gas of Ar + Ethane (C_2H_6) = 50 : 50 was flowed. It was stuffed in a gas tank of 47l with 3.9Mpa. For long-term operation, we have developed “ no dead time ” gas supply system by using two tanks. The pressure of main tank was monitored

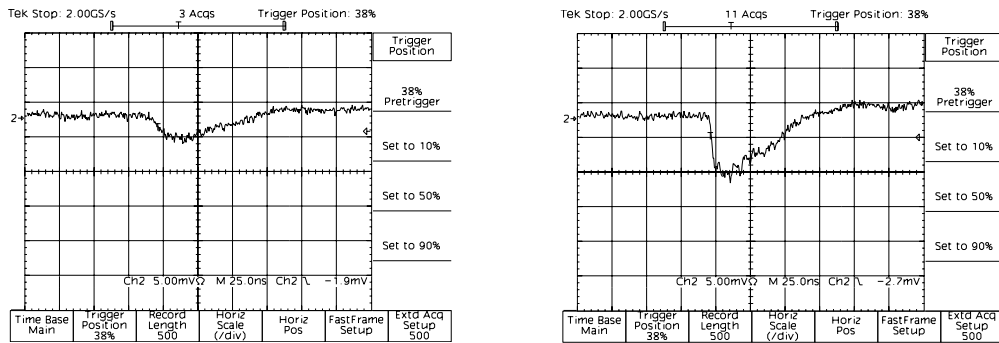


Fig. 5.33: The output pulse with two different HV. (a) $V=3.2\text{kV}$, (b) $V=3.65\text{kV}$.

by the pressure sensor (PE22-Z, manufactured by SUNX Co. Ltd). If the main tank was empty, the electric valve was switched to the reserve tank.

In order to avoid the gain drop of the tubes due to the contamination of oxygen, the gas was supplied with slightly high pressure. The pressure of the tubes was approximately 0.0118MPa after distributing the gas from the tank with 0.22MPa secondary pressure. There were 24 lines to supply gas to drift tube and the flow rate was 2cc/min for each line.

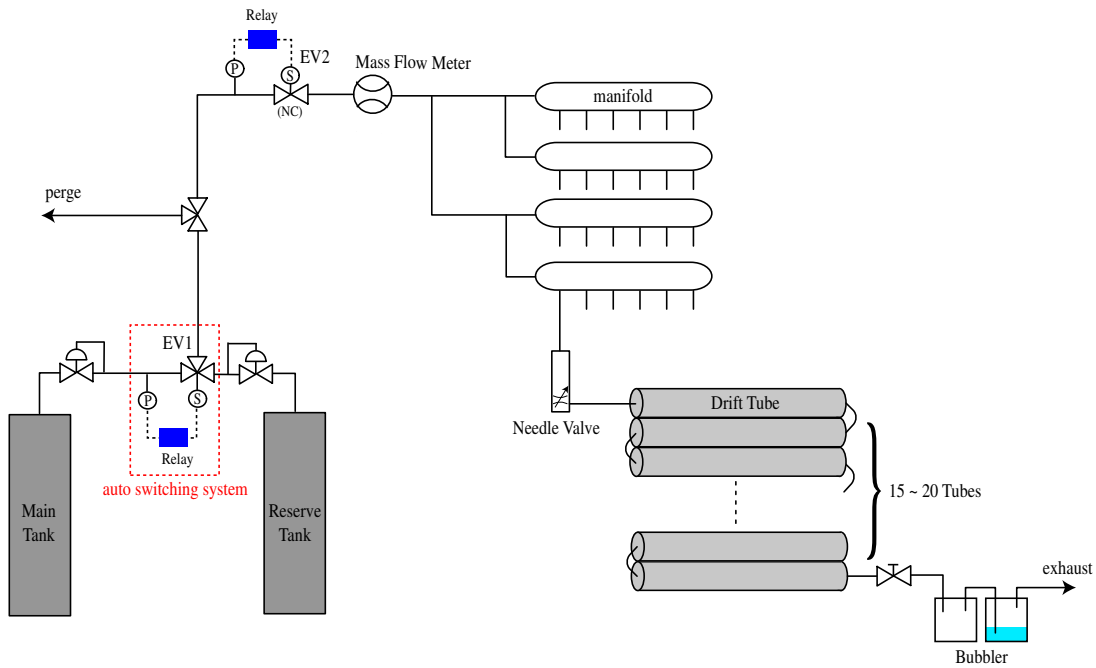


Fig. 5.34: The gas system for the Drift Tube. A three-ports electric valve (EV1) controlled to two tanks, main and reserve, was switched automatically by monitoring the remained pressure.

5.4.3.3 Readout

The analog signal of the drift tube was amplified, shaped and discriminated by the ASD described in section 4.5. To evaluate noise and/or cross-talk contamination, “multiplicity” of drift tube was used. Multiplicity was defined as number of hits in each super-layer within 1 event. Fig. 5.35 shows

the number of events of various multiplicity as a function of V_{th} . For lower V_{th} increase of multiplicity was obviously shown because of noise and/or cross-talk signals were counted. There was a plateau $V_{th} > 150\text{mV}$. Thus, we adopt $V_{th} = 190\text{mV}$.

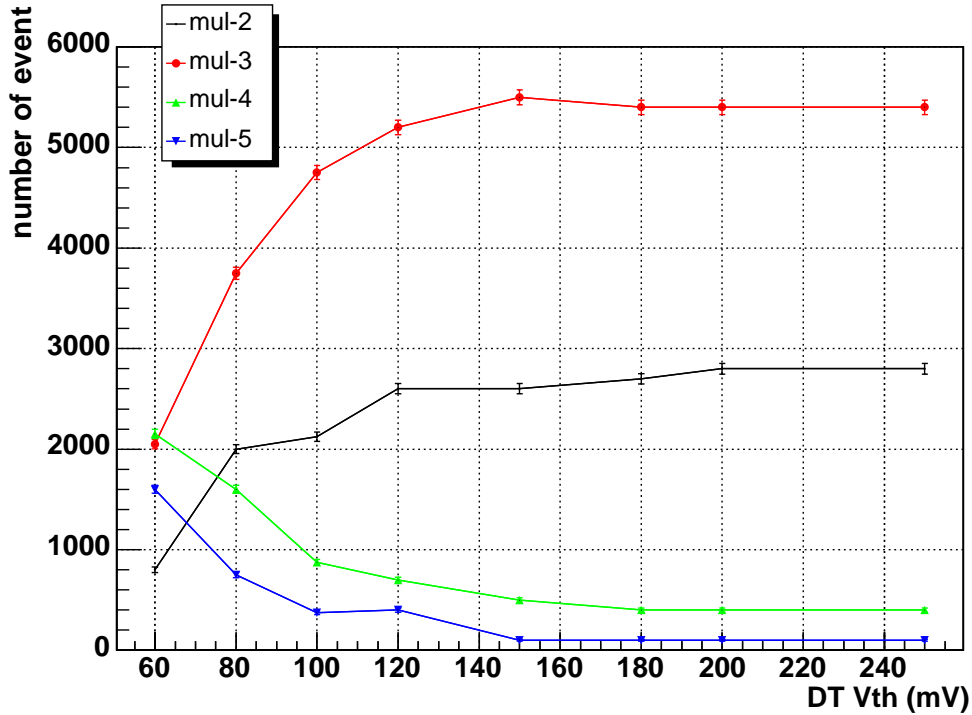


Fig. 5.35: Multiplicity distribution for various threshold voltages.

5.4.3.4 x-t relation

In order to convert the drift time to the drift length, the following quadratic function was assumed as “ x-t relation ”:

$$X(t) = P_2(T_0 - T)^2 + P_1(T_0 - T), \quad (5.3)$$

where P_1 and P_2 was the coefficient, T_0 is the origin of the time.

Fig. 5.38 shows the timing distribution of a drift tube (using DownY). Since the hit data was fed by common stop mode, larger number of abscissa indicates the faster time. Therefore, T_0 , the time of Drift Length = 0 (corresponding to the red arrow on the Fig. 5.38), was determined as 1070nsec from the fastest time of the timing distribution.

In order to decide P_1 and P_2 , the fitting of data was iterated. First, events with such hit pattern as shown red circle in Fig5.36 were selected. Drift time t_{layer} were obtained, where layer is numbered 0, 1, and 2. The drift length (x_0, x_2) were computed from drift time (t_0, t_2) by an assumption of P_1 and P_2 value. Two circles (C_0 and C_2) with the diameter of (x_0, x_2) were drawn, and were calculated a common tangent line (L). Then the distance d between the line and the center of the tube in layer1 was computed. Therefore, a scatter plot between d and t_1 could be obtained as Fig.5.39. The plot were divided into constant time bin width and searched the highest density point. Finally, the new relation between d and t_1 was obtained by fitting these points. Using new relation, the same procedure was iterated, and the value of P_1 and P_2 were converged. Since the drift velocity was

approximately $5\text{cm}/\mu\text{sec}$ in this condition, we set the initial value as $P_1 = 5.0 \times 10^{-3} \text{ cm/nsec}$ and $P_2 = 0 \text{ cm}/(\text{nsec})^2$. After iteration, we obtained

$$P_1 = 0.556 \times 10^{-2} \text{ cm/nsec}, \quad P_2 = -0.311 \times 10^{-5} \text{ cm/nsec}^2. \quad (5.4)$$

Fig.5.37 shows the variation of the parameters during the fitting and we found these were converged.

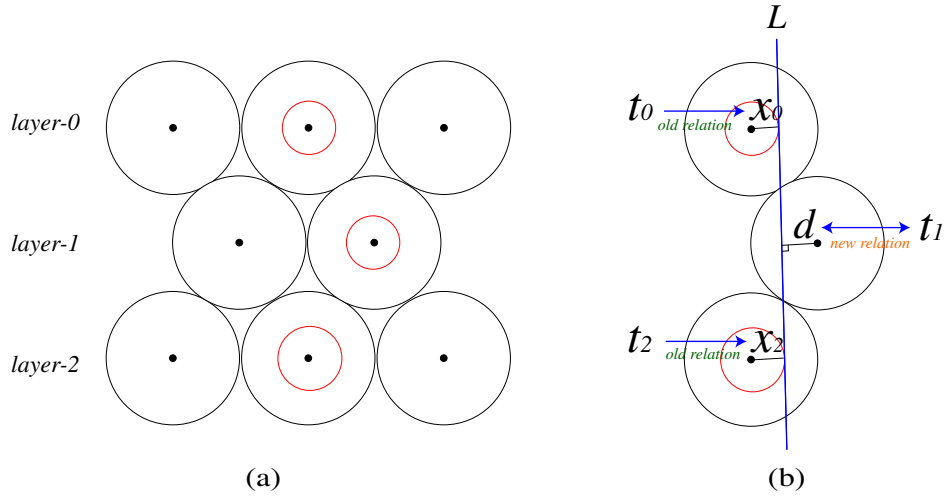


Fig. 5.36: (a) Ideal Hit Pattern. (b) Schematic View of the Iteration.

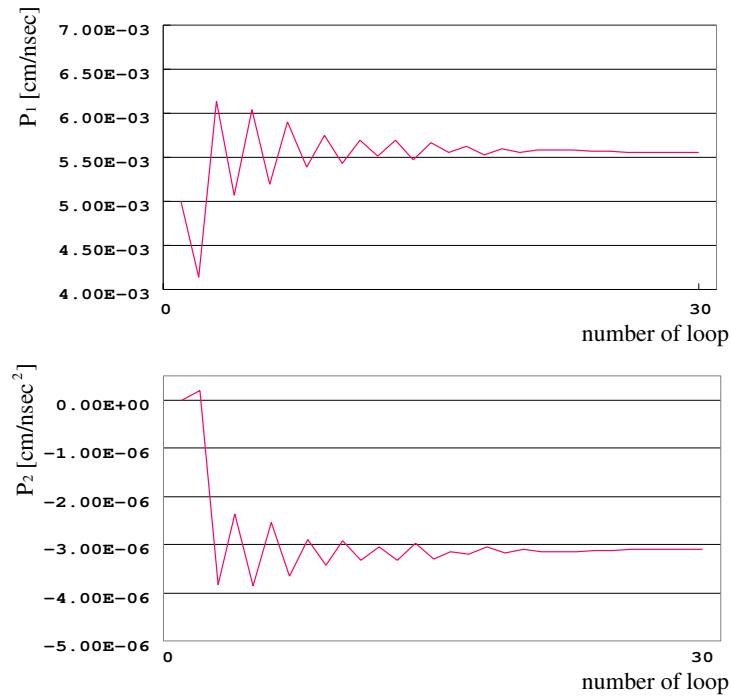


Fig. 5.37: Parameter Iteration.

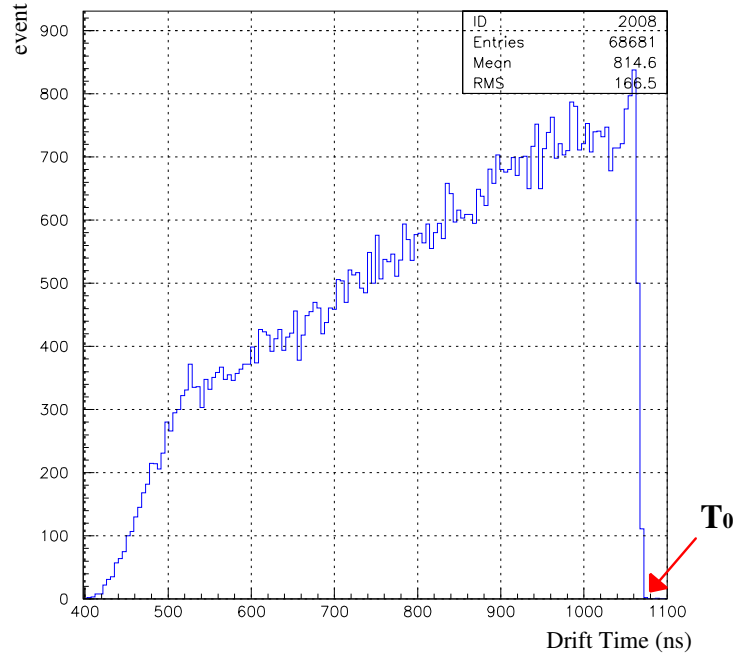


Fig. 5.38: Timing distribution of one drift tube. Since this graph was obtained using “ common stop mode ”, large time value is corresponding to the earlier signal. The red arrow indicates the origin of the drift time, T_0 . In this case, $T_0 = 1070[nsec]$.

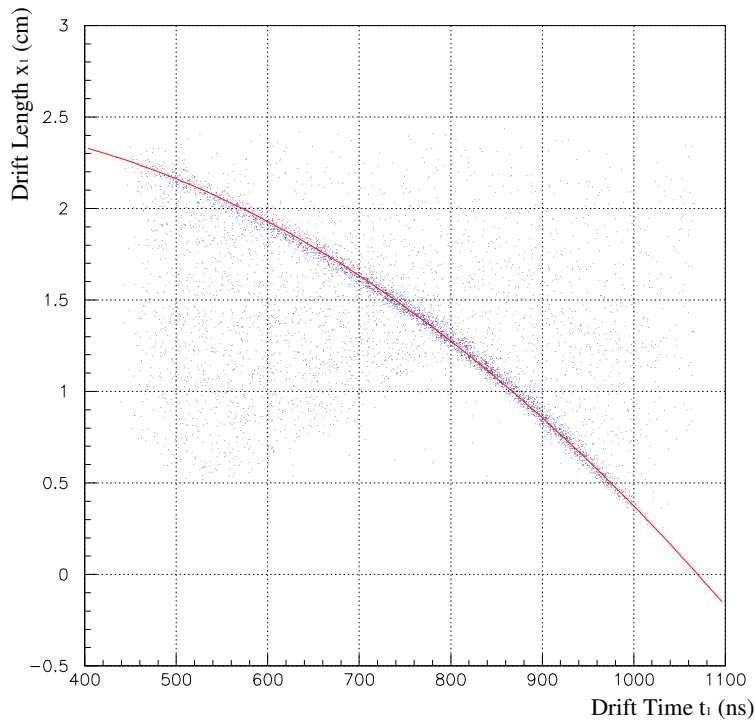


Fig. 5.39: The scatter plot between d and t_1 after converging the parameter P_1 and P_2 . Red line indicate the fit by Eq.(5.4) with $P_1 = 0.556 \times 10^{-2}[cm/ns]$, $P_2 = -0.311 \times 10^{-5}[cm/ns^2]$.

5.4.3.5 Spatial Resolution

In order to evaluate the validity of the parameter P_1 and P_2 , the spatial resolution of one tube was examined. If these parameters were correct, the residual $R = d - x_1$ was to have been distributed around zero. Fig.5.41 (a) shows the scatter plot between x_1 and R . This graph shows R is distributed around zero in whole drift region. Thus, we found P_1 and P_2 were correct.

Fig.5.41 (b) shows the projection of (a) to R-axis. The sigma of this distribution is $\sigma \sim 355\mu\text{m}$. This sigma contained the error of three tubes. In order to estimate the single tube resolution, the approximation was carried out as follows. Since the incident angle of the cosmic ray was around 10 degree for events selected, R could be approximated as follow (see also Fig.5.40):

$$R = 2.5 - \left(\frac{x_0 + x_2}{2} + x_1\right). \quad (5.5)$$

If the error of each tube was assumed to be equal, σ , the error of R (σ_R) was estimated by the propagation of error:

$$\sigma_R^2 = \left(\frac{\partial R}{\partial x_0}\right)^2 \sigma^2 + \left(\frac{\partial R}{\partial x_2}\right)^2 \sigma^2 + \left(\frac{\partial R}{\partial x_1}\right)^2 \sigma^2 \quad (5.6)$$

$$= \left(\frac{1}{2}\right)^2 \sigma^2 + \left(\frac{1}{2}\right)^2 \sigma^2 + \sigma^2 \quad (5.7)$$

$$= \frac{3}{2} \sigma^2. \quad (5.8)$$

Therefore, we found the single tube resolution was

$$\sigma = \sqrt{\frac{2}{3}} \sigma_R \sim 290 [\mu\text{m}/\text{tube}]. \quad (5.9)$$

5.4.4 DAQ System

In this section, data acquisition system (DAQ system) is described. In order to analyze the data of each detector, the signal of them should be recorded in computers. Since their signals were analog, we should digitize them to handle in computers.

DAQ system consists of three parts: front-end electronics, read-out electronics, and computers. The procedures of the DAQ system could be summarized as follow:

1. Front-end electronics digitized the analog signal of each detector.
2. The digitized data was fed to readout electronics.
3. Computers collected these data from readout electronics.
4. The data was recorded and analyzed in the computer.

Fig.5.42 shows the schematic diagram of the detectors and their readout electronics. As described section5.4.1, the signals of scintillation counter were digitized in the NIM-Discriminator modules. Trigger signal was generated in the trigger module and distributed to the readout electronics for drift tube and TGC. In order to eliminate other trigger signals during the data conversion, Interrupt & I/O resistor module (RPV-130, manufactured by REPIC corporation) was used for generating VETO signals. The signals of drift tube were digitized in the ASD and fed to TMC (Time Memory Cell) module to measure the drift time. There were 14 modules mounted for readout of 428 drift tubes. The signals of TGC were digitized in the ASD and fed to SWINE (Super-Wire Net Encoder) module[63].

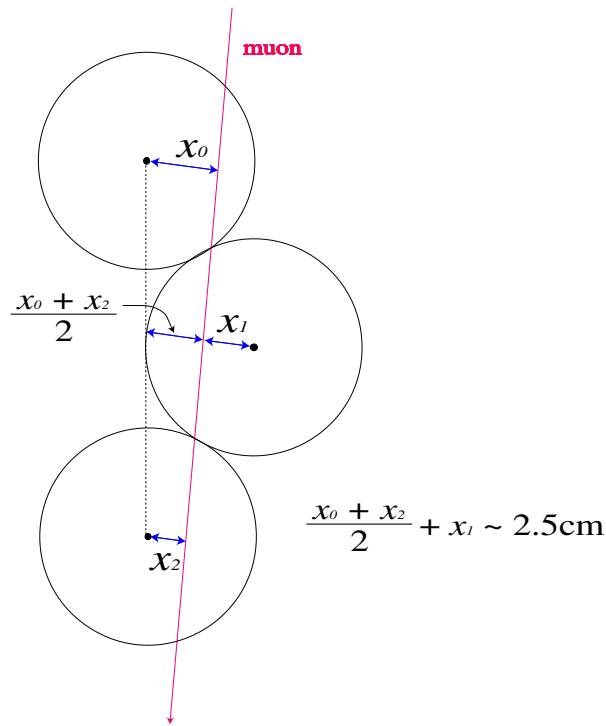


Fig. 5.40: Schematic view of the estimation of the drift tube resolution.

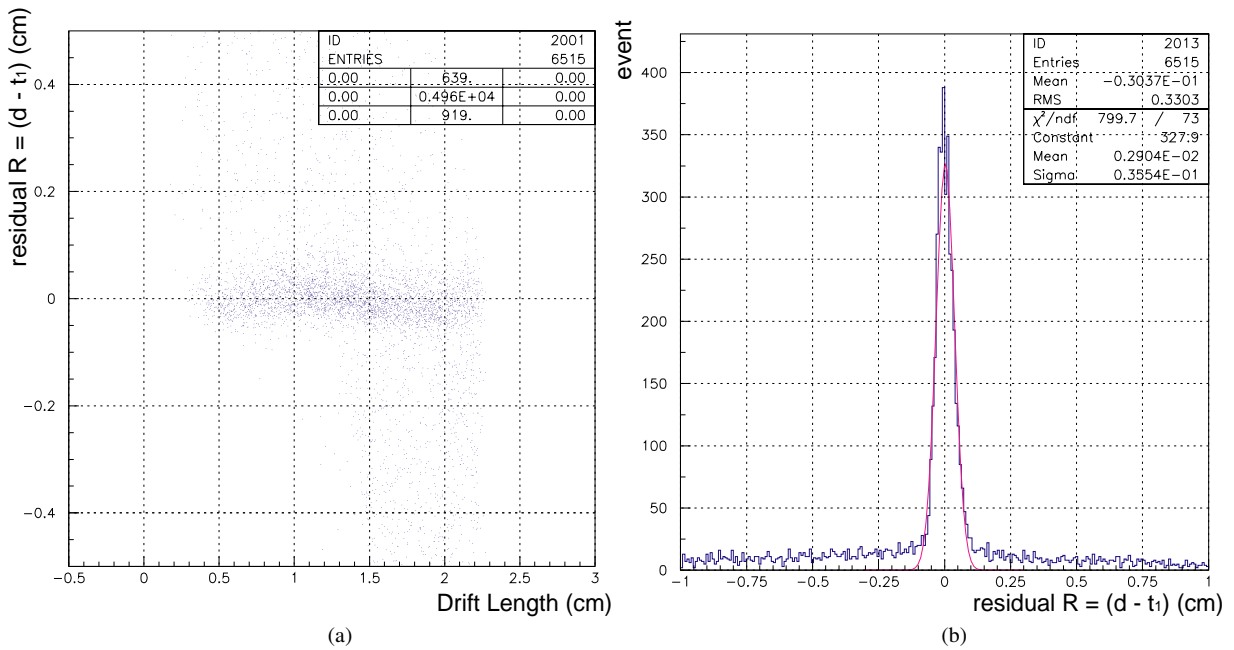


Fig. 5.41: (a) shows the scatter plot between x_1 and R . (b) is the projection of (a). We found the spatial resolution of is $\sigma \sim 355 [\mu\text{m}/\text{super-layer}]$.

SWINE was the module developed in KEK to latch the MWPC hit signal within gate timing. In addition, 16ch ORed signal of each ASD card from SWINE is fed to TMC modules to analyze the TGC timing. There are 10 ASDs on T7 Triplet (6 for wire and 4 for strip), so 20 HOG modules are required for 8 modules of T7 Triplet (12 for wire and 8 for strip). Three TMC modules are required for 8 modules of T7 Triplet.

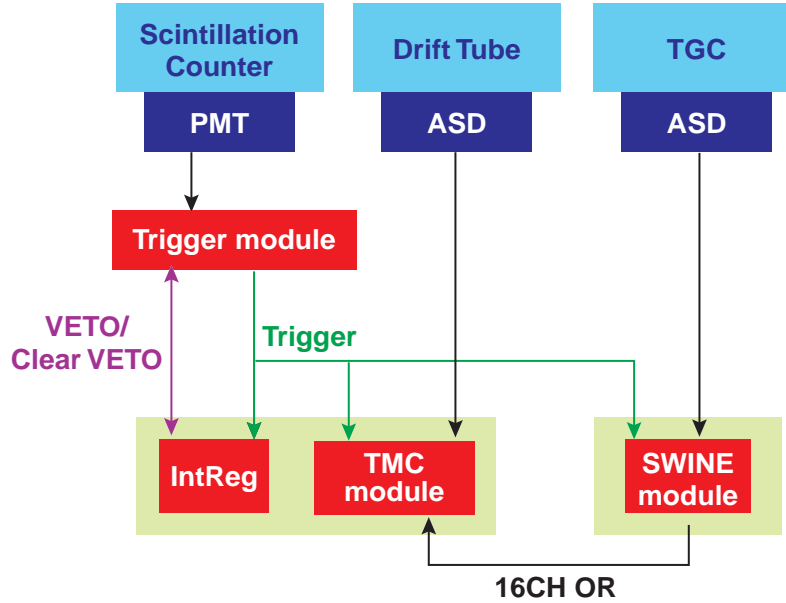


Fig. 5.42: Composition of the detector and readout electronics.

5.4.4.1 TMC (Time Memory Cell)

TMC[62] developed in KEK is a kind of the high accuracy time-to-digital converter (TDC) device. We used a general purpose TMC module (contains 8 TMC-TEG3 chips) with 32ch readout implemented in a 6U VME card.

Fig.5.43 shows the block diagram of the TMC chip. Each TMC chip contains 4 channels of circuit. An asymmetric ring oscillator is controlled with a phase locked loop (PLL). The oscillator generates 32 precise timing signals, each of which is delayed by 1/32 of the clock cycle. The frequency of the PLL is 40MHz. TMC has a least count of $25ns/32 = 0.78ns/bit$. Both the rising- and falling-edge times are encoded and stored in 128-word dual-port memories (DPM). The chip can store $2.56\mu s$ to $12.8\mu s$ data depend on the system clock frequency ($3.2\mu s$ at 40MHz). Although the TMC records all of the timing information, a second edge which appeared within the same cycle will be neglected at the encoding stage.

The module has an 8-bit parallel host port in the VME space. Input signals are received by fast comparators (MAX901) which receive ECL or small differential signals ($> \Delta 100mV$) in a common voltage range of $\pm 3V$.

This module has two data acquisition modes, called “ common start mode ” and “ common stop mode ” respectively. We selected the “ common stop mode ”. Fig.5.44 shows the signal timing chart of the TMC using common stop mode. The stop signal indicates the trigger signal from trigger module. The all signal within the time range was fed to TMC. This time range was set to $1.25\mu sec$. ($25[nsec/row] \times 50[row] = 1.25[\mu sec]$)

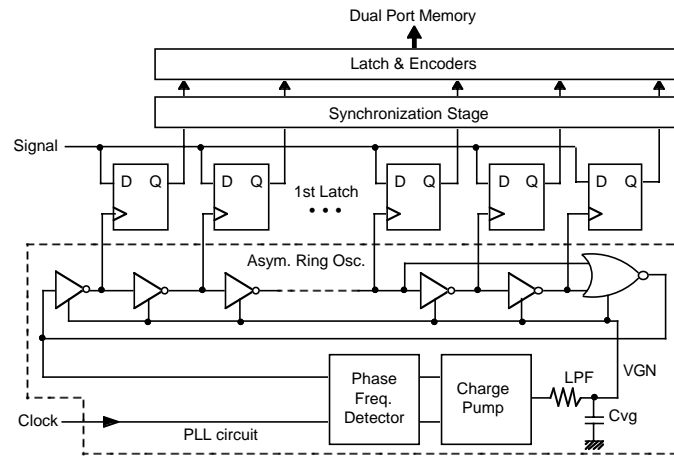


Fig. 5.43: The block diagram of TMC chip [62].

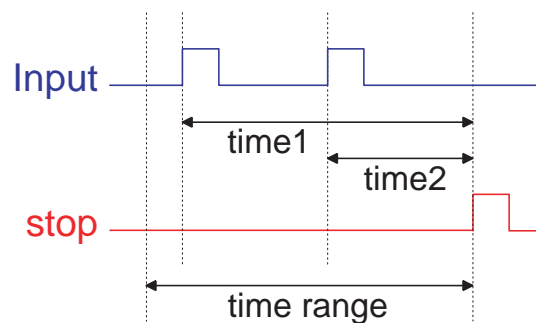


Fig. 5.44: The timing diagram of the TMC (common stop mode). The signal within the time range is recorded.

5.4.4.2 SWINE (Super WireNet Encoder)

SWINE is a gated coincidence module developed at KEK for MWPC READOUT SYSTEM. VME standard is adopted as its system bus. The system consists PORQ (Pulse On ReQuest), HOG (Hold On Go) module and original J2 back plane³. J2 back plane has two functions. One is to supply power for ASD through HOG module ($V_{cc} = \pm 3.3[V]$). The other is to distribute control signals including threshold voltage for ASDs from PORQ to HOG.

PORQ is a control device of HOG. One PORQ is required in each VME crate. It generates the 50MHz internal clock, gate width and delay to collect the data. They are distributed to each HOG module through the J2 back plane. It additionally receives the external trigger signal (test pulse) to open the gate.

HOG is used to latch signals from each TGC through its front panel connector. Each HOG has 64 inputs corresponding to 4 ASD card. 15HOGs can be mounted on one VME crate. They receive the control signals from PORQ through J2 back plane. Fig.5.45 shows the timing block diagram of the SWINE system. The TGC hit data was delayed in several nsec to adjust the signal timing of each chamber. After delaying, it fed to digital delay circuit with FIFO (Fast-In Fast-Out) memory. The signal is judged as the hit when the delayed signal is within the gate; we set delay as 200nsec (delay = $20[\text{nsec}/\text{row}] \times 10[\text{row}] = 200[\text{nsec}]$) and the gate width as 300nsec (gate = $20[\text{nsec}/\text{row}] \times 15[\text{row}] = 300[\text{nsec}]$) for TGC readout.

³Circuit board or device on receiving side with socket and slot to connect other circuit board

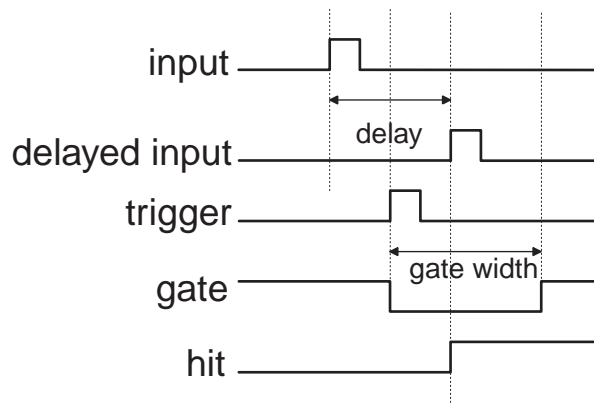


Fig. 5.45: The timing diagram of SWINE system.

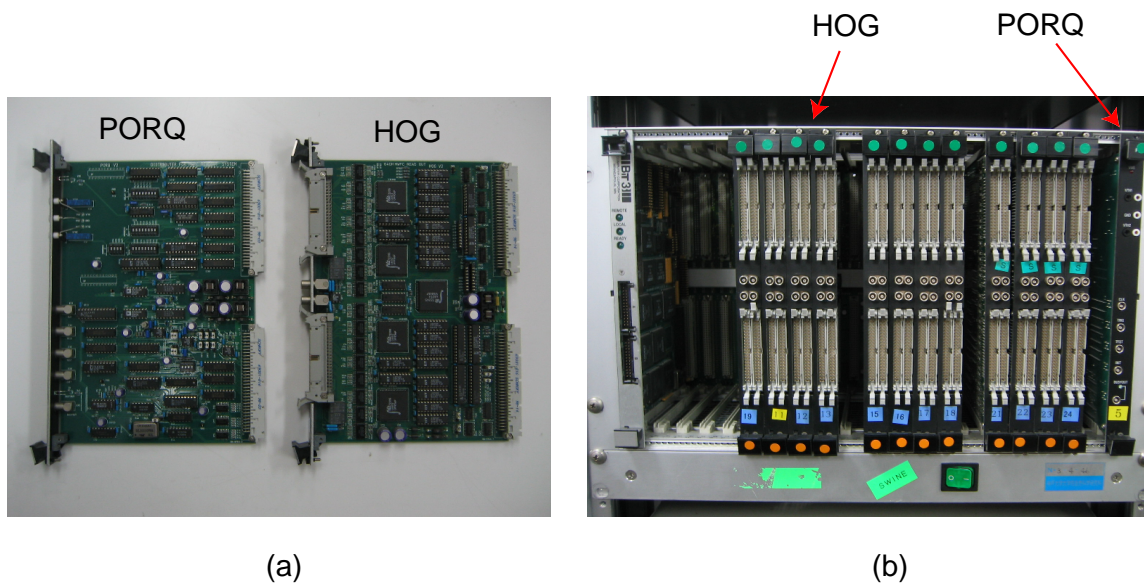


Fig. 5.46: Photograph of SWINE system. (a) left: PORQ module, right: HOG module (b) 1 PORQ module and 12 HOG modules mounted on original J2 back plane.

5.4.4.3 DAQ Process

Fig.5.47 shows the diagram of computers for DAQ and readout electronics. There were five PCs; three PCs were for data acquisition from SWINE or TMC, one for data storage, and one for off-line analysis. DAQ PCs were connected to each VME crate through a PC-VME bus adopter (model616 manufactured by SBS Technologies Inc.[64]) mounted in each crate. All PCs were connected via Fast Ethernet (100 BASE-T). The data was stored on the hard disk drive of the storage machine. The drive was shared using NFS (Network File System) protocol.

One DAQ process runs on each PC connected to VME bus. The process for TMC was called master and one for SWINE was called slave. In order to synchronize the DAQ processes between the master and the slave, socket communication technology was adopted. Fig.5.48 shows the flow-chart for the data taking and communication processes. Each PC opened the TCP port to send/receive the data packet at first. When the I/O Register module received a trigger signal, it asserted the VETO signal. If the master received the trigger signal, it sent " trigger message " to all slave processes. Then the master read the TMC data and the slaves read the SWINE data. After the slave processes finished

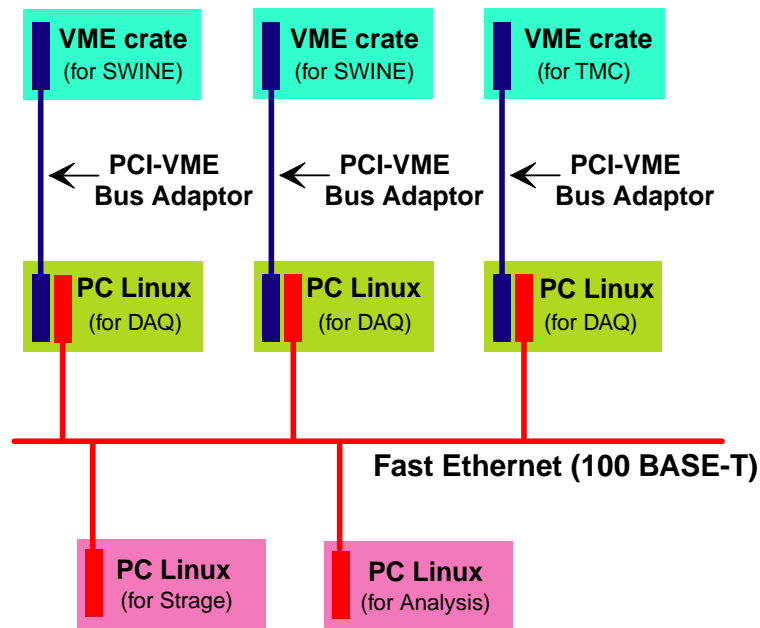


Fig. 5.47: Diagram of the DAQ machine. PC and VME crate.

reading the data, they sent back the “ ready message ” to the master. If the master finished reading the data and received the “ ready ” from all slaves, it sent “ accept message ” to each slave process. Finally, each process wrote the collected data to the file on the storage.

5.4.4.4 Raw Data Format

The raw data from each sub detector was stored in binary format. Table 5.5 shows its format. Left of the table indicates the data processed in master process. Right indicates the data processed in slave processes. For each data, START_FLAG and END_FLAG indicates the start and the end of one data taking period (called “ run ”). There are the following 4 blocks for each data:

- (1) a configuration block (CFG),
- (2) a start block of the data taking (RUNbegin),
- (3) an event information block (EVT),
- (4) a end block of the data taking (RUNend)

CFG block has the information of the configuration file recorded the correspondence between the module ID and the channel number. RUNbegin block has the run number, the run start time, and comment (given by operator). EVT block has the hit data obtained from each module. For a data-acquisition period, all events are recorded by piling these blocks. The data from TMC, which is the data size and the signal response time, was recorded. The data from SWINE, which is the data of the hit channel, was recorded. The RUNend block terminated this file by writing the run number and the time of termination.

5.4.4.5 Data Conversion

There were 3 files of the raw data created by each data acquisition process. They were combined into one file and converted to ASCII format. We used a configuration file in which the relation

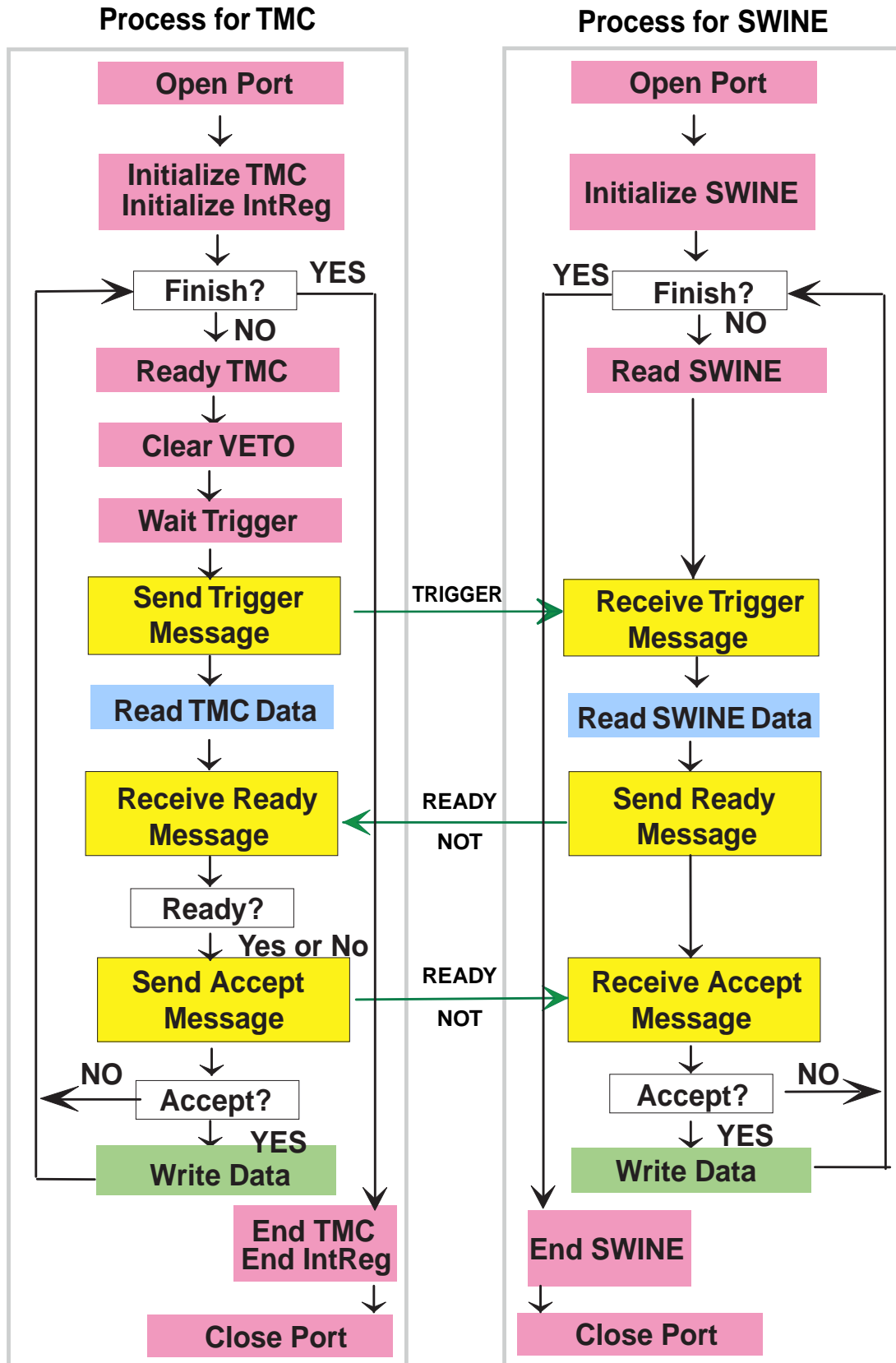


Fig. 5.48: The flow-chart for the data taking and communication processes. The master and the slave were communicated using socket communication technology

START_FLAG	START_FLAG
CFG_FLAG cfg data size < configuration >	CFG_FLAG cfg data size < configuration >
CFG_END_FLAG	CFG_END_FLAG
RUNbegin_FLAG run number DAQ start time configuration file name comment	RUNbegin_FLAG run number DAQ start time configuration file name
RUNbegin_END_FLAG	RUNbegin_END_FLAG
EVT_FLAG event number	EVT_FLAG event number
TMC_FLAG all TMC data size < data >	SWINE_FLAG all SWINE data size < data >
TMC_END_FLAG	SWINE_END_FLAG
EVT_END_FLAG	EVT_END_FLAG
• • • • •	• • • • •
RUNend_FLAG run number DAQ end time	RUNend_FLAG run number DAQ end time
RUNend_END_FLAG	RUNend_END_FLAG
END_FLAG	END_FLAG

Table 5.5: Raw Data Format. Right shows the data for master (TMC) process, Left shows for slave (SWINE) process.

between the channel of the detectors and the pin assignment of the readout electronics modules was written. These three files were combined and converted by referring the configuration file.

5.4.4.6 Data Confirmation

In order to confirm the responses from the detectors and the electronics modules, we checked the following histogram in the beginning at cosmic ray test.

- (1) the hit profiles of top and bottom scintillation counters (Fig.5.49)
- (2) the hit profiles of drift tubes for each super-layer (Fig.5.50)
- (3) the multiplicity distributions of drift tubes for each super-layer (Fig.5.51, Fig.5.52)
- (4) the hit profiles of TGCs for wire and strip (Fig.5.53)

If there were no signal channels on TGC, the causes of no signal were miss-insertion of the ASD card in most cases. If there were too many hit counts compared with other channels, this channel was judged as noisy channel. In order to repair the noisy channel, the shield on the adapter-board was strengthened by putting some copper tapes on it.

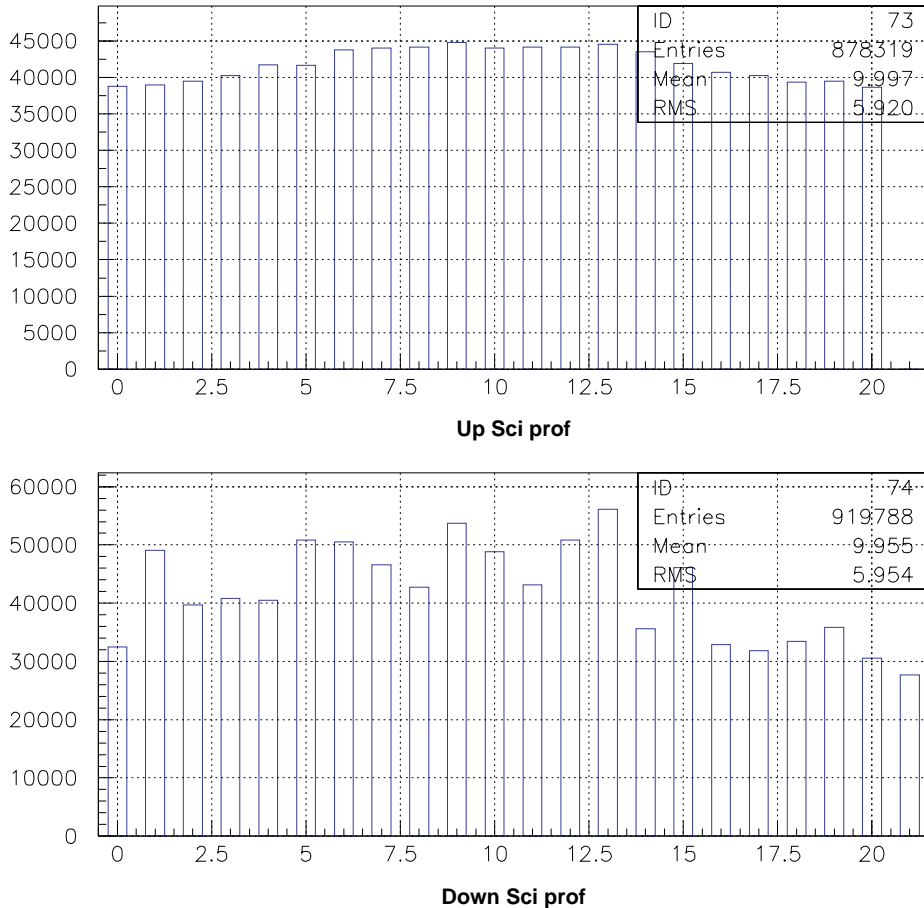


Fig. 5.49: Hit profile for scintillation counter.

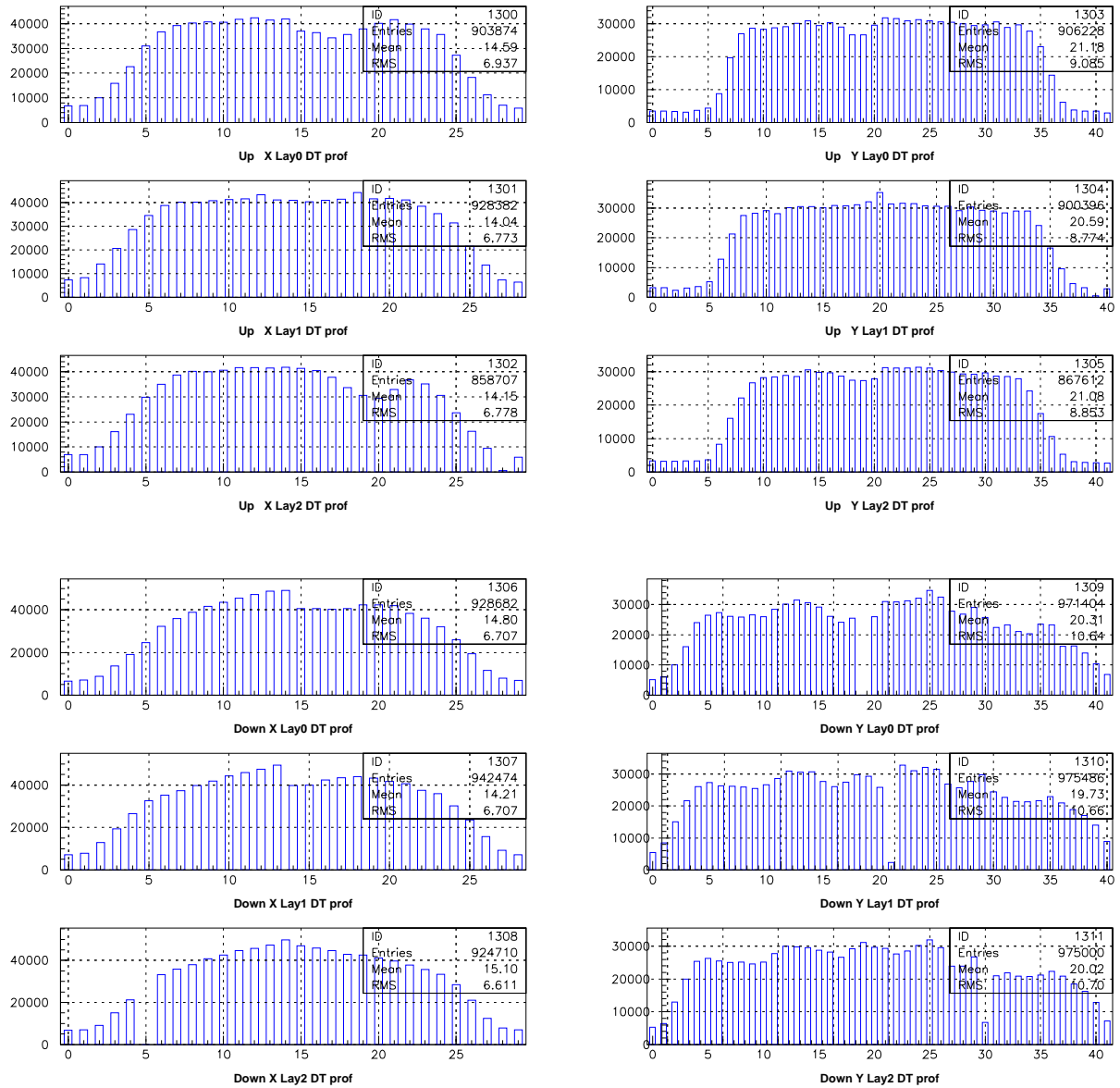


Fig. 5.50: Hit profile for drift tube.

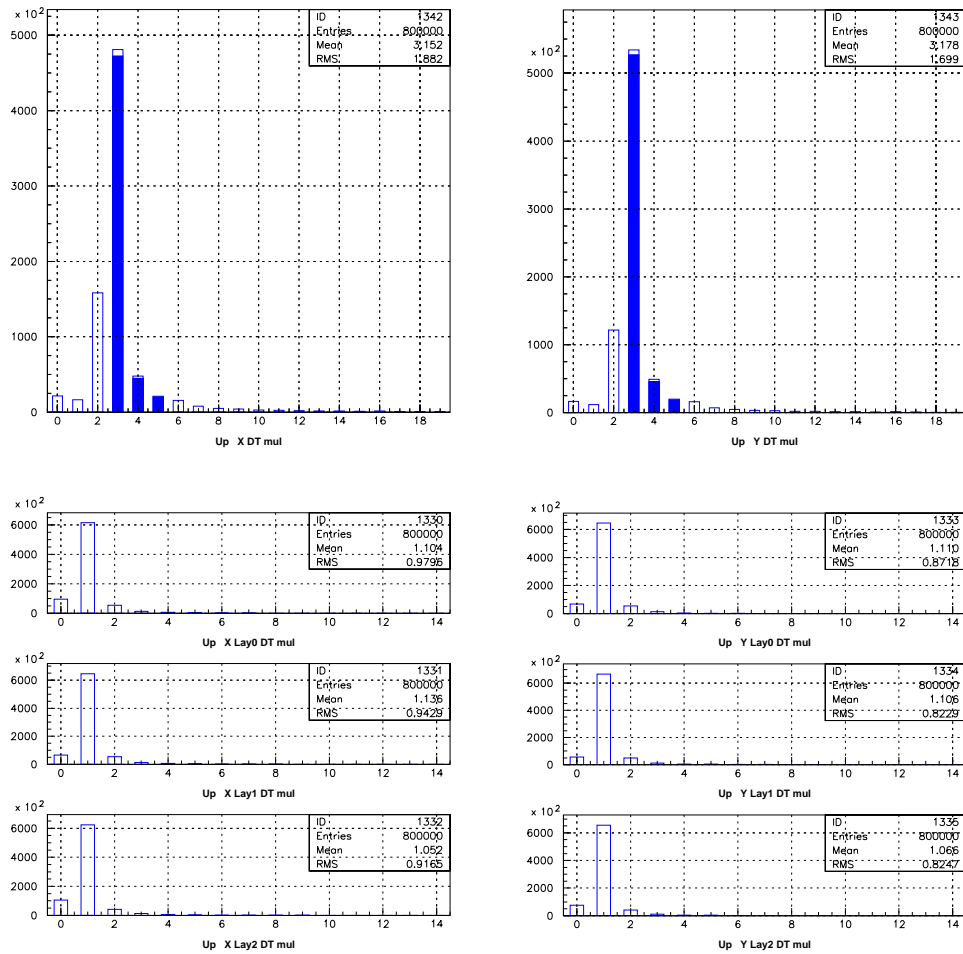


Fig. 5.51: Multiplicity distribution for UP drift tube. Large graph shows the multiplicity for each super-layer. Small graph shows the multiplicity for each layer of each super-layer.

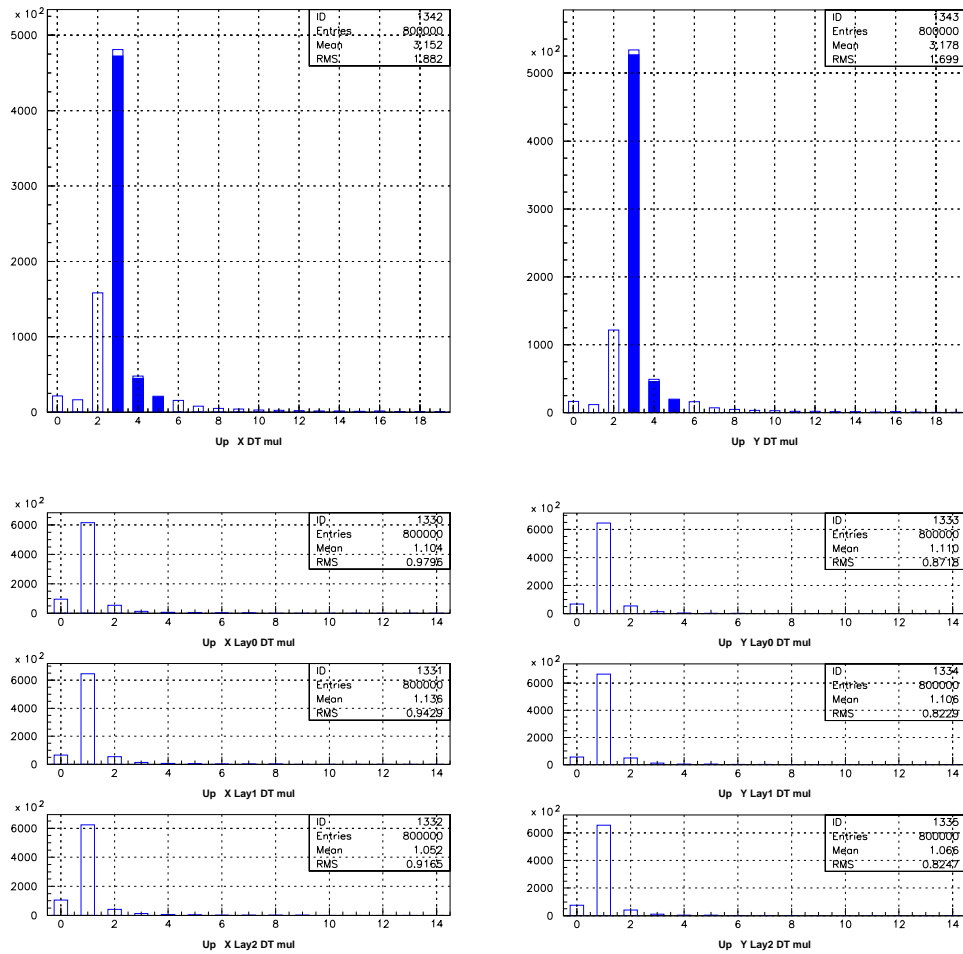


Fig. 5.52: Multiplicity distribution for DOWN drift tube. Large graph shows the multiplicity for each super-layer. Small graph shows the multiplicity for each layer of each super-layer.

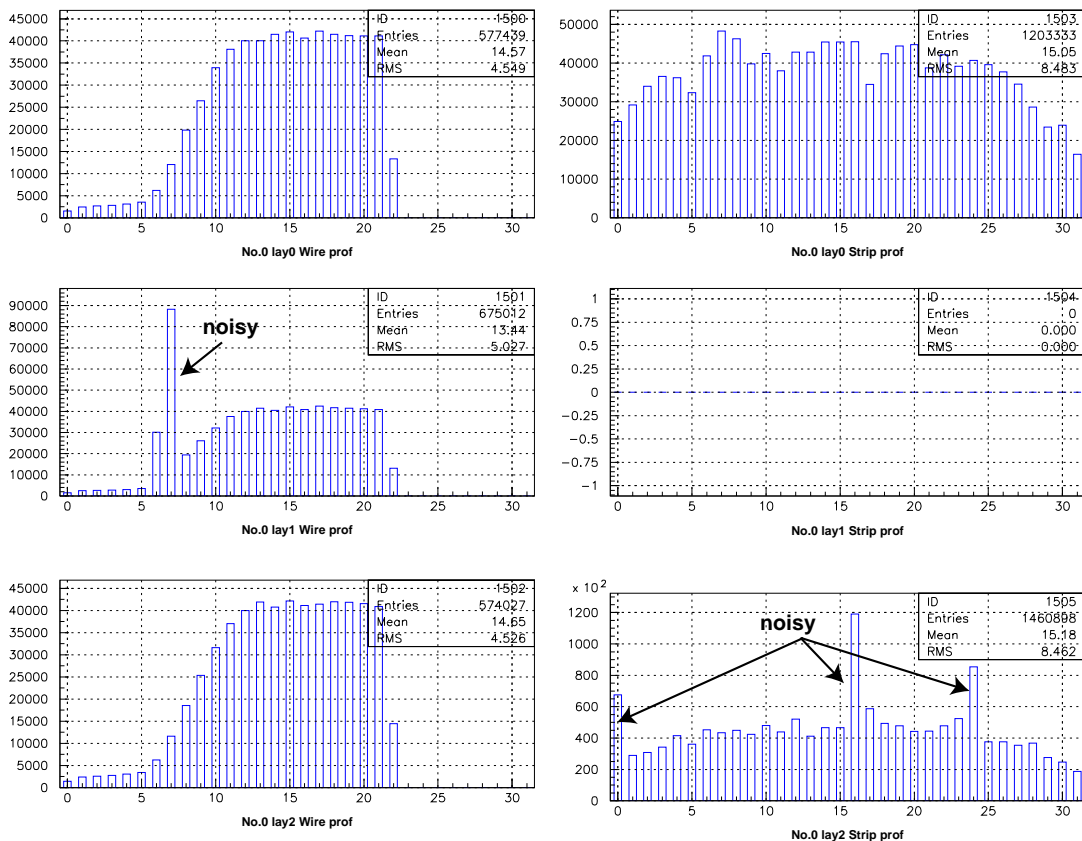


Fig. 5.53: Hit profile for TGC

5.5 Gas System

The dedicated gas system was developed for the cosmic ray test. In order to achieve the stable operation of TGCs during the test periods, a stable gas mixture ratio and flow rate were required. There were two systems; one was for mixing CO₂ and n-pentane, and another was for the distribution of the gas to each TGC inserted into the test stand. In addition, the safety system to protect TGC from the over-pressure should be provided.

5.5.1 Chemical Tolerance Test of the Tube

Because n-pentane is a corrosive organic gas, it may remove grease/plasticizer from the plastic and rubber materials. If the removed plasticizer were flowed to downstream with mixed gas, TGC would break down. Therefore, chemical tolerance test for gas tubing materials should be applied.

12 materials were investigated. The tubes were cut in about 1cm, and were soaked in liquid n-pentane filled in the glass bottles. After some days, the n-pentane in these bottles was sampled on the SUS⁴-made clean plate and then it evaporated. If small quantity of remaining oil, which was liquated out from material, was observed, the material of the tube was not suitable for mixed gas for TGC. Results are summarized in Table.5.6. PTFE⁵ has good tolerance, but it is very expensive. We found PFA⁶ has enough tolerance and is cheap plastic. So PFA and SUS were adopted as the tubing materials.

⁴Stainless Steel

⁵Poly Tetra Fluoro Ethylene

⁶PerFluoro-Alkoxyalkane

material	oil
nylon (polyamide, PA)	○
Tygon [®]	○
poly vinyl chloride (PVC)	○
poly urethane (PU)	○
poly ethylene (PE)	○
natural rubber (NR)	○
styrene butadiene rubber (SBR)	○
silicon rubber	○
PTFE	×
PFA	×
SUS	×
epoxy resin	×

Table 5.6: Results of chemical tolerance of n-pentane. Tygon[®] is a clear tube made of soft PVC. It is the registered trademark of U.S.Stoneware Co..

5.5.2 Mixing System

Fig.5.54 shows the gas piping diagram for the cosmic ray test. In order to realize the constant mixture ratio, the flow rate of liquid n-pentane and CO₂ gas were controlled by Mass Flow Controller (LV-310MC manufactured by ESTEC Co. Ltd.). The flow rate was determined by analyzing the mixture ratio using gas chromatography (described in detail in Appendix). Liquid n-pentane stored in a 10l SUS-made tank was flowed to a temperature controlled bath through a sintering metallic filter with 0.5 μ m diameter minute hole. Because the boiling point of n-pentane is 36.05°C, the temperature inside the bath was controlled around 40°C by a ribbon heater and a thermostat. The temperature was also monitored by a thermocouple and recorded by voltage recorder (TR-71, manufactured by T&D corporation). The bath with 75cm depth and 30cm diameter was made by SUS. In order to evaporate n-pentane effectively, glass beads of 1cm in diameter were stuffed about 40cm from the bottom.

A safety system for power failure was mounted (red dashed-line rectangle shown in Fig.5.54). In case of power failure, the pressure of the n-pentane reserver will be released to prevent n-pentane feed into the tank. So electric valve (EV1) should close and EV2 should open to release the pressure applied to the reserver tank. Normal Close (NC) valve is closed without power supply and Normal Open (NO) valve is opened without power supply. We adopted NC valve for EV1 and NO valve for EV2. CO₂ was kept flowing to remove the remained n-pentane in the bath.

5.5.3 Distribution System

After mixing, the mixed gas was distributed into 8 lines for TGCs. Fig.5.56 shows the gas piping diagram for the distribution system. As described in section 5.1.1, the inner pressure of TGC should not exceed 600Pa. Therefore, the mixed gas should be supplied with low pressure. It is , however, difficult to keep equal flow rate for all lines in such low pressure. The flow rate depends on the conductance of each line very much. Total conductance of each line is not same due to differences

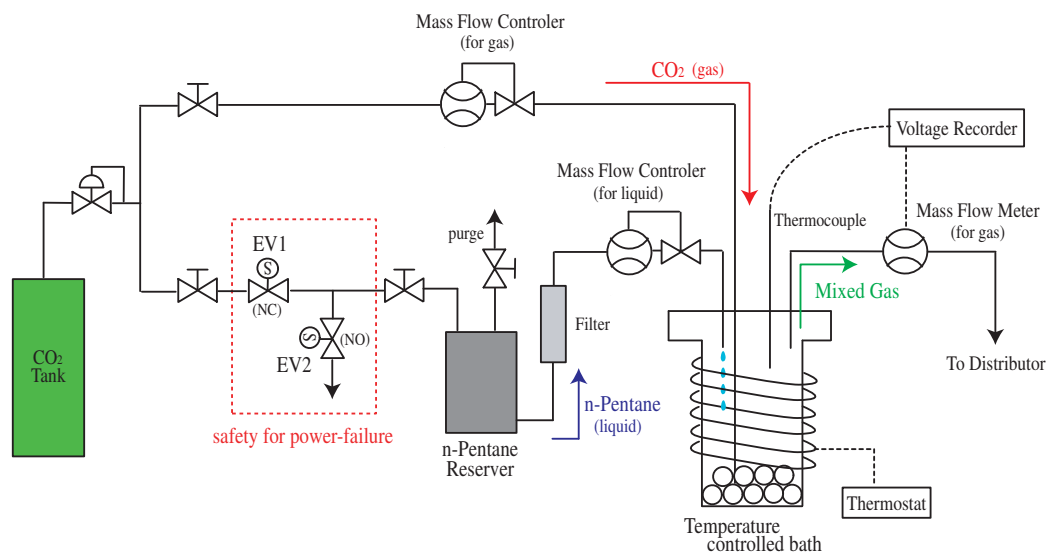


Fig. 5.54: Gas piping diagram for the Mixing System. The flow rate of liquid n-pentane and CO_2 was controlled by Mass Flow Controller.



Fig. 5.55: Image of the Gas Mixing System.

of conductance of individual TGCs. In order to achieve the low-pressure distribution, an oil bubbler was mounted on exhaust side of each line. The level of the oil was adjusted to keep the flow rate of all lines equivalent. The silicon oil was adopted to avoid evaporation. The flow rate of each line was monitored by a Mass Flow Meter (3080 series, manufactured by KOFLOK Co, Ltd.) and recorded by voltage recorder (TR-71). Fig.5.58 shows the flow rate as a function of the time. Red line indicates the output from the mixing system, and other lines indicate the output monitored after distributing.

A safety system to avoid the over-pressure was equipped. If n-pentane liquefied in the tube, the pressure of TGC may be increased. The differential pressure switch (MS61H, manufactured by Yamamoto Electronic Works Co., Ltd.) to monitor the pressure was provided on each line to release an electric valve in case of over-pressure.

In order to avoid the liquefying of n-pentane, the room temperature was maintained over 20°C by air-conditioner. In addition, the gas rack was covered with the heat insulator (5cm thick polyurethane).

The safety system for power failure was also provided (red dashed-line rectangle as shown in Fig.5.56). If power failure was caused, electric valve EV3 closed, and EV4 and EV5 opened to release the pressure.

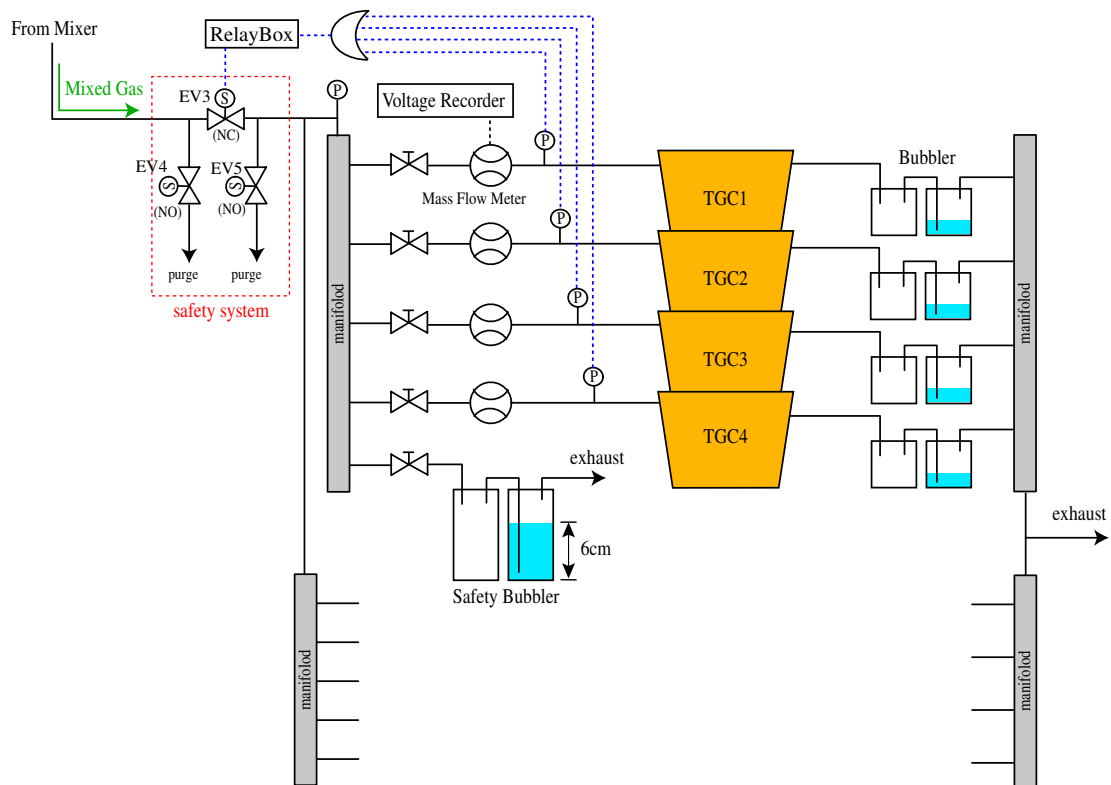


Fig. 5.56: Gas Piping diagram for Distribution System

5.6 Measurement of Mixture Rate

In order to evaluate the performance of the gas system, the mixture ratio of CO₂ and n-pentane was measured using gas chromatography (GC, the detail was described in Appendix). The gas systems for cosmic ray test and for HV test were investigated respectively.



Fig. 5.57: This image shows the Gas Distribution System.

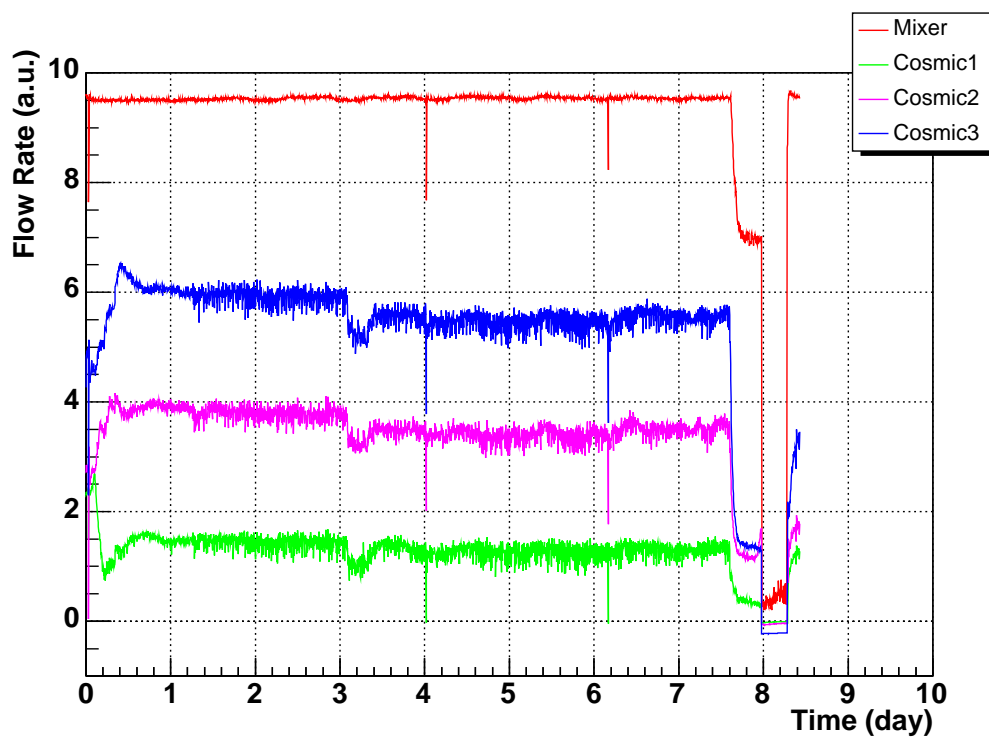


Fig. 5.58: Mass Flow Output. “ Mixer ” indicates output for the mixing system. Others (from “ Cosmic1 ” to “ Cosmic3 ”) indicate the distributed output.

5.6.1 Cosmic Ray Test

The mixture ratio of the gas system for the cosmic ray test was analyzed using GC with a VZ-7 column. Fig.5.59 shows the mixture ratio as a function of the flow rate of liquid n-pentane. The flow rate of n-pentane was set using this result.

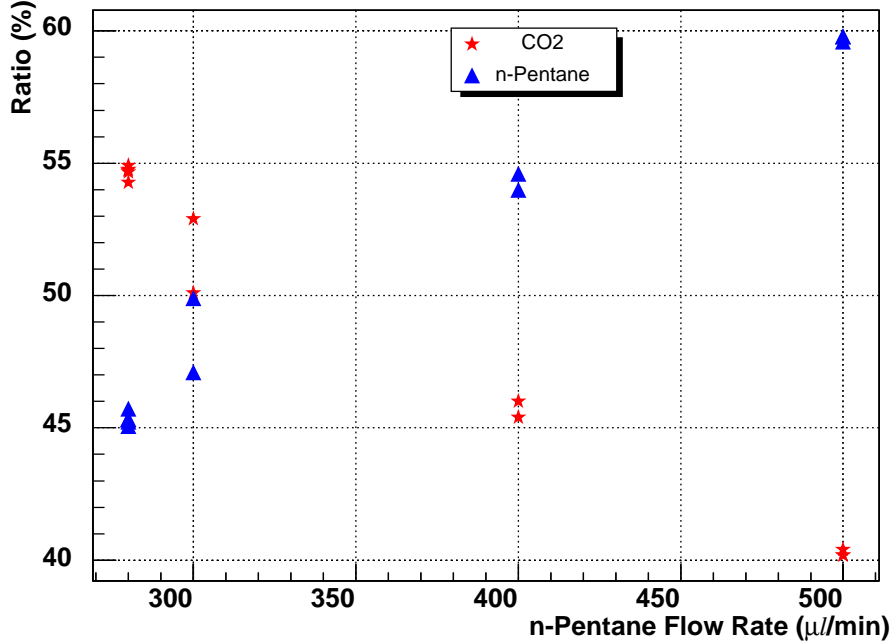


Fig. 5.59: This figure shows the dependency of the mixture ratio on the flow rate of n-pentane ($\text{CO}_2 = 100\text{cc}/\text{min}$).

5.6.2 HV Test

As described in section 5.3.3, the gas system for HV test was adopted bubbling method. Fig.5.60 shows the mixture ratio as a function of the temperature of water. We found that the ratio of n-pentane was $44.8 \pm 0.8\%$ at 14°C .

5.7 Operation Condition

In cosmic ray test, all chambers were tested with 3.0kV applied high voltage and 100mV threshold voltage (V_{th}) of amplifier card. This threshold voltage was higher than the nominal voltage of 50mV, because the electric noise level in this system was higher than 50mV. In order to determine the applied high voltage of TGC for 100mV threshold voltage, the efficiency dependence on the applied high voltage was examined. Fig.5.61 shows efficiencies as a function of the applied high voltage. The efficiency at 3.0kV was in “ plateau ” region as shown in this graph.

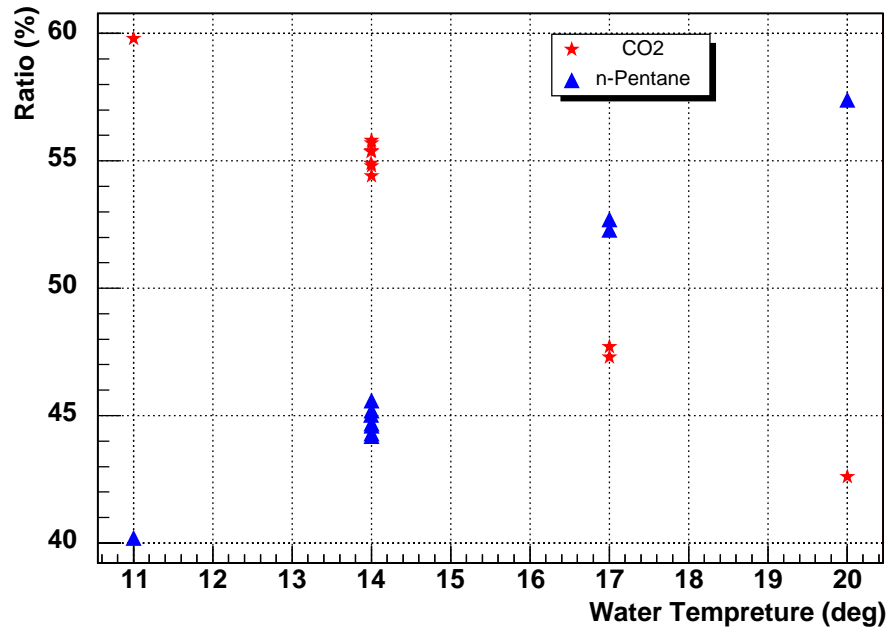
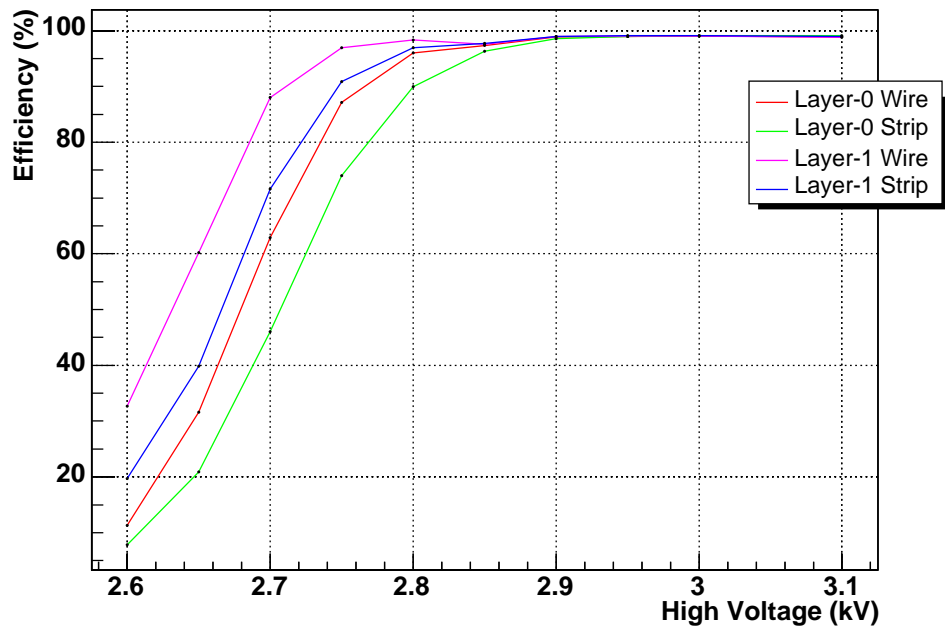


Fig. 5.60: The water temperature vs mixture rate.

Fig. 5.61: TGC efficiency as a function of applied high voltage ($V_{th} = 100mV$).

5.8 System Modification

The systems for T7 Triplet type (T7T) were described above. In order to inspect the other type, we modified the test station because of the difference of their dimensions (as shown in Fig.4.16). There were three modification during three years test; first was from T7T to T7 Doublet (T7D), second was from T7D to T4 Doublet (T4D) and last was from T4D to T5 Doublet (T5D).

5.8.1 T7T \rightarrow T7D

The differences between T7T and T7D are 1) the thickness of the module and 2) the number of ASDs. The number of T7D modules in the test station was increased from 8 to 12. The number of gas distribution was also increased to 12 lines. T7D has 4ASDs for wire and 4ASDs for strip. It corresponded to Therefore, 12 HOG modules for wire and 12 HOG modules for strip were used.

5.8.2 T7D \rightarrow T4

The differences between T7D and T4D are 1) the shape, 2) the number of ASDs. As shown in Fig.4.16, the size of T4D is quite different from T7D, especially the height of the trapezoid (2m) is much larger than T7D (1.2m). In order to widen the acceptance of the test station, 4 scintillation counters for upper layer were added. The size of these scintillators was $123mm \times 1300mm \times 10mm$. PMTs (R329-02) were attached on both ends. Consequently, the trigger rate increased about 20%, to 40Hz.

The number of the ASDs attached on one T4D module is 18 (14 for wires and 4 for strips). The number of T4D modules in the test station was 8. Total number of the cables for ASDs was 144. In total, 28 HOG modules for wire and 8 HOG modules for strip were mounted. It corresponded to 2304 readout channels in total. One VME crate together with a PC was added to operate the HOG modules.

5.8.3 T4 \rightarrow T5

The differences between T4D and T5D are 1) the shape, 2) the number of ASDs. The size was a little bit smaller than T4D. The number of ASDs is 12 for wires and 4 for strips, and is less than T4D.

During the test of T5D, the computer for TMC was upgraded. The readout rate was increased to approximately 40Hz almost same as trigger rate.

The number of TGC module, ASD, and HOG module for each type were summarized in Table.5.7.

	TGC	ASD_W	ASD_S	HOG_W	HOG_S
T7T	8	6	4	12	8
T7D	12	4	4	12	12
T4D	8	14	4	28	8
T5D	8	12	4	24	8

Table 5.7: Summary of the number of TGC module, ASD and HOG module.

6 Data Analysis

6.1 Analysis Process

There were the following seven parts of the analysis process:

- the combination process of three raw data files (**Event Building**)
- the conversion process of the combined raw data file to ASCII file (**Convert**)
- track reconstruction process (**Tracking**),
- efficiency and timing analysis process (**Analysis**)
- efficiency mapping process (**Efficiency Mapper**)
- visualization of hits and geometry (**Event Display**)
- histogramming tool (**PAW: Physics Analysis Workstation**[65])

The data flow chart was shown in Fig.6.1. The red character indicate the process name. The Event Building and the Convert processes were already described in section 5.4.4.5. Tracking, Analysis and Efficiency Mapper process will be described in this section.

The blue rectangle indicates the data file. There were five data files; Raw data, DAT file, DST file, EFF file, and RZ file. Raw data is binary data file containing the hit information of the detectors (see section 5.4.4.4 for detail). One Raw data file is created by one DAQ process. All Raw data files is combined to one DAT file in by Event Building and Convert process (see section 5.4.4.5 for detail). DAT file is recorded in the ASCII format and contains of hit channel and timing information for each detector. In addition, the drift length computed from drift time information using $x-t$ relation is included. DST file is also an ASCII file created by Tracking process. This file contains reconstructed track information in addition to DAT file. Each event in DST files could be displayed by Event Display. EFF file is also an ASCII file created by Analysis process. This file contains values of TGC efficiency calculated using track and TGC hits information. RZ file has some histograms recorded in the HBOOK format[66]. These histograms can be displayed and manipulated by using PAW.

6.2 Tracking Process

In order to reconstruct a trajectory of incoming cosmic muon, the drift tubes were used. The measured drift time was converted to drift length using $x-t$ relation (Eq.(5.4)) by Convert process. A “ drift circle ” for each tube with a hit is defined so that its radius is equal to the drift length. The track was reconstructed using the common tangent line of these drift circles.

6.2.1 Hit Pattern Selection

To reconstruct the cosmic ray track, events with specific hit patterns of drift tubes were selected. Hit patterns used in this analysis were categorized into four; pattern1 with 3hits, pattern2 and 3 with

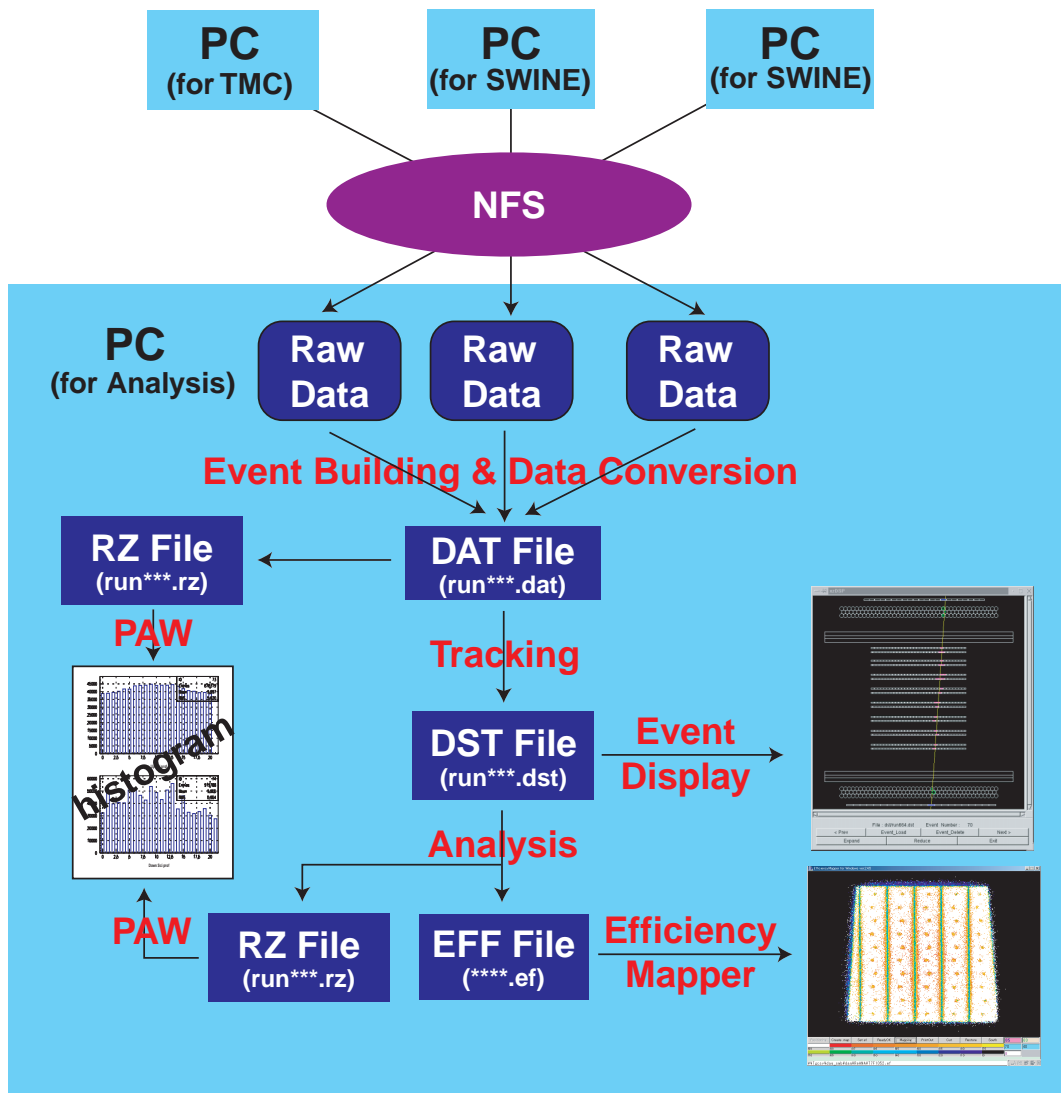


Fig. 6.1: Flow chart of the analysis

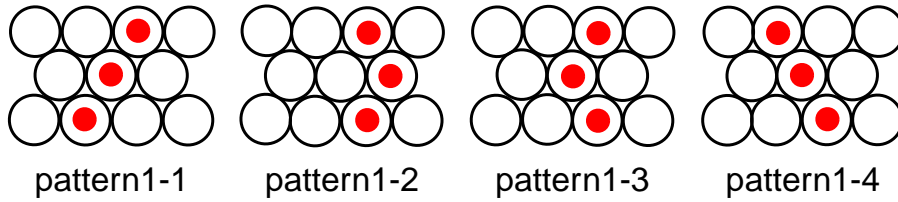


Fig. 6.2: Hit Pattern 1. Pattern1 are most ideal 3 hits patterns.

4 hits, and pattern4 with 2 hits in a super-layer. Fig.6.2 shows the hit pattern in pattern1. The circle with red mark indicates a fired drift tube by the cosmic ray muon.

Next, the four hit patterns of pattern2 shown as Fig.6.3 were examined. In these patterns, a fake hit (by electrical cross-talk or noise) was included as shown by a red blank circle. By neglecting this fake hit, these patterns could be recognized same as pattern1. Fig.6.4 shows 4 hit patterns of pattern3. A fake hit is also included for these patterns, but it is difficult to point out among two hits shown by blank circle. These patterns can be regarded as a combination of two patterns in pattern1.

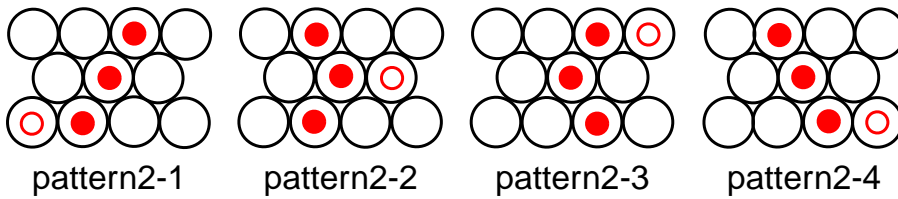


Fig. 6.3: Hit Pattern2. These are 4 hits in these patterns and are judged as the type that added the fake hit to pattern1.

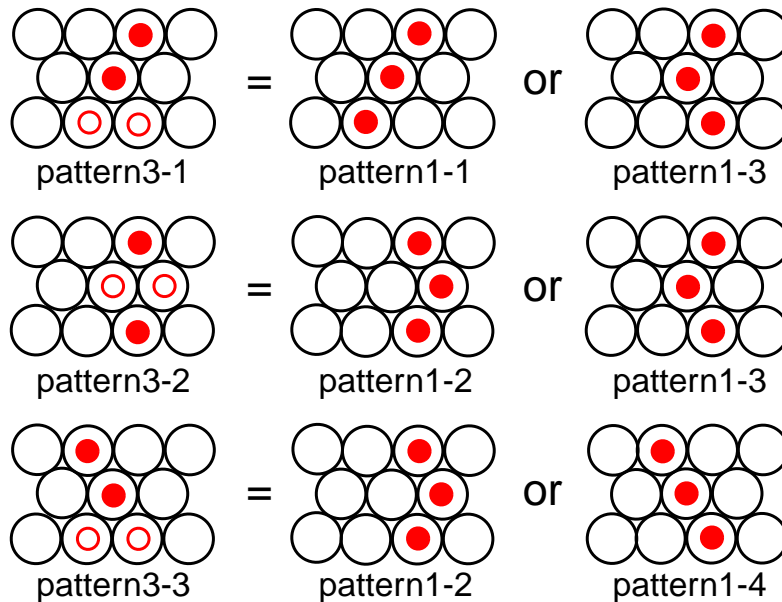


Fig. 6.4: Hit Pattern3. These are obtained by combining the two pattern1-types.

If there was no matched pattern, hit patterns with 2 hits shown in Fig.6.5 were searched (pattern4). In contrast to pattern1, these were the event that one drift tube was not fired by some reason.

The hit patterns other than pattern 1-4 were disregarded. If each super-layer on each coordinate system - UpX and DownX, or UpY and DownY - had one or two good-patterns, the event was moved

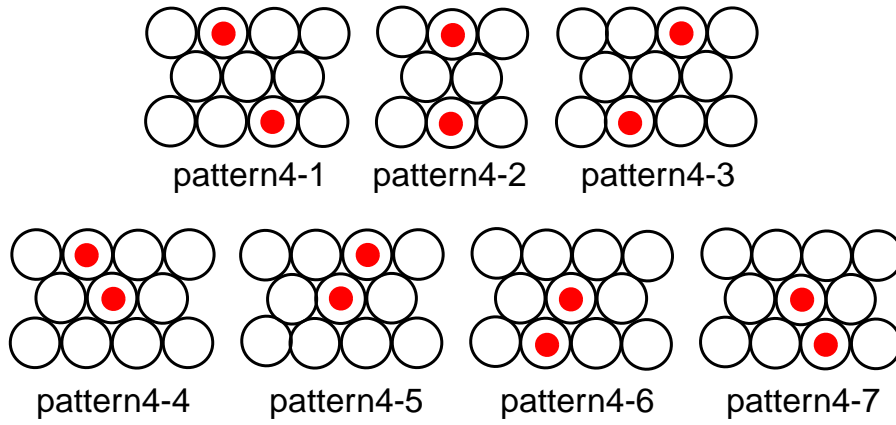


Fig. 6.5: Hit Pattern 4. These are 2 hits in these patterns. These patterns are obtained by subtracting one hit from pattern1.

into the following “ track reconstruction ” process. If there were more than two patterns, the event was judged as a noisy event and was disregarded.

6.2.2 track reconstruction

After pattern recognition, the track was reconstructed. Fig.6.6 shows the schematic view of the track reconstruction algorithm. At first, four tangent lines (green dotted-lines) of both top and bottom drift circles (red circle) were calculated. A trajectory was selected out of these candidate lines based on the least square method. Here, χ^2 is defined by

$$\chi^2 = \sum (d_i - x_i) \quad (i = 0, 1, 2, 3), \quad (6.1)$$

where i is the number of the tube excluding the top and bottom tube (blue circle), d_i is the distance between the candidate line and the center of the i -th tube, x_i is the radius of the drift circle of the i -th tube. The line which has minimum χ^2 was regarded as a trajectory. Trajectories in x-z plane and y-z plane were determined independently. Thus, a cosmic ray track was reconstructed.

Fig.6.7 shows the χ^2 distribution of the reconstructed track for each plane. Each distribution has a peak around zero, so the track was reconstructed correctly. However, it has a long tail. This tail was mostly electrical noise or cross talk of drift tube. This will be discussed in section 7.3.7.

The reconstructed track and hits in detectors can be displayed using Event Display. Fig.6.8 shows a sample event. Yellow line indicates the reconstructed track and red rectangles indicate the TGC hit channel of wires.

6.2.3 Rejection of Fake Track

In order to reject fake tracks, the hits of TGC were required. If the reconstructed track was a true cosmic ray, a TGC, which the cosmic ray passed through, should have associated hits. Fig.6.9 shows the efficiency of TGC (red line) and the track reconstruction (blue line) as a function of the number of the required TGC layer. As the result, there was little dependence on the number of the layer. Therefore, only the event with no hit layer was disregarded.

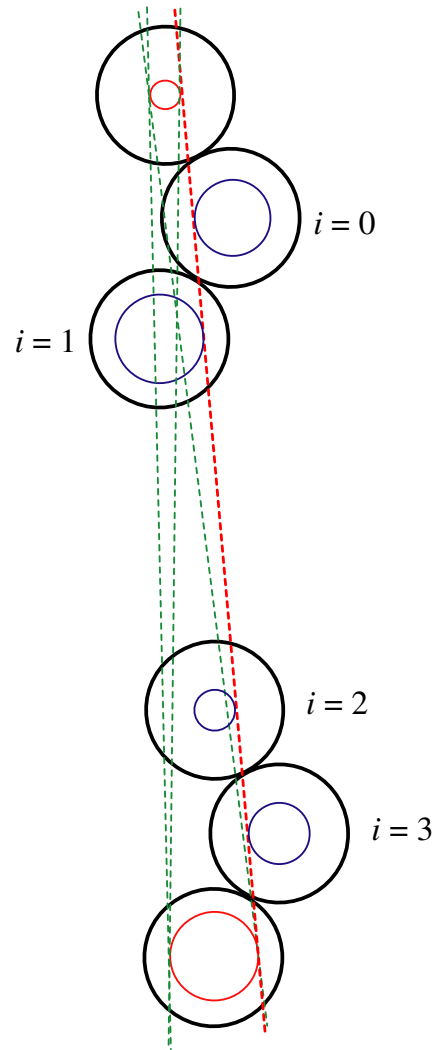
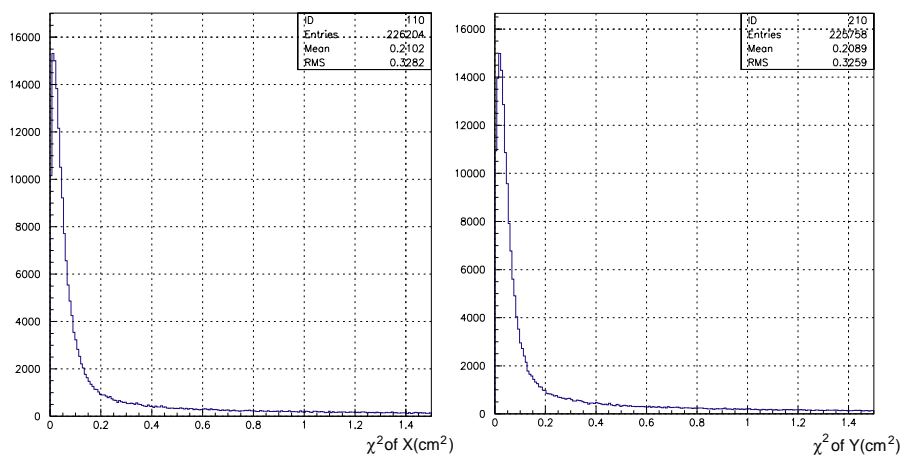


Fig. 6.6: The schematic view of track reconstruction.

Fig. 6.7: χ^2 distribution.

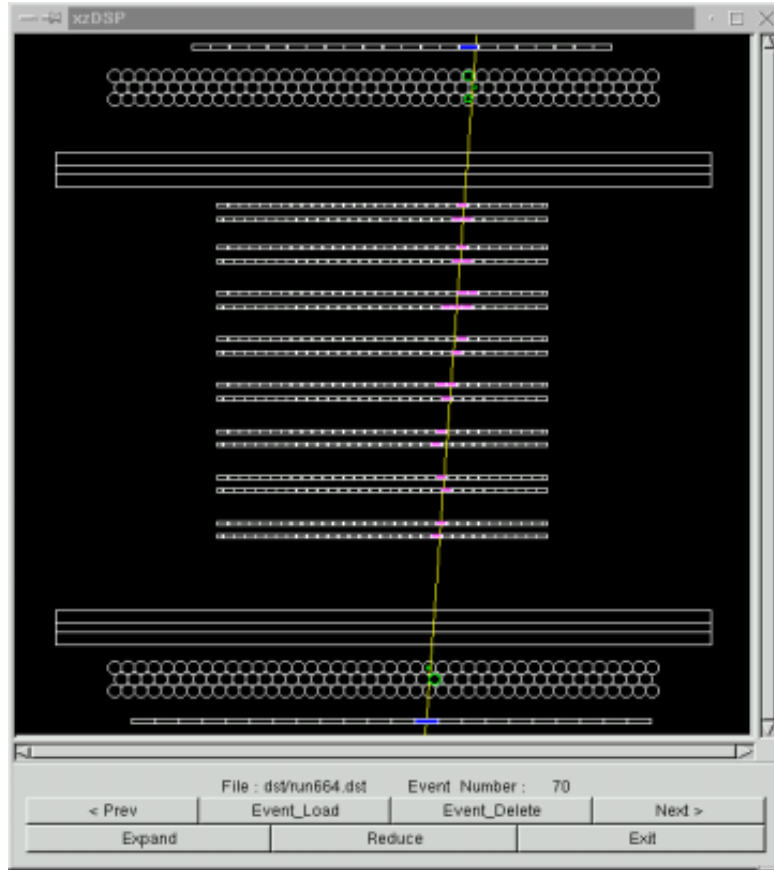


Fig. 6.8: Event Display (xz plane).

6.3 Efficiency Measurement

The detection efficiency of TGC was computed by examining whether a layer has a hit associated with the reconstructed track. Efficiency of TGC can be varied position by position. So, efficiency was calculated in each small cell. In order to check the efficiency, an image plotted it in each cell called “ efficiency map ” was created. The detection efficiency of TGC was defined by the ratio ϵ ,

$$\epsilon[\%] = \frac{N_{\text{hit}}}{N_{\text{track}}} \times 100, \quad (6.2)$$

where N_{track} is the number of the reconstructed track passed in each cell and N_{hit} is the number of events with any TGC hit associated with the track. Efficiency was calculated for wire and strip individually.

The area of support structures was intrinsically inefficient. Therefore, it is necessary to exclude the support area in the calculation of the efficiency. In order to recognize support structures, the granularity of the efficiency measurement was set as $5\text{mm} \times 5\text{mm}$ cell. The average value of the efficiency without the support structure was used for the quality assurance. More than 100 tracks were required in each cell to reduce the statistical error. In total, 6×10^6 tracks were required in whole TGC detection area of 2m^2 .

In order to exclude the support area, the precise position of TGC should be know. However, TGC was not aligned precisely in the test station. So the geometrical intersection between TGC plane and the reconstructed track may not agree with the position of TGC fired channel, i.e. the intersection

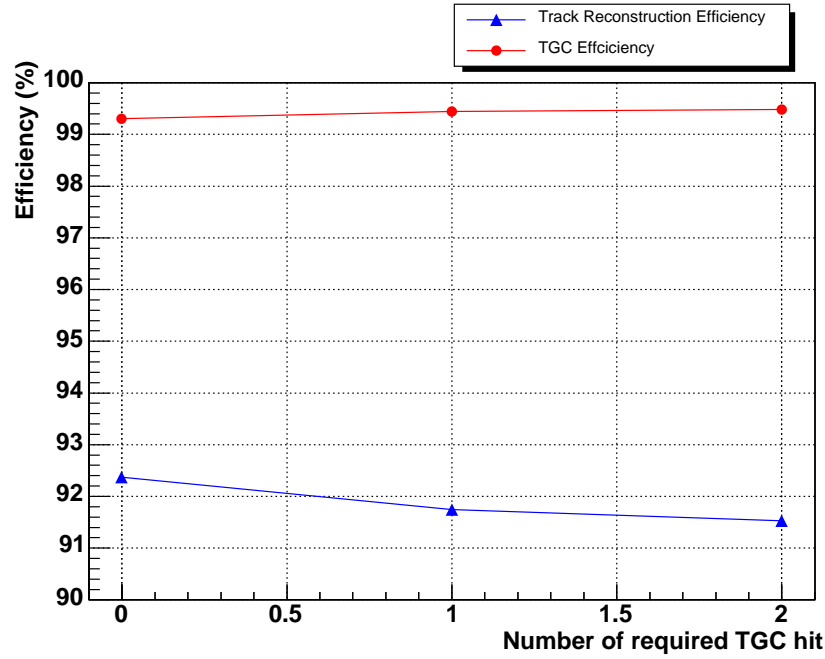


Fig. 6.9: TGC efficiency (red line) and the track reconstruction efficiency (blue line) as a function of the number of the required TGC layer.

calculated in the analysis program may be different from the hit position on TGC in actual (see Fig.6.10).

It was measured by using this map to recognize the position of the support structure of TGC by Efficiency Mapper, called “positioning” process. In order to find the actual position of TGC chambers (called “positioning process”), an efficiency map was created by using a part (about 20%) of acquired events. In this “positioning process”, a hit within 30 cm from the reconstructed track was judged as the “associated hit”. Fig.6.11 shows the schematic view of the positioning process for T7 type, and Fig.6.12 shows for T4/T5 type. The aberration of the center position O' from the nominal center position O in the software was measured using button support (3rd button support from short side). The rotation angle θ was measured using the inclination angle of wire support for T7 type. In T4/T5 types, one chamber plane is divided into two area and high voltage for each area is supplied individually. So, there is an inefficient area without wires (corresponding one or two wires) between these two area. The rotation angle for T4/T5 types was measured using this low efficiency region. The information of the aberration (coordinate of the center and θ) was written to a file.

After the positioning process, the complete efficiency map was created by using all events. Here, a hit within 8 cm from the reconstructed track was judged as the “associated hit”. The calculated efficiency was recorded in EFF file. The detection efficiencies for wire and strip were measured separately. There are three layers for wire and two layers for strip in Triplet type, so five efficiency maps were created. In doublet type, there are two layers for both wire and strip, so four maps were created.

The complete efficiency map was displayed by Efficiency Mapper shown in Fig.6.13 and Fig.6.14. Efficiency Mapper is a viewer for TGC efficiency map (i.e. EFF file). The value of the efficiency in each cell was classified by colors. For example, white indicates more than 99% and red indicates between 98% and 99%. As shown in these figures, support structures could be clearly observed. In Fig.6.14, the gap of two areas in T4/T5 types was clearly observed. Therefore, the fiducial area of each

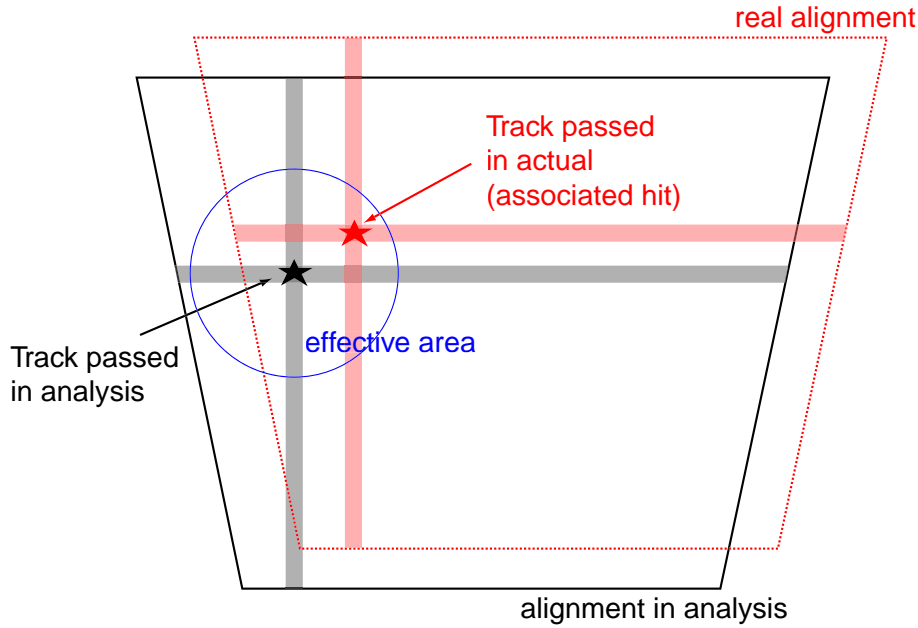


Fig. 6.10: The schematic view of Effective Area. The star marks indicate the intersection between the reconstructed track and TGC; black star indicates the position obtained by analysis program, and red star indicates the position through which the cosmic ray muon passed actually.

plane (wire or strip), where inefficient areas around the supports were excluded, could be defined in order to calculate the average efficiency.

6.4 Synthesize the Maps

The acceptance of the test station was enough to cover whole TGC detection area. However, due to the zenith angle distribution of cosmic ray, the distribution of the position passed through the incident cosmic muon was concentrated around the central area. Fig.6.15 and Fig.6.16 show the number of the reconstructed track passed through each cell on TGC. The concentration of the track at center position is apparent. Therefore, the statistics on TGC edge region became low. In addition, the dependence on the slot position of TGC in the test station is clearly seen. The trapezoidal shape of the distribution is due to the effect of the fake track rejection described in section 6.2.3.

In order to obtain sufficient statistics on TGC edge region, the data was acquired at two different alignments. TGC was shifted horizontally so that the long side of TGC could be aligned at near the center of the station. After acquiring the data for a long side, TGC was shifted to obtain the data for a short side. Consequently, two partial efficiency maps were obtained. These partial maps were combined by using the each positioning information. The left two figures of Fig.6.17 and Fig.6.18 show the partial maps obtained at each position. The complete map (the right figure of Fig.6.17 and Fig.6.18) was obtained by synthesizing two partial maps.

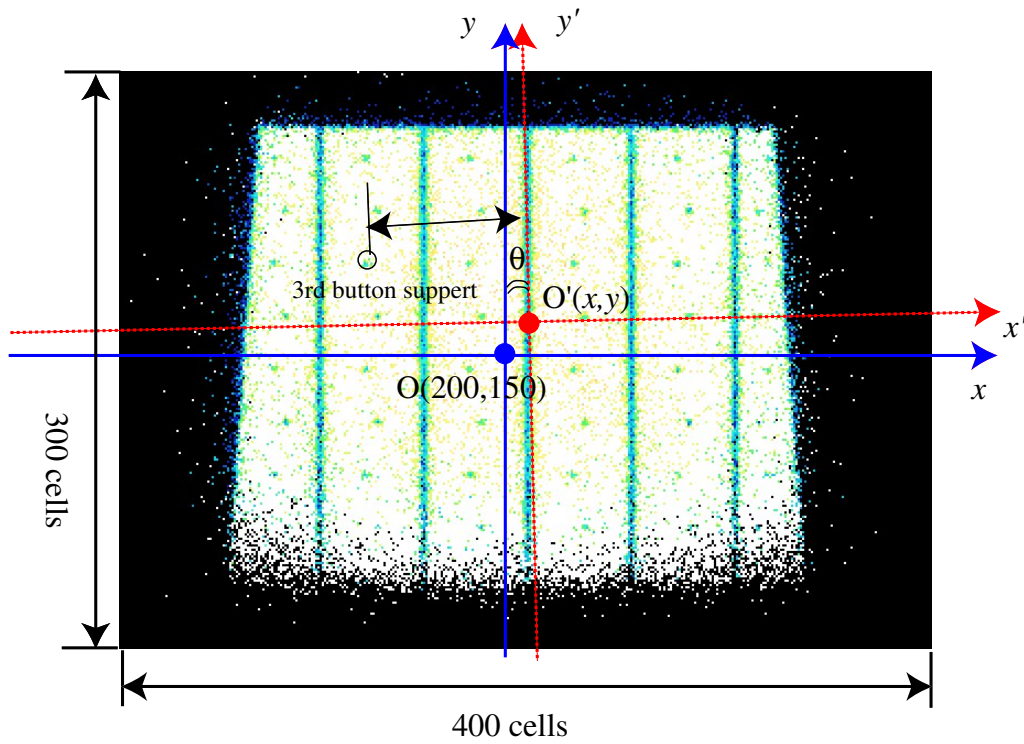


Fig. 6.11: Positioning Method for T7 type. Red line indicates the coordinate system for the Data, and blue indicates for software.

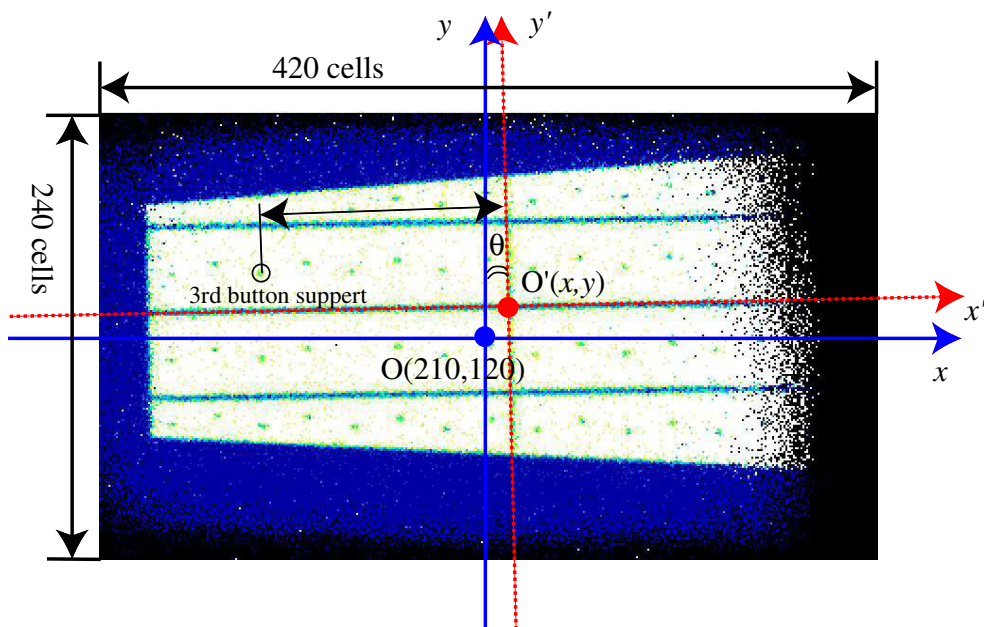


Fig. 6.12: Positioning Method for T4/T5 type. Red line indicates the coordinate system for the Data, and blue indicates for software.

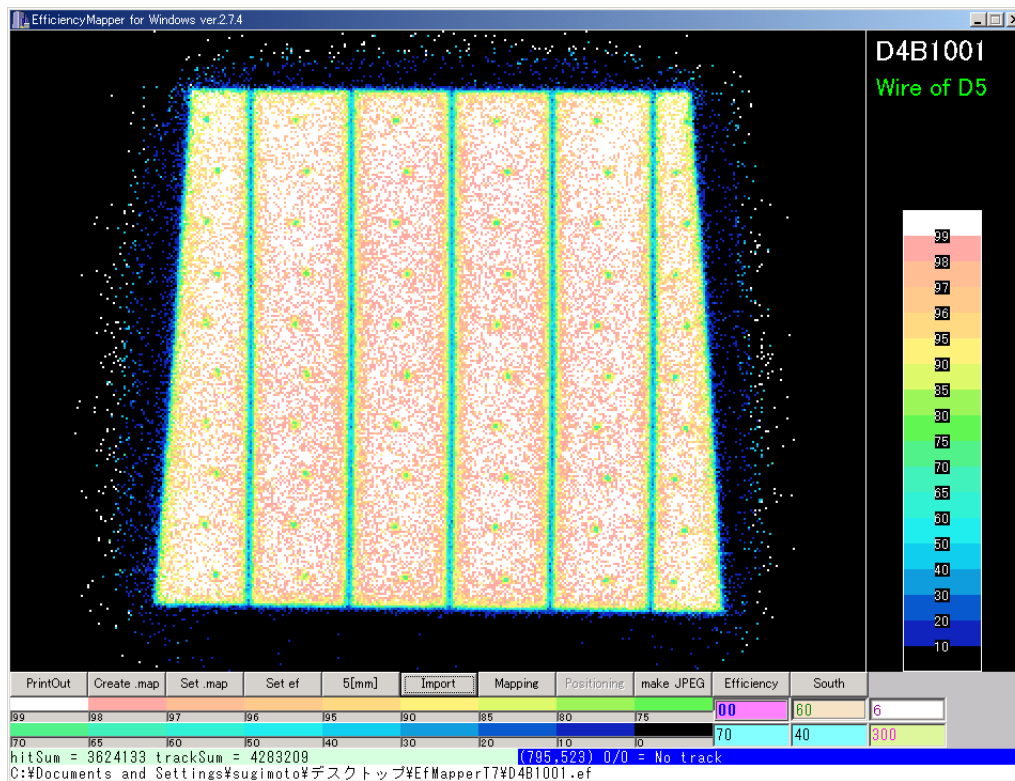


Fig. 6.13: Efficiency Mapper for T7 type.

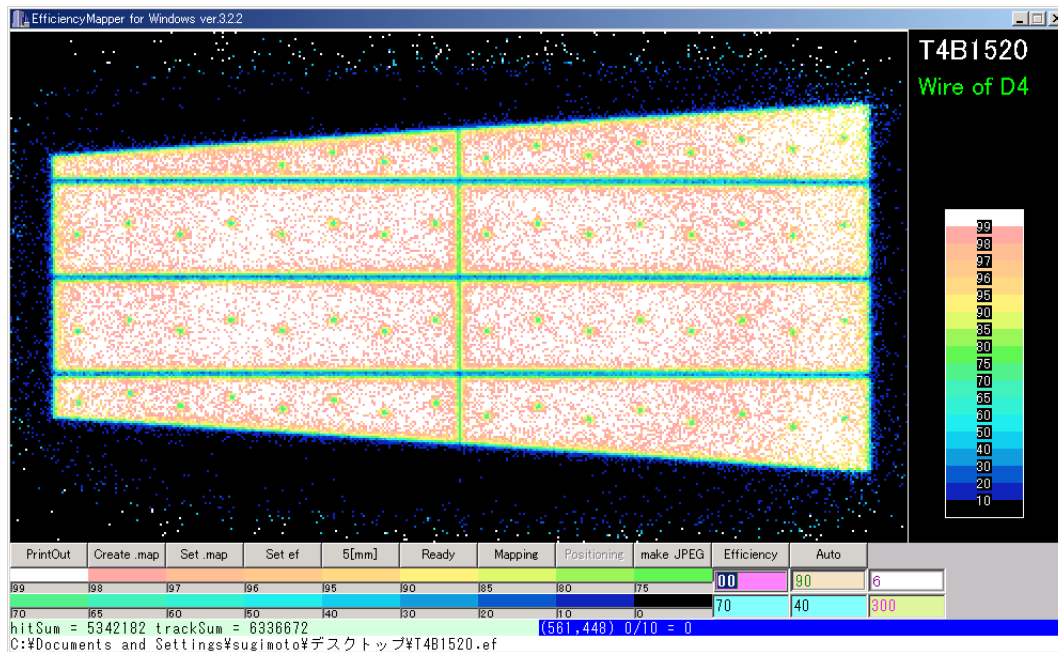


Fig. 6.14: Efficiency Mapper for T4/T5 type.

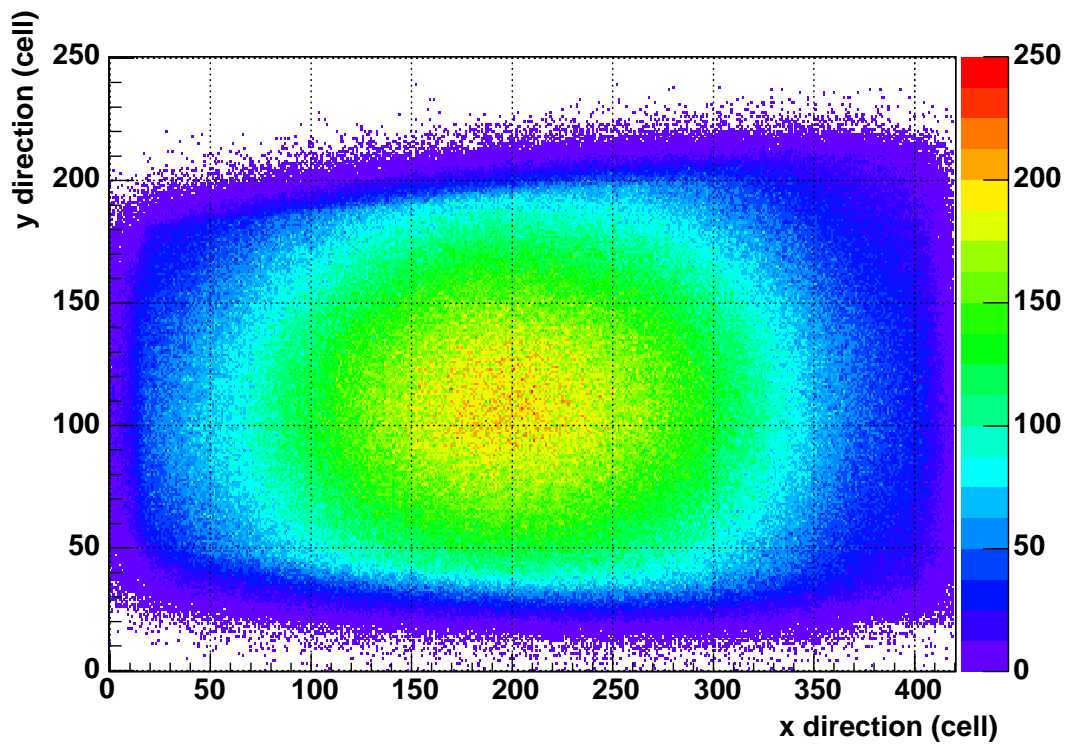


Fig. 6.15: The distribution of the track number passed through in each cell (0th slot).

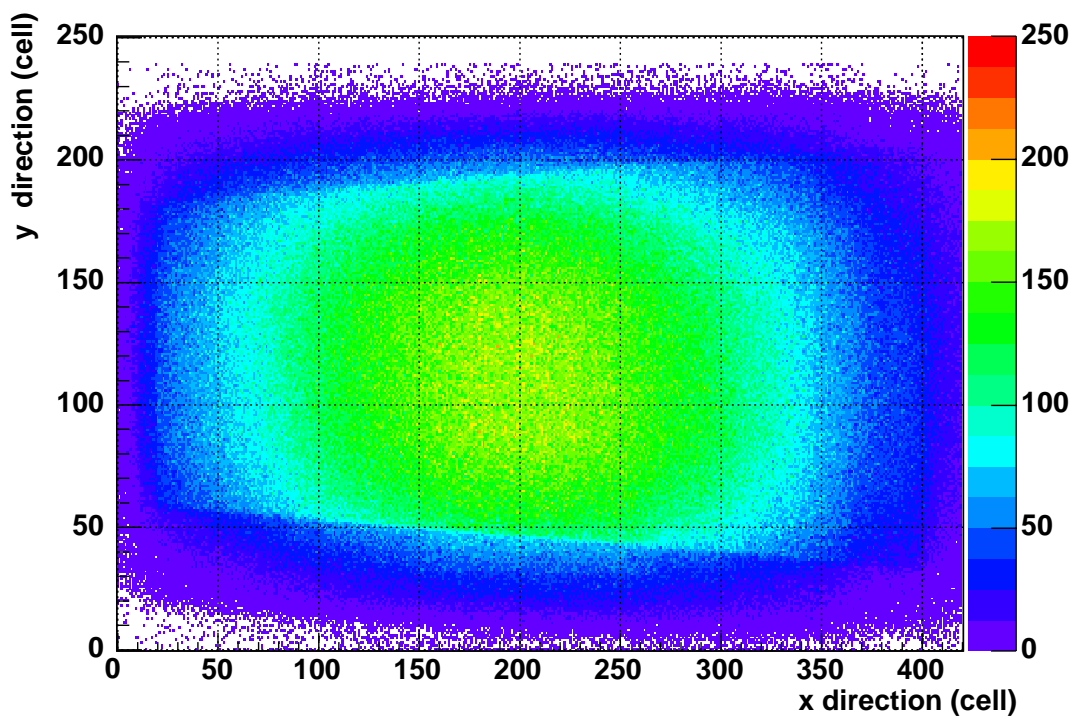


Fig. 6.16: The distribution of the track number passed through in each cell (4th slot).

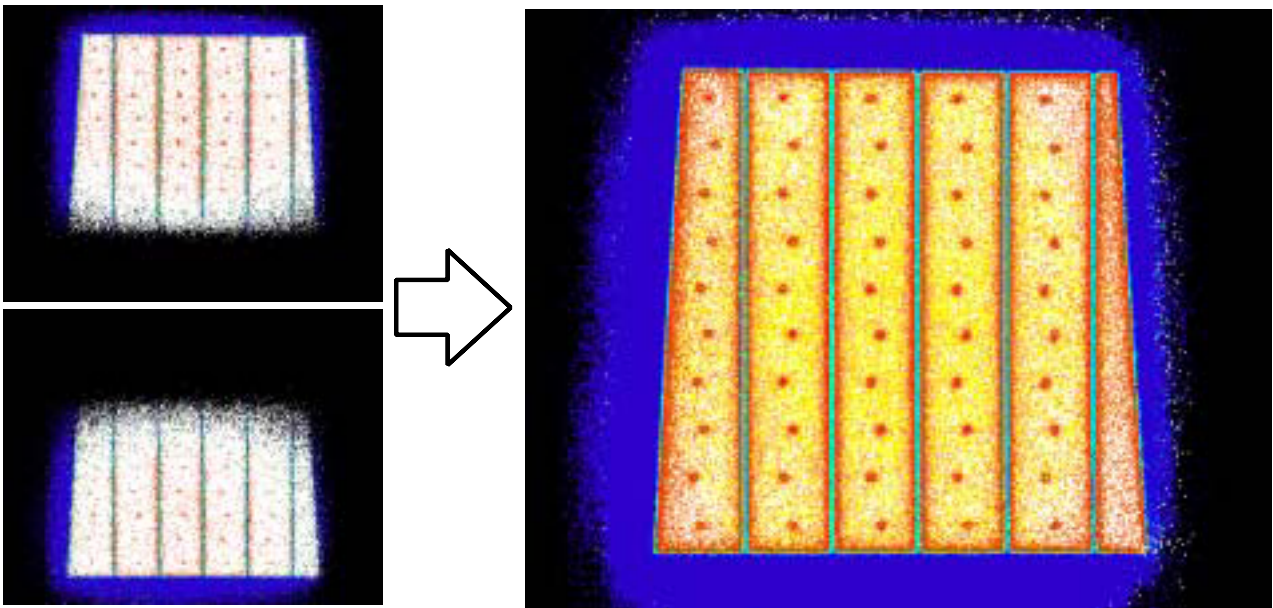


Fig. 6.17: Two partial maps are synthesized to one map for T7 type.

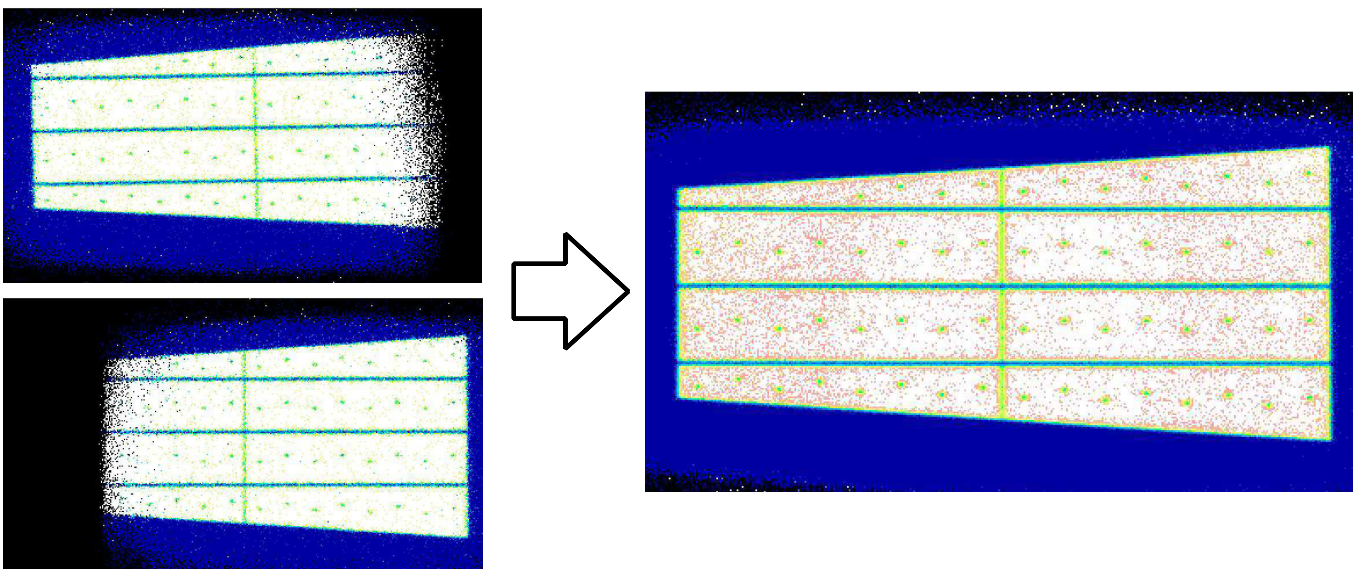


Fig. 6.18: Two partial maps are synthesized to one map for T4/T5 type.

6.5 Time response

Time response of TGC was analyzed by measuring the timing for 16ch ORed signals of a layer of TGC. Fig.6.19 shows an example of the timing distribution for one TGC layer; left indicates the distribution for wire timing and right for strip timing. Typically, 5nsec fast rise time and 20nsec fall time is shown in the distribution for wire. The measured time width within 99% efficiency for wire and strip are 24.5nsec and 29.6nsec respectively. This width includes differences of propagation time depending on hit position of TGC and time jitter of the trigger signal as well as intrinsic time jitter of TGC. The fall time distribution is varied by an angle of incident particles, vertical incident to be 30nsec, while 40° to be 10nsec[14]. The cosmic ray muon passes the chamber with having distribution of the incident angle and the observed value is reasonable.

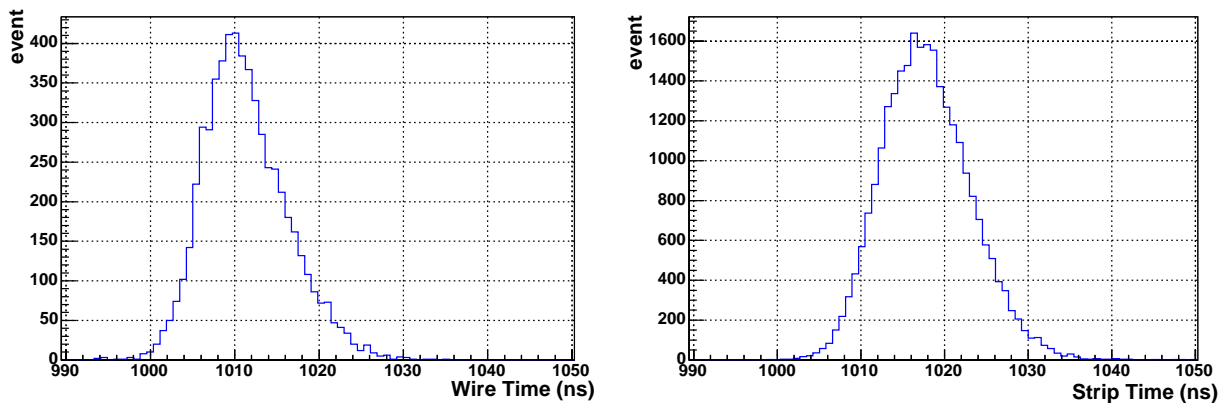


Fig. 6.19: Timing Distribution of TGC (left for wire and right for strip)

Fig.6.20 shows the distribution of the measured time width within 99% efficiency for wire (red chart) and strip (blue chart). The measurement for only T4 type was performed. The propagation time in the strip is large due to its long base (about 2m).

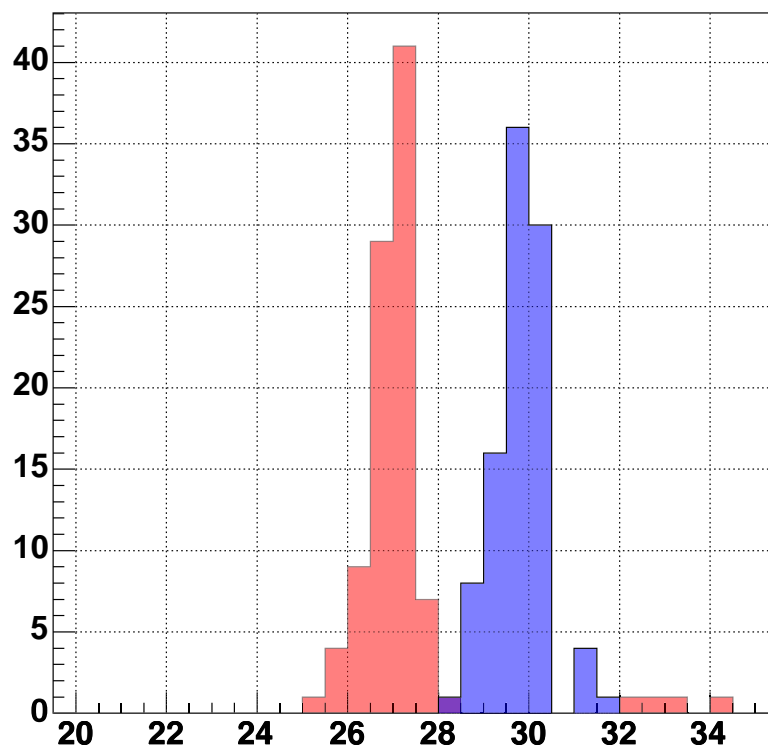


Fig. 6.20: The distribution of the signal response time for T4 type. Blue chart indicates the measured value for wire and red chart for strip.

7 Performance of the Test Station

Having described the setup and analysis method, let us now turn to the performance of the test station. The position resolution and the efficiency of the reconstructed track will be described. In addition, the trigger rate in the scintillation counter will be described.

7.1 Geant4 Simulation

In order to understand the performance of the cosmic ray test system, a Monte Carlo simulation based on Geant4 [67] was performed. For this simulation, all the geometrical configurations and materials of the scintillation counter, drift tube, and TGC were implemented together with support structures of test system. The thickness of each detector and structure is summarized in Table 7.1.

	thickness (g/cm ²)	materials
TGC singlet	0.47	FR4, Tungsten, mixed gas
drift tube	~ 1.3	Aluminum, Tungsten, mixed gas
scintillator	0.6	scintillator
support structure	~ 7.1	Steel
aluminum honeycomb panel	0.82	Aluminum
air	~ 0.63	

Table 7.1: Total thickness of materials. FR4 is a glass epoxy resin with SiO₂:52.8% and epoxy(C₂H₂):47.2%. Scintillator is C₉H₁₀ with a density of 1.032g/cm³. Steel is implemented with Fe:99.8%, C:0.2%. The density of the aluminum honeycomb panel is calculated from volume (2200 × 1500 × 27 cm³) and weight (2700g). Mixed gas for TGC is CO₂ + n-pentane, for drift tube is Ar + Ethane.

The anode wire for TGC was implemented as a tungsten-made plate with 0.5μm thickness (not implemented wire by wire). Fig.7.1 shows the geometry constructed by Geant4. A particle with some momentum and direction was created at the top of the station. Each particle trajectory consists of some small segments, called “ step ”. Each step was created when the particle was interacted with a material. The energy, passing point, momentum direction, and TOF of each step can be obtained. A hit information can be obtained when a step passed through each detector. This simulation computed the detector hit information and output the DAT file of the same format as real data.

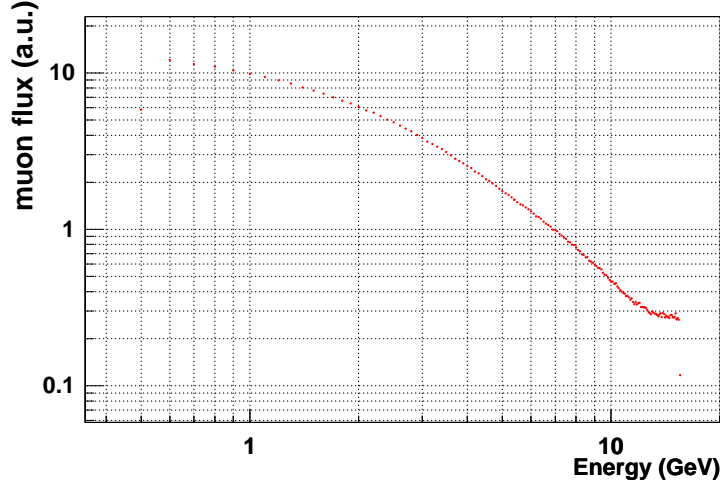


Fig. 7.2: Energy distribution of muons by BESS experiment[70].

Similarly, the rate R_{after} could be estimated after adding four scintillation counters,

$$R_{\text{after}} = 63.4[\text{m}^2/\text{sec}/\text{sr}] \times \frac{2.6[\text{m}^2]}{(2.6[\text{m}])^2} \times 2.6[\text{m}^2] \sim 63[\text{Hz}] \quad (7.3)$$

In order to confirm the performance of this simulator, the trigger rate of this station was evaluated. Firstly, consider the distribution function $f(p, \cos\theta, \phi, x, y, t)$ $[(\text{GeV}/c)^{-1}\text{sr}^{-1}\text{m}^{-2}\text{t}^{-1}]$. This function indicates the number of particles generated at a certain time with a momentum p , a zenith angle θ , an azimuthal angle ϕ , and a generated position (x, y) . The total number N_0 of the generated muons was obtained by integrating the distribution f in whole generated angle, area and time:

$$N_0 = \int_{p_{\min}}^{p_{\max}} dp \int_{\cos\theta_{\max}}^1 d\cos\theta \int_0^{2\pi} d\phi \int_{x_{\min}}^{x_{\max}} dx \int_{y_{\min}}^{y_{\max}} dy \int_0^T dt f(p, \cos\theta, \phi, x, y, t). \quad (7.4)$$

Now, the function f is assumed to depend on only the energy and the zenith angle;

$$f(p, \cos\theta, \phi, x, y, t) = f(p)\cos\theta^2. \quad (7.5)$$

Therefore, Eq.(7.4) is

$$N_0 = \int_{p_{\min}}^{p_{\max}} f(p)dp \int_{\cos\theta_{\max}}^1 \cos\theta^2 d\cos\theta \int_0^{2\pi} d\phi \int_{x_{\min}}^{x_{\max}} dx \int_{y_{\min}}^{y_{\max}} dy \int_0^T dt. \quad (7.6)$$

Here, we set the momentum range of cosmic ray muon as $0.6\text{GeV}/c < p < 10\text{GeV}/c$, the generated area as $3\text{m} \times 3\text{m}$ and the maximum generated angle θ_{\max} as $\pi/2$. Therefore, Eq.(7.6) is calculated as

$$N_0 = 63.4[\text{m}^{-2}\text{sec}^{-1}\text{sr}^{-1}] \times \frac{2\pi}{3}[\text{sr}] \times 3[\text{m}] \times 3[\text{m}] \times T[\text{sec}]. \quad (7.7)$$

The event passed through both layers of the scintillation counter was judged as a “ triggered event ” (as same method as the real trigger logic). Then trigger rate is obtained from N_{trig}/T , where N_{trig} is the number of triggered event. The result of the Monte Carlo is summarized in Table.7.2. The increase of about 20% is good agree with the result of the system modification discussed in section5.8.

	before	after	unit
Generated event (N_0)	7849342	7836086	event
T	6516.75	6505.75	sec
Triggered event (N_{trig})	234065	289028	event
Trigger Rate	35.9	44.4	Hz

Table 7.2: Results of the simulation for trigger rate

The result of the rate is summarized in Table.7.3. The rate by the simulation was about 70% less than that by rough estimation because low energy muons were scattered by materials in the station and may not be triggered. The difference between Monte Carlo and the real data (about 86%) can be due to the detection efficiency of the scintillation counters and the decrease of the acceptance of the counters caused from a twist or a distortion of themselves.

	R_{before}	R_{after}
rough estimation	49	63
Monte Carlo	36	44
real data	27	38

Table 7.3: The summary of the trigger rate.

7.2 Track Reconstruction Efficiency

The efficiency of track reconstruction is defined as the ratio of $N_{\text{track}}/N_{\text{trigger}}$, where N_{track} is the number of the reconstructed track and N_{trigger} is the number of the triggered event. The efficiency is calculated as 73.3% using real data. The ratio for recognized hit pattern are summarized in Table.7.4. The column of “ subtotal ” means the sum of 3hits and 2hits pattern. The value obtained by multiplying each subtotal is different from the efficiency value of 73.3%. There is about 10% difference between them. This is caused from some correlations between each super-layer, especially the combination of (UpX, UpY) or (DownX, DownY). That is, UpX (DownX) tend to detect an incoming muon together with UpY (DownY). The number of the dead channel in lower drift tube layers is more than upper ones. Therefore, the probability recognized as 3hits pattern for Down super-layer is lower than that for Up super-layer.

	3hits pattern	2hits pattern	subtotal	no pattern
UpX	75.08	14.11	89.18	10.82
UpY	75.14	15.68	90.82	9.18
DownX	68.43	19.49	87.91	12.09
DownY	69.23	18.63	87.86	12.14

Table 7.4: The ratio for recognized hit pattern.

7.3 Tracking Resolution

The resolution of the track was required to be approximately 1mm because of the identification of the support structure of TGC. So the position resolution of the track was evaluated using “ knife-edge ” method. This method is usually used in the evaluation of the optical beam profile; the profile is measured by concealing the knife-edge. The detail of this is given in next subsection.

7.3.1 Knife-edge method

Fig.7.3 shows the conceptual view of the knife-edge method. Consider an ideal source that passes like a step function (the blue line in Fig.7.3 (a)). If the source is detected using a detector with finite position resolution, the edge of the step function becomes round (the red line in Fig.7.3 (a)). The distribution within the small range dx can approximate to a point-like source distribution, i.e. delta function $F(x)=\delta(x - x_0)$ (the blue line in Fig.7.3 (b)). If the point-like distribution was detected using the detector, the delta function becomes a gaussian distribution $G(x)$,

$$G(x) = \frac{1}{(\sqrt{2\pi})\sigma} \exp\left(-\frac{(x - x_0)^2}{2\sigma^2}\right). \quad (7.8)$$

It corresponds to the red line in Fig.7.3 (b).

The total number of tracks struck into one bin (dx) is $\Delta x \delta(x - x')$, and they are measured as the distribution of $\Delta x G(x)$. Therefore, the step function is distributed as

$$\int_x^\infty dx' \cdot F(x'), \quad (7.9)$$

and they are measured as

$$\int_\infty^x dx' \cdot G(x'). \quad (7.10)$$

Consequently, the gaussian distribution is obtained by differentiating the observed distribution if the round distribution was observed by measuring the step function input. The resolution is defined as σ of the gaussian distribution.

7.3.2 Estimation of the resolution

Fig.7.4 shows the conceptual view of the method to make the step function. If the hit channel of TGC for wire was limited to half, the distribution of the intersection between the reconstructed track and TGC plane becomes step function. The edge corresponds to the border of the limited channel. Fig.7.5 shows the result. Above histogram shows the step function and below shows its differentiation. The differentiation of the histogram was carried out by filling $(N_i - N_{i+1})$ to new one, where N_i is the number of the entry within i th bin. The resolution is obtained $\sigma \sim 6\text{mm}$ by fitting the histogram to gaussian function (red line of Fig. 7.5). This value is thought too large in contrast to the resolution of each tube achieved around $290\mu\text{m}$. Following effects can be causes of deterioration.

- multiple Coulomb scattering,
- miss alignment of TGC,
- miss track selection.

From now on, these items will be investigated.

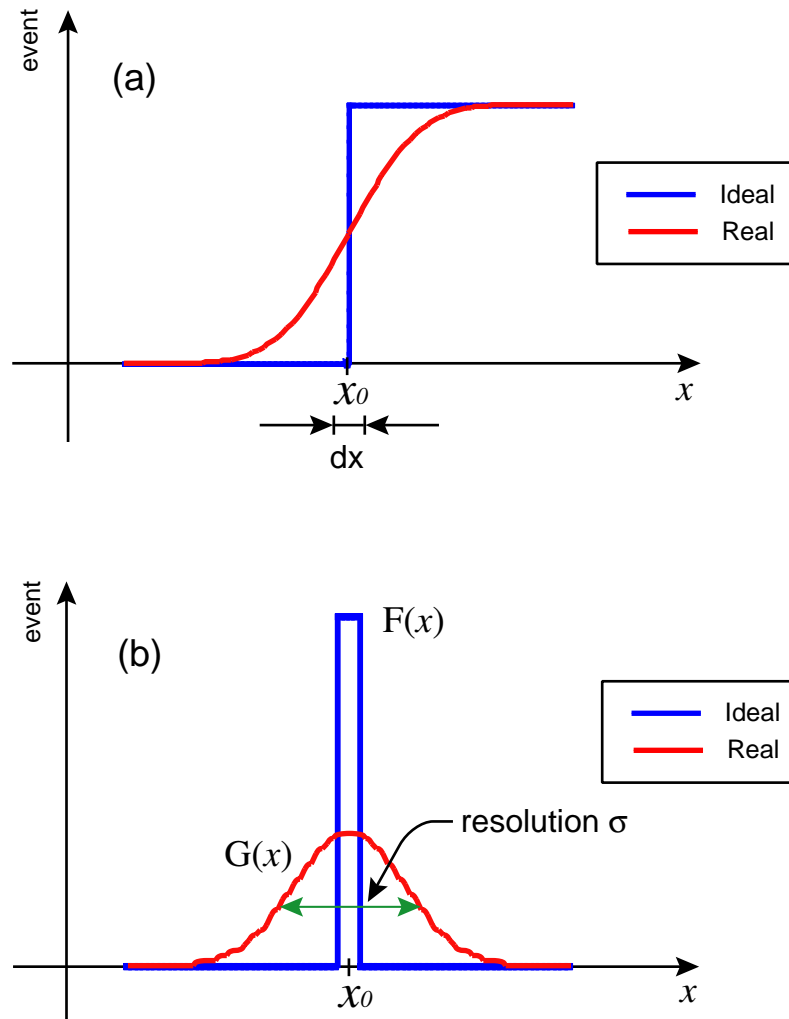


Fig. 7.3: Concept of the Knife-Edge Method.

7.3.3 Multiple Coulomb Scattering

A charged particle traversing a medium is deflected by many small-angle scatters. Most of this deflection is due to Coulomb scattering from nuclei, and hence the effect is called multiple Coulomb scattering (MCS). (However, for hadronic projectiles, the strong interactions also contribute to multiple scattering.) The Coulomb scattering distribution is well represented by the theory of Molière[72]. It is roughly Gaussian for small deflection angles, but at larger angles (greater than a few θ_0 , defined below) it behaves like Rutherford scattering, having larger tails than does a Gaussian distribution.

The root mean square of the projected scattering angle distribution is given by [71]

$$\langle \theta_0 \rangle = \frac{13.6 \text{ MeV}}{\beta c p} z \sqrt{\frac{x}{X_0}} \left[1 + 0.38 \ln\left(\frac{x}{X_0}\right) \right], \quad (7.11)$$

where p , βc , and z are the momentum, velocity, and charge number of the incident particle, and x/X_0 is the thickness of the scattering medium in radiation lengths. There were some materials in the test station; almost all were iron or aluminum, as summarized in Table 7.5.

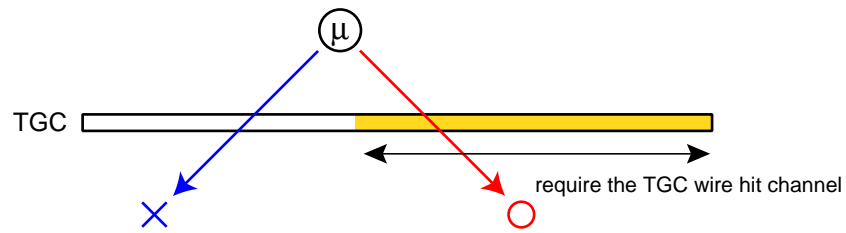


Fig. 7.4: Method to make a step function.

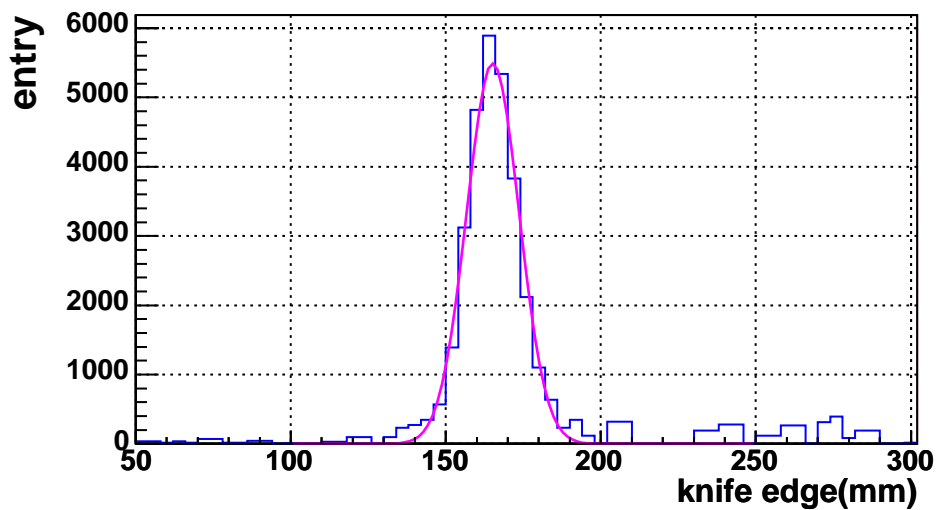
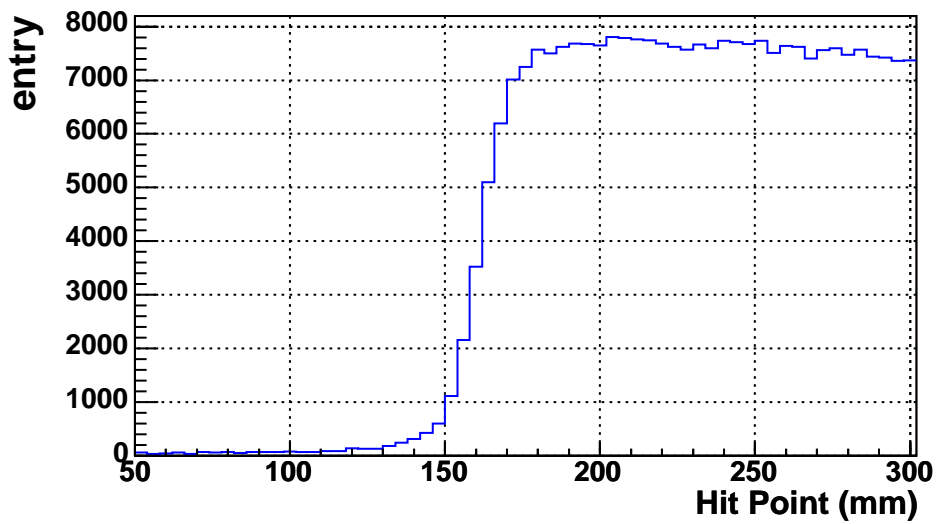


Fig. 7.5: Knife-Edge Method sample. Above shows the distribution of the track obtained from limited TGC channel. Below shows the differentiation distribution of left. The resolution is obtained $\sigma \sim 6\text{mm}$ by fitting to gaussian function (red line).

	X_0 [g/cm ²]	x [g/cm ²]	x/X_0
Al	24.0	103.6	4.3
Fe	13.8	78.7	5.7
Cu	12.9	21.5	1.7
FR4	33.0	13.9	0.4
Air	36.66	0.241	0.007
total			~ 12.1

Table 7.5: Total radiation length of the test station

7.3.4 Dependence on MCS

The influence of MCS by the material of the test station was estimated by Geant4 simulation. Fig.7.6 (a) shows the schematic view of the method of the estimation. Note that this analysis was not carried out by using knife-edge method. The passed positions of the track on the upper and lower super-layer of the drift tube are set to be A and B. A straight line AB corresponding to the reconstruct track is drawn (blue line in Fig.7.6). The line AB intersects the plane of TGC at point C. The point D corresponds to the crossed point of the particle in the simulator. If there was no effect of the MCS, the point C is equaled to the point D. Fig.7.6 (b) shows an example of the distribution of length CD at 4th slot (corresponding to the center of the test station). The energy of muons are generated with the distribution described in section 7.1.1. In order to estimate the contribution of MCS for the resolution, this histogram is fitted with gaussian function. The range of gaussian fitting is set to three times of FWHM. The resolution is defined as the sigma of the gaussian function; $\sigma = 1.07\text{mm}$ in this example. Fig.7.7 shows the resolution as a function of the number of the slot of TGC. The resolution becomes the maximum at slot4, because the influences of the extrapolation error become the maximum at the center of the station. As the result, the resolution was estimated about 1mm in MCS dominant case.

7.3.5 Dependence on the energy of the cosmic ray muon

In order to estimate the energy dependence on the resolution, the muon with constant energy was generated in Geant4. Fig.7.8 shows the resolution as a function of the energy of the generated muon. The energy dependence is clearly seen. The high resolution is obtained for high energy muons, because they are less scattered by MCS. For low energy muons, they are scattered by large angle by the material, especially the iron plate with 9mm thickness placed between the slot-7 TGC and the bottom drift tube super-layers. The resolution of 6mm obtained by the real data is a superimposition of the effect for all energy muons.

7.3.6 Dependence on the alignment of the TGC

In order to confirm the correctness of the TGC alignment information in the analysis program, the resolution was scanned by shifting the TGC z-position. Fig.7.9 and Fig.7.10 show the resolution as a function of z-position of TGC in each slot by using real data and Monte Carlo data respectively. The origin of this graph is equal to the original measured value. By adjusting the z-position so as to minimize the resolution, the resolution becomes 5.18mm in 4th slot (moved -0.2mm from nominal position). Each new z-position is used in the following analysis.

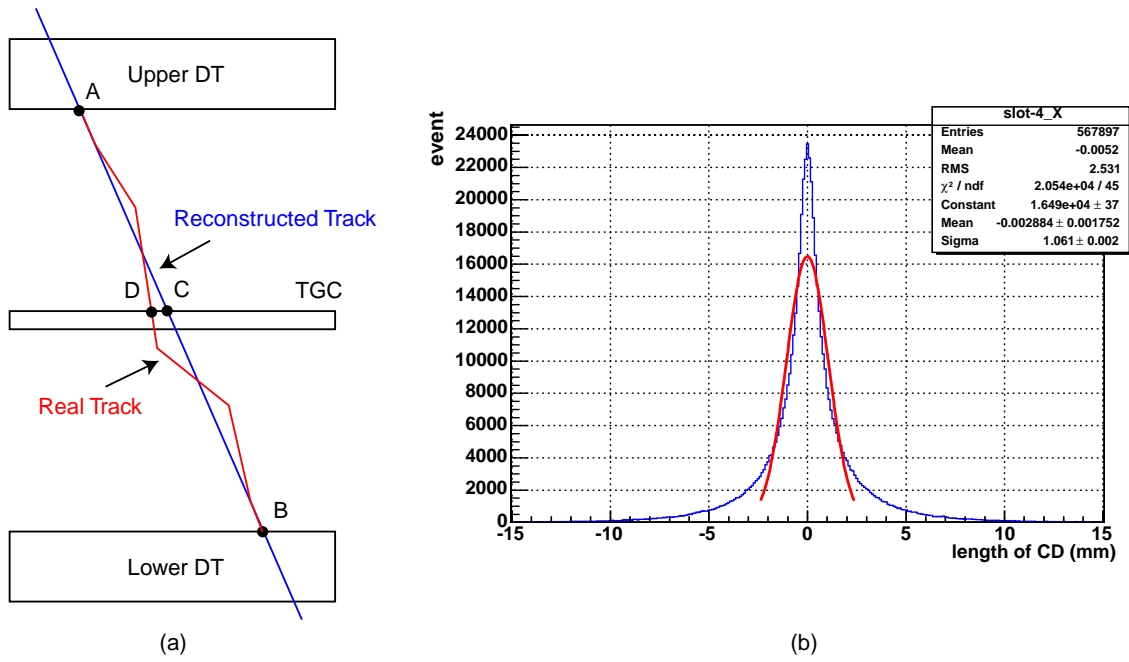


Fig. 7.6: (a) The schematic view of the estimation of MCS dependence. (b) The distribution of the length CD. The resolution is $\sigma = 1.07\text{mm}$ at 4th slot of the test station.

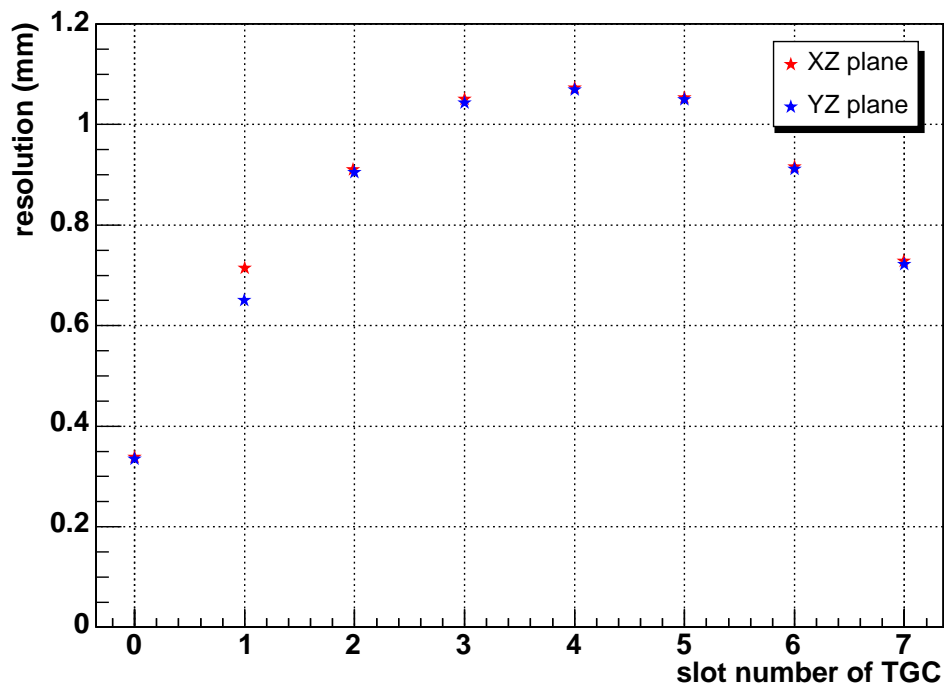


Fig. 7.7: The resolution dependence on slot number of TGC.

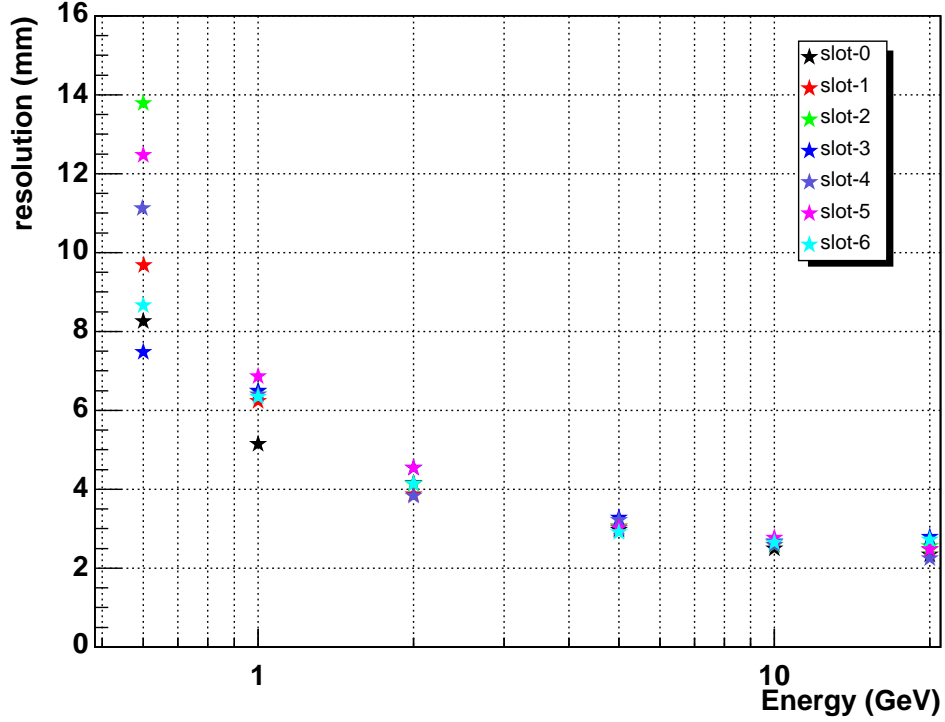


Fig. 7.8: Energy of cosmic ray muon vs resolution

7.3.7 Miss Track Rejection

In this subsection, miss track reconstruction is discussed. Two approaches were performed to reject the following event; noise event and large angle scattered event.

7.3.7.1 χ^2 constraint

As described in section 6.2, the track was reconstructed using the drift circle of top and bottom drift tube. So if either or both of these two tubes were fired by the electric noise or cross-talk, the track is not reconstructed correctly. χ^2 of such events tends to become large because the measured time of them is not correct. In order to estimate the effect of the resolution for large χ^2 value, the resolution was examined by restricting the χ^2 value.

Fig.7.11, Fig.7.12 and Fig.7.13 represent the resolution as a function of the value of restricted χ^2 in only x-z plane, only y-z plane and both x-z and y-z planes respectively. The resolution was improved less than $\chi^2 = 0.2$ because the reconstructed tracks using the incorrect hit events were rejected by this selection cut. The difference between slot-0 and the others is mostly caused from the distance from the drift tube super-layers. The distance between slot-0 and the UpY super-layer is about 20cm, and there are no material excluding air. So there is less extrapolation error for the reconstructed track on slot-0. However, the track reconstruction efficiency was decrease by χ^2 constraint as shown in Fig.7.14. Therefore, χ^2 constraint was not performed for the efficiency measurement for TGC.

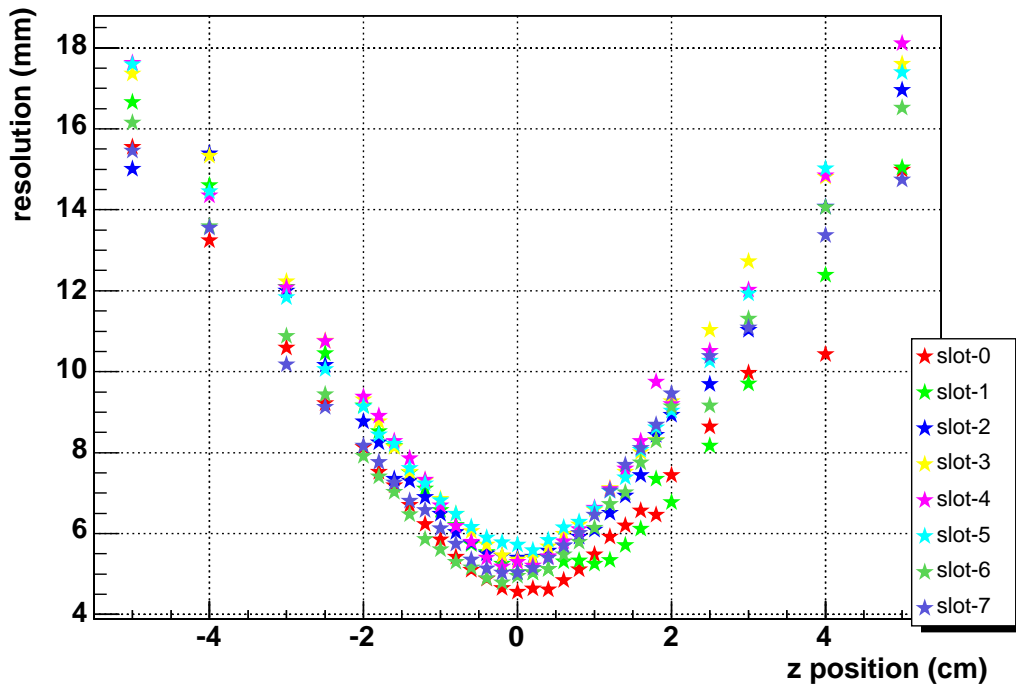


Fig. 7.9: The resolution as a function of z-position of TGC.

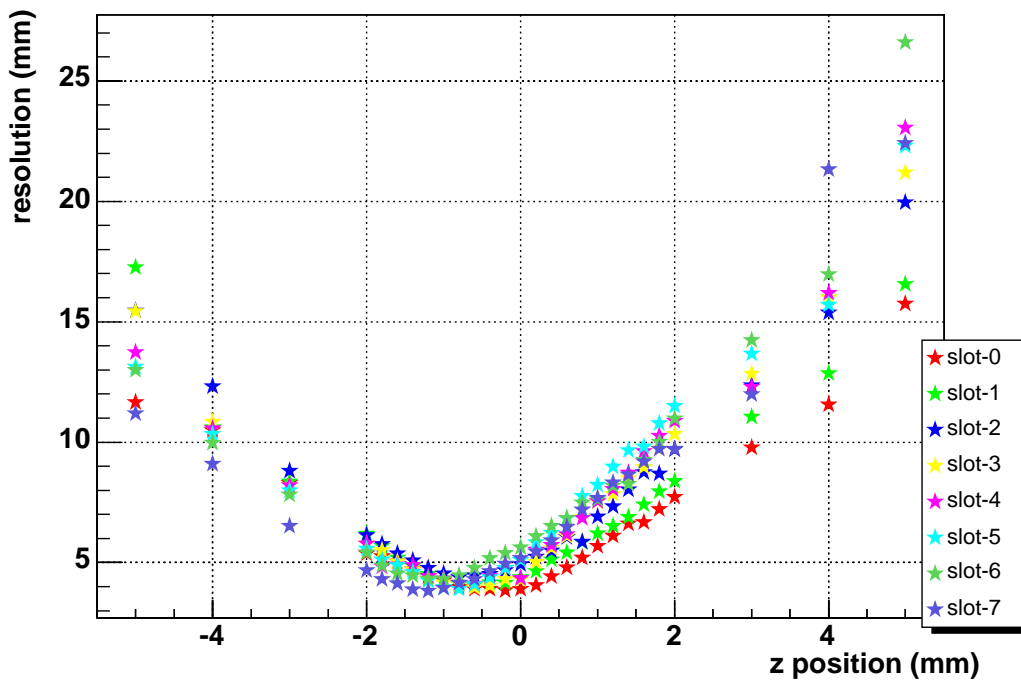


Fig. 7.10: Z direction scan (simulation).

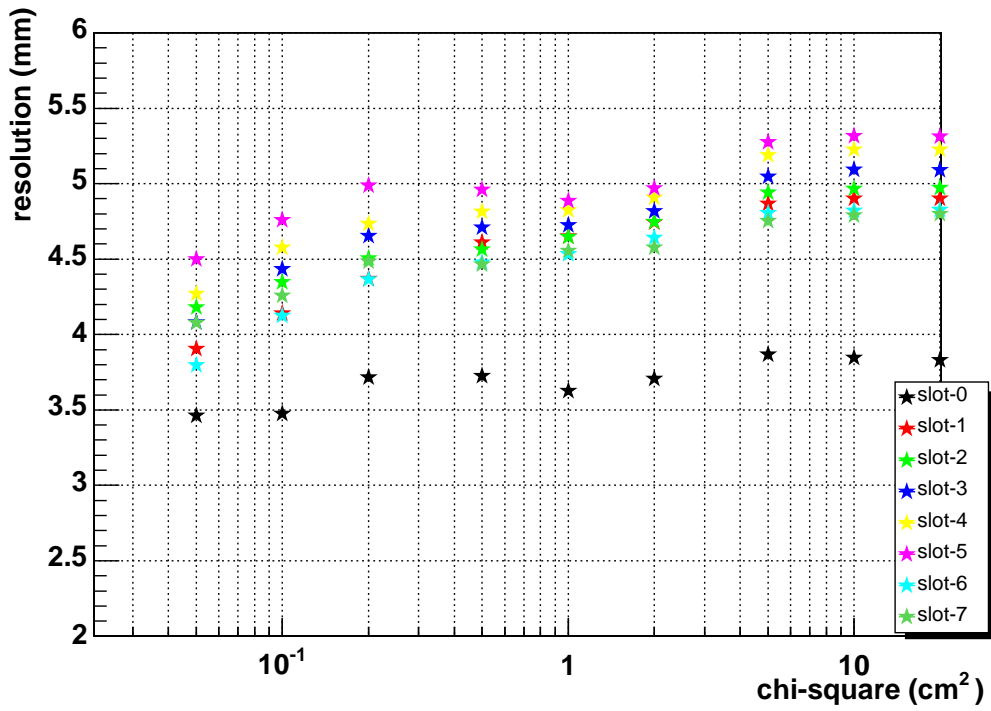


Fig. 7.11: The resolution as a function of the χ^2 cut (restricted in only xz plane).

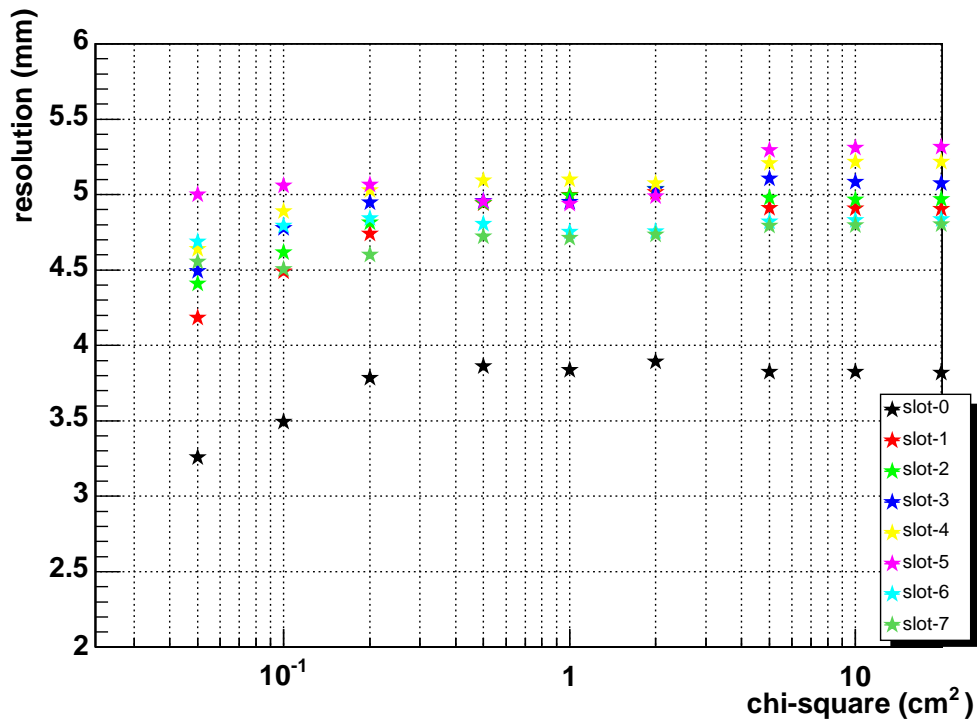


Fig. 7.12: The resolution as a function of the χ^2 cut (restricted in only yz plane).

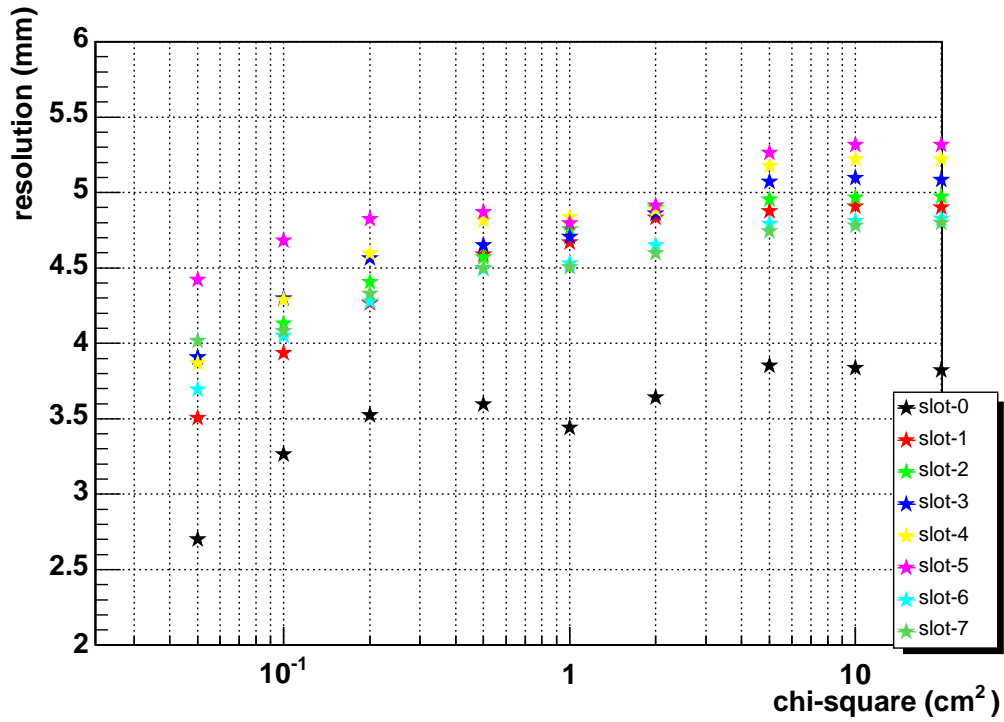


Fig. 7.13: The resolution as a function of the χ^2 cut (restricted in both xz and yz plane).

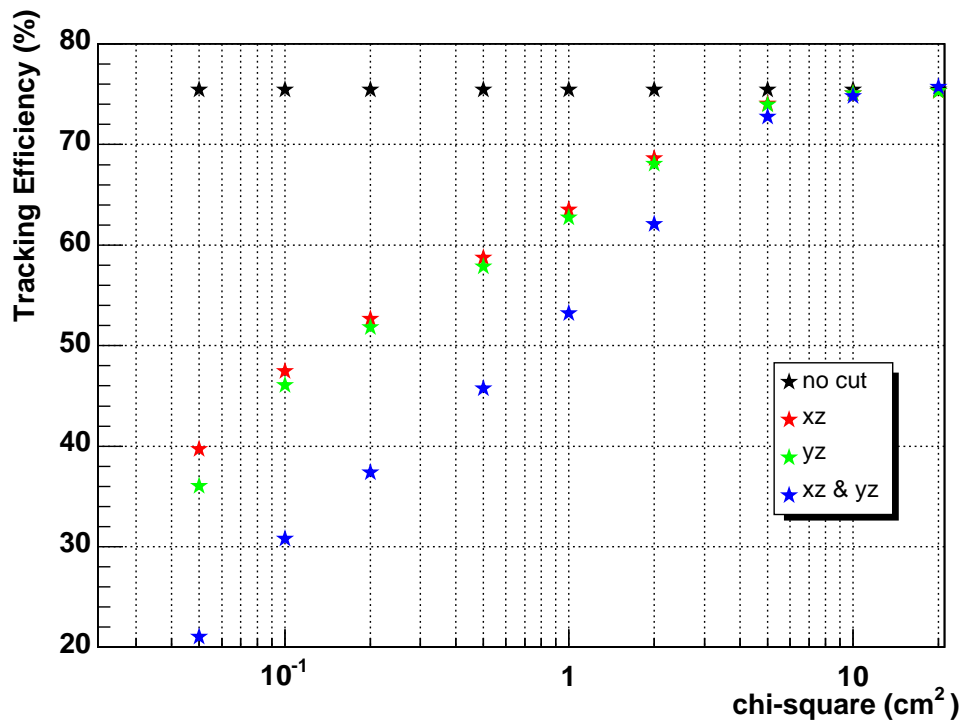


Fig. 7.14: The track reconstruction efficiency as a function of the χ^2 cut.

7.3.7.2 angle constraint

In order to reduce the large scattered event by MCS, the angle α between the tracks determined by using the top and bottom super-layer separately was examined. Fig.7.15 shows the distribution of the α using real data and Fig.7.16 shows that using Monte Carlo data. In both figures, the left histogram indicates the distribution in x-z plane and the right indicates that in y-z plane. These distributions have two peaks and long tail. One peak around $\alpha = 60^\circ$ is due to the uncertainty of the track selection from left-right ambiguity. Fig.7.17 shows the schematic view of this ambiguity. In this track reconstruction algorithm, these two lines could not be distinguished. If this ambiguity was occurred in both top and bottom super-layers, the angle α became near 0° or 60° .

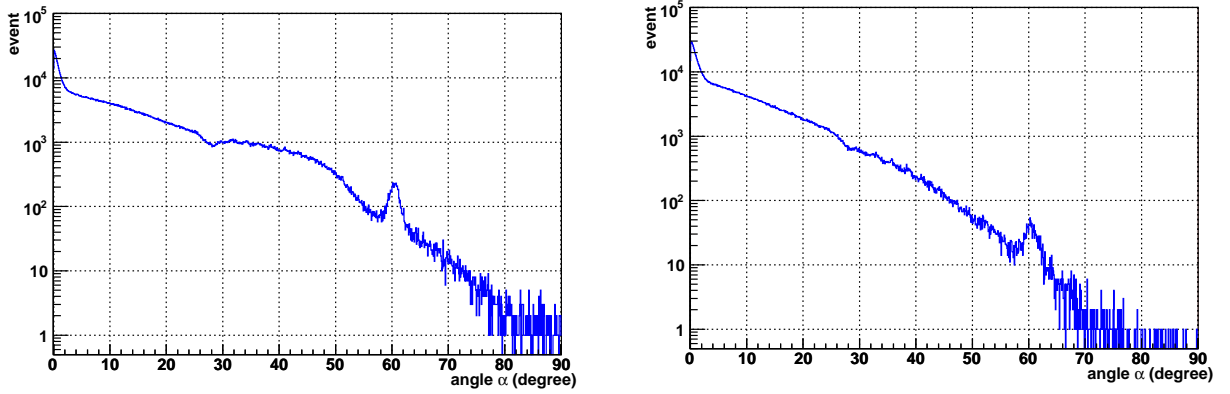


Fig. 7.15: Angle distribution between 2 lines that decided by Up and Down super-layer. (real data)

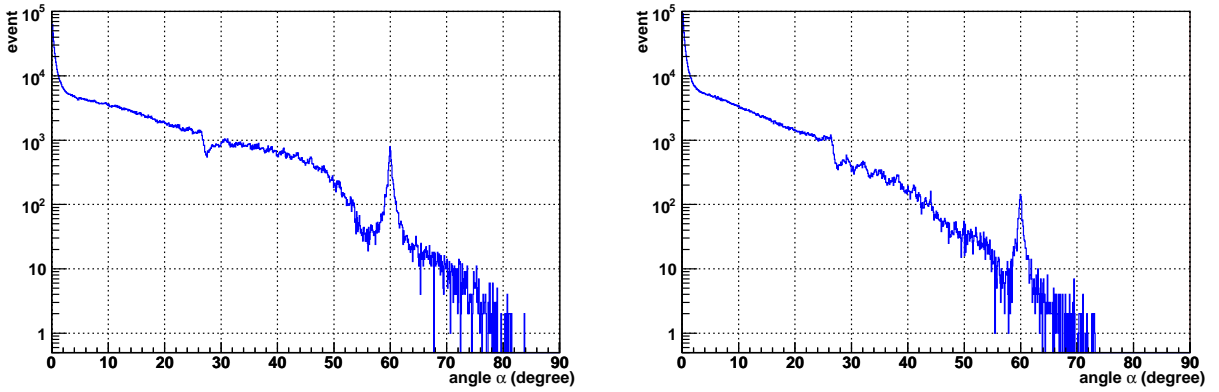


Fig. 7.16: Angle distribution between 2 lines that decided by Up and Down super-layer. (simulation data)

If the incoming muon was scattered by large angle by MCS, the passing point was different from the point extrapolated the initial trajectory. The difference x on the ground was estimated by the following relation;

$$\begin{aligned}
 x &= \frac{d}{\tan(\pi - (\pi/2 - \theta + \phi))} + \frac{d}{\tan(\pi/2 - \phi)} \\
 &= d(\tan \phi - \tan(\phi - \theta)),
 \end{aligned} \tag{7.12}$$

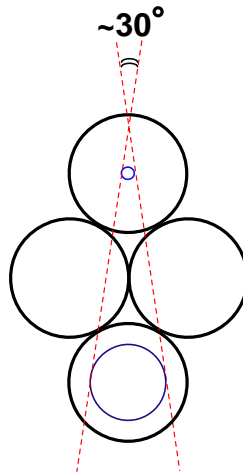


Fig. 7.17: Left-Right ambiguity in track reconstruction.

where d is the distance between the scattered point and the ground, ϕ is the incident zenith angle and θ is scattered angle. For example, if a muon with $\theta = 30^\circ$ is scattered by $\phi = 5^\circ$ at $d = 600\text{mm}$, x is calculated as 66.6mm . This result corresponds to the diameter of one or two tubes.

Fig.7.18 shows the position distribution for the event which have more than 5° scattered steps in the Geant4 (for x-z plane). As these figures shown, many muons are scattered at the steel plate with 9mm thickness and the steel H beams at 600mm from the ground. Fig7.19 shows the ratio of triggered event with large scattered steps as a function of each material name. We found most of the muons were scattered at steel structure.

7.3.7.3 χ^2 and angle constraint

Fig.7.20 and Fig.7.21 show the scatter plots of χ^2 and angle α for real data and Monte Carlo data respectively (1.5M event sample). The difference between these plots is mainly based on the noise and cross talk event. The positive correlation is clearly seen on both plots.

Fig.7.22 shows the resolution as a function of the χ^2 with some angle α constraint . There is little difference on the resolution for slot-0 whether the cut is performed or not. We found, however, that for slot-4 becomes good by restricting χ^2 and α .

7.3.8 Conclusion for Tracking Resolution

In conclusion for the analysis of tracking resolution, the cause for the tracking resolution of 6mm is the following;

1. the miss track reconstruction by the noise and/or cross-talk
2. the extrapolation error for the large scattered event by MCS.

By restricting the χ^2 and scattered angle α , we found the resolution could be improved up to 4mm. However, these constraints were not performed because the efficiency of track reconstruction became low and the support structure of TGC could be clearly seen in the efficiency map.

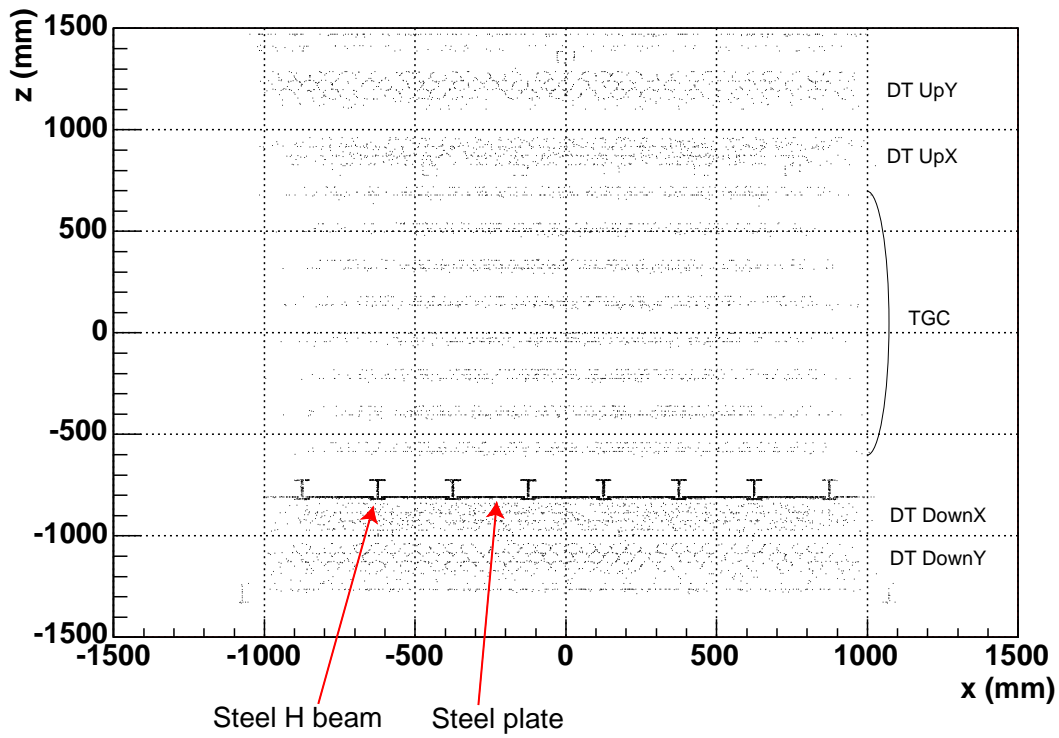


Fig. 7.18: Position dependence of large scattered step in Geant4 (x-z plane).

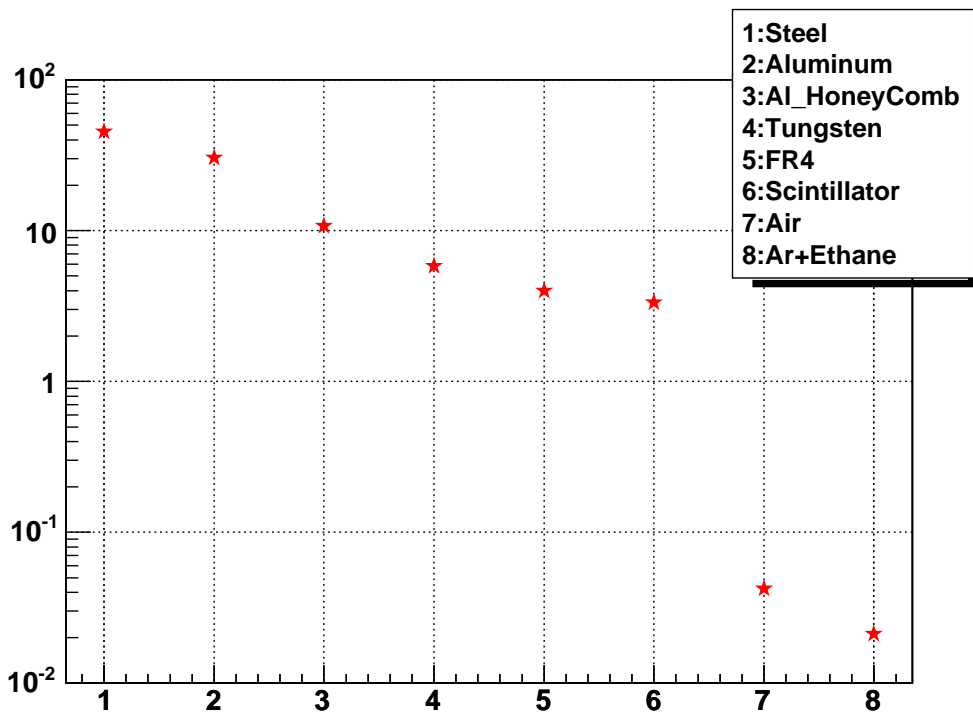
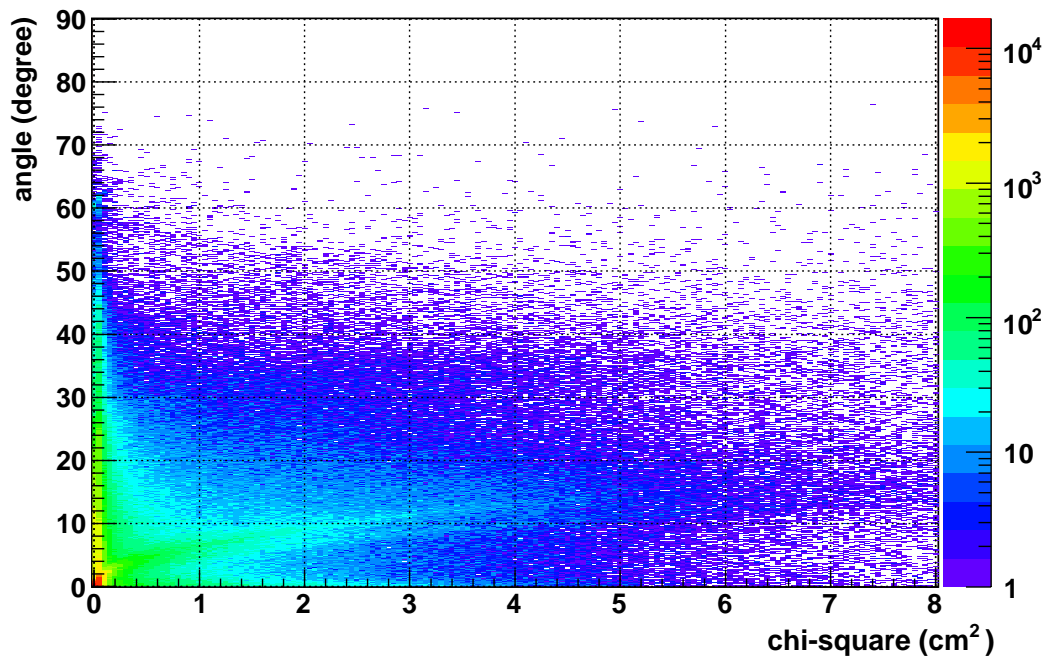
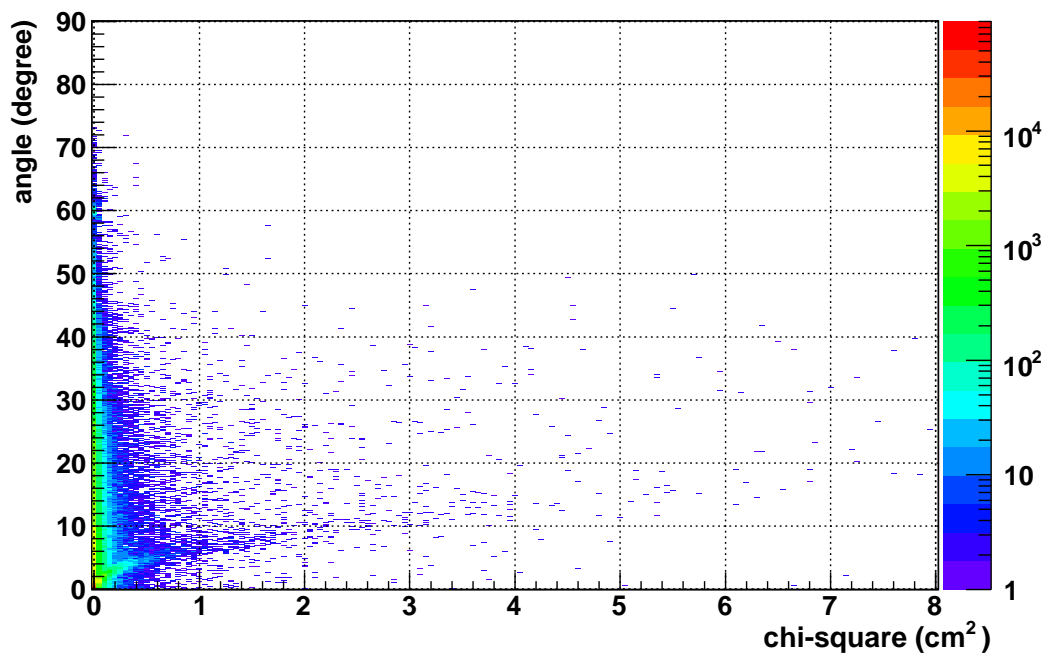


Fig. 7.19: The ratio of triggered event with large scattered step as a function of each material name.

Fig. 7.20: χ^2 vs angle scatter plot. (real data)Fig. 7.21: χ^2 vs angle scatter plot. (simulation data)

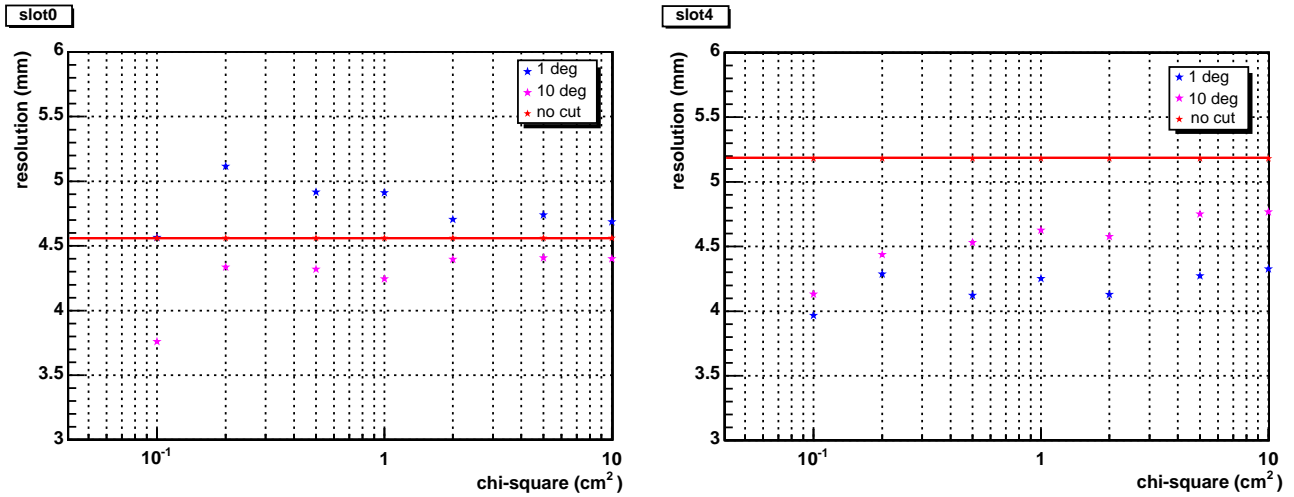


Fig. 7.22: The resolution as a function of chi-cut.

7.4 Inspection Progress

Fig.7.23 shows the progress of each test procedure. Three plateau regions indicate the period of the system modification described in section5.8. The detail inspection period of each type are summarized in Table.7.6. Comparing with Table.4.4, the requirement was satisfied. Table.7.7 is the summary of the average test week. Fig.7.24, Fig.7.25 and Fig.7.26 show the histogram of the test day for Leak Test, HV Test and Cosmic ray Test, respectively.

TGC Type	Inspection Period	month
T7 Triplet	May. 2002 to May. 2003	13
T7 Doublet	Jun. 2003 to Feb. 2004	9
T7D \rightarrow T4D	Mar. 2003 to Apr. 2004	2
T4 Doublet	May. 2004 to Nov. 2004	7
T5 Doublet & spare	Dec. 2004 to Jul. 2005	8

Table 7.6: Summary of inspection period.

Type	Leak	HV	Cosmic
T7 Triplet	1.81	2.04	1.92
T7 Doublet	5.05	5.82	6.38
T4 Doublet	3.18	3.28	4.04
T5 Doublet	4.1	4.19	4.96

Table 7.7: The average week of each test. (unit: module/week)

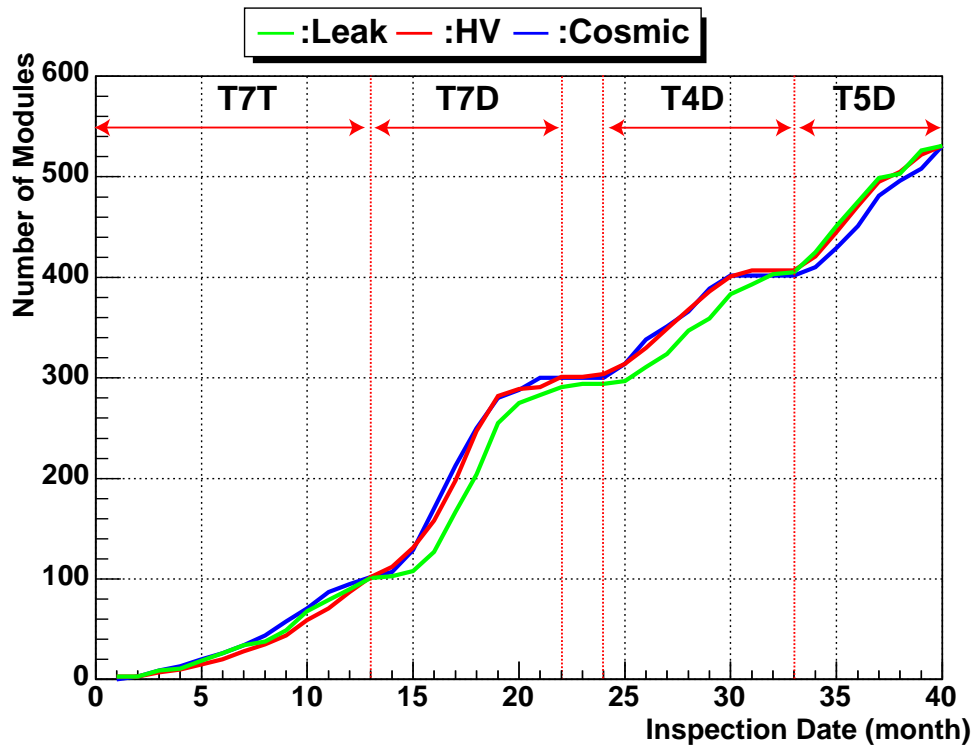


Fig. 7.23: The progress of the Inspection

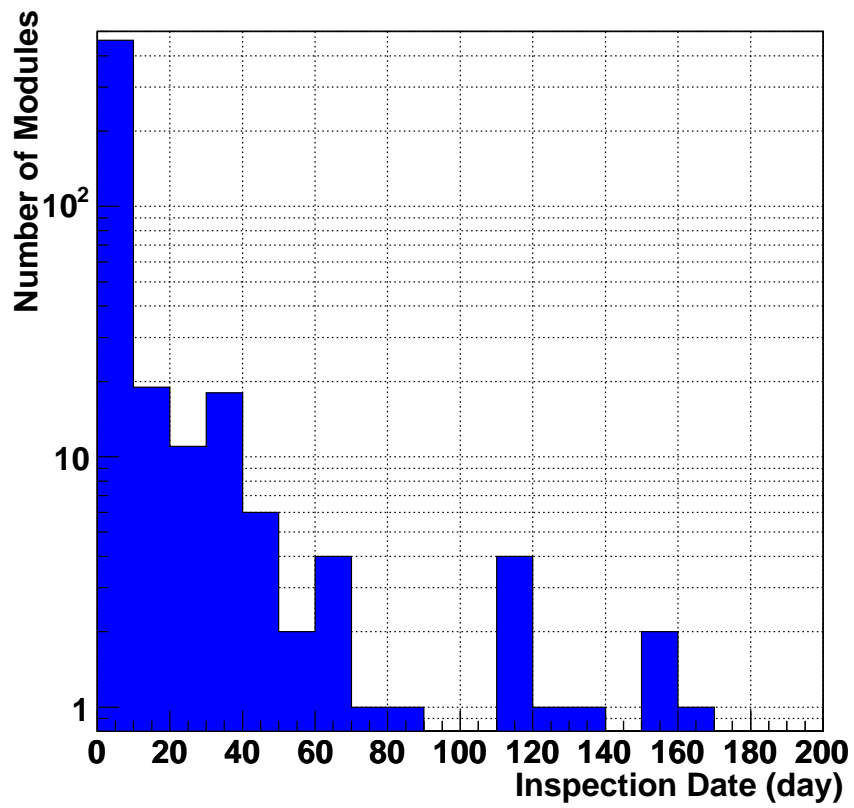


Fig. 7.24: The progress of the Leak Test

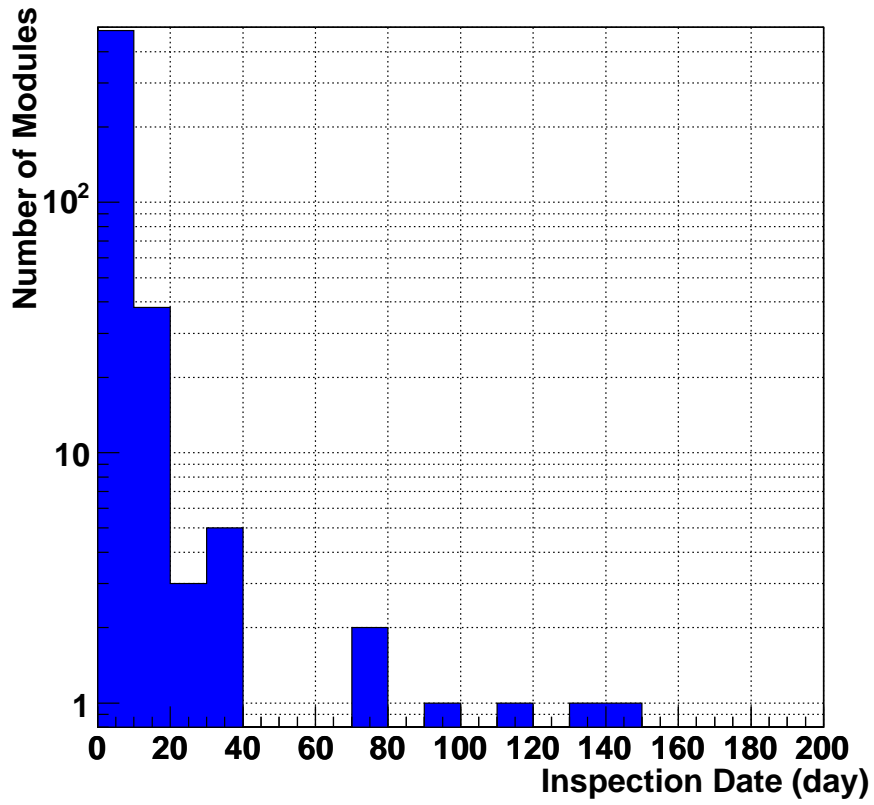


Fig. 7.25: The progress of the HV Test

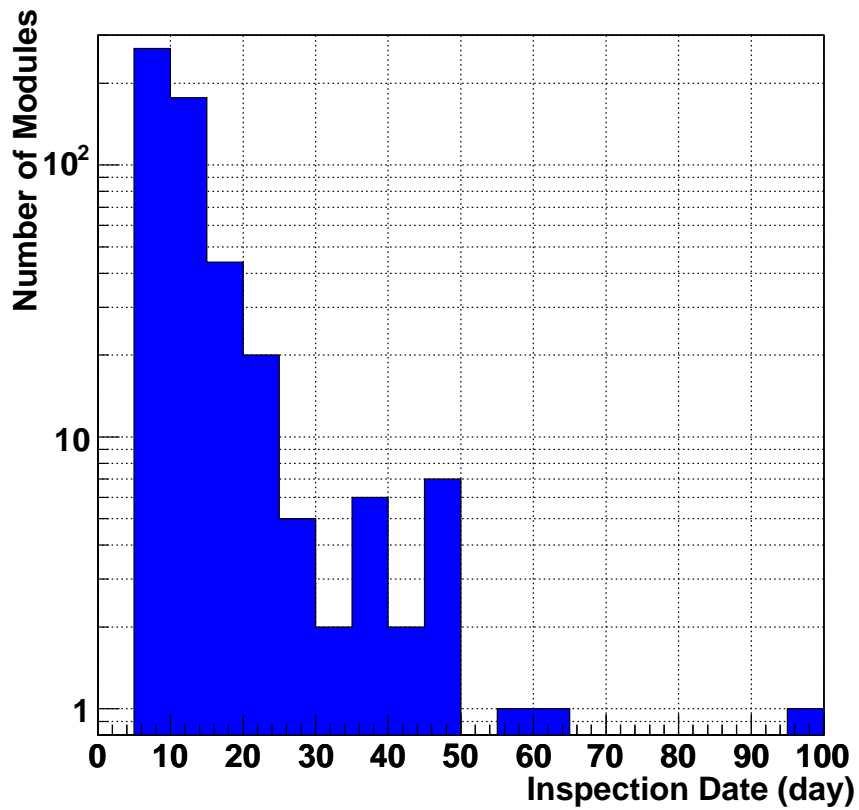


Fig. 7.26: The progress of the Cosmic Ray Test

8 Quality of the TGCs

In this chapter, the quality of the TGC produced in Japan is described; especially the detection efficiency is described. Tabel.8.1 shows the summary of the inspection. The result for Leak Test and HV Test was described in section5.2 and 5.3.6 respectively.

Type	Production	Gas Tightness	Leakage	HV	HV Short	Cosmic OK	low eff
T7T	113	112	1	111	1	99	12
T7D4	106	106	0	106	0	106	0
T7D6	109	109	0	106	3	106	0
T4	107	105	2	104	1	104	0
T5	107	106	1	105	1	105	0
Total	542	538	4	532	6	520	12

Table 8.1: Summary of the inspection.

8.1 Efficiency

Fig.8.1 shows the distribution of the efficiency value for all 2239 measured maps. From Fig.8.2 to Fig.8.6 show the distribution of the efficiency for each type. Red chart indicates the efficiency for wire, and blue indicates for strip. All chambers except 12 modules have more than 95% efficiency excluding the area of the support structure. Fig.8.7 is an example of a bad chamber with locally inefficient regions. These chambers were produced in relatively early period of the series production. The reason could be a gluing-off or applying thicker glue during the triplet assembly. This could be a result of failure in the viscosity control of the epoxy adhesive. We found the cause of low efficiency was bad flatness of the chamber due to the distortion of itself.

- A: All of the efficiency are more than 99%.
- B: One or more efficiency are from 98% to 99%.
- C: One or more efficiency are from 95% to 98%.
- D: One or more efficiency are below 95%.
- E: One or more efficiency are locally low.

rank	T7T	T7D4	T7D6	T4	T5
A	78	97	96	94	97
B	8	1	2	7	5
C	11	7	5	1	1
D	2	1	3	2	2
E	12	0	0	0	0
sum	111	106	106	104	105

Table 8.2: Rank of the modules ordered by efficiency value.

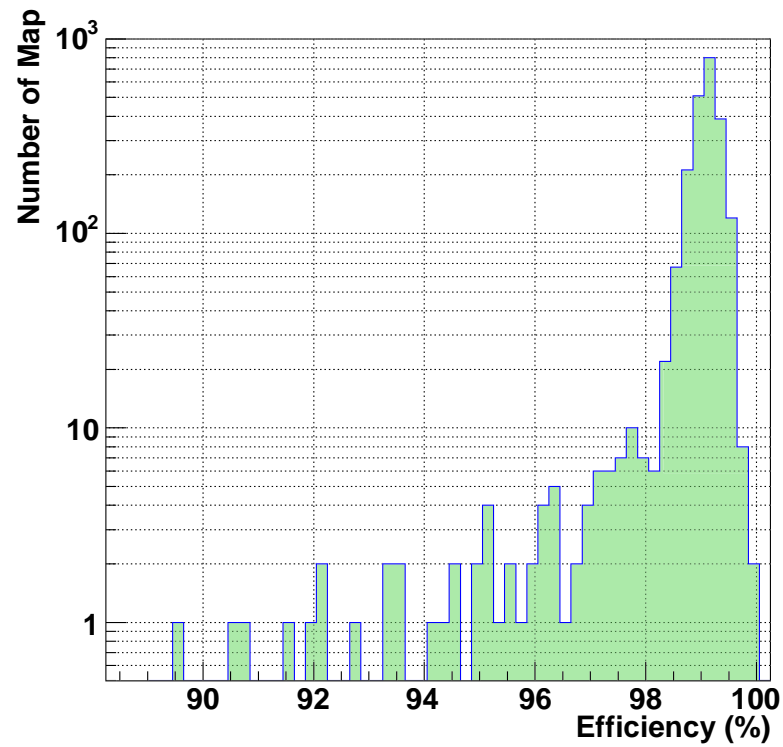


Fig. 8.1: Histogram of Efficiency for all chambers.

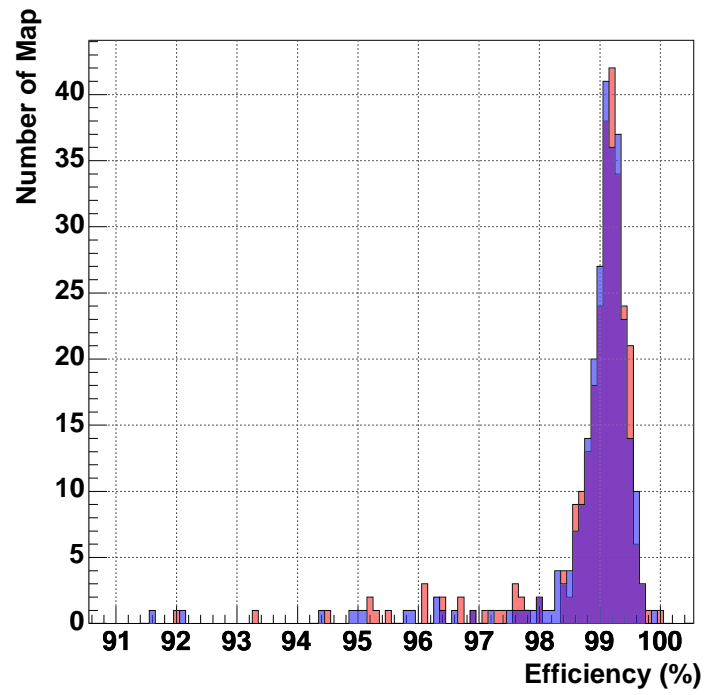


Fig. 8.2: Histogram of Efficiency for T7 Triplet

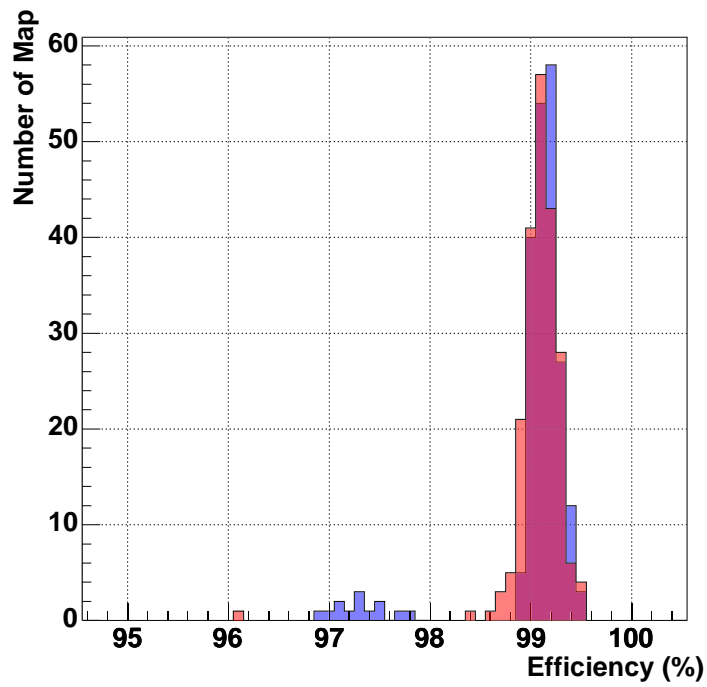


Fig. 8.3: Histogram of Efficiency for T7 Doublet (D4 type)

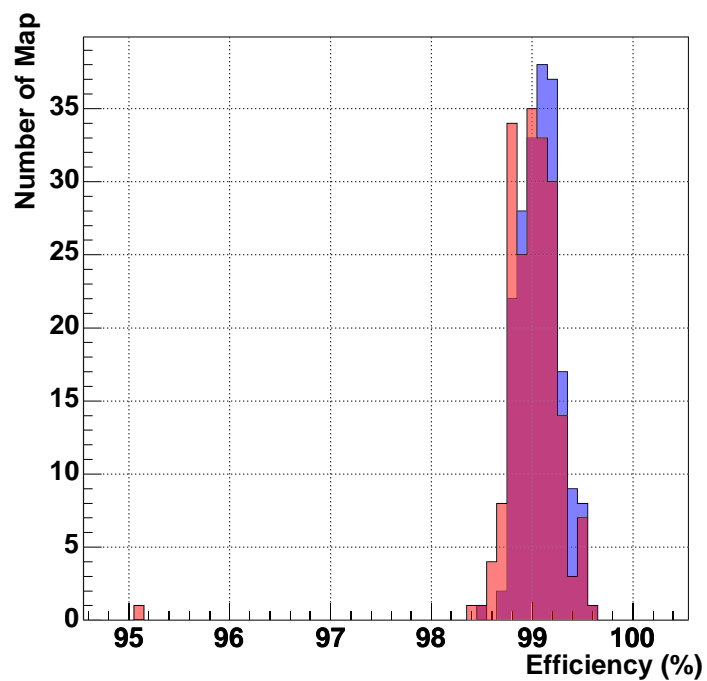


Fig. 8.4: Histogram of Efficiency for T7 Doublet (D6 type)

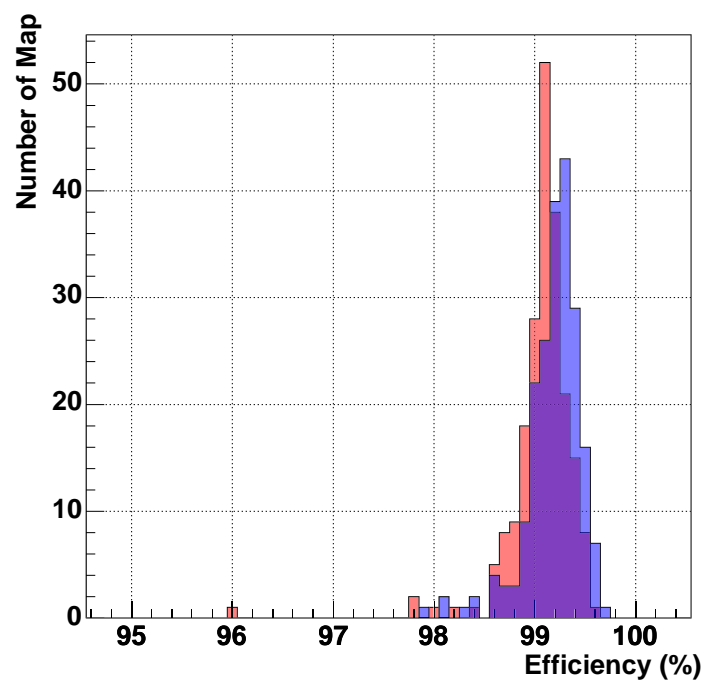


Fig. 8.5: Histogram of Efficiency for T4 Doublet

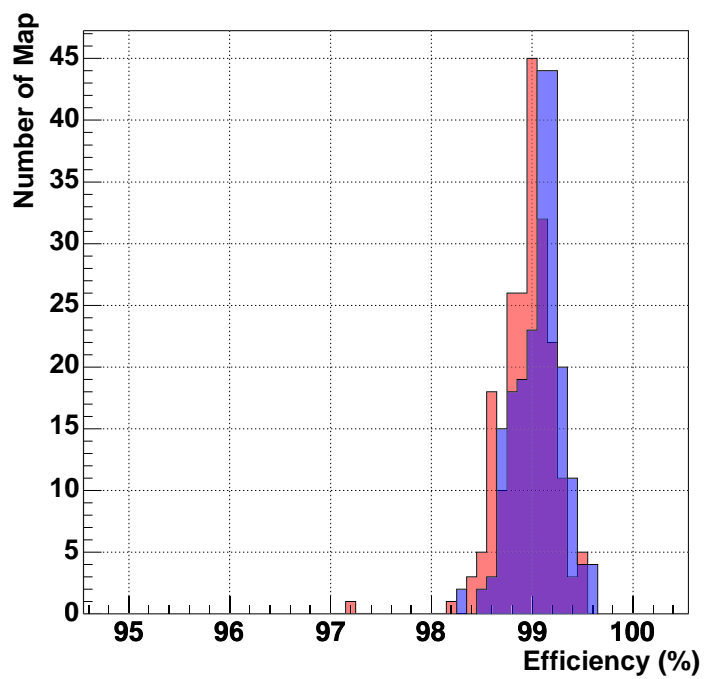


Fig. 8.6: Histogram of Efficiency for T5 Doublet

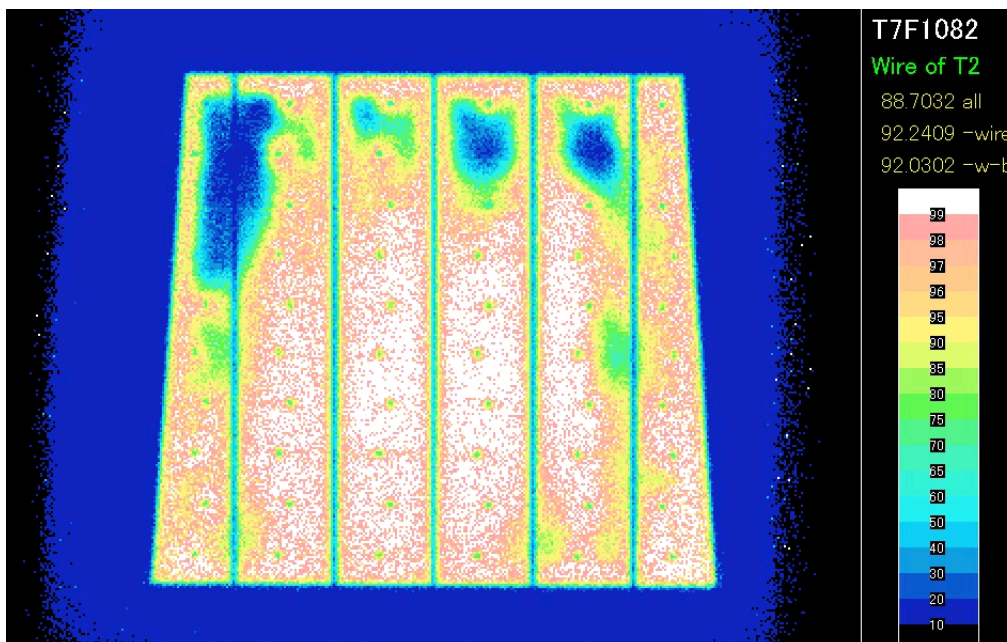


Fig. 8.7: Bad example of efficiency map.

9 Summary

Thin gap chamber modules giving function of the end cap muon trigger to the ATLAS detector in the LHC experiment have been constructed at High Energy Research Organization (KEK) in Japan. They have been tested in their performances at Kobe University.

The following three inspections were carried out;

(1) CosmicRay Test

It is necessary to inspect the uniformity of efficiency over all detection area. Detection efficiency is required more than 99% by excluding the inefficient area. Signal response is less than 25nsec for bunch identification. These characteristics were confirmed by using the cosmic rays muon.

(2) High Voltage Test

This process was the first test for TGC to flow the mixed gas ($\text{CO}_2 + \text{n-pentane} = 55 : 45$) and apply the positive high voltage (HV) of 3.1kV. The stability of the chamber was checked by measuring current of chamber with mixed gas. In this process, unstable chamber can be found by applying HV for a long time and monitoring the current.

(3) Leak Test

In order to measure leakage from a chamber, we applied pressure to the gas volume. However the chamber can be damaged due to over-pressure because the chamber is manufactured only by gluing its parts and is fragile with respect to inner pressure - the maximum pressure allowed to 600Pa.

The inspection of 542 TGC modules produced in KEK was started from May 2002 and was finished in July 2005. Out of them, 531 modules were satisfied the requirements and were shipped to CERN. From this study, all TGCs shipped to CERN are assured for endcap muon trigger chambers in ATLAS experiment.

Appendix

Gas Chromatography

A gas chromatograph (GC) is a chemical analysis instrument for identifying ingredients in a sample. A GC uses a thin capillary fiber known as the column, through which different chemicals pass at different rates depending on their chemical and physical properties. As the chemicals exit from the end of the column, they are detected. The function of the column is to separate and concentrate different components in order to maximize the detection signal.

Fig.9.1 shows the schematic view of a GC. In a GC analysis, a known volume of gaseous analyte¹ is injected into the entrance of the column. We used the constant volume of the SUS tube as a gas sampler ($\phi 6\text{mm} \times 8\text{cm}$). Although the carrier gas sweeps the analyte molecules through the column, this motion is inhibited by the adsorption of the analyte molecules either onto the column walls or onto packing materials in the column. The rate at which the molecules progress along the column depends on the strength of adsorption, which in turn depends on the type of molecule and on the column materials. Since each type of molecule has a different rate of progression, the various components of the analyte mixture are separated as they progress along the column and reach the end of the column at different times. A detector is used to monitor the outlet stream from the column; thus, the time at which each component reaches the outlet and the amount of that component can be determined. Generally, substances are identified by the order in which they emerge from the column and by the residence time of the analyte in the column.

Packed columns contain a finely divided, inert, solid support material (eg. diatomaceous earth) coated with a liquid or solid stationary phase. The nature of the coating material determines what type of materials will be most strongly adsorbed. Thus numerous columns are available that are designed to separate specific types of compounds. Most packed columns are 1.5 - 10m in length and have an internal diameter of 2 - 4mm. The outer tubing is usually made of stainless steel or glass.

Because molecular adsorption and the rate of progression along the column depend on the temperature, the column temperature is carefully controlled for precise work. Reducing the temperature produces the greatest level of separation, but can result in very long elution times.

A number of detectors are used in gas chromatography. The most common one is the thermal conductivity detector (TCD), which monitors changes in the thermal conductivity of the effluent. The main advantage of the TCD is that it can detect any substance (except the carrier gas). Some of the other detectors are sensitive only to specific types of substances.

Fig.9.2 shows a sample of the output voltage from TCD analyzing the mixed gas for TGC (CO_2 + n-pentane). A column of VZ-7 with $1/4$ " \times 6m SUS tube was used. The temperature of the column oven was set at 30°C. In VZ-7, the retention time for CO_2 is shorter than that for n-pentane. Therefore, the peak for CO_2 was detected at first.

¹Analyte is the substance or chemical constituent that is undergoing analysis.

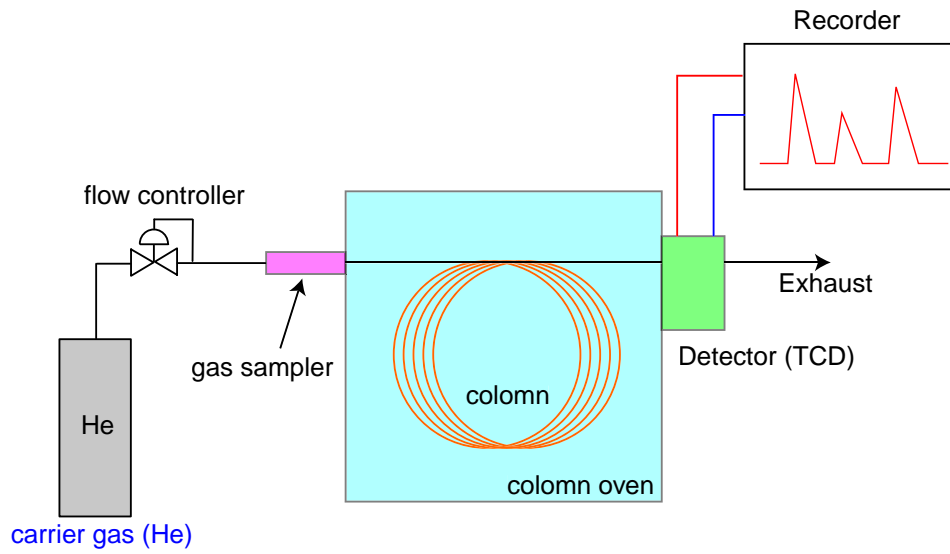


Fig. 9.1: Schematic view of a gas chromatography.

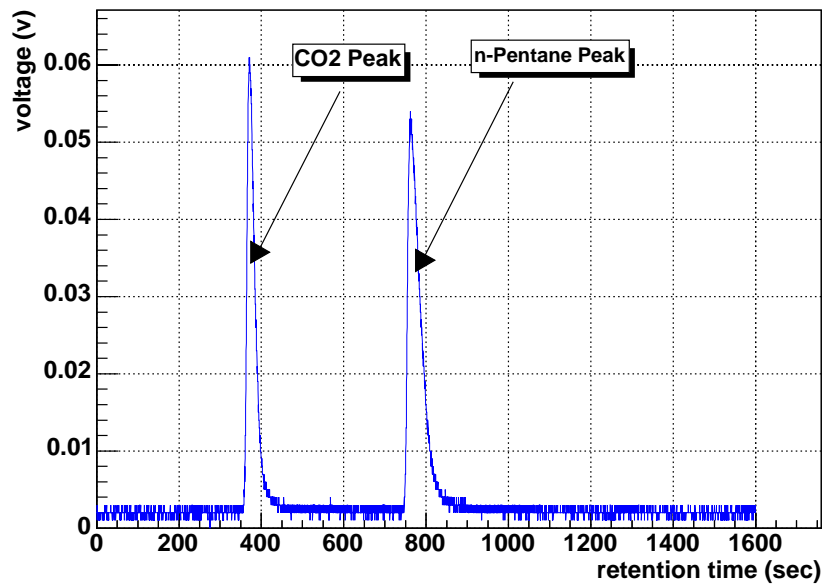


Fig. 9.2: The output from the gas chromatogram analyzing mixed gas ($CO_2 + n\text{-Pentane} = 55\ 45$)

Acknowledgement

I am deeply grateful to Prof. Hiroshi Takeda and Prof. Hisaya Kurashige for their guidance and encouragements in this work. This thesis would not be completed without their supports.

I would like to thank Prof. Mitsuaki Nozaki, Prof. Kiyoto Kawagoe, Prof. Yasuhiro Homma and Dr. Atsuhiko Ochi for the helpful advice of the development of the inspection system.

I sincerely thank Dr. Koji Ishii (KEK) for his continuous discussions and encouragements. I also deeply thank Dr. Shuji Tanaka (KEK) who taught me the various knowledge and technique for developing the system. I thank Dr. Masaya Ishino(ICEPP) who helped me to stay in CERN. I appreciate Prof. Hiroyuki Iwasaki (KEK), Prof. Tomio Kobayashi (ICEPP), Prof. Tasuo Kawamoto (ICEPP), Prof. Tohru Takeshita(Shinshu University), Dr. Chiaki Yokoyama(ICRR) for their kind advice. I would like to thank Mr. Hidetoshi Oshita for his encouragement. I appreciate my all collaborators.

Finally, I thank my family and Keiko for their kind support and encouragement.

Reference

- [1] S.Weinberg, Phys. Rev. Lett. **19** (1967) 1264
- [2] A.Salam, *Elementary Particle Theory*, ed. N.Svartholm (Almqvist and Wiksells, Stockholm, 1968) 367
- [3] S.L.Glashow, J.Iliopoulos and L.Maiani, Phys. Rev. **D2** (1970) 1285
- [4] P.W. Higgs, Broken symmetries, massless particles and gauge fields, Phys. Lett. **12** (1964) 132-133.
- [5] P. W. Higgs, Spontaneous symmetry breakdown without massless bosons, Phys. Rev. **145** (1966) 1156-1163.
- [6] P. W. Higgs, Broken symmetries and the masses of gauge bosons, Phys. Rev. Lett. **13** (1964) 508-509.
- [7] LEP Collaborations and LEP Electroweak Working Group, A Combination of Preliminary Electroweak Measurements and Constraints on the Standard Model, LEPEWWG/2005-01, hep-ex/0511027, 9 November 2005
- [8] R.K.Ellis and S.Veseli, Phys. Rev. **D60** (1999) 011501.
- [9] H.Georgi, S.Glashow, M.Machacek, and D.V.Napnoulos, Phys. Rev. Lett. **40** (1978) 692.
- [10] A.Djouadi, M.Spira, and P.M.Zerwas, Phys. Lett. B264 440 (1991); S. Dawson, Nucl. Phys. **B359** (1991) 283.
- [11] CERN Public home ,<http://public.web.cern.ch/public/>
- [12] ATLAS Technical Proporsal for a General-Purpose pp Experiment at the Large Hadron Collider at CERN, CERN/LHCC/94-43 LHCC/P2 (1994)
- [13] ATLAS Collaboration, Muon Spectrometer Technical Design Report, CERN/LHCC 97-22 (1997).
- [14] ATLAS Collaboration, ATLAS DETECTOR AND PHYSICS PERFORMANCE Technical Design Report Volume I, CERN/LHCC/99-14 ATLAS TDR (1999)
- [15] ATLAS Collaboration, ATLAS DETECTOR AND PHYSICS PERFORMANCE Technical Design Report Volume II, CERN/LHCC/99-15 ATLAS TDR (1999)
- [16] M.Spira and P.M.Zerwars, Electroweak Symmetry Breaking and Higgs Physics, hep-ph/9803257 (1997)
- [17] J.F.de Troconiz and F.J.Yndurain, Phys. Rev. **D71** (2005) 073008.

- [18] S.Asai et al., Prospects for the Search for a Standard Model Higgs Boson in ATLAS using Vector Boson Fusion, *Eur. Phys. J.* **C32S2** (2004) 19-54
- [19] LHC Design Report, CERN/-2004-003, 4 June 2004.
- [20] ATLAS Collaboration, ATLAS Level1 Trigger Technical Design Report, ATLAS TDR-12 (1998)
- [21] ATLAS Collaboration, ATLAS Trigger Performance Status Report, CERN/LHCC 98-15 (1998)
- [22] ATLAS Muon Spectrometer, Thin Gap Chamber Gas System Safety Report, TGC-002-98 ATLAS TGC Collaboration (1 Jan 1999)
- [23] R. L. GLUCKSTERN, UNCERTAINTIES IN TRACK MOMENTUM AND DIRECTION, DUE TO MULTIPLE SCATTERING AND MEASUREMENT ERRORS, *Nucl. Instrum. Methods* **24** (1963) 381-389
- [24] ATLAS Public page, <http://atlas.web.cern.ch/Atlas/index.html>
- [25] M.Aleksa and W.Riegler, Non-Linear MDT Drift Gases like Ar/CO₂, ATLAS Internal Note (1998)
- [26] G.Avolio et al., Test of the first BIL tracking chamber for the ATLAS muon spectrometer, *Nucl. Instrum. Methods* **A523** (2004) 309-322
- [27] H.A.Bethe, *Annalen d. Physik* **5** (1930) 413.
- [28] H.A.Bethe, *Z. Physik.* **76** (1932) 293.
- [29] H.A.Bethe, *Hdb. Physik.* **24** (1933) 518.
- [30] L.D.Landau, *J. Exp. Phys. (USSR)* **8** (1944) 201.
- [31] J.S.Townsend, *Electricity in Gases*, Oxford 315 (1915).
- [32] G.Charpak et al., *Nucl. Instrum. Methods* **62**, 262 (1968).
- [33] G.Charpak, *Filet à Particules*, Découverte (1972).
- [34] F.Sauli, Principles of Operation of Multiwire Proportional and Drift Chambers, CERN Yellow report **CERN 77-09** (1977).
- [35] A. Peisert, F. Sauli, Drift and diffusion in gases, CERN Internal Report (1994) 84-08.
- [36] R.Veenhof, GARFIELD program: simulation of gaseous detectors, version 6.32, CERN Program Library Pool W999 (W5050).
- [37] O.Jinnouchi, O.Sasaki, Study on muon level-1 trigger scheme for TGC, Atlas Internal Note DAQ-No-082 (1998).
- [38] R.I.Shoen, Absorption, ionization and ion-fragmentation cross-section of hydrocarbon vapors under vacuum-ultraviolet radiation, *J.Chem.Phys* **17** (1962) 2032
- [39] S.Majewski, G.Charpak, A.Breskin, and G.Mikenberg, A THIN MULTIWIRED CHAMBER OPERATING IN THE HIGH MULTIPLICATION MODE, *Nucl. Instrum. Methods* **217** (1983) 265-271

- [40] G.F.Knoll, Radiation Detection and Measurement. John Wiley & Sons, New York (1989).
- [41] H.Hofer et al., Some properties of thin gap gas chambers, Nucl. Instrum. Methods **A309** (1991) 422-426
- [42] S.Brehin et al., Some observations concerning the construction of proportional chambers with thick sense wires, Nucl. Instrum. Meth. **123** (1975) 225.
- [43] Y.Arai et al., Timing optimization of thin gap chambers for the use in the ATLAS muon endcap trigger, Nucl. Instrum. Methods **A367** (1995) 398-401
- [44] G.Bella et al., Development of calorimeters using thin chambers operating in a high gain mode, Nucl. Instrum. Methods **A252** (1986) 503-510
- [45] S.Dado et al., A new high gain thin gap detector for the opal hadron calorimeter, Nucl. Instrum. Methods **A252** (1986) 511-516
- [46] K.Nagai, "Thin gap chambers in ATLAS", Nucl. Instrum. Methods **A384** (1996) 219.
- [47] A.Rimoldi, "The ATLAS muon trigger chamber system", Nucl. Instrum. Methods **A409** (1998) 669.
- [48] D.Lazic et al., Drift velocity in n-Pentane mixtures and its fluence on timing properties of thin gap chambers, Nucl. Instrum. Methods **A410** (1998) 159-165.
- [49] H.Fukui et al., Studies on ageing effects and rate dependence of Thin Gap Chambers, Nucl. Instrum. Methods **A419** (1998) 497-502
- [50] S.Tsuno et al., Gamma-ray sensitivity of a thin gap chamber, Nucl. Instrum. Methods **A482** (2002) 667-673
- [51] V.Smakhtin, Testing TGC detectors in a high rate environment, Nucl. Instrum. Methods **A494** (2002) 500-503
- [52] V.Smakhtin, General gamma-radiation test of TGC detectors, NSS-MIC 2003 , Portland, OR, USA , 19-24 Oct 2003 Vol.2 1148-1150
- [53] A.Aloisio et al., The trigger chambers of the ATLAS muon spectrometer: production and tests., Nucl. Instrum. Methods **A535** (2004) 265-271
- [54] S.Tanaka et al., Development of mass-production technique of the ATLAS thin gap chamber in Japan, NSS-MIC 2003, Portland, USA, **Vol.5** (2003) 3750-3754
- [55] H.Nanjo et al., Neutron sensitivity of thin gap chambers, Nucl. Instrum. Methods **A543** (2005) 441-453
- [56] S.Baranov et al., *Estimation of Radiation Background, Impact on Detectors, Activation and Shielding Optimization in ATLAS*, ATL-GEN-2005-001 (2005).
- [57] M.Atac, A.V.Tollestrup, and D.Potter, Self-Quenching Streamer, Nucl. Instrum. Methods **200** (1982) 345
- [58] Claus Grupen, Particle Detectors, CAMBRIDGE UNIVERSITY PRESS (1996)

- [59] The web site of CONTEC Co. Ltd., <http://www.contec.com/>
- [60] E.Etzion et al, The Certification of ATLAS Thin Gap Chambers Produced in Israel and China, CERN-ATL-COM-MUON-2004-019, CERN, 30 Oct 2004.
- [61] O. Sasaki and M.Yoshida, "ASD IC for the Thin Gap Chambers in the LHC Atlas Experiment", *IEEE Trans. Nucl. Sci.*, 1998, Tronto, Ontario, Canada, pp. 1871-1875
- [62] Y.Arai, M.Ikeno et al., A VME 32 ch Pipeline TDC Module with TMC LSIs, *IEEE Trans. Nucl. Sci.*, IEEE Nuclear Science Symposium, San Francisco, Oct. 1995.
- [63] MWPC READOUT SYSTEM, KEK Internal Report.
- [64] SBS Technologies Inc. HomePage, <http://www.sbs.com/>
- [65] R.Brun, O.Couet, C.Vandoni, and P.Zanarini, PAW users guide, Program Library Q121, CERN (1991).
- [66] R.Brun and D.Lienart, HBOOK users guide (Version 4), Program Library Y250, CERN (1987).
- [67] V. N. Ivanchenko et al., Geant4 toolkit for simulation of HEP experiments, *Nucl. Instrum. Methods* **A502** (2003) 666-668
- [68] M.P.De Pascale et al., *J. Geophys. Res.* **98** (1993) 3501
- [69] P.K.F. Grieder, *Cosmic Rays at Earth*, Elsevier Science (2001).
- [70] M. Motoki et al., Precise Measurements of Atmospheric Muon Fluxes with the BESS Spectrometer, *Astropart. Phys.* **19** (2003) 113-126.
- [71] L.Alvarez-Gaume et al., REVIEW OF PARTICLE PHYSICS, *Phy. Let.* **B592** (2004)
- [72] H.A.Bethe, Molière's Theory of Multiple Scattering, *Phys. Rev.* **89** (1953) 1256-1266
- [73] S. Agosteo et al., A facility for the test of large area muon chambers at high rates, CERN-EP-2000-031 (February 16 2000)

Figure List

2.1	The Higgs potential V (2.23) for a complex scalar field with $\mu^2 < 0$ and $\lambda > 0$	11
2.2	$\Delta\chi^2 = \chi^2 - \chi_m^2$ vs. m_H curve. The line is the result of the fit using all LEP data [7]; the band represents an estimate of the theoretical error due to missing higher order corrections. The vertical band shows the 95% CL exclusion limit on m_H from the direct search. The dashed curve is the result obtained using the evaluation of $\Delta\alpha_{had}^{(5)}(m_Z^2)$ from [17].	13
2.3	Higgs Production diagram : (a)gluon fusion process, (b)Vector Boson Fusion process, (c) $t\bar{t}H$ production process, (d)W/Z associate production	14
2.4	Production cross section of Higgs[16]	14
2.5	Decay Width of Higgs boson as a function of Higgs Mass (M_H)[16].	15
2.6	Left: ATLAS sensitivity for the discovery of a Standard Model Higgs boson with full range (100-1000 GeV). The statistical significances are plotted for individual channels, as well as for the combination of all channels, assuming an integrated luminosity of $100fb^{-1}$ [15]. Right: Intermediate mass range (100-200GeV) with an integrated luminosity of $30fb^{-1}$ [18]. The blue line indicate the significance of the VBF process.	18
3.1	Schematic view of the CERN accelerator complex.	20
3.2	A selection of proton-(anti)proton cross-sections as function of interaction energy. The Tevatron collides protons onto antiprotons, whereas the LHC collides protons onto protons. The right-axis indicates the resulting number of events per second expected at the LHC, operated at high luminosity[21].	22
3.3	The interaction of various particles with the different components of a detector. Neutrinos are not shown on this chart because they rarely interact with matter, and can only be detected by missing matter and energy.	23
3.4	ATLAS Detector [11]	24
3.5	Atlas Inner Detector consisting of a pixel detector system, the SCT and the TRT. The whole Inner Detector has a length of 6.8m and a radius of 1.15m [14].	25
3.6	Layout of the ATLAS Calorimetry [14]	26
3.7	Side view of one quadrant of the ATLAS Detector[13].	27
3.8	Mesurement of sagitta.	29
3.9	Geometry of magnet windings and magnetic masses. Visible are the eight barrels toroid coils, with the end-cap coils interleaved. The solenoid winding lies inside the calorimeter volume. The tile calorimeter is modeled by four layers with different magnetic properties, plus an outside return yoke; the forward shielding disk is not displayed, for the sake of clarity. [14]	30
3.10	Photo of barrel troid magnet[24].	31
3.11	Monitored Drift Tube [14]	32

3.12	Momentum Resolution for ATLAS MDT Chamber [14]. Left shows the barrel region ($ \eta < 1.5$) and right shows the end-cap region ($ \eta > 1.5$).	33
3.13	Cathode Strip Chamber [14]	34
3.14	Resistive Plate Chamber [14]	35
3.15	Fluences in the muon chamber locations at high luminosity ($10^34\text{cm}^{-2}\text{s}^{-1}$) as described in Ref [56]. The n and γ fluences are in units of kHz/cm^2 and the μ and p fluences in Hz/cm^2	37
3.16	Block diagram of the Trigger/DAQ system. [20]	38
3.17	Longitudinal view of the TGC system, showing trajectories of high- and low- p_T muons and their trigger windows. M1 is the TGC triplet, M2, M3 are the TGC doublets, S and L are the small and large MDTs, I is the inner-station TGC. To allow overlapping of the physical chambers, doublets and triplets at adjacent ϕ are at slightly different z; the bold lines show a doublet/triplet at two adjacent ϕ 's. [14]	40
4.1	Time development of an avalanche near to an anode wire in a proportional chamber. [33]	44
4.2	Output signal from a wire chamber as a function of anode voltage with two different energy deposition, α particle and β particle. Different operation modes are indicated. [40]	45
4.3	Electric field lines in a MWPC with an anode pitch of 2mm as calculated with GARFIELD programm [36].	46
4.4	Cross section of TGC [14]	47
4.5	Left is the electric field lines in a TGC and right is the equipotential line (both were calculated with TARFIELD programm [37]).	47
4.6	Ionization and ion-fragmentation cross-section of hydrocarbon vapors under vacuum-ultraviolet radiation. n-pentane has largest cross section[38].	48
4.7	Support structure of TGC	49
4.8	Measured arrival time distribution for a minimum-ionizing particle and the fraction of the arrival times within a given time width. There is 99% efficiency for a gate width of 25ns, at 0° incident angle [13].	49
4.9	The relation between gas gap and output pulse height. [14]	50
4.10	Cross section of TGC Module. Left indicates Doublet and Right indicates Triplet. [14]	51
4.11	Left: R- ϕ view of the first trigger plane (triplet). Right R- ϕ view of the third trigger plane (pivot plane doublet). Each cell shown represents a single TGC unit (doublet or triplet). Chamber boundaries are shown. A single octant has been shaded and the chamber type at each radius indicated [14].	51
4.12	Block diagram of the ASD chip [61].	52
4.13	Picture of ASD card (without shield)	53
4.14	Picture of ASD (with shield)	53
4.15	The schematic view of the structure for wire readout part [14].	53
4.16	The size of the TGC produced in Japan.	55
5.1	The schematic view of CO_2 Channel for T7 type. CO_2 is flowed in the green and red volume to collect the n-pentane if there are some leakage.	58
5.2	Gas Leak Test Machine. There are 4 lines. The gas piping diagram is also shown in Fig.5.3.	59

5.3	The gas piping diagram for leak test. One line is the reference to check the change of the environment. Other three lines are used for the test. The pressure of each line is monitored by a manometer and a pressure sensor. The safety bubbler to avoid the overpressure is mounted on main line. The pressure is applied by the small pump. The flow rate is adjusted by a needle valve.	60
5.4	An example of the test result of gas tightness check. The pressure is shown as the function of the elapsed time of the test. Red line and blue line indicate the pressure of the reference and chamber, respectively.	60
5.5	There are 2 types of the repairing method. (a) a jig attached to a cleaner. (b) decompressing by the cleaner. (c) applying the pressure by compressed air-gun.	61
5.6	The schematic view of the Inner Leak. CO ₂ Channel and the paper-honeycomb are connected together through the pinhole. Since the pressure of the CO ₂ Channel (P) comes off to the paper-honeycomb, the pressure of the paper-honeycomb (P') rises up to P. In most case, there are some holes outside in the paper-honeycomb.	62
5.7	The pressure variation of the Inner Leak. After applying the pressure for appropriate period, it is released by opening a shutoff valve for the outlet of the CO ₂ channel. When $P = 0$, the valve is closed again and the pressure is returned from the paper-honeycomb. This graph shows the pressure return and its time constant clearly. . . .	62
5.8	Histogram of Chamber Leak	63
5.9	Histogram of CO ₂ channel (Main)	64
5.10	Histogram of CO ₂ channel (Side)	64
5.11	Example of the large continuous current. Red line indicates the current and blue line indicates the high voltage. The large current, about $1\mu A$, started to flow suddenly, and continued to flow for 30 minutes. The gradual decreasing of the current indicates that the dust or the thorn was burnt off by spark, and the anode wire and cathode plane became smoother.	65
5.12	The schematic view of Wire-Short phenomenon during the HV Test.	67
5.13	The schematic view of the electrical circuit inside the TGC. R_{HV} is the input resistor, R_C the surface resistivity of the graphite paint, C_{SS} the capacitance of adjoining pickup strips, C_{WS} the capacitance between the anode wire and cathode plane, C_{SC} the capacitance between the cathode plane and the pickup strip and C_{HV} the coupling capacitor for the anode wire readout.	68
5.14	Gas System for HV Test (using Bubbling Method)	69
5.15	The boiling point curve of n-pentane	69
5.16	The diagram of HV Test Gas Piping.	70
5.17	The system diagram of the Current Monitor System	71
5.18	(a) shows the amplifier circuit. (b) shows the schematic diagram of open-corrector output.	71
5.19	Monitor Programs	73
5.20	Timer Programs	73
5.21	Auto control Programs	73
5.22	The data sample of HV Test with mixed gas. Red line indicates the current and blue line indicates the high voltage.	74
5.23	The current distribution before and after HV Test. " Before " means the data before passing the 3.1kV Test. " After " means the data after passing the 3.3kV Test. . . .	75

5.24	The distribution of ($N_{\text{before}} - N_{\text{after}}$), where N_{before} and N_{after} indicate the number of the data exceeding $2\mu\text{A}$ in Fig.5.23.	75
5.25	(a) is the schematic view of the Cosmic Ray Test Stand and (b) is its picture.	76
5.26	(a) the side view of the Test Station. (b) picture of the station.	77
5.27	Image of Scintillator system (upper layer)	78
5.28	The Diagram of the trigger scheme.	78
5.29	The number of coincidence for a scintillation counter as a function of applied HV.	79
5.30	Timing difference between top and bottom scintillation counters.	80
5.31	Cross section of the Drift Tube	81
5.32	The relation between the electric field strength E and the drift velocity v with several gas mixture ratio and pressure[35].	81
5.33	The output pulse with two different HV. (a) $V=3.2\text{kV}$, (b) $V=3.65\text{kV}$	82
5.34	The gas system for the Drift Tube. A three-ports electric valve (EV1) controlled to two tanks, main and reserve, was switched automatically by monitoring the remained pressure.	82
5.35	Multiplicity distribution for various threshold voltages.	83
5.36	(a) Ideal Hit Pattern. (b) Schematic View of the Iteration.	84
5.37	Parameter Iteration.	84
5.38	Timing distribution of one drift tube. Since this graph was obtained using “ common stop mode ”, large time value is corresponding to the earlier signal. The red arrow indicates the origin of the drift time, T_0 . In this case, $T_0 = 1070[\text{nsec}]$	85
5.39	The scatter plot between d and t_1 after converging the parameter P_1 and P_2 . Red line indicate the fit by Eq.(5.4) with $P_1 = 0.556 \times 10^{-2}[\text{cm/ns}]$, $P_2 = -0.311 \times 10^{-5}[\text{cm/ns}^2]$	85
5.40	Schematic view of the estimation of the drift tube resolution.	87
5.41	(a) shows the scatter plot between x_1 and R . (b) is the projection of (a). We found the spatial resolution of is $\sigma \sim 355 [\mu\text{m}/\text{super-layer}]$	87
5.42	Composition of the detector and readout electronics.	88
5.43	The block diagram of TMC chip [62].	89
5.44	The timing diagram of the TMC (common stop mode). The signal within the time range is recorded.	89
5.45	The timing diagram of SWINE system.	90
5.46	Photograph of SWINE system. (a) left: PORQ module, right: HOG module (b) 1 PORQ module and 12 HOG modules mounted on original J2 back plane.	90
5.47	Diagram of the DAQ machine. PC and VME crate.	91
5.48	The flow-chart for the data taking and communication processes. The master and the slave were communicated using socket communication technology	92
5.49	Hit profile for scintillation counter.	94
5.50	Hit profile for drift tube.	95
5.51	Multiplicity distribution for UP drift tube. Large graph shows the multiplicity for each super-layer. Small graph shows the multiplicity for each layer of each super-layer.	96
5.52	Multiplicity distribution for DOWN drift tube. Large graph shows the multiplicity for each super-layer. Small graph shows the multiplicity for each layer of each super-layer.	97
5.53	Hit profile for TGC	98
5.54	Gas piping diagram for the Mixing System. The flow rate of liquid n-pentane and CO_2 was controlled by Mass Flow Controller.	100

5.55	Image of the Gas Mixing System.	100
5.56	Gas Piping diagram for Distribution System	101
5.57	This image shows the Gas Distribution System.	102
5.58	Mass Flow Output. “ Mixer ” indicates output for the mixing system. Others (from “ Cosmic1 ” to “ Cosmic3 ”) indicate the distributed output.	102
5.59	This figure shows the dependency of the mixture ratio on the flow rate of n-pentane (CO ₂ = 100cc/min).	103
5.60	The water temperature vs mixture rate.	104
5.61	TGC efficiency as a function of applied high voltage ($V_{th} = 100mV$).	104
6.1	Flow chart of the analysis	107
6.2	Hit Pattern 1. Pattern1 are most ideal 3 hits patterns.	108
6.3	Hit Pattern2. These are 4 hits in these patterns and are judged as the type that added the fake hit to pattern1.	108
6.4	Hit Pattern3. These are obtained by combining the two pattern1-types.	108
6.5	Hit Pattern 4. These are 2 hits in these patterns. These patterns are obtained by subtracting one hit from pattern1.	109
6.6	The schematic view of track reconstruction.	110
6.7	χ^2 distribution.	110
6.8	Event Display (xz plane).	111
6.9	TGC efficiency (red line) and the track reconstruction efficiency (blue line) as a function of the number of the required TGC layer.	112
6.10	The schematic view of Effective Area. The star marks indicate the intersection between the reconstructed track and TGC; black star indicates the position obtained by analysis program, and red star indicates the position through which the cosmic ray muon passed actually.	113
6.11	Positioning Method for T7 type. Red line indicates the coordinate system for the Data, and blue indicates for software.	114
6.12	Positioning Method for T4/T5 type. Red line indicates the coordinate system for the Data, and blue indicates for software.	114
6.13	Efficiency Mapper for T7 type.	115
6.14	Efficiency Mapper for T4/T5 type.	115
6.15	The distribution of the track number passed through in each cell (0th slot).	116
6.16	The distribution of the track number passed through in each cell (4th slot).	116
6.17	Two partial maps are synthesized to one map for T7 type.	117
6.18	Two partial maps are synthesized to one map for T4/T5 type.	117
6.19	Timing Distribution of TGC (left for wire and right for strip)	118
6.20	The distribution of the signal response time for T4 type. Blue chart indicates the measured value for wire and red chart for strip.	119
7.1	The geometry of the Test Station by Geant4 Toolkit.	121
7.2	Energy distribution of muons by BESS experiment[70].	122
7.3	Concept of the Knife-Edge Method.	125
7.4	Method to make a step function.	126

7.5	Knife-Edge Method sample. Above shows the distribution of the track obtained from limited TGC channel. Below shows the differentiation distribution of left. The resolution is obtained $\sigma \sim 6\text{mm}$ by fitting to gaussian function (red line).	126
7.6	(a) The schematic view of the estimation of MCS dependence. (b) The distribution of the length CD. The resolution is $\sigma = 1.07\text{mm}$ at 4th slot of the test station.	128
7.7	The resolution dependence on slot number of TGC.	128
7.8	Energy of cosmic ray muon vs resolution	129
7.9	The resolution as a function of z-position of TGC.	130
7.10	Z direction scan (simulation).	130
7.11	The resolution as a function of the χ^2 cut (restricted in only xz plane).	131
7.12	The resolution as a function of the χ^2 cut (restricted in only yz plane).	131
7.13	The resolution as a function of the χ^2 cut (restricted in both xz and yz plane).	132
7.14	The track reconstruction efficiency as a function of the χ^2 cut.	132
7.15	Angle distribution between 2 lines that decided by Up and Down super-layer. (real data)	133
7.16	Angle distribution between 2 lines that decided by Up and Down super-layer. (simulation data)	133
7.17	Left-Right ambiguity in track reconstruction.	134
7.18	Position dependence of large scattered step in Geant4 (x-z plane).	135
7.19	The ratio of triggered event with large scattered step as a function of each material name.	135
7.20	χ^2 vs angle scatter plot. (real data)	136
7.21	χ^2 vs angle scatter plot. (simulation data)	136
7.22	The resolution as a function of chi-cut.	137
7.23	The progress of the Inspection	138
7.24	The progress of the Leak Test	138
7.25	The progress of the HV Test	139
7.26	The progress of the Cosmic Ray Test	139
8.1	Histogram of Efficiency for all chambers.	141
8.2	Histogram of Efficiency for T7 Triplet	142
8.3	Histogram of Efficiency for T7 Doublet (D4 type)	142
8.4	Histogram of Efficiency for T7 Doublet (D6 type)	143
8.5	Histogram of Efficiency for T4 Doublet	143
8.6	Histogram of Efficiency for T5 Doublet	144
8.7	Bad example of efficiency map.	144
9.1	Schematic view of a gas chromatography.	147
9.2	The output from the gas chromatogram analyzing mixed gas ($CO_2 + \text{n-Pentane} = 5545$)	147

Table List

2.1	Electroweak coupling constants of fermions	10
3.1	The parameter list for the LHC Accelerator. [19]	19
3.2	MDT Parameter [25] [26]	32
3.3	CSC Parameter [14]	33
3.4	RPC Parameter [14]	35
4.1	The electron caputure cross section for various gas.	48
4.2	TGC type name in each sector.	50
4.3	Summary of the production of TGC Units at KEK.	54
4.4	The goal of inspection and system modification.	54
5.1	Summary of Leak Test	63
5.2	The list of HV Test Procedure.	66
5.3	HV Module OutPut	71
5.4	HV Test Summary	74
5.5	Raw Data Format. Right shows the data for master (TMC) process, Left shows for slave (SWINE) process.	93
5.6	Results of chemical tolerance of n-pentane. Tygon [®] is a clear tube made of soft PVC. It is the registered trademark of U.S.Stoneware Co..	99
5.7	Summary of the number of TGC module, ASD and HOG module.	105
7.1	Total thickness of materials. FR4 is a glass epoxy resin with SiO ₂ :52.8% and epoxy(C ₂ H ₂):47.2%. Scintillator is C ₉ H ₁₀ with a density of 1.032g/cm ³ . Steel is implemented with Fe:99.8%, C:0.2%. The density of the aluminum honeycomb panel is calculated from volume (2200 × 1500 × 27 cm ³) and weight (2700g). Mixed gas for TGC is CO ₂ + n-pentane, for drift tube is Ar + Ethane.	120
7.2	Results of the simulation for trigger rate	123
7.3	The summary of the trigger rate.	123
7.4	The ratio for recognized hit pattern.	123
7.5	Total radiation length of the test tation	127
7.6	Summary of inspection period.	137
7.7	The average week of each test. (unit: module/week)	137
8.1	Summary of the inspection.	140
8.2	Rank of the modules ordered by efficiency value.	141